

Lecture Notes in Mechanical Engineering

Alexander N. Evgrafov *Editor*

Advances in Mechanical Engineering

Selected Contributions
from the Conference “Modern
Engineering: Science and Education”,
Saint Petersburg, Russia, June 2019

 Springer

Lecture Notes in Mechanical Engineering

Lecture Notes in Mechanical Engineering (LNME) publishes the latest developments in Mechanical Engineering—quickly, informally and with high quality. Original research reported in proceedings and post-proceedings represents the core of LNME. Volumes published in LNME embrace all aspects, subfields and new challenges of mechanical engineering. Topics in the series include:

- Engineering Design
- Machinery and Machine Elements
- Mechanical Structures and Stress Analysis
- Automotive Engineering
- Engine Technology
- Aerospace Technology and Astronautics
- Nanotechnology and Microengineering
- Control, Robotics, Mechatronics
- MEMS
- Theoretical and Applied Mechanics
- Dynamical Systems, Control
- Fluid Mechanics
- Engineering Thermodynamics, Heat and Mass Transfer
- Manufacturing
- Precision Engineering, Instrumentation, Measurement
- Materials Engineering
- Tribology and Surface Technology

To submit a proposal or request further information, please contact the Springer Editor in your country:

China: Li Shen at li.shen@springer.com

India: Dr. Akash Chakraborty at akash.chakraborty@springernature.com

Rest of Asia, Australia, New Zealand: Swati Meherishi at swati.meherishi@springer.com

All other countries: Dr. Leontina Di Cecco at Leontina.dicecco@springer.com

To submit a proposal for a monograph, please check our Springer Tracts in Mechanical Engineering at <http://www.springer.com/series/11693> or contact Leontina.dicecco@springer.com

Indexed by SCOPUS. The books of the series are submitted for indexing to Web of Science.

More information about this series at <http://www.springer.com/series/11236>

Alexander N. Evgrafov
Editor

Advances in Mechanical Engineering

Selected Contributions from the Conference
“Modern Engineering: Science
and Education”, Saint Petersburg, Russia,
June 2019

 Springer

Preface

The “Modern Mechanical Engineering: Science and Education” (MMESE) Conference was initially organized by the Mechanical Engineering Department of Peter the Great St. Petersburg Polytechnic University in June 2011, St. Petersburg, Russia. It was envisioned as a forum to bring together scientists, university professors, graduate students, and mechanical engineers, presenting new science, technology, and engineering ideas and achievements.

The idea of holding such a forum proved to be highly relevant. Moreover, both the location and timing of the conference were quite appealing. Late June is a wonderful and romantic season in St. Petersburg—one of the most beautiful cities, located on the Neva river banks and surrounded by charming greenbelts. The conference attracted many participants, working in various fields of engineering: design, mechanics, materials, etc. The success of the conference inspired the organizers to turn the conference into an annual event.

More than 70 papers were presented at the seventh conference MMESE-2019. They covered topics ranging from the mechanics of machines, material engineering, structural strength, and tribological behavior to transport technologies, machinery quality, and innovations, in addition to dynamics of machines, walking mechanisms, and computational methods. All presenters contributed greatly to the success of the conference. However, for the purposes of this book, only 22 papers, authored by research groups representing various universities and institutes, were selected for inclusion.

I am particularly grateful to the authors for their contributions and all the participating experts for their valuable advice. Furthermore, I thank the staff and management of the university for their cooperation and support, and especially all members of the Program Committee and the Organizing Committee for their work in preparing and organizing the conference. Last but not least, I thank Springer for its professional assistance and particularly Mr. Pierpaolo Riva who supported this publication.

Saint Petersburg, Russia

Alexander N. Evgrafov

Contents

Axial Rotary Forging of Inner Flanges at Thin Wall Tube Blanks	1
L. B. Aksenov, S. N. Kunkin and N. M. Potapov	
On Vibrational Movements in a Testing Bench	11
Pavel A. Andrienko, Vladimir I. Karazin, Denis P. Kozlikin and Igor O. Khlebosolov	
Research of the Antifriction Properties of Carbon	17
Anatoly A. Asheichik and Daniil K. Zorin	
New Methodology for Kinematic Analysis in the Context of III-Class Six-Bar Linkage Study	27
Dmitry T. Babichev and Sergey Yu Lebedev	
Algorithm for the Placement of Orthogonal Polyhedrons for the Cutting and Packing Problems	41
Vladislav A. Chekanin and Alexander V. Chekanin	
Friction Steering Devices as an Object of Impulse Control	49
Roman Yu. Dobretsov, Nicolai N. Demidov and Andrei O. Kaninskii	
The Mechatronic Device Impulse Control in Vehicle Powertrains	63
Roman Yu. Dobretsov and Darya V. Uvakina	
Consideration of Friction in Linkage Mechanisms	75
Alexander N. Evgrafov, Gennady N. Petrov and Sergey A. Evgrafov	
Energy Flux Analysis of Axisymmetric Vibrations of Circular Cylindrical Shell on an Elastic Foundation	83
George V. Filippenko	

Research on Possibilities of Reaching Ultra-Low Speeds on Centrifugal Workbenches, and Selection of System Components	93
Vladimir I. Karazin, Anna V. Karazina, Denis P. Kozlikin, Anatolii V. Koshkin and Andrey V. Khisamov	
Strength Capabilities of Argon-arc Welded Joints of Shape Memory Alloy Ti–55.42 wt% Ni Wires	103
Elisey A. Khlopkov, Dmitry V. Kurushkin, Valerii V. Burkhovetskyi, Valeri M. Khanaev, Eugeny S. Ostropiko, Sergey A. Lyubomudrov and Yuriy N. Vyunenko	
Steel Fiber Manufacturing by Turning with Intense Self-oscillations . . .	111
Mikhail T. Korotkikh, Dmitriy Y. Kryazhev and Vladimir N. Kudryavtsev	
A New Way of Manufacturing Bimetal Products on the Basis of the Technology of Casting with Crystallization Under Pressure	119
Ruslan V. Kuznetsov and Pavel A. Kuznetsov	
Local Buckling of Box-Shaped Beams Due to Skew Bending	129
Konstantin Manzhula, Alexander Naumov and Sergei Sokolov	
Thinnest Finishing Treatment with a Focused Jet of Electrolytic Plasma	139
Alexander I. Popov, Mikhail M. Radkevich and Vasily G. Teplukhin	
On the Calculation of Blades Highly-Effective Impellers of Centrifugal Compressors	151
Vladimir A. Pukhliy, Sergey T. Miroshnichenko, Olga G. Lepekha, Alexander A. Zhuravlev and Alexandra K. Pomeranskaya	
Determination of Dynamic Errors in Machines with Elastic Links	163
Yuri A. Semenov and Nadezhda S. Semenova	
Localization of Plastic Deformation in Austenitic Steel at Low-Temperature Cycling Loading	175
Margarita A. Skotnikova, Angelina A. Strelnikova, Galina V. Ivanova, Alexander A. Popov and Ilnur S. Syundyukov	
Research of Vibrations of the Drive of Cycle Machines Under Powering Closure of Mechanisms	183
Iosif I. Vulfson	
Electrolyte-Plasma Polishing Ionization Model	193
Sergey V. Zakharov and Mikhail T. Korotkikh	

**Research and Development of a Spring Drive with Recovery Energy
in the Presence of a Variable Inertial Load** 209
Victor L. Zhavner, Wen Zhao, Chuanchao Yan and Long Wu

**Research of Spring Accumulators with Output Rotary Link Used
in Technological Equipment to Reduce Energy Consumption** 221
Milana V. Zhavner, Sen Li and Chuanchao Yan

Author Index 233

Axial Rotary Forging of Inner Flanges at Thin Wall Tube Blanks



L. B. Aksenov, S. N. Kunkin and N. M. Potapov

Abstract The paper presents the results of a study of the process of axial rotary forging by a conical roll performing a complex movement. In addition to the usual rotational motion the forming roll moves progressively at the initial moment of rotary forging and changes the angle of inclination relative to the workpiece at the final stage of the process. The technology was designed for the manufacture of axisymmetric parts with developed internal flanges, when the usual rotary forging process is limited by the loss of stability of the tube blank. The proposed technology ensures the stability of the workpiece during processing, and allows you to get a wide inner flange. Computer simulation of technology in the complex Deform 3D made it possible to determine the rational values of the parameters of the tool movement.

Keywords Axial rotary forging · Tube blank · Stability · Hollow flanges · Conical roll · Angle of inclination · Computer simulation

1 Introduction

The technology of axial rotary forging is intended for production of axisymmetric details from bar or tube blank (Fig. 1). This technology is a representative of processes with local deformation of the formed blank. In this case, only a part of the blank is in contact with the deforming tool, which reduces the contact area and the value of contact stresses, and, accordingly, the necessary deformation force, which ensures the efficiency of the technology, especially in small-scale production [1–3]. The cold axial rotary forging has the great advantages, which does not require heating and it is characterized by high accuracy and good quality of the processed surfaces. It is

L. B. Aksenov (✉) · S. N. Kunkin · N. M. Potapov
Peter the Great St. Petersburg Polytechnic University, St. Petersburg, Russia
e-mail: I_axenov@mail.spbstu.ru

S. N. Kunkin
e-mail: kunkin@spbstu.ru

N. M. Potapov
e-mail: nicitanic@yadex.ru

© Springer Nature Switzerland AG 2020
A. N. Evgrafov (ed.), *Advances in Mechanical Engineering*,
Lecture Notes in Mechanical Engineering,
https://doi.org/10.1007/978-3-030-39500-1_1

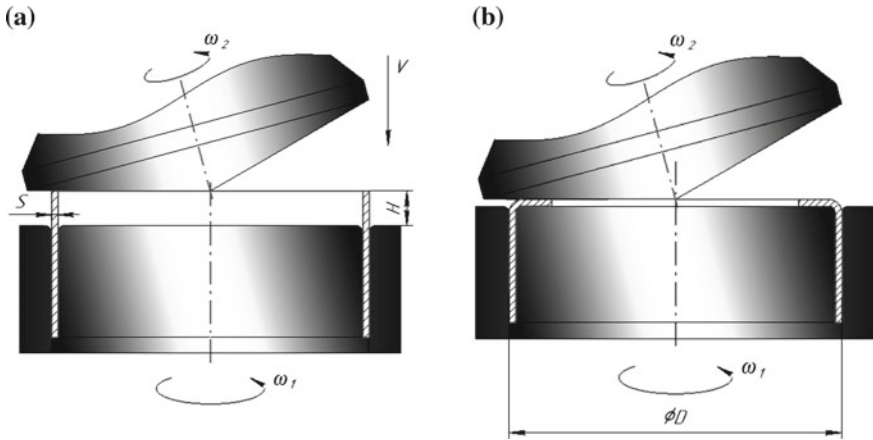


Fig. 1 Scheme of axial rotary forging of tube blanks: initial (a) and final (b) stages of the process

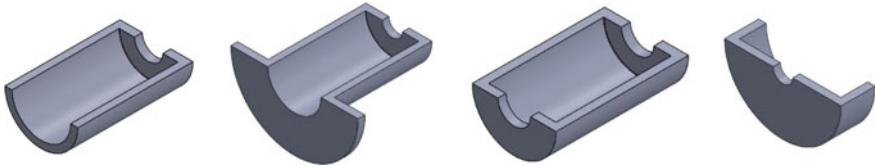


Fig. 2 Typical parts with inner flanges

natural that during cold forming the forming force will be higher than during hot rotary forging, and the plasticity of the deformed metal is lower, which imposes higher requirements for their analysis [4, 5].

A significant amount of axisymmetric parts are internal flanges, as well as parts of the type “cups with a bottom” (Fig. 2).

Narrow flanges with a thickness of the flange part about the thickness of the initial tube blank can be successfully obtained using the technology of rotary forging with flanging [6]. For thickened flanges with a small flange width (less than two wall thicknesses of the original tube workpiece), the technology of axial rotary forging with the upsetting of the deformed part of the workpiece is effective [7].

2 Research Methods

The problem is to form flanges with a developed flange width. The height of the deformable part of the workpiece is determined by the shape stability of the workpiece and usually should not exceed two wall thicknesses of the tube workpiece. At this value of the deformable part of the pipe billet, its volume may not be enough to form

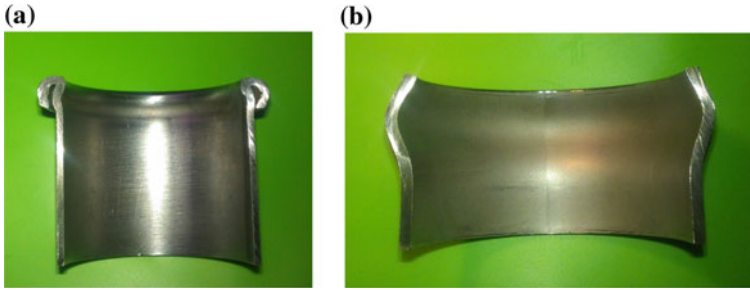


Fig. 3 Typical cases of tube work piece stability loss during axial rotary forging: folding outside (a) and inside (b) of the tube blank

the required flange geometry. But the height of the deformed part of the workpiece cannot be increased because of the loss of stability of the workpiece, as well as the formation of folds and cracks on the top part of the blank (Fig. 3).

The possibilities of controlling the flow of metal in the axial rotary forging processes are very limited. Different types of tools are used (cross roll, finned rolling rolls, mandrels, etc.) for directing the flow of metal in a required direction, and after forming some part of the flange to redirect the metal in a direction where the formation of the flange is not yet completed [8]. These technologies require considerable technological force, since most of the metal, in the final stage of the formation of the part, is a rigid zone with a stress state close to 3D compression. It is more effective to influence the direction of movement of the metal, using a change in the direction of the friction forces acting on the contact surface of the workpiece with the forming roll [9].

Some change in the direction of friction forces can be achieved by shifting the deformed rolls relative to their traditional location. So for the operation of obtaining internal flanges by flanging it requires to direct the flow of metal inside the workpiece. To direct the frictional forces in the desired direction, the deformed roll should be positioned with some displacement of the roll axis relative to the longitudinal axis of the tube blank [10]. The displacement of the top of the conical roll significantly changes the direction of the friction forces on the contact surface and facilitates the flow of metal in the radial direction. The recommended values of the forging cone roll offset for stable flanging depend on the ratio of the thickness and diameter of the tube blank, as well as on the material of the blank.

However, these technologies do not have sufficient stability and require strict compliance with the values of technological parameters, which makes it difficult to use them in industry. It is more efficient to control the flow of metal by changing the angle of inclination of the conical forming roll in the process of rotary forging.

The scheme of the investigated process of axial rotary forging is presented in Fig. 4. This scheme was used to identify opportunities and parameters of axial rotary forging to obtain internal wide flanges at tube blanks by a conical roll performing

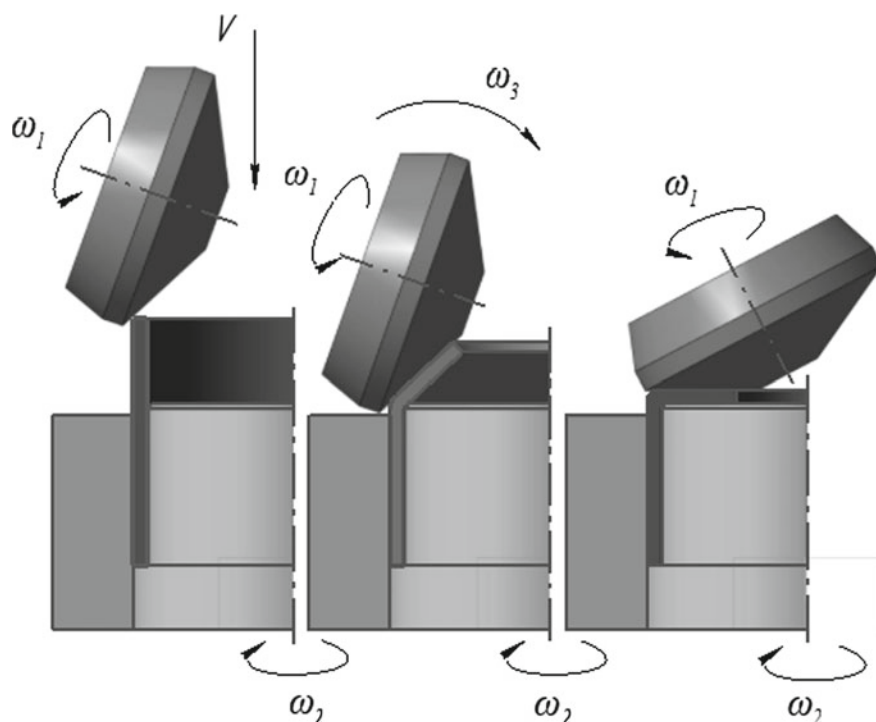


Fig. 4 The scheme of motion of the conical forming roll when rotary forging the inner flanges: ω_1 —axial angular velocity of rotation of the forming roll; ω_2 —angular velocity of rotation of the workpiece; ω_3 —angular velocity of inclination of the roll; V —the speed of translational motion of the forming roll

a complicated movement: rotational relative to its own axis, translational relative to the axis of the workpiece, as well as changing the angle of inclination.

The process consists of two stages. At the first stage of the process, the forming roll rotating at a speed of ω_1 and makes a translational movement at a speed V in the direction of the workpiece axis. At this stage, the roll bends the open part of the workpiece around the rounded edge of the die. After that, the vertical movement of the roll stops. In the second stage of rotary forging, the forming roll begins to rotate around an axis passing through the center of the arc of the outer rounded edge of the workpiece with an angular velocity ω_3 . The choice of this axis ensures uniform thickness over the entire flange surface. The rotation of the roll is carried out until the workpiece is completely pressed against the inner mandrel.

To implement the process of axial rotary forging, a fairly simple type of machine was used with a drive for rotation the workpiece and a passive roll receiving movement from the workpiece due to friction forces on the contact surface (Fig. 5).

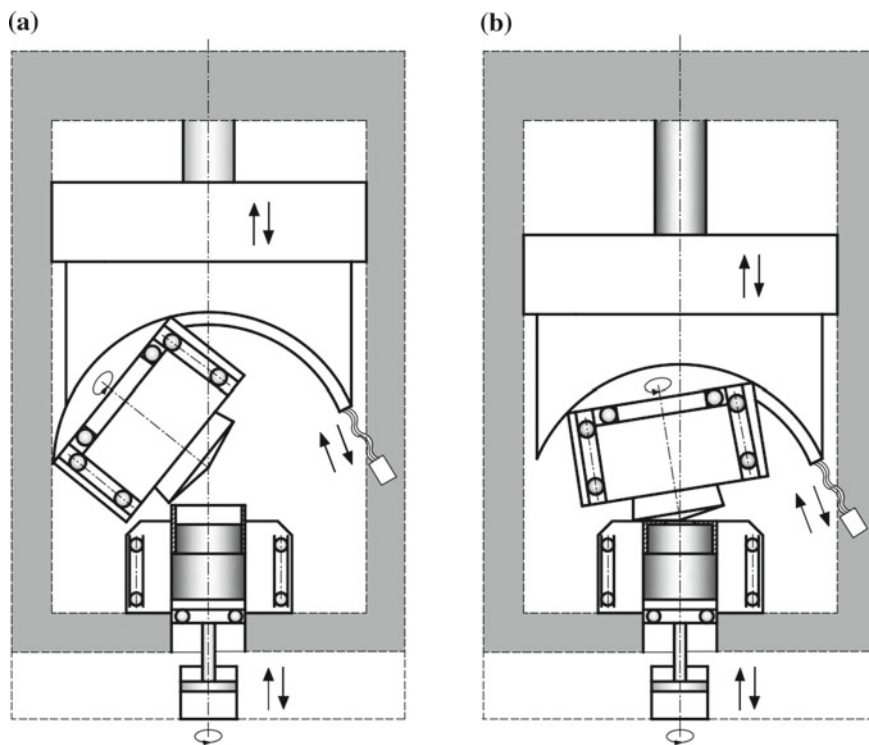


Fig. 5 Kinematics scheme of rotary forging machine with variable angle of inclination of the forming roll: **a** The initial stage of rotary forging, **b** the final stage of rotary forging

To determine the rational values of technological parameters, computer modeling was carried out in the project complex Deform-3D (V11). Modeling conditions: workpiece material AISI 1045; initial workpiece temperature 20 °C; Young's modulus 200 GPa; Poisson's ratio—0.3; plasticity condition—Misses-Huber; type of strain-hardening—isotropic, linear model; Coulomb friction between the forming roll and the workpiece, as well as between the die and the workpiece with a coefficient—0.1. Dimensions of the workpiece: outer diameter- $D = 100$ mm, wall thickness— $S = 5$ mm, blank height—90 mm, height of the formed part of the workpiece— $H = 20$ mm. the angle of inclination of the forming roll at the beginning of the process—15°.

The number of finite elements at the initial moment of rotary forging was—43,500 (Fig. 6) with the maximum side length of the element 5 mm, and the minimum 2.6 mm. In the process of calculation, the number of elements changed.

In addition, the fine mesh was installed at a height of 44.0 mm from the upper end of the workpiece, which was used for vertical movement of the roll more than 4 mm. By the end of the first phase of the process (the end of the vertical movement of the roll), the number of elements was 52,400, and by the end of rotary forging—55,000.

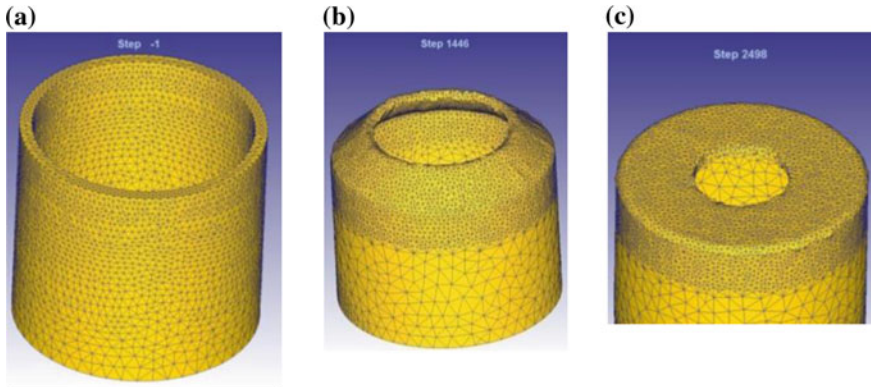


Fig. 6 Changing the finite element mesh in the process of axial rotary forging of the inner flange: **a** The beginning of the process; **b** the end of the translational movement of the rolling roll; **c** the final stage

Computer simulation of an ordinary rotary forging process has specific features due to the rotational movement of the forming roll relative to the workpiece and the local application of an external load [11–17]. This fact significantly distinguishes the simulation of these machines from the classical versions of mechanisms [18]. In presented process with more complex movement of the forming roll, which requires special techniques of combining the axes of the tool and the workpiece, as well as synchronization of their movement. These features lead to a significant increase in the calculation time. However, the simulation showed that the plastic deformation is localized mainly in the forming part of the workpiece. Therefore, the lower part of the workpiece can be considered non-deformable and the calculation to carry out for the workpiece with a height equal to twice the height of the formed part. As a result, it was possible to achieve a sufficiently fast and adequate modeling of the workpiece shaping at all stages of the process under study (Fig. 7).

Variation simulation allowed determining rational values of technological parameters presented in Table 1.

These parameters provide a stable rotary forging process, which allows obtaining the required geometry of the inner flange with its width from 3 to 15 wall thicknesses of the tube blank (Fig. 8).

The considered technology imposes increased requirements to the possibilities of kinematics of rotary forging machines. The present period of development of these machines is characterized by the development of multifunctional machines with multiple degrees of freedom for tool [19–21], capable of implementing different, almost any, schemes of movement of the forming roll with the use of modern and specialized CNC systems [22, 23]. Such machines open up new prospects for the synthesis and implementation of new technologies of axial rotary forging. The presented technology is focused on this new class of rotary forging machines.

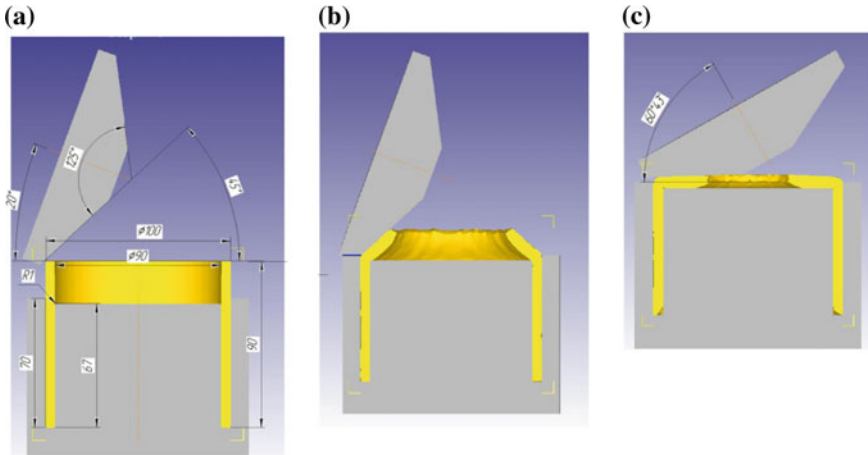


Fig. 7 Stages of forming computer simulation of the inner flange by the conical roll with a variable angle of inclination: **a** The beginning of the process; **b** the end of the translational motion of the forming roll; **c** the final stage

Table 1 Values of technological parameters rotary forging of internal flanges

Parameter	ω_1 (rev/min)	ω_2 (rev/min)	ω_3 (rad/s)	V (mm/s)
Value	~60	~60	~0.075	~1.5



Fig. 8 Inner flanges rotary forged from thin-walled tubes

3 Summary

1. The technology of axial rotary forging by a conical roll, which performs a complex movement: rotational relative to its own axis, translational in the direction of the workpiece axis, and changing the angle of inclination provides a stable process of manufacturing internal wide flanges on thin-walled tube blanks.
2. Adequate simulation of the axial rotary forging process is possible with the use of the calculation complex “Deform”. It is permissible without significant loss of accuracy of calculation to reduce the time of calculation when computer modeling the process using the height of the workpiece model approximately equal to two heights of the formed part of the workpiece.
3. The greatest efficiency of the process can be achieved with the use of multifunctional, rotary forging machines capable of implementing complex schemes of movement with multi degrees of freedom of the forming roll and using CNC.

References

1. Groche P, Fritsche D, Tekkaya EA, Allwood JM, Hirt G, Neugebauer R (2007) Incremental bulk metal forming. *Ann CIRP* 56:635–656
2. Nowak J, Madej L, Ziolkiewicz S, Plewinski A, Grosman F, Pietrzyk M (2008) Recent development in orbital forging technology. *Int J Mater Form (Supp 1)*:387–390
3. Plancak ME, Vilotic DZ, Stefanovic MC, Movrin DZ, Kacmarcik IZ (2012) Orbital forging—a plausible alternative for bulk metal forming. *J Trends Dev Mach Assoc Technol* 16(1):35–38
4. Han X, Hua L (2009) Comparison between cold rotary forging and conventional forging. *J Mech Sci Technol* 23:2668–2678
5. Loyda A, Reyes LA, Hernández-Muñoz GM, García-Castillo FA, Zambrano-Robledo P (2018) Influence of the incremental deformation during rotary forging on the microstructure behavior of a nickel-based super alloy. *Int J Adv Manuf Technol* 97:2383–2396
6. Aksenov L, Kunkin S (2014) Cold axial rotary outward-flanging of tube blanks by cylindrical rollers. In: III international scientific conference on global science and innovation, Chicago, pp 306–310, 23–24 Oct 2014
7. Sovremennoe mashinostroenie: nauka i obrazovanie: materialy 5-j Mezhdunarodnoj nauchno-prakticheskoy konferentsii./Pod red. A.N.Evgrafova i A.A.Popovicha.- SPb.: Izd-vo Politekhn.un-ta, 2016, pp 1062–1073 (in Russian)
8. Aksenov LB, Kunkin SN, Elkin NM (2011) Tortsevaya raskatka flantseyvkh detalej trubnykh soedinenij. *Metalloobrabotka №3(63)*:31–36
9. Kunkin SN, Aksenov LB (2014) Upravlenie techeniem metalla v protsessakh kholodnoj tortsevoj raskatki. *Sovremennoe mashinostroenie: nauka i obrazovanie: materialy 4-j Mezhdunarodnoj nauchno-prakticheskoy konferentsii/pod red. M.M.Radkevicha i A.N.Evgrafova. - SPb.: Izd-vo Politekhn. un-ta, pp 608–614 (in Russian)*
10. Evgrafov A (ed) (2016) Advances in mechanical engineering, Lectures Notes in Mechanical Engineering, Springer International Publishing, Switzerland, pp 175–181
11. Wang GC, Zhao GQ (2002) Simulation and analysis of rotary forging a ring workpiece using finite element method. *Finite Elem Anal Des* 38(12):1151–1164
12. Liu G, Yuan S, Zhang M (2001) Numerical analysis on rotary forging mechanism of a flange. *J Mater Sci Technol* 17(1):129–131

13. Munshi M, Shah K, Cho H, Altan T (2005) Finite element analysis of orbital forming used in spindle/inner ring assembly. In: 8th ICTP 2005—international conference on technology of plasticity, Verona, 9–13 Oct 2005
14. Deng XB, Hua L, Han XH (2011) Numerical and experimental investigation of cold rotary forging of a 20CrMnTi alloy spur bevel gear. *Mater Des* 32:1376–1389
15. Han X, Hua L (2012) Investigation on contact parameters in cold rotary forging using a 3D FE method. *Int J Adv Manuf Technol* 62:1087–1106
16. Standring PM (2006) Simulating rotary forging. In: Modelling of incremental bulk forming processes. Technical University of Darmstadt, Germany, 17/18 May 2006
17. Qin X (2014) Modelling and simulation of contact force in cold rotary forging. *J Cent South Univ* 21:35–42. <https://doi.org/10.1007/s11771-014-1912-9>
18. Evgrafov AN, Petrov GN (2017) Computer simulation of mechanisms. *Lecture Notes in Mechanical Engineering*, pp 45–56. https://www.scopus.com/inward/record.uri?eid=2-s2.0-85019231622&doi=10.1007%2f978-3-319-53363-6_6&partnerID=40&md5=2b3497f0d3d637746e659e041f3765ba, https://doi.org/10.1007/978-3-319-53363-6_6
19. Kocañda A (2015) Development of orbital forging processes by using Marciniak rocking-die solutions. In: Tekkaya AE et al (eds) 60 excellent inventions in metal forming. Springer, Heidelberg, pp 319–324. https://doi.org/10.1007/978-3-662-46312-3_49
20. Evgrafov AN, Petrov GN (2016) Drive selection of multidirectional mechanism with excess inputs. *Lecture Notes in Mechanical Engineering*, pp 31–37. https://www.scopus.com/inward/record.uri?eid=2-s2.0-84961279378&doi=10.1007%2f978-3-319-29579-4_4&partnerID=40&md5=86ab1468e9b804704bf69fc7b2d4b320, https://doi.org/10.1007/978-3-319-29579-4_4
21. ENN innovation & experience in metalforming. Retrieved: <https://www.denn.es/index.php/en/technologies/rotary-forging>. Accessed 17 Nov 2019
22. MJC Engineering & Technology. Rotary forging equipment. Retrieved: <http://www.mjceengineering.com/>. Accessed 13 Feb 2019
23. Global Metal Spinning Solutions Inc. CNC wheel forming and rotary forging machines. Retrieved: <http://www.globalmetalspinning.com/>. Accessed 10 Feb 2019

On Vibrational Movements in a Testing Bench



Pavel A. Andrienko, Vladimir I. Karazin, Denis P. Kozlikin
and Igor O. Khlebosolov

Abstract The paper considers the issues of imitation of real conditions of movement of various objects of navigation systems in laboratory conditions using a vibrafuge, a bench representing a centrifuge, on the rotor of which there is a device providing additional reciprocating movement of the table with a test object. The main type of testing is vibration with different frequencies and amplitudes in the field of linear acceleration, changing in a certain range, is a very common type of load in real objects. Evaluation was carried out of the influence of Coriolis accelerations and forces on the object under the action of vibration load in the field of linear accelerations. According to the results of the study, a methodology for their evaluation using side component coefficients is proposed, which can be used for test objects with different geometries and different radii of the basic centrifuge.

Keywords Vibration test bench · Vibrafuge · Coriolis acceleration · Vibration acceleration · Test impact · Vibration in the field of linear accelerations

1 Introduction

Imitation of real conditions of movement of various objects of navigation systems is the most economical way of testing in laboratory conditions. Vibrafuge is quite rare at present time as a simulation and testing bench. It is a centrifuge, the rotor of which has a device that provides additional reciprocating movement of the table with a test object.

When designing new equipment for aerospace systems, the issue of testing prototypes is very acute. Field tests are expensive and complex in terms of organization. Using simulation benches makes it possible to increase availability of the necessary tests, conducting them in a laboratory environment and providing good informational content of the research. Reproduction of combined effects, to which this paper is devoted, is extremely important for the testing of devices with a short operational

P. A. Andrienko (✉) · V. I. Karazin · D. P. Kozlikin · I. O. Khlebosolov
Peter the Great Saint-Petersburg Polytechnic University, St. Petersburg, Russia
e-mail: pavandrienko@spbstu.ru

© Springer Nature Switzerland AG 2020
A. N. Evgrafov (ed.), *Advances in Mechanical Engineering*,
Lecture Notes in Mechanical Engineering,
https://doi.org/10.1007/978-3-030-39500-1_2

life. They should not have excess strength reserves to ensure minimum masses. Therefore, in the case of sequential loads, the so-called “overtesting” is possible (the operational life of the test object is longer than required). Vibrafuge testing is one of the means of solving this problem [1].

Vibration with different frequencies and amplitudes in the field of linear accelerations, changing in a certain range, is a very common type of load in real objects. In testing benches, this additional movement of the object is created by a controlled electrodynamic vibrator. To ensure its normal functioning it is necessary to use some additional devices [2–7], providing balancing of moving masses in the process of rotation.

However, in connection with the presence of translational and relative motions on the vibrafuge, there is an additional lateral force caused by the Coriolis acceleration.

The goal of the proposed study is to develop methodology for evaluating the effect of Coriolis acceleration on the type of test impact.

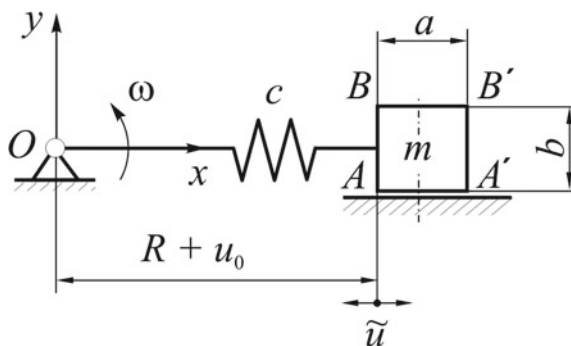
Coriolis acceleration is orthogonal to the main linear acceleration vectors from centrifuge rotation and harmonic vibration. Parameters of relative and translational motion fully determine the value of Coriolis acceleration, which is also a harmonic variable. For testing some products that have a multidirectional sensitivity, the evaluation of these ratios is very significant.

As it was shown in works [8–13], there are various possibilities of realization of this problem in laboratory conditions. However, in most cases, in order to reproduce the alternating component, different types of vibration test benches [14, 15] are used, depending on the required parameter values, and the background acceleration is set in a centrifugal way, carrying out translational rotation by an electric motor with a constant or variable-specified speed of rotation. Thus, we must consider the design model in Fig. 1, in which m is the mass of the moving system, including the test object with dimensions $a \times b$.

Mass m moves along a circular trajectory at an angular velocity $\omega = \text{const}$ and reciprocating movement

$$\tilde{u} = u_0 \sin vt, \quad (1)$$

Fig. 1 Single-mass design model



where u_0 is static displacement and v is rotational frequency. Mass m is held on the trajectory by an element of rigidity c , the value of which is the cause and measure of the above-mentioned static displacement u_0 :

$$u_0 = \frac{m\omega^2(R + u_0)}{c} = \frac{mw_L}{c}, \quad (2)$$

where w_L is centripetal acceleration and the product of $|mw_L|$ determines the magnitude of the centrifugal force acting on the test object. Considering that stiffness c is selected from the condition $c = mv^2$, we have

$$u_0 = \frac{R \cdot \omega^2/v^2}{1 - \omega^2/v^2} = \frac{w_L}{v^2}, \quad (3)$$

The system is stable at $\omega^2/v^2 < 1$, so with an allowable inaccuracy it can be assumed that

$$u_0 \approx R \cdot \omega^2/v^2, \quad (4)$$

As a result of the interaction between translational velocity ω and relative movement u , there is a Coriolis acceleration, which is geometrically summed up with the two accelerations described above.

Let us consider in detail the Coriolis acceleration that occurs. The relative motion of mobile mass m takes place along axis x according to the given law

$$x = r \sin vt, \quad r = \frac{w_b}{v^2}, \quad (5)$$

where w_b is specified vibration acceleration. Movement also occurs along axis y because of gaps and deformation of supports. The inertial force of Coriolis acceleration has the form of

$$\overline{\Phi_C} = 2m \left| \begin{pmatrix} \bar{i} & \bar{j} & \bar{k} \\ \dot{x} & \dot{y} & 0 \\ 0 & 0 & \omega \end{pmatrix} \right| = 2m\dot{y}\omega\bar{i} - 2m\dot{x}\omega\bar{j}, \quad (6)$$

Harmonic force acts in the direction of axis y

$$\Phi_{C_y} = -2m\dot{x}\omega = -2m\omega\frac{b}{v} \cos vt, \quad (7)$$

We will find the angular velocity knowing linear acceleration w_L :

$$\omega = \sqrt{\frac{w_L}{R}}.$$

Table 1 The values of Coriolis acceleration and inertia force for different frequencies

f (Hz)	w_{Cy} (m/s ²)	Φ_{Cy} (N)
10	1000	20,000
100	100	2000
1000	10	200
2000	5	100

For more clarity of the above reasoning, let us consider numerical examples.

Let us take the following values: $w_L = 200$ g, $R = 0.5$ m, $\omega = 63$ 1/s. Then, with $m = 20$ kg, $w_b = 500$ m/s² the moduli of Coriolis acceleration $|w_{Cy}| = 2\omega w_b/v$ and inertia force $|\Phi_{Cy}| = m|w_{Cy}|$ have the values presented in Table 1.

To create the required vibration acceleration $w_b = 50$ g with frequency $f = 10$ Hz, amplitude $r = 0.13$ m, which is 10 times the maximum amplitude of the electrodynamic vibrator, is required. Therefore, at this frequency we will limit the inertia force modulus $|\Phi_{Cy}| = 2000$ N and consequently the Coriolis acceleration will have amplitude $|w_{Cy}| = 100$ m/s².

Taking into account that the Coriolis acceleration amplitude is equal to $2\omega|\tilde{u}|$, we obtain the coefficient of transverse component of the vibration acceleration

$$K_y^e = \frac{2\omega|\dot{\tilde{u}}|}{u_0 v^2} = 2 \frac{\omega}{v} = 2 \frac{\sqrt{w_L}}{v\sqrt{R}}. \quad (8)$$

For the parameters in Table 1

$$\begin{aligned} R = 1.0 \text{ m} &\Rightarrow K_{yI}^e = 2 \frac{\sqrt{2000}}{2\pi\sqrt{1,0}} \approx 14.2, \\ R = 1.0 \text{ m} &\Rightarrow K_{yII}^e = 2 \frac{\sqrt{500}}{2\pi\sqrt{1,0}} \approx 7.12, \\ R = 2.0 \text{ m} &\Rightarrow K_{yIII}^e = 2 \frac{\sqrt{250}}{2\pi\sqrt{2,0}} \approx 3.56. \end{aligned} \quad (9)$$

The obtained coefficients should be compared with the coefficients of transverse K_{yA} , K_{yB} and longitudinal $K_{xA A'}$ components determining the “spread” of acceleration over the area of the test object.

According to Fig. 1:

$$\begin{aligned} w_{yA'} &= 0; \quad w_{yB'} = w_{xB'} \frac{b}{2(R+a)}; \\ K_{yA} &= \frac{w_{yA}}{w_{xA}}; \quad K_{xAB} = \frac{w_{xA}}{w_{xB}}. \end{aligned}$$

A maximum value of the transverse component coefficient for point B :

$$K_{yB} = \frac{w_{yB}}{w_{xB}} = \frac{b}{2R}. \quad (10)$$

The change in the longitudinal component coefficient from point A to point A' is

$$K_{xAA'} = \frac{w_{xA'}}{w_{xA}} = \frac{R+a}{R} = 1 + \frac{a}{R}. \quad (11)$$

Thus, at the value of radius $R = 1.0$ M with the test object with dimensions 0.5×0.5 m we obtain the coefficient of the transverse component at point B :

$$K_{yB} = \frac{0.5}{2} = 0.25,$$

and the coefficient of the longitudinal component of acceleration

$$K_{xAA'} = \frac{1.5}{1} = 1.5.$$

Returning to calculations (6), it should be noted that the transverse component coefficients of Coriolis phenomena are quite significant, and the total transverse component of acceleration at the extreme points of the test object can be more than 100%.

The results of the above research confirm the need to take into account and evaluate side loads that occur due to interaction of the two movements in the vibrafuge. If a testing bench is designed for products with known dimensions, the value of the transverse component coefficient can be influenced by changing the radius of the centrifuge arm. As the radius increases, the side components decrease.

2 Conclusion

One of the important results of the research presented is the very fact of discussing this problem. As laboratory practice shows, it is not always possible to take into account additional impacts that were not pre-planned. Coriolis forces and gyroscopic moments always occur when there is a corresponding mutual orientation of the vectors of translational and relative velocities.

For sufficiently large test objects, knowing the location of the overload-sensitive elements in them, it is possible to select the most advantageous positions and, using the coefficients of lateral components, to determine the true impact with sufficient accuracy.

Using the proposed method, it is easy to construct nomograms for practical use in laboratory tests on multi-motor testing benches.

References

1. Samsonov LM, Kalyaev AK, Markov AV et al (1981) Rotational methods of testing instrument devices/M.: Mashinostroenie, 135p
2. Evgrafov AN, Karazin VI, Kozlikin DP, Khlebosolov IO (2018) Some characteristics of linear acceleration reproduction with flexible harmonical component. *Lecture Notes in Mechanical Engineering, PartF5*, pp 71–81
3. Karazin VI, Kozlikin DP, Sukhanov AA, Tereshin VA, Khlebosolov IO (2017) Some ways of stable counterbalancing in respect to moving masses on centrifuges. *Lecture Notes in Mechanical Engineering*, pp 73–85
4. Evgrafov AN, Karazin VI, Kozlikin DP, Khlebosolov IO (2017) Centrifuges for variable accelerations generation. *Int Rev Mech Eng* 11(5):280–285
5. Karazin VI, Kozlikin DP, Sloushch AV, Khlebosolov IO (2007) Dynamic model of vibratory stand. *Theory of mechanisms and machines. Periodic Sci Methodical J* 1(9):38–44 (rus, V. 5, St. Petersburg: Publishing House of the Polytechnic University Press)
6. Karazin VI, Kozlikin DP, Khlebosolov IO (2006) Dynamic stands for vibro-rotary tests. In: *Scientific and technical reports of SPbGPU. SPb: Publishing House of SPbGPU; №3(45)*, pp 44–49 (rus)
7. Karazin VI, Kozlikin DP, Khlebosolov IO (2007) On balancing the inertial forces in vibrotsentrifugal. *Theory of mechanisms and machines. Periodic Sci Methodical J* 2(10):63–71 (rus, V. 5, St. Petersburg: Publishing House of the Polytechnic University Press)
8. Andrienko PA, Karazin VI, Khlebosolov IO (2017) Bench tests of vibroacoustic effects. *Lecture Notes in Mechanical Engineering*, pp 11–17
9. Karazin VI, Kozlikin DP, Sukhanov AA, Khlebosolov IO (2016) One stable scheme of centrifugal forces dynamic balance. *Lecture Notes in Mechanical Engineering*, pp 75–85
10. Andrienko PA, Karazin VI, Khlebosolov IO (2014) On an integrated approach to laboratory testing of navigation systems. *Modern mechanical engineering. Sci Educ* 4:121–130 (rus)
11. Karazin VI, Kozlikin DP, Sukhanov AA, Tereshin VA, Khlebosolov IO (2016) Certain ways is relatively stable balancing of moving masses on the centrifuges. *Modern mechanical engineering. Sci Educ* 5:216–229 (rus)
12. Evgrafov AN, Karazin VI, Khlebosolov IO (2003) Playing motion parameters on rotary stands. *Theory of mechanisms and machines, vol 1, issue 1. Publishing House of the Polytechnic University Press, St. Petersburg*, pp 92–96 (rus)
13. Karazin VI, Kozlikin DP, Sukhanov AA, Khlebosolov IO (2014) About the same scheme sustainable dynamic razgryzaniya centrifugal forces. *Modern mechanical engineering. Sci Educ* 4:203–216 (rus)
14. Astashev VK, Babitsky VI (2007) *Ultrasonic processes and machines. Dynamics, control and applications. Springer, Heidelberg*, 330p
15. Ksenofontov VI, Nikolaev VN, Chernokrylov SYu (1992) Multifunctional dynamic stand. *Testing and control stands. L.: LGTU*, pp 29–32 (rus)

Research of the Antifriction Properties of Carbon



Anatoly A. Asheichik and Daniil K. Zorin

Abstract For delivery of a measurement complex into an oil well for the analysis of a condition of an oil well and its possible restoration special cables pushers are used. A matrix of such cable most often is carbon which has high strength, chemical resistance to influence of sea water and gas-oil mix and to an explosive decompression. In this work antifrictional properties of carbon were investigated: friction coefficient and wear resistance in the wide range of loadings and friction in various environments. The stand design for researches of materials at back and forth movement and procedure of testing of samples of cables with carbonic matrixes are described. Experimental data on change of friction coefficient of carbon at loadings from 3 to 520 N at friction without lubricant and greasing by crude oil or hydraulic oil are given. The methodology and results of an experimental study of carbon samples for wear during friction on steel and reciprocating without lubricant and when lubricating with liquid lubricants are presented.

Keywords Oil · Cable pusher · Carbon · Friction coefficient · Wear resistance · Antifrictional properties

1 Introduction

Nowadays, in the aerospace industry, automotive industry, shipbuilding, mechanical engineering, oil industry are widely used carbon, which have high strength, stiffness, low specific gravity, increased chemical resistance and high modulus of elasticity [1–7]. So in the oil industry for the delivery of the measuring complex to the oil well in order to analyze the condition of the well and its possible recovery, special push cables are used, the matrix of which is made of carbon fiber. In this research, we studied the antifriction properties of carbon fibers of two types of carbon with the conventional names “OLD” and “V15” [8–11]: the friction coefficient and wear resistance over a wide range of loads and friction in various environments.

A. A. Asheichik (✉) · D. K. Zorin
Peter the Great St.-Petersburg Polytechnic University, 29, Polytechnic St., 195251 St.-Petersburg,
Russian Federation

2 The Design of the Stand for the Study of Carbon on Friction and Wear

In Fig. 1 we can see the appearance of the stand which was used to study the coefficients of strength and wear resistance of materials. The design of the stand [12–15] includes the following main components: a crank group and a system for loading samples. The drive of the stand consists of an electric motor, a worm gear and two elastic sleeve-finger couplings. The loading system consists of a lever with suspension for cargos, a wedge-shaped plunger and a mandrel with a holder for the upper specimen installed in it. For testing in a liquid medium, a bath is installed.

The pressure on the friction surface varies depending on the weight of the cargo and the size of the samples. The friction coefficient was measured using a beam with strain gauges. The value of the signal from the output of the strain gauge was measured by a PCS-500A digital storage oscilloscope, which was bundled with a personal computer [16–20]. While studying the antifriction properties of carbon, two cable samples were installed at once. The stand was assembled: an upper steel specimen was installed in the upper holder, and was loaded with loads through the plunger and lever.

Using a set of instrumentation, the experimenter receives a signal on a computer screen. Markers measure the double amplitude of the signal change and its period. In addition, a file with a digital test report is recorded. Thus, the value of the friction force was measured on a computer screen and could be determined with high accuracy by the results of processing a digital protocol. The results of measuring the friction force were obtained in mV. To translate the frictional force into Newtons when setting up

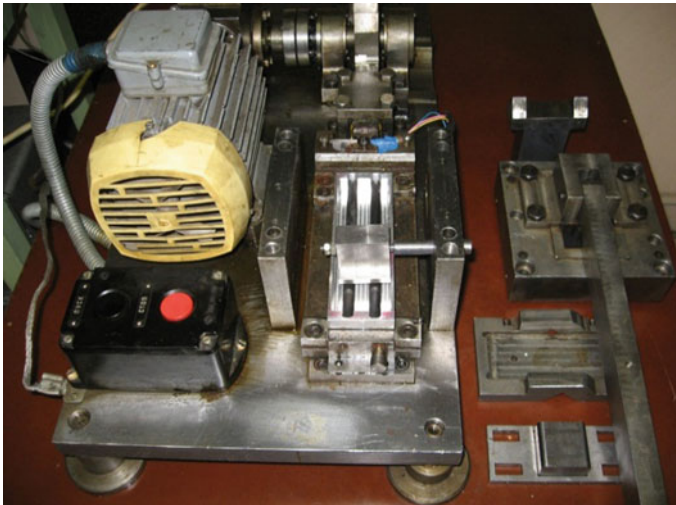


Fig. 1 The appearance of the stand for testing materials

the stand, it was calibrated by installing various strain gauges and using an electronic dynamometer.

The friction coefficient was determined for two cables under the conventional names “OLD” and “V15”, which differ in the chemical composition of the cable matrix. The values of the friction force and the coefficient of friction were determined under normal efforts on two cables: 3.11; 50; 100, 200, 291, 403, 515 N. The friction coefficient was calculated as the ratio of the friction force, measured during testing at the stand, to the normal load on two cable samples.

3 The Results of Experimental Studies of the Friction Coefficients of Carbon

The tests were carried out with friction without lubricant, friction when lubricated with crude oil and lubricated with hydraulic oil with the same viscosity as crude oil. The results of all measurements and calculations are presented in Table 1. The dependences of the change in the coefficient of friction on the normal load are shown in Figs. 2, 3 and 4.

4 Methodology and Test Results of Carbon Wear

The experimental finding of the wear of the composite cable samples was carried out on a stand, which was used to find the coefficient of friction of carbon during reciprocating motion. To determine the wear of the composite cable, two cable samples were installed in the holder at the same time. A sample of steel 45 was placed on top of them, for which the dimensions of the friction surface, its roughness and weight (260 g) corresponded to the actual parameters during cable exploitation. The sample was mounted on the shaft and due to the presence of a groove in it had the ability to self-install relative to the cable samples (three degrees of freedom).

Wear tests were carried out during friction without lubricant, as well as with lubricant, which was crude oil and hydraulic oil. The appearance of the friction unit during wear tests with oil is shown in Fig. 5. After conducting wear tests, the width of the wear pad was measured and the height of the worn layer was calculated. Wear was measured at three points on each cable. Measurement schemes for the length of the cable and its diameter are shown in Figs. 6 and 7. The wear along the length of the carbon sample was found at three points (Fig. 6) for the two carbon fibers already indicated under the conventional names “OLD” and “V15”. Taking into account the exploitation of the pusher cable under real conditions, studies of the wear resistance of carbon matrices were carried out only at normal load $F_n = 2.6$ N and the number of double cycles was 17,000.

Table 1 The results of measurements and calculations of the friction force and friction coefficient for carbons “OLD” and “V15”

№	Carbon type	Lubricant	Normal load F_n , H	Friction force F_{TP} , H	Coefficient of friction f
1	OLD	Friction without lubricant	3.11	1.19	0.383
			50	16.7	0.334
			100	31.2	0.312
			200	58.4	0.292
2	OLD	Crude oil	3.11	0.740	0.238
			50	10.9	0.218
			100	20.8	0.208
			200	39.4	0.197
3	OLD	Hydraulic oil	3.11	0.665	0.214
			50	9.70	0.194
			100	18.1	0.181
			200	33.4	0.167
4	V15	Friction without lubricant	3.11	0.921	0.296
			50	13.7	0.274
			100	26.1	0.261
			200	49.4	0.247
5	V15	Crude oil	3.11	0.507	0.163
			50	7.50	0.150
			100	14.1	0.141
			200	26.4	0.132
6	V15	Hydraulic oil	3.11	0.457	0.147
			50	6.65	0.133
			100	12.5	0.125
			200	22.8	0.114

Scheme measuring the width of the wear pad L of the worn surface of the cable is shown in Fig. 7. The height of the worn layer was calculated by the Eq. 1.

$$h = \frac{d - \sqrt{(d)^2 - (L)^2}}{2}, \quad (1)$$

where d is the cable diameter, $d = 9$ mm, L is the width of the wear pad, mm.

The tests were carried out with friction without lubricant, friction when lubricated with crude oil and lubricated with hydraulic oil with the same viscosity as crude oil. Since wear measurements were carried out for two cables, then in Table 2 for each point of wear measurement (see Fig. 7) shows the average values of wear measurements of these cables.

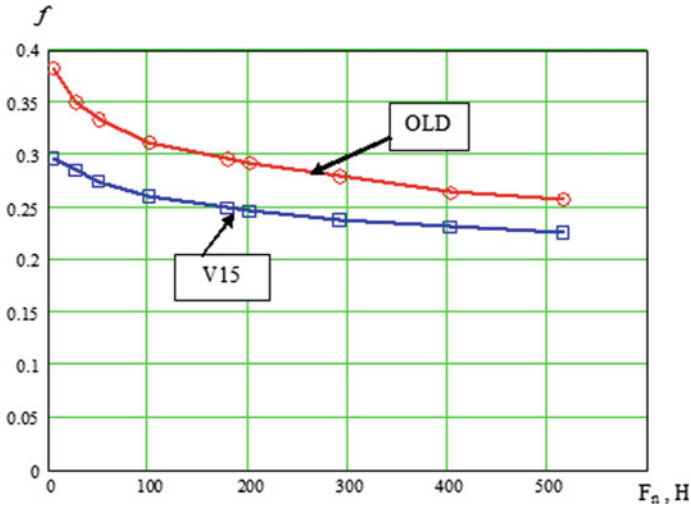


Fig. 2 Dependence of the coefficient of friction on normal load during friction without lubricant

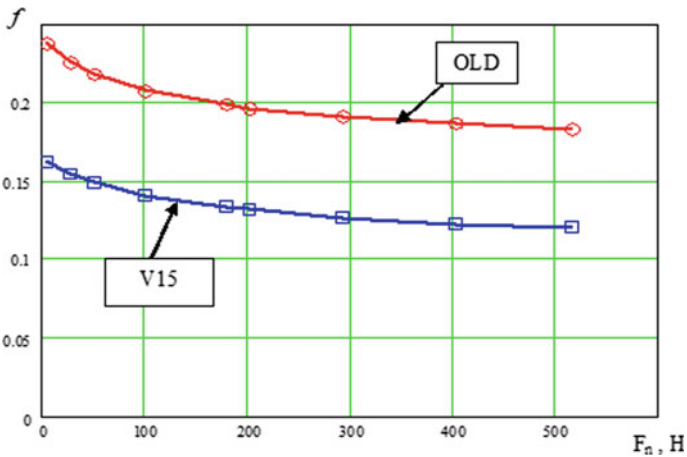


Fig. 3 The dependence of the coefficient of friction on the normal load when lubricating with crude oil

5 Conclusion

The permissible value of the width of the wear pad for the cable matrix in the real unit of the injection head under the above test conditions and any type of lubrication was 1 mm. Thus, from the analysis of the test results of the two types of carbon for wear, it follows that the carbon OLD does not meet the specified criteria for wear. From experiments with dry friction it follows that the width of the wear area of this

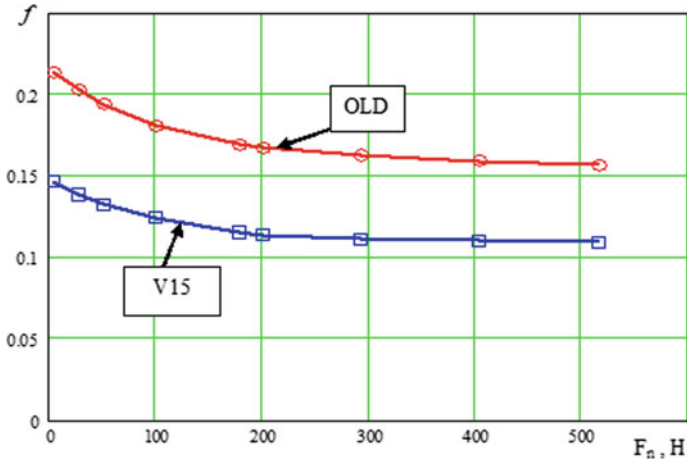


Fig. 4 The dependence of the coefficient of friction on normal load when lubricated with hydraulic oil

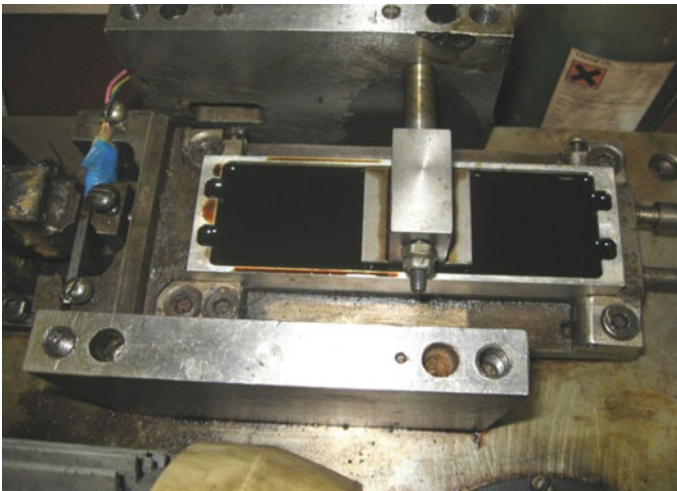


Fig. 5 The design of the unit to study the wear of the cable matrix

carbon was at the measurement points 1, 2, 3, respectively: 1.27; 1.41; 1.25 mm. Carbon “V15” fully complies with the specified criterion in terms of the allowable wear under all friction conditions.

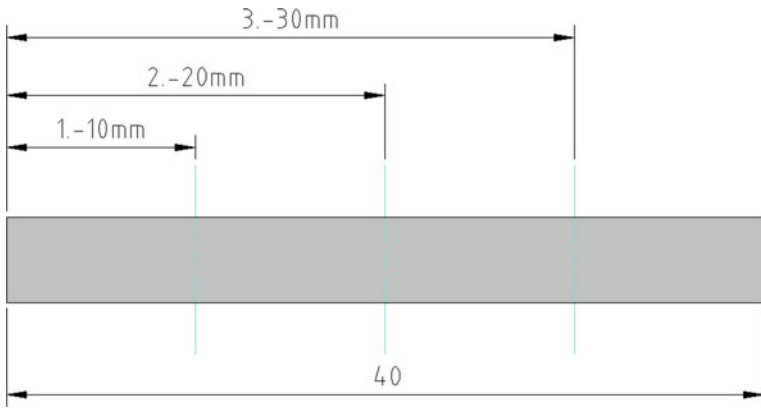


Fig. 6 Scheme for measuring wear along the length of a worn surface

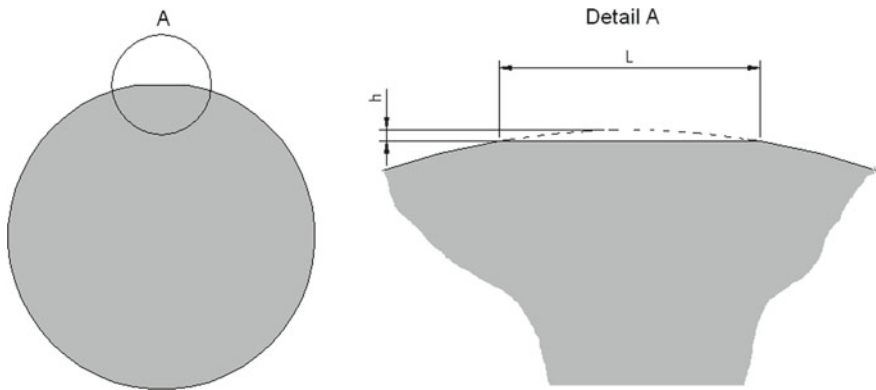


Fig. 7 Scheme for cable diameter wear measurement

From the analysis of the results of determining the friction coefficients given in Table 1 and Figs. 4, 5 and 6, it follows that carbon “V15” has a friction coefficient 1.3–1.4 times lower than carbon “OLD” in the entire range of normal loads. Therefore, according to the results of the research of antifriction properties of the matrices of cables, the V15 carbon matrix is the best.

Table 2 The results of measurements and calculations of wear for carbons “OLD” and “V15”

№	Carbon type	Lubricant	№ of point (Fig. 7)	Wear pad width L (mm)	Worn layer height h (mm)
1	OLD	Friction without lubricant	1	1.27	0.042
			2	1.41	0.054
			3	1.25	0.041
2	OLD	Crude oil	1	0.81	0.018
			2	0.85	0.021
			3	0.79	0.016
3	OLD	Hydraulic oil	1	0.54	0.010
			2	0.58	0.012
			3	0.51	0.009
4	V15	Friction without lubricant	1	0.61	0.010
			2	0.67	0.013
			3	0.62	0.011
5	V15	Crude oil	1	0.40	0.004
			2	0.43	0.005
			3	0.39	0.004
6	V15	Hydraulic oil	1	0.32	0.003
			2	0.36	0.004
			3	0.33	0.003

References

- Breki AD, Nosonovsky M (2018) Ultraslow frictional sliding and the stick-slip transition. *J Appl Phys Lett* 113(24):241602. <https://doi.org/10.1063/1.5064820>
- Breki AD, Didenko AL, Kudryavtsev VV, Vasilyeva ES, Tolochko OV, Kolmakov AG, Gvozdev AE, Provotorov DA, Starikov NE, Fadin YA (2017) Synthesis and dry sliding behavior of composite coating with (R-OOO) FT polyimide matrix and tungsten disulfide nanoparticle filler. *J Inorg Mater: Appl Res* 8(1):32–36. <https://doi.org/10.1134/S2075113317010063>
- Breki AD, Aleksandrov SE, Tyurikov KS, Kolmakov AG, Gvozdev AE, Kalinin AA (2018) Antifriction properties of plasma-chemical coatings based on SiO₂ with MoS₂ nanoparticles under conditions of spinning friction on ShKh15 steel. *J Inorg Mater: Appl Res* 9(4):714–718. <https://doi.org/10.1134/S2075113318040081>
- Breki AD, Nosonovsky M (2018) Einstein’s viscosity equation for nanolubricated friction. *Langmuir: ACS J SurfS Colloids* 34(43):12968–12973. <https://doi.org/10.1021/acs.langmuir.8b02861>
- Fadin YA, Kireenko OF, Sychev SV, Breki AD (2014) Acoustic emission and surface roughness of brittle materials. *J Tech Phys Lett* 40(12):1089–1091. <https://doi.org/10.1134/S1063785014120232>
- Asheichik AA, Bahrami MR (2017) Prediction of leakage in the fixed mechanical seal. *J MATEC Web Conf* 129:06002. <https://doi.org/10.1051/mateconf/201712906002>
- Lebedev VM, Radchenko VM (1984) Study of wear resistance of tribojunctions operating in the boundary lubrication regime. *Sov J Frict Wear (English translation of Trenie i Iznos)* 5(5):146–149

8. Golubev AI, Kondakov LA (1986) Seals and sealing machines. Engineering, Moscow
9. Lebedev VM (1981) Study of the anti-frictional properties metal-filled vulcanisates based on SKF-32 in use under vacuum. *Sov J Kauch & Rezina* 6(33–3):5
10. Lebedev VM, Bashkarev AY, Zaborskii EV (1981) Use of metal-filled polymer coatings to prolong service life of traction chains. *Dev Sov J Izv Vyss Ucebn Zaved Mas* 6:44–48
11. Lebedev VM, Bashkarev A Ya, Bukreev VV (1980) Increasing the abrasion resistance and antifrictional property of polyamide coatings. *Sov J Plast Massy* 10:29–30
12. Asheichik AA, Bahrami MR (2017) Investigation of Grafalon Antifriction Feature under Friction in Seawater. *J Procedia Eng* 206:642–646. <https://doi.org/10.1016/j.proeng.2017.10.530>
13. Bashkarev AY, Bukreev VV, Kuschenko AV, Stukach AV (2017) Adhesive bonding strength of polyamide coating on steel substrate in friction units of machines. *Int Rev Mech Eng* 11(9):673–676. <https://doi.org/10.15866/ireme.v11i9.11595>
14. Evgrafov AN, Petrov GN (2013) Calculation of the geometric and kinematic parameters of a spatial leverage mechanism with excessive coupling. *J Mach Manuf Reliab* 42(3):179–183. <https://doi.org/10.3103/S1052618813030035>
15. Evgrafov AN, Petrov GN (2016) Drive selection of multidirectional mechanism with excess inputs. *Lect Notes Mech Eng* 31–37. https://doi.org/10.1007/978-3-319-29579-4_4
16. Karazin VI, Kozlikin DP, Sukhanov AA, Khlebosolov IO (2016) One stable scheme of centrifugal forces dynamic balance. *Lect Notes Mech Eng* None:75–85. https://doi.org/10.1007/978-3-319-29579-4_8
17. Evgrafov AN, Petrov GN (2017) Computer simulation of mechanisms. *Lect Notes Mech Eng* 45–56. https://doi.org/10.1007/978-3-319-53363-6_6
18. Evgrafov AN, Karazin VI, Kozlikin DP, Khlebosolov IO (2017) Centrifuges for variable accelerations generation. *Int Rev Mech Eng* 11(5):280–285. <https://doi.org/10.15866/ireme.v11i5.11577>
19. Karazin VI, Kozlikin DP, Sukhanov AA, Tereshin VA, Khlebosolov IO (2017) Some ways of stable counterbalancing in respect to moving masses on centrifuges. *Lect Notes Mech Eng* 73–85. https://doi.org/10.1007/978-3-319-53363-6_9
20. Evgrafov AN, Petrov GN (2018) Self-braking of planar linkage mechanisms. *Lect Notes Mech Eng PartF5*:83–92. https://doi.org/10.1007/978-3-319-72929-9_10

New Methodology for Kinematic Analysis in the Context of III-Class Six-Bar Linkage Study



Dmitry T. Babichev and Sergey Yu Lebedev

Abstract The fundamentals of a new methodology for kinematic analysis of planar lever mechanisms are presented in this paper. The methodology is based on the representation of a mechanism as a set of two-, one-, and zero-link initial structural units. A distinctive feature of the described methodology is that the analysis of any multi-link planar mechanism is carried out, as the calculation mainly involves the sets of one- and two-link primary structural units of which this mechanism consists. At the same time, the difficult task of identifying assembly options in mechanisms with multi-link Assur groups is virtually solved. The methodology is focused on the automatic generation of algorithms and programs for mechanisms computer simulation.

Keywords Planar lever mechanisms · Kinematics

Nomenclature

W	Mechanism or kinematic chain degree of mobility
W_S	Structural (topological) mobility. It is determined by the Chebyshev's formula (yr. 1870 [1]) or Dobrovolsky's formula [2]
W_K	Kinematic (actual) mobility. It depends on the scheme, size, and position of the mechanism and should be determined with the help of power screws [3] or other approaches [4–6]. Difficulties in calculating W_K are connected with Grubler's chains [7], Baranov trusses [8], etc. [6, 8, 9]
W_{LOK}	Local kinematic mobilities (on a significant, but limited motion)
W_{GLOB}	Global kinematic mobilities (on the entire motion of the cycle)

D. T. Babichev · S. Y. Lebedev (✉)
Industrial University of Tyumen, Tyumen, Russia

D. T. Babichev
e-mail: babichevdt@rambler.ru

© Springer Nature Switzerland AG 2020
A. N. Evgrafov (ed.), *Advances in Mechanical Engineering*,
Lecture Notes in Mechanical Engineering,
https://doi.org/10.1007/978-3-030-39500-1_4

1 State of the Problem and Research Objectives

In mechanism design, the two following tasks should be solved: to choose the mechanism scheme and to determine dimensions that ensure required properties and motion trajectory.

The choice of the scheme is commonly based on mechanisms structural classifications according to Gruebler's [7], Assur's [10], etc. [1, 2, 9] classifications.

To determine mechanism dimensions and parameters that provide desired properties and required motion trajectories is a complicated task of parametric synthesis. It can be solved either numerically or analytically. Numerical methods are frequently based on kinematic and force analysis of a great number of various calculations for the specified scheme. The process of determination of optimum dimensions and properties can be simplified, if universal methods and algorithms, modern computer programs and similar databases are used while computing. However, it is necessary to closely align analysis with description methods for:

- the mechanism structure;
- motion requirements;
- the applied qualitative performance indicators.

This area of design is successfully developing and applying for *spatial kinematic chains*, in particular, for parallel mechanisms [3, 5]. Herewith special attention is given to all mobilities types (W_K , W_{LOK} , W_{GLOB}) calculation.

Kinematic analysis and parametric synthesis of *planar lever mechanisms* tend to be carried out based on analysis algorithms for separate Assur groups composing the mechanism [1, 2, 4, 9, 11]. However, this approach is hard to implement for several reasons. First, there is a tremendous number of Assur groups types: several dozens of four-bar groups with rotating pairs, and several thousands of four-bar groups with translatory and rotating pairs. Second, the issue of possible assembly variants analyzing and identification is rather complicated. Third, degrees of mobility W_K , W_{LOK} , and W_{GLOB} , are frequently not taken into account or are considered on a more intuitive level (e.g. «before determining W , repeated links should be excluded»). Assur groups do not imply analytical or algorithmic determination of their W_K , W_{LOK} и W_{GLOB} depending on links dimensions and external kinematic pairs positions. Difficulties considering the use of Assur groups can be further enumerated. It should be noted that, for the past 100 years, typical approaches for analyzing Assur groups have been created only for two classes of four-bar groups with *rotating* pairs [8, 11], and for all five types of two-bar groups [1, 4, 11]. Moreover, the mechanism during the motion should not get into a special position (in order to exclude the division by zero).

The key objective of the work is to create a system for describing the mechanisms structure and the new methodology for their kinematic analysis and synthesis, which would allow, according to the description of the mechanism, to build an algorithm and computer simulation programs of the mechanisms motion.

The objectives of the report are:

- (1) to briefly outline the basics and potentialities of the new methodology;
- (2) to demonstrate how to simulate motion and to partially determine dimensions of the III-class link mechanism according to the proposed methodology.

The research was carried out at the Chair of Applied Mechanics, Industrial University of Tyumen, experienced in problem-oriented programming languages developing [12–17]. The research was also supported by SPbPU, the Department of the Theory of Machines and Mechanisms—one of the front-runners in the field of lever mechanisms analysis in Russia [18–23].

2 Two Approaches for Mechanisms Structure Description

This section briefly discusses the main features of the two approaches: traditional and suggested. The following positions are compared:

- (a) approaches to specify mechanism structure (topology);
- (b) main features of kinematic analysis;
- (c) methods for specifying mechanism properties requirements.

The object of comparison is a six-bar linkage with three external tugs (III class four-link Assur group) [11].

Traditional approach

Assur's structural classification. Figure 1 shows the scheme of the III class mechanism [4], used, in particular, in grain conditioning machines. To specify the structure, structural schemes (Fig. 1a), structural formulae (Fig. 1b), and graphs in the form of tables and diagrams (do not represented in Fig. 1) are used. In Fig. 1b rotating pair at point A identified as R_{01}^A ; here, link 1 is adjusted to link 0 at the point, which is the coordinate origin for the link appearing in the structural formula for the first time.

- (b) *Main features of kinematic analysis.* Let us consider that all the mechanism dimensions are assumed to be known; it is necessary to carry out kinematic analysis for the whole motion cycle. The significant contribution in developing the traditional approach in kinematic analysis and optimization synthesis of mechanisms with four-link Assur groups was made by E.E. Peisakh in the works [8, 11]. He highlighted that kinematic analysis of III and IV class Assur groups is a highly complicated matter. One of the challenging issues is the necessity to consider *all possible* structural group assembly variants instead of *a single* (operation) *one* during motion analysis in mechanisms of high classes. Herewith identification of all the possible assembly variants is required. However, such a procedure can be realized only using complex algorithms with a large number of calculations required.

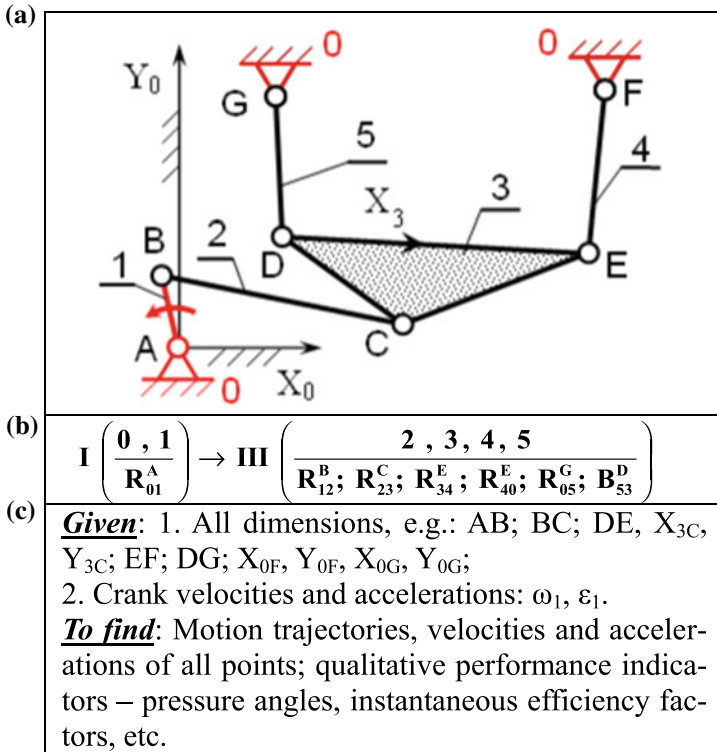


Fig. 1 The III class third-order mechanism (according to Artobolevski): **a** structural scheme; **b** structural formula; **c** kinematic analysis tasks

(c) Methods for specifying mechanism properties requirements. There are no recognized methods for specifying mechanism properties requirements in traditional approaches. A set of requirements commonly include a design diagram, verbal or mathematical description of decision procedure, and “given” and “to find” statements—see Fig. 1c.

The new (proposed) approach

(1) **The main principles of the work:**

- (1a) *The set of structural units* should allow for analysis and synthesis of any planar lever mechanism to be held based on these structural units model calculations: geometric, kinematic, and force. The term “any” is understood to mean:
- mechanisms with multi-link Assur groups of high classes;
 - mechanisms with repeat (passive) constraints;
 - mechanisms with links dimensions errors resulting in “tightening” in pairs, etc.

(1b) *The number of initial structural units* should be minimal in order to improve the algorithms of their analysis and synthesis. The number of links and kinematic pairs of *initial* units should also be small. This allows for simplifying calculation dependencies and not identifying multiple assembly versions. It is necessary to consider a *secondary* structural unit as a set of *initial* units. Thus in user's and system libraries, there will be a set of standard mechanisms and kinematic chains. The user can choose and compose elements to create the required mechanisms. The set of structural units should allow for specifying the scheme and methods of its analysis for *any* planar lever mechanism even with Assur groups of high classes.

(2) **To implement the above-mentioned ideas the following steps were undertaken:**

- (2a) *The set of structural units*—see Table 1—that would allow, according to the description of the mechanism, to build an algorithm and kinematic analysis program of the mechanisms in static and dynamic mode were developed.
- (2b) The basics of a language for describing planar mechanisms schemes and specifying requirements for mechanism motion and its qualitative performance indicators were developed. Proposed symbol nomenclature for structural elements and link motion requirements are used. Several dozens of the structural elements are proposed. The main elements of various types of planar kinematic pairs are described in the paper [24]. These elements are used in structural schemes and formulae (see Figs. 2 and 3).

In Fig. 2 rotating pairs are identified as **R** or **r**, translatory pairs—as **P** and **p**. Lower case letters are used if *previous link covers next link*: compare to the seat **H₆/h₅**; **r**—shaft inserted in a bore; **R**—bore covers the shaft.

Figure 3 shows six-bar linkage scheme; motion requirements and analysis sequence are represented with symbols.

Let us explain some special symbols shown in Fig. 3:



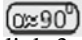




- Symbol  indicates that during mechanism motion, two links dyad are to fold and form one straight line, i.e., the mechanism will get into special positions, and its W_{LOK} will increase by 1.
- Symbol —Dimensions to be calculated: if the symbol specifies the point, it is necessary to find its coordinates; if the symbol specifies the link, it is necessary to find its length. If the symbol placed near two points of the mechanism A и F, it is necessary to find their coordinates. If the symbol specifies link AB, it is necessary to find its length.
- Symbol  означает—the next link 4 is rotated by $\approx 90^\circ$ counterclockwise towards link 3. *Dyad assembly version is specified in the following way: $\alpha > 0$ detour of $\triangle DEF$ —counterclockwise.* It is also necessary to obtain the average pressure angle value equal to $DEF = 90^\circ$. If $\alpha = 0$ at point C, it is required that the average pressure angle (V_C and BC) will be equal to zero.

Table 1 The set of planar structural units with lower pairs

Nomenclature	Group	Scheme	Number of links	Number of pairs	Mobility		Kinematic		Number of types		
					Structural	Global	Local	Basic	Structural	Graphic	
O	Begin	-	0	0	0 or 3	0	0	-	-	-	-
II	Two-link		2	3	0 (or 1)	0 or 1	1	6	15	53.84	
I	Passive		1	2	-1	0 or -1	1 or -1	3	6	15.21	
I ₋	One-link		1	1	1	1	1	2	3	6	
R	Constraint		0	1	-2	0	0	2	3	6	
M	Mechanism	-	?	?	?	?	?	?	Great number		

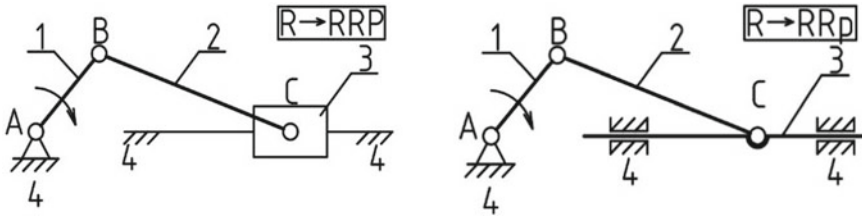


Fig. 2 Structural schemes of two types of slider-crank mechanism

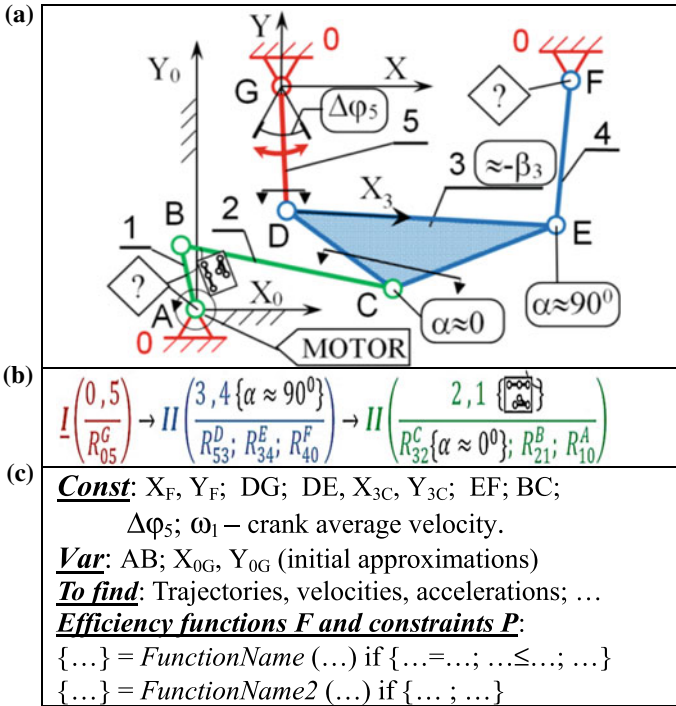


Fig. 3 The new approach—mechanism scheme and requirements for its motion: **a** structural scheme; **b** structural formula; **c** what to find and how to find

- Numerical values in frames—*constants or ranges*—which values should be set during mechanism links motion: $\approx -\beta_3$ —average link DE slope angle to the axis X_0 ; $\Delta\varphi_5$ —specified link pivot angle 5; crank AB rotates with set average velocity ω_1 .

Important note. The scheme given in Fig. 3a may seem complicated. May seem confusing. We believe that if the dialogue with the computer will be based on the data shown in Figs. 3b, c and the computer displays Fig. 3a, then the user can easily master and be able to use all the basic symbols for specifying mechanism requirements.

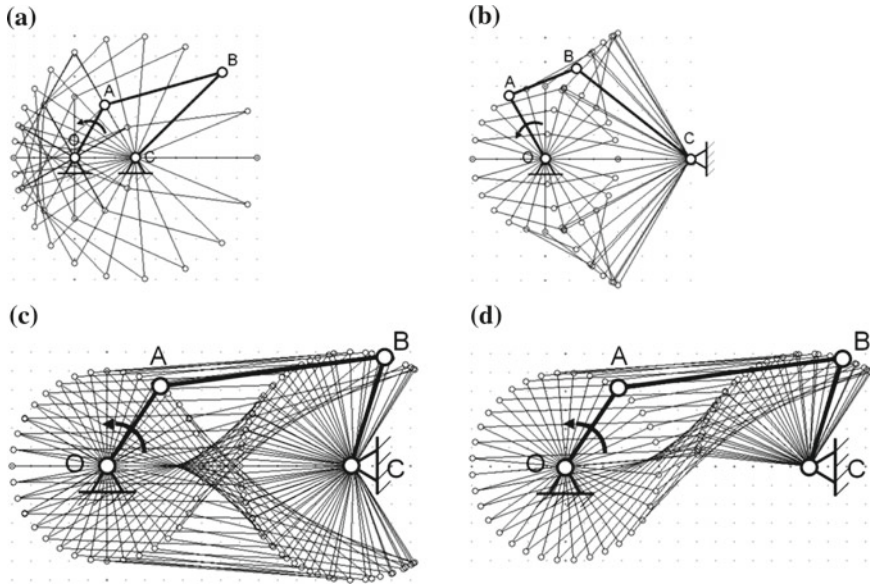


Fig. 4 Motion simulation of the four-bar linkage near limiting positions: **a** two-crank mechanism; **b** isosceles crank-and-rocker mechanism. Convex crank-and-rocker mechanism with links lengths errors: **c** low velocity of the crank (“jumping” takes place); **d** low velocity of the crank

(2c) *The new method for motion simulation* of the mechanisms in special positions was developed and verified. In Fig. 4 the examples of three mechanisms (taken from [25], including one with dimensions errors in positions c and d) motion simulation are presented.

The mechanisms illustrated in Fig. 4. reassemble in the process of motion:

- the crank BC performs one complete rotation per two rotations of the crank OA (Fig. 4a);
- the rocker BC performs one big oscillation per two rotations of the crank OA (Fig. 4b);
- the rocker BC performs one big oscillation alongside reassembling per two rotations of the crank OA (Fig. 4c);
- the rocker performs one small oscillation without reassembling per one rotation of the crank in the same mechanism with the other, small, crank rotation velocity (Fig. 4d).

The detailed description of illustrated in Fig. 4 mechanisms performance is given in [26]. The new method of simulating mechanism motion is named kinetic-dynamic and is briefly presented in part 3 of paragraph 2.2. of the current paper.

(2d) *The fundamentals of synthesis methodology* for mechanisms consisting of structural units given in Table 1 (including the mechanisms with the negative structural mobility W_S , i.e. statically indeterminate mechanisms) were

developed. These mechanisms have local kinematic mobility $W_{LOK} = 1$ alongside limited but valuable movement of input link (Fig. 5). The statically indeterminate mechanisms shown in Fig. 5a, b have the following features:

- different dimensions, in particular, EF—the length of link 4;
- the rotation degree of link 1 differ in 1.6 times under the same displacement $\delta = \pm 0.102$ mm in pair R_{24}^E ;
- the approximation of points E_2 и E_4 trajectories was made according to Chebyshev method and respectively 5 and 4 identical displacements were obtained;

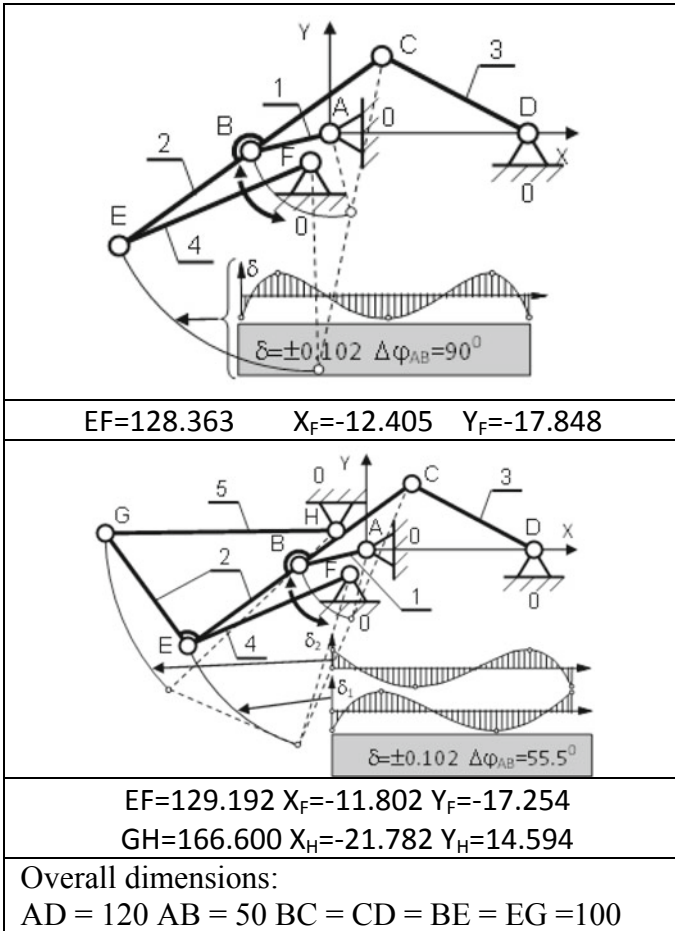


Fig. 5 Mechanisms with kinematic mobilities $W_{LOK} = 1$ and $W_{GLOB} = 0$: **a** five-bar mechanism with structural mobility $W_S = -1$; **b** six-bar mechanism with $W_S = -2$

- the motion simulation of these mechanism is almost impossible to perform while using the standard algorithms.

The developments results of which are given in Table 1 and Figs. 2, 3, 4 and 5 are not described in details in this article.

(3) *The fundamentals of proposed kinematic analysis methodology*

The algorithm of kinematic analysis and basic (not optimizational) metric synthesis of mechanism which contains four-link Assur group and is illustrated in Fig. 1. is described further. The mechanism scheme and requirements, composed according to the rules given, are shown in Fig. 3. The algorithm of analysis and synthesis is described as for the case of manual operation.

The motion analysis of the initial group I(0,5)

Step 1. The multitude $\sum D_i$ of points D is determined by changing the rotation degree of driving pair G by degree $\Delta\varphi_5$. The velocity $\sum V_{D_i}$ and acceleration $\sum W_{D_i}$ vectors of point D are found for the case of “forward-backward” motion. The value of velocity $\sum V_{D_i}$ and acceleration $\sum W_{D_i}$ can be calculated by defining velocity V_{D_0} of point D or by picking the function $k_{v_i} = f(i)$ from the standard set, which allows to calculate V_{D_i} at i -th position according to the formula $V_{D_i} = V_{D_0} * k_{v_i}$. Then the motion trajectory of point D is drawn and the edge positions are determined.

The motion analysis of the first dyad II(3,4)

Step 2. Based on coordinates of points $\sum D_i$ and point F, the dyad DEF is constructed considering assembly version ($\alpha \approx 90^\circ > 0$), i.e. $\sum E_i$, $\sum V_{E_i}$ and $\sum W_{E_i}$ are determined. Then the motion trajectory of point E is drawn and the edge positions are determined.

Step 3. According to $\sum D_i$ and $\sum E_i$ multitudes the triangle DEC is constructed, i.e. $\sum C_i$, $\sum V_{C_i}$ and $\sum W_{C_i}$ are found based on the $\sum V_{D_i}$, $\sum W_{D_i}$, $\sum V_{E_i}$, $\sum W_{E_i}$ values. Then the motion trajectory of point D is drawn and the edge positions C_{left} and C_{right} are determined.

The adjustment, synthesis and motion analysis of the second dyad II(2,1)

Step 4. The average values of slope angle $\sum V_{C_i}$ and point position $\sum C_i$ are calculated. According to this values and the defined average pressure angle C ($\alpha \approx 0^\circ$) the straight line is drawn through the point C. The point A will be located on the line.

Step 5. According to the line parameters, link BC length, C_{left} and C_{right} , the coordinates of point A and AB link length are determined.

Step 6. According to $\sum C_i$, $\sum V_{C_i}$ and point A, the dyad CBA is constructed. In addition the assembly version is determined considering V_{C_i} and ω_1 direction. Then the $\sum B_i$, $\sum V_{B_i}$ and $\sum W_{B_i}$ values are calculated.

Kinematic analysis and synthesis final stage

Step 7. Velocity and acceleration values of all points are recalculated based on the suggestion that the crank angular velocity ω_1 is changing according to the defined

function, e.g. is equal to the constant. This restructuring of calculation results is performed to simplify the results of design and represent them in more convenient for the future purposes form. This stage is the key part of design and, in particular, of mechanisms synthesis with use of proposed methodology.

Step 8. Mechanism performance quality factors are defined. The mechanism and points trajectories are illustrated, the results of synthesis and analysis are presented.

Proposed kinematic analysis methodology computer-based performance

Each step of the algorithm can be performed by means of separate standard computer operations, e.g. steps 2 and 6 for two-link dyads despite their difference: the dyad DEF is standard (Fig. 3) and the dyad CBA reassembles in the process of motion. The algorithm of this standard operation for **II**-group **RRR** has been developed and is depicted in [24]. The algorithm of this operation is massive, but the calculations are simple. The functional area of the first version of this standard operation:

- to determine dyad inner pair coordinates (sometimes with specifying assembly version);
- to define special positions and calculate nearest points parameters;
- to proceed through special positions considering deformations and clearances;
- to avoid dividing by zero;
- to take rounding error into account, etc.

The first version of program didn't determine dimensions according to required dyad performance conditions. The values ω_1 , ω_2 , ε_1 и ε_2 near special positions are calculated by extrapolating the velocity and acceleration values at previous mechanism positions. The program efficiency can be demonstrated by Fig. 4, which illustrates the calculation results for complex in terms of analysis four-link mechanisms.

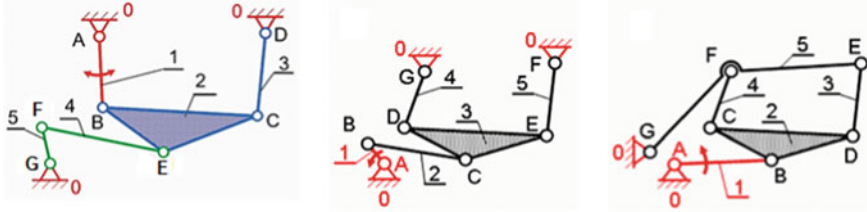
The way of developing algorithm and kinematic analysis program according to structural scheme and formula of planar mechanism is not considered in this paper.

(4) The class as a criterion of lever mechanisms complexity

The class of a lever mechanism is usually a criterion of its complexity degree. The class is determined with the complexity of structural groups. The complexity of groups is estimated [1, 2, 8–11] according to the number of links and kinematic pairs in group and the complexity of the equation for determining links location, e.g. by equation degree or the amount of roots. Figure 5 illustrates the same mechanism with different input links. This mechanism can belong to three classes of different complexity at the same time. However the EFG group, containing special positions where the equation degenerates (requires to be divided by 0), should be analyzed in case of class II; the groups of classes III and IV contain one sixth degree of equation (Fig. 6).

Summary: The method of determining the complexity of mechanism only by its class is not reliable. The following motion properties should be added to the complexity criterion:

- existence of special positions and parallel kinematic chains;
- occurrence of local and global mobilities;



II class, second order

III class, third order

IV class, second order

Fig. 6 The same mechanism belongs to all three classes according to the accepted classification

- assembly modifications;
- micro- and nanomechanisms features;
- mechanism control;
- existence and effect of errors.

The mechanism features listed above should also be reflected in courses of the theory of machines and mechanisms.

3 Conclusions

1. The fundamentals of the work:

- (a) A mechanism is a set of two types of units: links and kinematic pairs.
- (b) Each type of unit has its property set, including structural and motion properties.
- (c) The mechanism is composed of several structural groups that consist of several units, i.e., links and pairs.
- (d) Motion properties of structural groups depend on their structure and the properties of units (i.e., links and pairs) composing the group.
- (e) Motion properties of a mechanism are defined by their structure and the properties of structural groups in the mechanism.
- (f) A set of typical structural groups should allow for specifying motion properties through units properties and mechanism properties through groups properties.

2. The following results are presented in the article:

- (a) The proposed set of five initial structural groups and one «large» secondary Mech-group suitable for operation with mechanisms and kinematic chains from user and system libraries.

- (b) The developed planar mechanisms structural-kinematic schemes Description System that enables us to visualize all the data necessary for algorithms processing when solving tasks of analysis and metric synthesis of any specified mechanism.
 - (c) The fundamentals of the new—kinetodynamic—method that allows simulating the motion of the mechanisms with passive and repetitive constraints and changing in motion assembly variant. In this approach, deformations in pairs, links length errors, and moving pairs energy may be taken into account.
 - (d) A part of kinematic analysis and synthesis algorithms and several examples of motion analysis carried out according to the new method.
3. The proposed method is designed for metric synthesis of motion and computer simulation of various planar lever mechanisms. The method can be applied to education sector.

Acknowledgements The authors of the paper would like to express their gratitude to Industrial University of Tyumen and SPbPU, the Department of the Theory of Machines and Mechanisms, for supporting the project.

References

1. Artobolevsky II (2015) Theory of mechanisms and machines: textbook, Moscow, Alliance, 639p (in Russian)
2. Dobrovolsky VV (1939) Basic principles of rational classification of mechanisms. In: Structure and classification of mechanisms. Moscow, Publishing House of Sciences Academy of the USSR, pp 5–48 (in Russian)
3. Kong X, Gosselin CM (2007) Type synthesis of parallel mechanisms. Springer-Verlag, Berlin Heidelberg. ISBN 978-3-540-71989-2
4. Baranov GG (1967) Course of theory of mechanisms and machines. Mashgiz, Moscow (in Russian)
5. Gosselin G, Angeles J (1990) Singularity analysis of closed-loop kinematic chains. IEEE Trans Robot Autom 6:281–290
6. Doronin FA (2016) Kinematics of a flat manipulator of a parallel structure with three degrees of freedom in a mathcad environment. Theory Mech Mach 1(29):6–18 (in Russian)
7. Grübler M (1883) General properties for inevitable planetary kinematic chains. Civining 29:167–200 (in German)
8. Peysakh EE (2007) About Assur groups, Baranov farms, Grubler's chains, flat hinge mechanisms and their structural synthesis. Sci Educ J. www.technomag.ldu.ru (in Russian)
9. Baranov GG (1952) Classification, structure, kinematics and kinetostatics of plane mechanisms with pairs of the first kind. In: Proceeding seminar of Theory of Mechanisms and Machines, № 46, Sciences Academy of the USSR, pp 15–39 (in Russian)
10. Assur LV (1952) Study of flat rod mechanisms with lower pairs in terms of their structure and classification. Publishing House of Sciences Academy of the USSR, Moscow (in Russian)
11. Peysakh EE, Nesterov VA (1988) Design system of flat lever mechanisms. Mashinostroenie, Moscow (in Russian)

12. Babichev DT (1982) Development of a language for problems of geometric analysis and link synthesis, automated design of mechanical transmissions. In: Theses of reports, Izhevsk, pp 7–9 (in Russian)
13. Babichev DT, Langofer AR, Dolgushin V (1989) Development of a problem-oriented language and database for solving on a computer problems of analysis and optimization synthesis of gear-processing tools and gearing with gearing. Problem-oriented language and basics of the instrumental system for engineering calculations. In: Research Report on the topic of the federal task, Industrial Institute of Tyumen (in Russian)
14. Babichev DT (1991) Features of development of programs for PC on calculation of gears and their elements. Bull Eng 7:19–21 (in Russian)
15. Babichev DT, Langofer AR (1991) Fundamentals of problem-oriented language and interactive tool system for performing engineering calculations, problems of quality of mechanical gears and gearboxes. In: Accuracy and control of gears and gears: materials of the all-union scientific and technical conference. Leningrad, pp 37–39 (in Russian)
16. Babichev DT Computer simulation of flat mechanisms and the multivariate design of single-stage cylindrical gears. Theory Mech Mach 2(18):38–47 (2011) (in Russian)
17. Golovanev V, Babichev D Use of blocking circuits in design of involute cylindrical gears: state, problems, prospects. In: ASCON OJSC website. http://machinery.asccon.ru/source/info_materials/2014/ (in Russian)
18. Evgrafov AN, Kolovsky MZ, Petrov GN (2015) Theory of mechanisms and machines: textbook, St. Polytechnic Publishing House. University, Petersburg (in Russian)
19. Evgrafov A, Petrov G (2016) Drive selection of multidirectional mechanism with excess inputs. In: Advances in mechanical engineering. selected contributions from the conference “Modern Engineering: Science and Education”, Springer-Verlag. Berlin-Heidelberg, pp 31–38 (2016)
20. Kolovsky MZ, Evgrafov AN (2003) On some areas of modernization course theory of mechanisms and machines. Theory Mech Mach 1(1):3–29 (in Russian)
21. Evgrafov AN, Petrov GN (2008) Computer animation of kinematic schemes in excel and MathCAD. Theory Mech Mach 1:71–80 (in Russian)
22. Evgrafov AN, Petrov GN (2018) Effect of self-braking of linkage mechanisms. In: MMESE-2018. Proceeding of an international scientific and practical conference. Saint Petersburg, pp 111–121 (in Russian)
23. Semenov YA, Semenova NS (2018) Investigation of mechanisms with account of friction forces in kinematic pairs. In: MMESE-2018. Proceeding of an international scientific and practical conference. Saint Petersburg, pp 147–159 (in Russian)
24. Evgrafov A, Babichev D, Lebedev S (2019) Flat lever mechanisms: new strategy for kinematic analysis and computer simulation of motion. In: Advances in mechanism and machine science. Proceeding of the 15th IFToMM world congress on mechanism and machine science, vol 73, pp 537–548
25. Grodzenskaya LS, Levitsky NI (1967) German-Russian terminology of theory of mechanisms and machines. Mach Mech 9–10:69–87 (in Russian)
26. Babichev D, Evgrafov A, Lebedev S (2019) Structural-kinematic synthesis method for (planar) link. In: Advances in mechanism and machine science. Proceeding of the 15th IFToMM world congress on mechanism and machine science, vol 73, pp 2937–2953

Algorithm for the Placement of Orthogonal Polyhedrons for the Cutting and Packing Problems



Vladislav A. Chekanin and Alexander V. Chekanin

Abstract The paper is devoted to the algorithm for the placement of orthogonal polyhedrons represented as a set of orthogonal objects with a fixed position relative to each other. The proposed algorithm is implemented invariantly with respect to the dimension of the objects to be placed, which makes it applicable for solving the cutting and packing problems of arbitrary dimension. Examples of the placement of two-dimensional and three-dimensional orthogonal polyhedrons are presented.

Keywords Orthogonal polyhedron · Placement algorithm · Cutting problem · Packing problem

1 Introduction

The problem of orthogonal polyhedrons (OP) packing is a special case of the optimization orthogonal packing problem [1–3], in which one or more objects to be placed are presented in the form of orthogonal polyhedrons composed of orthogonal objects with a fixed position relative to each other [4, 5]. The need to work with orthogonal polyhedrons, considered as separate objects, arises when solving a number of resource allocation problems [5–7]. The most common application of this problem is to solve the problems of industrial cutting of cardboard or plywood [8] and the problem of active electronically scanned arrays generation [9]. The problem of creation and packing sets of orthogonal polyhedrons can take place when solving optimization problems using functional voxel modeling [10, 11].

In general, the statement of the D -dimensional problem of orthogonal polyhedrons packing implies two sets of elements:

1. Set of N orthogonal containers in the form of D -dimensional parallelepipeds with the dimensions $\{W_j^1; W_j^2; \dots; W_j^D\}$, $j \in \{1, \dots, N\}$;
2. Set of n objects O_i , $i \in \{1, \dots, n\}$ represented in the form of orthogonal polyhedron, each of which consists of m_i orthogonal objects in the form

V. A. Chekanin (✉) · A. V. Chekanin
Moscow State University of Technology «STANKIN», Moscow, Russia

of D -dimensional parallelepipeds $o_{i,k}$, $k \in \{1, \dots, m_i\}$ with the dimensions $\{w_{i,k}^1; w_{i,k}^2; \dots; w_{i,k}^D\}$, the position of which relative to each other is specified using vectors $\{z_{i,k}^1; z_{i,k}^2; \dots; z_{i,k}^D\}$ containing the coordinates of orthogonal objects in the local coordinate system associated with each orthogonal polyhedron O_i .

In the particular case, when all orthogonal polyhedrons consist of only one orthogonal object ($m_i = 1 \forall i \in \{1, \dots, n\}$), the D -dimensional problem of placement orthogonal polyhedrons will be the classic D -dimensional orthogonal packing problem [2].

The paper contains a description of the developed algorithm which provides the placement of orthogonal polyhedrons into orthogonal containers of arbitrary dimension.

2 Algorithm for the Placement of Orthogonal Polyhedrons

In order to increase the packing formation speed, before placing each OP O_i , the set of its objects $o_{i,k}$, $k \in \{1, \dots, m_i\}$ is arranged in descending order of the volumes occupied by them $v_{i,k} = \prod_{d=1}^D w_{i,k}^d$.

When solving the problem of orthogonal polyhedrons packing, the model of potential containers [12, 13] is used. This model describes all free spaces of each container as a set of so-called potential containers (PC) which are the orthogonal areas in the form of D -dimensional parallelepipeds with the largest possible dimensions. In contrast to the classic orthogonal packing problem when for each placed object it is necessary to find only one suitable PC for this object [14, 15], for each orthogonal polyhedron it is required to find a suitable set of PC. When some orthogonal polyhedron is placed into a container, the most suitable PC is searched to place only its first object and the remaining objects are placed both into this PC and into other PCs surrounding the considered PC.

Figure 1 shows the block diagram of the algorithm for the placement a set of orthogonal polyhedrons into containers.

When packing a set of orthogonal polyhedrons, for each OP all containers are checked sequentially until a container with a suitable set of PCs for placing this OP is found. If such a container cannot be found, then the transition to the next OP to be packed is carried out. Rotation or reflection of OP is performed, if necessary, in accordance with the parameters specified in the placement string formed by the algorithm used to optimize the solution of the packing problem [16, 17].

Placing a separate OP into a container is the most time-consuming part of the algorithm for placing a set of orthogonal polyhedrons. Figure 2 shows the block diagram of the algorithm for the placement one OP O_i into the current container.

In some cases, the placement of OP is possible only as a result of its shift entirely relative to the beginning of the PC selected for placement of the first object of this OP. Therefore, the developed algorithm for the placement of orthogonal polyhedrons

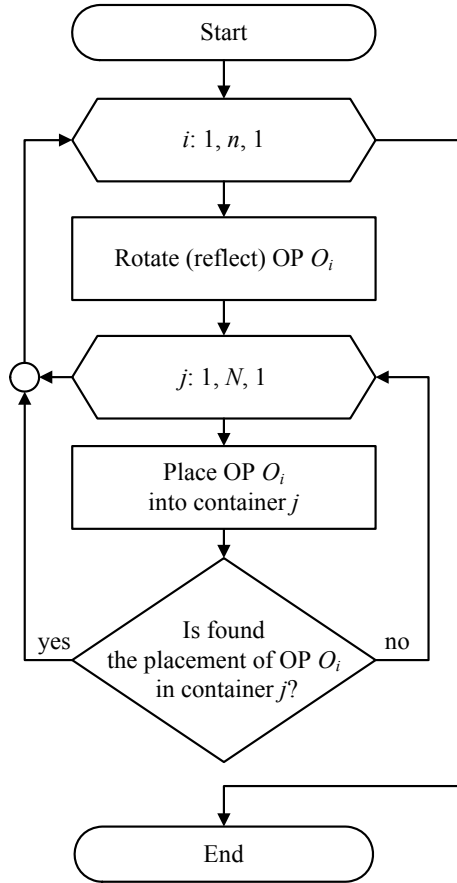


Fig. 1 Algorithm for the placement of orthogonal polyhedrons

provides the possibility of shifting the objects placed into the container during the packing formation process.

When placing the first object belonging to the OP O_i , a vector $\Delta_{i,1} = \{\Delta_{i,1}^1; \Delta_{i,1}^2; \dots; \Delta_{i,1}^D\}$ is formed that defines the maximum possible shift of this OP inside the selected PC, while the values $\Delta_{i,1}$ of the vector are determined as the maximum allowable movements of the first object inside the PC. In the process of placing each subsequent object belonging to the OP, the area of the maximum possible shift of this OP inside the container changes. When placing an object $o_{i,k}$, a vector $X_{i,k} = \{X_{i,k}^1; X_{i,k}^2; \dots; X_{i,k}^D\}$ is formed that determines the position of the intermediate OP formed from the first k objects of the considered OP, as well as a vector $\Delta_{i,k}$ that determines the area of a possible shift of this intermediate OP. If the orthogonal object $o_{i,k}$ cannot be placed into a container with a shift, then the next PC in order to search for a new position for placing the OP is selected.

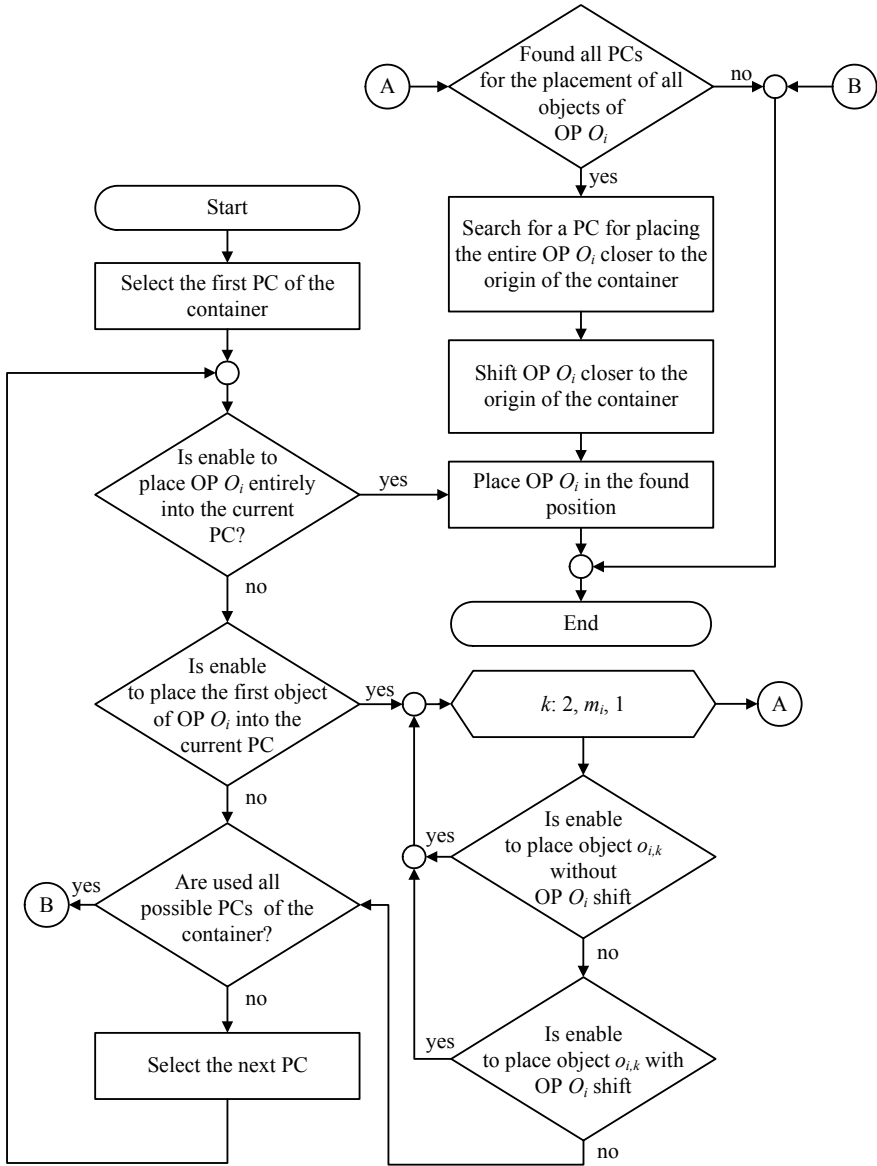


Fig. 2 Algorithm of placing the orthogonal polyhedron O_i into a container

For each placed object $o_{i,k}$, a set of PCs P_k is formed among which it can be placed. If the object $o_{i,k}$ cannot be placed in any PC from the set P_k , then the transition to the previous object $o_{i,k-1}$ is carried out, for the placement of which the next in order PC from the corresponding set P_{k-1} is selected. This part of the algorithm is not shown on Fig. 2.

If the placement of OP O_i in any selected container is possible, a vector $X_i = \{X_i^1; X_i^2; \dots; X_i^D\}$ will be formed that determines the position of this OP in the container.

The final step in finding the optimal position of the OP is to move it closer to the origin of the selected container. For this, the maximum possible shifts for each object $o_{i,k}, k \in \{1, \dots, m\}$ are calculated among all existing PCs. The possible shift of the OP will be determined as the minimum value among all the found possible shifts for each object of this OP. The shift algorithm is multi-pass. At each iteration of this algorithm, an attempt is made to shift the OP along one of the axes of the container, which are selected in the reverse order of the priority selection list $L = \{l^1; l^2; \dots; l^D\}$ of its coordinate axes [18, 19].

Consider an example of shifting one OP in the process of placing its objects. Figure 3 shows a rectangular container with the dimensions $\{100; 100\}$, the free space of which is described by a set of PCs, given in Table 1. The parameters of the placed OP are given in Table 2. Figure 4 shows the individual stages of the OP placement into this container.

After placing an OP O_i into a container, a series of operations are performed to update the set of PCs that describe the remaining free spaces of the container. To do this, for each orthogonal object $o_{i,k}$ from the placed OP, the following sequence of operations is performed:

Fig. 3 Original container

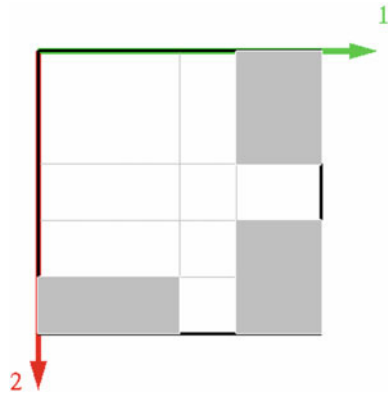
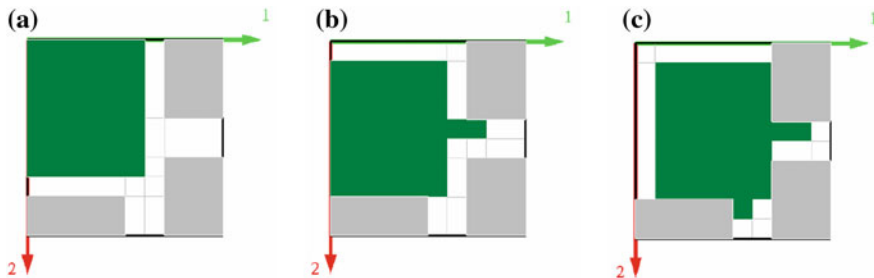


Table 1 Potential containers of the original container

No. of PC (t)	Position along the coordinate axis 1 (x_t^1)	Position along the coordinate axis 2 (x_t^2)	Dimension 1 (p_t^1)	Dimension 2 (p_t^2)
1	0	0	70	80
2	0	40	100	20
3	50	0	20	100

Table 2 Parameters of the placed orthogonal polyhedron O_1

No. of object (k)	Position along the coordinate axis 1 ($z_{1,k}^1$)	Position along the coordinate axis 2 ($z_{1,k}^2$)	Dimension 1 ($w_{1,k}^1$)	Dimension 2 ($w_{1,k}^2$)
1	0	0	60	70
2	60	30	20	10
3	40	70	10	10

**Fig. 4** Orthogonal polyhedron O_1 in the packing process: **a** placement of the object $o_{1,1}$ ($\Delta_{1,1} = \{10; 10\}$); **b** placement of the object $o_{1,2}$ ($\Delta_{1,2} = \{10; 0\}$); **c** result of placement of the OP O_1 ($\Delta_{1,3} = \{0; 0\}$)

- creation a vector $\{a_{i,k}^1; a_{i,k}^2; \dots; a_{i,k}^D\}$ defining the area of PCs update: $a_{i,k}^d = X_i^d + z_{i,k}^d + w_{i,k}^d$, $d \in \{1, \dots, D\}$;
- formation of new PCs entered into the region bounded by the origin of the container and the vector $\{a_{i,k}^1; a_{i,k}^2; \dots; a_{i,k}^D\}$;
- searching and removing of embedded PCs according to the algorithm described in article [19].

Figure 5 shows the examples of two-dimensional and three-dimensional OP sets placement.

3 Conclusion

An algorithm providing the placement of OP sets into containers is proposed. Usage of the model of potential containers when placing OP provides the ability to control all the free areas of the container in order to obtain a more dense packing.

Since the algorithm is implemented invariantly with respect to the dimension of the problem being solved, it can be used both in solving two-dimensional and three-dimensional packing problems, as well as in solving packing problems of higher dimension.

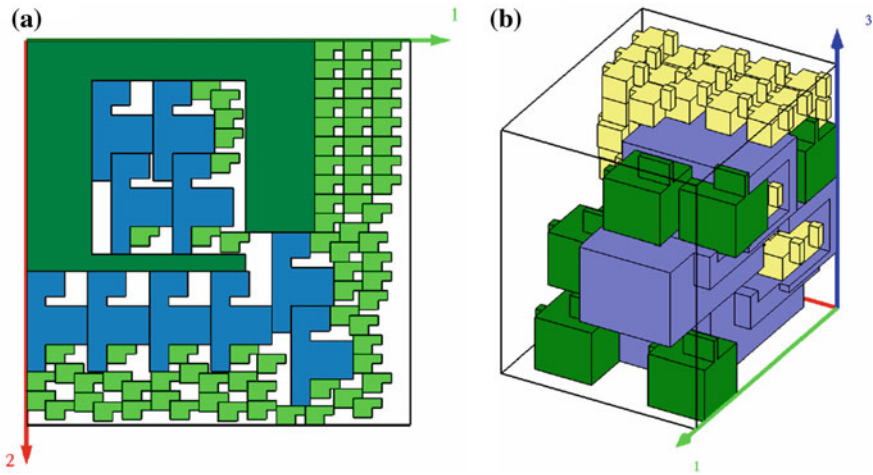


Fig. 5 Examples of placement OP sets: **a** placement of two-dimensional OP sets; **b** placement of three-dimensional OP sets

A prospective direction of this research is the development of heuristic and meta-heuristic algorithms [20] for optimizing the placement of OP sets, as well as the development of algorithms that provide the placement of OP sets into containers of arbitrary configuration which are also presented in the form of OP.

References

1. Wascher G, Haubner H, Schumann H (2007) An improved typology of cutting and packing problems. *EJOR* 183(3):1109–1130
2. Bortfeldt A, Wascher G (2013) Constraints in container loading—a state-of-the-art review. *EJOR* 229(1):1–20
3. Garey M, Johnson D (1979) *Computers intractability: a guide to the theory of NP-completeness*. W.H. Freeman, San Francisco, p 338
4. Bournez O, Maler O, Pnueli A (1999) *Orthogonal polyhedra: representation and computation*. International workshop on hybrid systems: computation and control. Springer, Berlin, Heidelberg, pp 46–60
5. Chekanin VA, Chekanin AV (2018) Algorithms for the formation of orthogonal polyhedrons of arbitrary dimension in the cutting and packing problems. *Vestnik MSTU «STANKIN»* 3:126–130 (in Russian)
6. Biedl T et al (2018) Partitioning orthogonal histograms into rectangular boxes. *Latin American symposium on theoretical informatics*. Springer, Cham, pp 146–160
7. Motorin DE, Popov SG, Chuvatov MV, Kurochkin MA, Kurochkin LM (2017) A study of the evaluation function for the cost of transport operations in distribution of purpose in a group of robots. In: *Proceedings of 2017 20th IEEE international conference on Soft Computing and Measurements, SCM 2017*, pp 536–538. <https://doi.org/10.1109/SCM.2017.7970642>
8. Chekanin VA, Chekanin AV (2014) Development of the multimethod genetic algorithm for the strip packing problem. *Appl Mech Mater* 598:377–381

9. Mailloux RJ, Santarelli SG, Roberts TM, Luu D (2009) Irregular polyomino-shaped subarrays for space-based active arrays. *J Antenn Propag, Int.* <https://doi.org/10.1155/2009/956524>
10. De Korte ACJ, Brouwers HJH (2013) Random packing of digitized particles. *Powder Technol* 233:319–324
11. Tolok AV, Tolok NB (2018) Mathematical programming problems solving by functional voxel method. *Autom Remote Control* 79(9):1703–1712
12. Chekanin VA, Chekanin AV (2015) An efficient model for the orthogonal packing problem. *Adv Mech Eng* 22:33–38
13. Chekanin VA, Chekanin AV (2016) Algorithms for management objects in orthogonal packing problems. *ARPN J Eng Appl Sci* 11(13):8436–8446
14. Chekanin VA, Chekanin AV (2016) New effective data structure for multidimensional optimization orthogonal packing problems. In: *Advances in mechanical engineering*. Springer International Publishing, pp 87–92
15. Chekanin AV, Chekanin VA (2014) Effective data structure for the multidimensional orthogonal bin packing problems. *Adv Mater Res* 962–965:2868–2871
16. Martinez MAA, Clautiaux F, Dell’Amico M, Iori M (2013) Exact algorithms for the bin packing problem with fragile objects. *Discret Optim* 10(3):210–223
17. Kierkosz I, Luczak M (2014) A hybrid evolutionary algorithm for the two-dimensional packing problem. *Cent Eur J Oper Res* 22(4):729–753
18. Chekanin VA, Chekanin AV (2016) Implementation of packing methods for the orthogonal packing problems. *J Theor Appl Inf Technol* 88(3):421–430
19. Chekanin VA, Chekanin AV (2017) Deleting objects algorithm for the optimization of orthogonal packing problems. In: *Advances in mechanical engineering*. Springer International Publishing, pp 27–35
20. Chekanin VA, Chekanin AV (2018) Design of library of metaheuristic algorithms for solving the problems of discrete optimization. In: Evgrafov A (ed) *Advances in mechanical engineering*. Lecture notes in mechanical engineering. Springer, Cham, pp 25–32

Friction Steering Devices as an Object of Impulse Control



Roman Yu. Dobretsov, Nicolai N. Demidov and Andrei O. Kaninskii

Abstract The use of closed-loop steering control system with friction steering device as an alternative of hydromechanical transmission is proposed. Pulse width modulation of operating pressure is used for compressive force and brake slipping control. The kinematic diagrams of single- and double-step friction steering device are presented. A schematic of double power flow transmission (double-flow transmission) with single gearbox is proposed. The conclusion about perspective of friction steering devices developing is given.

Keywords Tracked vehicles · Friction variators · Friction steering devices · Closed-loop steering systems · Slipping · Pulse width modulation · Double-flow transmissions

1 Introduction

The problem of ensuring high quality steering control (which means providing best controllability with minimal additional power use) is common for tracked vehicles of different purpose. This issue is closely related with automation of tracked vehicle control and development of unmanned tracked transport vehicles [1–8 etc.].

This problem is even more critical for high-speed transport vehicles. A traditional way of solving it is to select an optimal type of steering system for the designed vehicle.

It is considered [9, 10] that in terms of providing complete correspondence between controller position and turn radius value the best solution is use of hydromechanical transmission. This transmission type often consists of single gearbox or a pair of planetary gearboxes located on left and right sides of the vehicle. Hydrostatic variator located in parallel power flow allows continuous variation of turn radius. The first type of double-flow transmission is common for foreign vehicles. The tracked vehicle with double-flow transmission and two gearboxes was developed in the USSR.

R. Yu. Dobretsov (✉) · N. N. Demidov · A. O. Kaninskii
Peter the Great Saint-Petersburg Polytechnic University, Saint-Petersburg, Russia

The main flaw of that vehicle was the necessity of providing high power density in hydraulic drive and high operating pressure as a result. Serial production of such units in the USSR was impossible at that moment. The use of friction steering devices was proposed as an alternative.

The friction steering device is reasonable to use in closed-loop steering systems [11]. The development of that sort of transmission was managed in Leningrad Polytechnic University (now Peter the Great Saint-Petersburg Polytechnic University, SPbPU) for use in single-flow transmission with two gearboxes [11–13]. The solutions found during development allowed to provide slipping control of the disc brake used in the friction steering device and guarantee continuous variation of turn radius and complete correspondence between controller position and turn radius value.

The main goal of the article is to prove that use of friction steering devices in double-flow transmissions of tracked vehicles is perspective.

The following tasks were performed: the way of brake slipping control is considered; the steering systems with friction variators developed in the SPbPU are presented and kinematic diagrams of friction steering devices are provided.

The kinematic diagram of double-flow transmission of tracked vehicle with two gearboxes is shown in Fig. 1. A hydrostatic machine, friction device or controlled electric motor could be used as a variator located in parallel power flow. The use of electric motor allows to develop parallel [14] or series hybrid transmission [15, 16]. Research results provided by SPbPU scientists could be used in this case [17–19].

During vehicle linear motion output shaft of the device 2 is stopped. As a result, the solar gear of summing planetary gear system 3 is also motionless and this gear system operates as the reducing gear train.

During turn output shaft of device 2 is running. Differential connection between vehicle sides is provided by drive 7 which gear ratio is (-1) . The power flows from

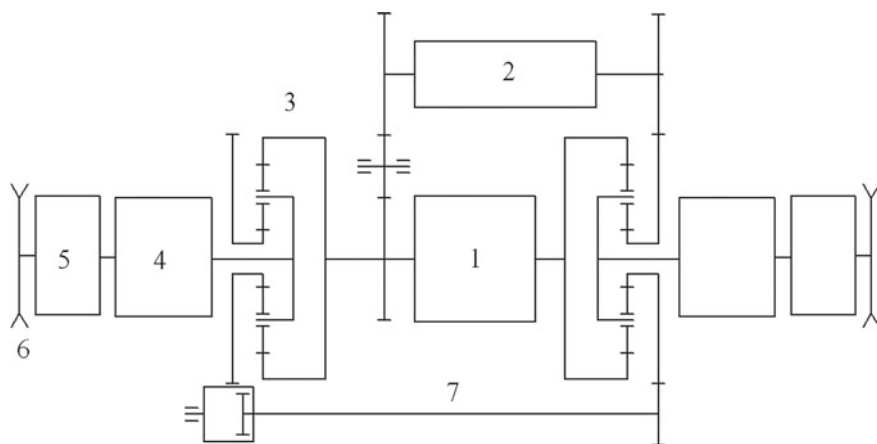


Fig. 1 Kinematic diagram of double-flow transmission with two gearboxes: 1—engine; 2—hydrostatic machine, friction device or electric motor; 3—summing planetary gear system; 4—gearbox; 5—final drive; 6—sprocket; 7—sides connection gear

the engine and the device 2 are summed by the planetary gear system 3. As a result, one of the vehicle tracks starts to move faster while opposite becomes slower and the vehicle performs a turn.

The use of closed-loop steering control system allows to provide continuous variation of a turn radius and complete correspondence between controller (lever or steering wheel) positions and turning radiuses. The feedback is provided by measuring angular speed of the vehicle or difference between angular speeds of the opposite sprockets.

If the layout of engine compartment of modern vehicles should not be changed, the only alternative to hydromechanical transmission is the friction device. Some solutions were considered and the friction steering device was developed as a result. This mechanism consists of a several brakes combined in single unit.

The friction device brake slipping control is provided by pulse width modulation of pressure [20]. The electromagnetic valve which is installed in the hydraulic system serves to supply it with liquid according to a law close to rectangular. Operational frequencies are between 5 and 15 Hz [21]. Impulse amplitude is constant and the ratio between valve opening and closing periods could change. Average operating pressure is forming in the system as a result. The value of the pressure is well-controlled. The control of brakes compressive force and slipping is provided as a result which allows constant variation of friction steering device output shaft velocity. The angular speed ratio of the opposite sprockets is used as the feedback parameter because the main control parameter in case of replacement hydrostatic variator with friction steering device is the angular speed of the vehicle.

The described methods of slipping control could be used during development of controlled power distribution mechanisms for wheeled vehicles [22–24], planetary gearboxes [25, 26] and other transmission and vehicle movement control systems [27].

2 Research Methods

The following methods were used during research: theory of ground vehicles methods, theory of planetary mechanism synthesis methods, transport vehicle transmission development methods, calculation and engineering experiment.

Friction steering devices as a part of double-flow transmission were the research object.

The use of a friction device implicates dissipation of some power portion transferred from engine. The diagram of a friction steering device is shown in Fig. 2. This schematics could be used to illustrate any mechanism that has linear connection between input and output speed or torque. Power loss value depends not on the friction device structure but on external parameters (such as gear ratios) and conditions.

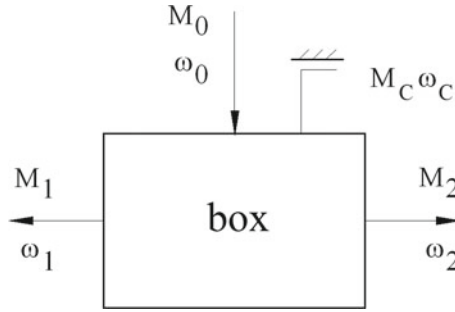


Fig. 2 Friction steering device diagram: the words M and ω signifies torque and velocity respectively; index 0 signifies input, C signifies slipping friction element, indexes 1 and 2 signifies output

The signification method shown above is used for steering mechanism analysis [28]. This method is also commonly used during power efficiency calculation of similar mechanism used in tracked chassis [29].

The detailed power balance analysis methods may be found in the study [28]. The equation of power losses N_C in slipping brake is expressed by

$$N_C = (P_1 + u_0 P_2)(V_{1^*} - V_1) \quad (1)$$

Here P_1 and P_2 is faster and slower track propulsion force; u_0 is steering device with motionless leading link gear ratio (for gearbox located on the vehicle side $u_0 = 0$); V_{1^*} and V_1 are fixed and current slower track speed [28]. Propulsion force values are calculated by use of common formulas for vehicle turning on horizontal surface without track skidding [9, 28]. This simplification may be used in considered case without major effect on calculation results. The expression for slower track fixed speed is given below:

$$V_{1^*} = V_F \frac{\rho^* - 0.5}{\rho^* + q_M} \quad (2)$$

Here V_F is linear motion speed of a vehicle before turn start; ρ^* is relative fixed turn radius; q_M is steering system kinematic parameter (in considered case $q_M = 0.5$; and values of uncontrolled and free turn are equal).

The value ρ^* is derived by gear ratio range:

$$\rho^* = \frac{1(u^* + 1)}{2(u^* - 1)} \quad (3)$$

The gear ratio between vehicle sides during considered turn mode could be expressed as a relation between gear ratio of each gearbox: $u^* = u_2 / u_1$.

Linear speed of the track is defined by turn kinematics [9, 28]:

$$V_1 = V_F \frac{\rho - 0.5}{\rho + q_M} \quad (4)$$

The expression below is used to calculate relative turn radius value for uncontrolled turn:

$$\rho_H = \left(\frac{\mu_{\max}}{\mu_H} - 0.925 \right) / 0.15 \quad (5)$$

where $\mu_H = 4q_M f B / L$ is turn resistance coefficient value for uncontrolled turn mode [28].

Calculations were made for main battle tank chassis with two gearboxes located on the vehicle right and left sides. Vehicle mass m is 42,000 kg; wheelbase and axle track values are $L = 4.31$ m and $B = 2.80$ m respectively; gear ratios are 4.378; 2.159; 1.459; 1.000.

Considered movement regime was based on statistic data provided by “Vniitransmash” [29, 30]. For the following calculations the rolling resistance coefficient f is 0.1; turn resistance coefficient μ_{\max} is 0.5; relative turn radius is ρ is 10, vehicle speed V is 7 m/s. The relative turn radius is considered as $\rho = R / B$, where R is vehicle turn radius, m.

The value N_c calculation results for turn of a vehicle with two gearboxes are shown in Fig. 3. Figure 3 illustrates that power losses on control elements (brakes) in range of most probable turn radiuses are less than 50 kWt. This value may be equal to 100 kWt while vehicle moves in harsh road condition (during turn with second gear switched on).

One of the main advantages of double-flow transmission (Fig. 1) is the reduction of slip power dissipation which makes this transmission type useful in considered case.

The single-flow friction steering device was developed in the first place for replacement of hydrostatic variator used in double-flow transmission (Fig. 1).

The hydrostatic variator used in double-flow transmission provides continuous change of vehicle turn radius from infinite (linear motion) to 12 m.

The main flaw of that transmission type is high hydromotor torque value which is needed to perform a turn with radiuses from 25 to 12 m.

Operating pressure value should be 600...800 kg/cm² to reach such torque.

The transmission efficiency in considered radius range is lesser it can overheat and cannot reach needed torque values.

In this situation hydraulic retarder (not shown on diagram, it is located in the gearbox hull) is switched on to assist the transmission.

The flaws of this operating type are high heat generation level and transmission control system complication.

The pivot turn that could be potentially performed by a vehicle with considered transmission cannot be achieved in practice because of high pressure values needed.

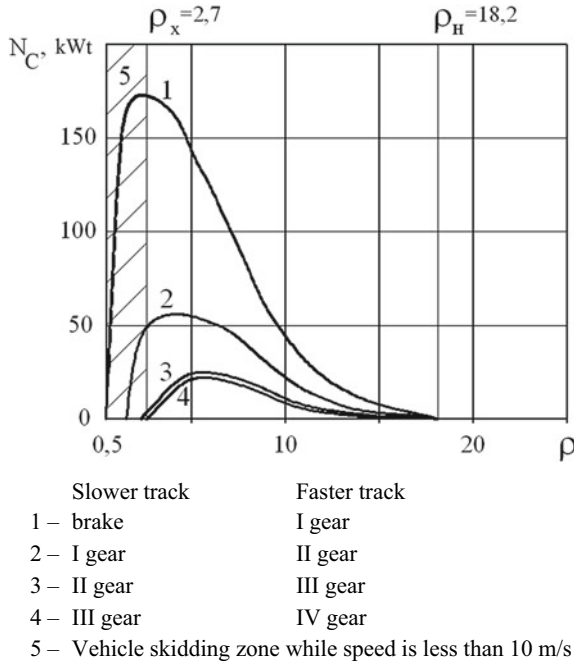


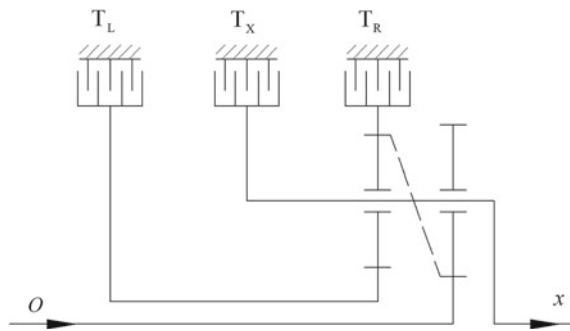
Fig. 3 Power dissipation on a slipping brake of tracked vehicle with two gearboxes while relative turn radius is smaller than ρ_H , indexes

3 Research Results

It is proposed that hydrostatic variator used in double-flow transmission could be replaced with controlled slip friction steering device to correct flaws shown previously.

Kinematic diagram of a single gear ratio friction steering device is shown in Fig. 4. The device structure was developed by professor V. B. Shelomov (SPbPU) during

Fig. 4 Single gear friction steering device kinematic diagram: O and x are driver and follower; T_R and T_L are right and left turn brake; T_x is output shaft brake



transmission modernization research. Transmission testing and future development were performed by department “Wheeled and tracked vehicles” scientific group: Lozin et al. [11].

The device consists of four gears in a double planetary gear set and three brakes: T_x is linear movement control element, T_R and T_L are control elements that should be switched on to perform right and left turn respectively. The input shaft O is forced to rotate by the engine, the output shaft x is connected with sun gear of corresponding side summing planetary gear set via gear train.

Friction steering device constructed according to diagram shown on Fig. 4 may be produced with same size and connection places as the hydrostatic variator which make them interchangeable. Friction device is similar to a planetary reverse reduction gear with gear ratio ± 2.25 . If used in considered transmission it allows vehicle to perform a turn with relative fixed turn radius 8.51.

The friction steering device allows to continuously change output shaft x speed via brakes (control units) T_R and T_L engagement control system which maintains slip with speed needed to perform a turn with considered radius. Therefore, continuous turn radius change, which is the main advantage of hydrostatic transmission may be achieved in considered case. Moreover, while vehicle performs a turn with radiuses, close to theoretical, while hydrostatic transmission power efficiency is reducing, the friction steering device operates with low slipping speed and power efficiency close to one hundred percent.

The main flaws of a friction steering device are heating and brake discs wear. This factors, however, may be reduced to minimum via rational selection of fixed turn radius (or two fixed radiuses), friction pairs number and control system operating pressure.

The device allows to continuously change turn radius from infinite (linear motion) to 23.83 m (fixed radius) with any gear switched on. Gear ratios of both right and left gearboxes should be equal.

It is necessary to switch on a gear with ratio larger than on the opposite gearbox to perform a turn with lesser radius. Output shaft brake should be switched on if the turn should be performed during movement with first gear switched on. The turn will be performed across stopped track with turn radius equal to 1.4 m. The friction device will not affect turn radius value.

The friction steering device allows vehicle to perform a turn on higher gears with lesser radius range. Radius range could be expanded by performing slip control of one opposite device's brake after another. For example, third gear may be switched on one of the opposite gearboxes during movement with fourth gear switched on. Engagement of brake T_L , allows to perform a turn with radius 10.8 m, while engagement of brake T_R decreases turn radius to 5.76 m.

A vehicle cannot perform a pivot turn with considered transmission type.

Turn radius could be continuously changed from 24.83 m to lesser theoretical values with lower gear switched on gearbox of a vehicle side which track should move slower. Vehicle control performs according to following rules. At first, all control elements of a friction steering device should be switched off. Next, low gear should be switched on slower track side (right side for example) gearbox. After that,

brake T_L should be smoothly engaged until theoretical turn radius is achieved. Next, brake T_L should be switched off and brake T_R should be smoothly engaged again until next theoretical turn radius is achieved.

Demonstrated type of control, however, may cause friction device overspeeding because device parts velocity increases while its control elements are switching on. Performed transmission kinematic analysis showed that at the moment of control mode change from normal to considered, while lower gear switched on slower track side gearbox and turn radius is equal to 23.83 m, left brake disc velocity is 4.68 times higher than input shaft ω_O velocity. It means that with input shaft velocity $\omega_O = 300$ rad/s, brake disc velocity will be equal to 1404 rad/s or 13,400 rpm. In this case considered control type is hardly acceptable.

One of the friction device brakes should be always under control to avoid device overspeeding. For example, while vehicle performs a turn with radius less than 23.83 m it is important to engage corresponding friction steering device brake and set lower gear on slower track side gearbox. The vehicle in this case will perform a turn with fixed radius not smoothly enough but without causing damage to the friction device.

The main factor which determines friction device operating capacity is its brake slip power. This power depends on turn radius and terrain characteristic. Theoretical turn brakes T_R and T_L power values are given in Tables 1 and 2 for different vehicle speed and input power on fourth gear.

It may be reasonable to use hydraulic retarder in slower track side powertrain for performing turn with radius lesser than fixed $R < 23.83$ m. All brakes should be disengaged in this case. The steering system will operate as simple differential because power does not transmit through friction device. However, if the hydraulic retarder will not be fully filled with liquid, it may cause a friction device overheat and destruction.

Friction steering device life may be increased via utilizing a double-step friction steering device in transmission. That device should allow vehicle to perform a turn with two different theoretical radiuses and optimize slip power distribution between

Table 1 Brake slipping power on different speeds and fourth gear, kWt

Turn radius R , m	Relative radius ρ	Vehicle speed, m/s			
		13	15	17	19
24.0	8.51	0.0	0.0	0.0	0.0
28.0	10.00	6.4	11.1	18.2	27.9
33.6	12.00	9.3	15.6	25.1	38.6
42.0	15.00	9.9	16.3	25.4	38.2
84.0	30.00	7.0	10.9	16.2	23.2
140.0	50.00	4.6	7.2	10.5	14.9
280.0	100.00	2.5	3.9	5.6	7.9
560.0	200.00	1.3	2.0	2.9	4.1

Table 2 Friction steering device input shaft power on different speeds and fourth gear, kWt

Turn radius R , m	Relative radius ρ	Vehicle speed, m/s			
		13	15	17	19
24.0	8.51	58.0	103.0	167.7	262.5
28.0	10.00	43.3	74.6	122.4	187.8
33.6	12.00	32.0	53.9	86.3	132.9
42.0	15.00	22.9	37.7	58.8	88.4
84.0	30.00	9.7	15.2	22.6	32.4
140.0	50.00	5.6	8.7	12.7	17.9
280.0	100.00	2.8	4.2	6.2	8.6
560.0	200.00	1.4	2.1	3.1	4.3

brakes. To calculate device first step gear ratio it is necessary to set fixed relative turn radius value ρ_1^* . Previous research, conducted for friction device gear ratio division optimization for single-step friction steering device shows that it is better to set the value ρ_1^* equal to 4.0. First gear ratio in this case will be equal to $i_1 = 1.507$.

The value ρ_1^* of fixed relative turn radius is set to calculate device gear ratio on first step. Previous research, conducted for friction device gear ratio division optimization for single-step friction steering device shows that it is better to set the value ρ_1^* equal to 4.0. First gear ratio in this case will be equal to $i_1 = 1.507$.

To calculate value ρ_2^* it is necessary to consider turn radius range from ρ_{x1} (relative turn radius which value is limited to prevent vehicle skidding) to ρ_f (relative radius of free turn).

Method of random selection was used during calculation. The value $N_C^* = N_C \cdot f(\rho)$ (kWt), where $f(\rho)$ is probability density of vehicle turn with relative radius set. [29] was calculated for each step.

The optimization criteria is local minimum of function showed below:

$$G(\rho_{x1}, \rho_{x2}) = \int_{\rho_{x1}}^{\rho_{x2}} N_{C1}^* d\rho + \int_{\rho_{x2}}^{\rho_f} N_{C2}^* d\rho \rightarrow \min \quad (6)$$

Here N_{C1}^* and N_{C2}^* are values, considered separately for first and second friction device steps. The local minimum is reached while parameter $\rho_{x2} = 12.1$. Step gear ratio is equal to $i_2 = 7.605$.

The most compact and easy-to-realize friction device structure was selected from all considered variants, each of which allows realizing slip control of a brake. The diagram of double-step friction steering device with planetary reverse system is shown on Fig. 5.

The friction steering device planetary reducing gear set has two control elements T_1 and T_2 and realizes two operational modes. The direction of an output shaft rotation

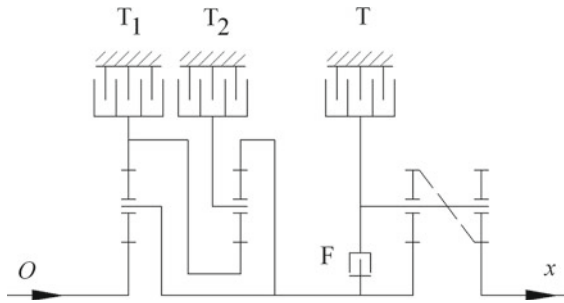


Fig. 5 Double-step friction steering device with planetary reverse system kinematic diagram: O and x —input and output shafts respectively; T_1 and T_2 —first and second step brakes: T and F —reverse brake and clutch

could be changed via switching on brake T or blocking clutch F with hydrostatic control.

Brakes T_1 and T_2 operates in slipping control mode while vehicle turns with turn radius value higher than theoretical.

4 Results Discussion

The expected flaws of a double-step friction steering device in comparison to single-step device are:

- Higher parts number (and therefore higher price and complication of mechanism and its lower reliability.);
- The device is harder to develop with size equal to hydrostatic variator (but at first glance each transmission size could be equal).

The expected advantages of a double-step friction steering device are:

- Lower expected friction disk wear;
- Continuous variation of turn radius during control element switching.

Control algorithms and element base of control system are expected to be not significantly different for both of considered friction steering device types in terms of reliability, complication and element price.

Hydrostatic variator used in transmission with single gearbox could be also replaced with friction steering device (Fig. 6).

The hydrostatic variator load in this case will be higher in comparison with variant shown in Fig. 1. This fact will cause hydrostatic variator size growth. Theoretically a triple-step friction steering device with a same size can be used in this case. Its first step will be used to perform a pivot turn. ($\rho_1^* = 0$). Second step will be used, similar to double-step device, to perform a turn with relative radius $\rho_2^* = 4$. It is possible to

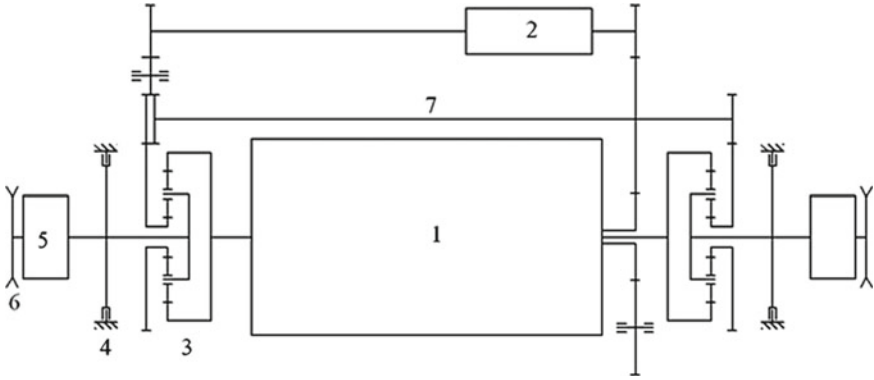


Fig. 6 Single gearbox double-flow transmission diagram: 1—gearbox; 2—hydrostatic variator, friction steering device or electric motor; 3—summing planetary gear system; 4—vehicle side brake; 5—final drive; 6—sprocket; 7—sides connection gear

use function minimization principle $G(0.4, \rho_3^*) \rightarrow \min$ shown early to set radius ρ_2^* value.

It appears that friction control element slipping speed will increase in case with single gearbox (Fig. 6) compared with two gearbox transmission.

Value $u_0 = -1$ is equal for both systems. This means that while external conditions is constant for considered vehicle, equation of power losses in slipping brake is expressed by:

$$N_C = f(\omega_1^* - \omega_1) = f(u^*) \tag{7}$$

In reality: $\omega_1^* = 2\omega_f / (u^* + 1)$. This means that as the value u^* grows, slipping speed and power reduce if sprocket velocity stays constant.

For vehicle with two gearboxes:

$$u^* = \frac{u_{SGT}^* - k}{-u_{SGT}^* - k} \tag{8}$$

where u_{SGT}^* is friction device step ratio given for sun gear of summing gear train (including parallel power flow gears gear ratios); $k < 1$ —summing gear kinematic parameter.

For vehicle with single gearbox:

$$u^* = \frac{u_{SGT}^* - ku_G}{-u_{SGT}^* - ku_G} \tag{9}$$

where u_G is gearbox gear ratio.

In real transmission for both cases values u_{SGT}^* will be different, but for comparison both of them considered as equal. In this case while u_G is equal to 1 (linear

motion) value u^* calculation formulas will be same for both transmission types. In other cases value u_G growth will cause value u^* reduction. It means that friction control element slipping power in single gearbox transmission on lower gear will increase and friction steering device will operate in harder conditions.

Friction steering device, however, could be used as an alternative to hydrostatic variator primarily because the production of domestic hydrostatic machines which has needed parameters and can operate in motor-transmission compartment dense structure is not exist. The case of friction steering device integrated in double-flow steering mechanism with nonlinear radius to vehicle speed dependency (or radius to gearbox output shaft velocity dependency) causes future research interest [31].

5 Conclusions

Friction steering device tests positive experience proves a possibility of developing considered mechanism for operation in transmission compartment dense conditions.

Friction steering device could be used as an alternative to hydromechanical transmission used in tracked vehicles.

Friction steering device expected advantage is its lifetime growth due to control element friction disc wear optimization.

The growth of power which is flows through friction device requires multistep mechanism structure, which allows friction disc lifetime growth while mechanism enlargement stays insignificant.

It is expected, that in case of transmission with two gearboxes the dissipation of power on friction device used in parallel power flow will be lower than in case of transmission with single gearbox.

References

1. Ahmadi M, Polotski V, Hurteau R (2000) Path tracking control of tracked vehicles. In: Proceedings of the IEEE international conference on robotics and automation. San Francisco, CA, pp 2938–2943
2. Kondakov SV, Kharlapanov DV, Vansovich EI (2015) Reliability of models describing the resistance of the turn of a high-speed tracked vehicle. *Russ Eng Res* 10:3–7
3. Kondakov SV, Kharlapanov DV, Vansovich EI (2016) Models of the turn resistance for high—speed caterpillar vehicles. *Russ Eng Res* 2016, N 1(36):1–5
4. Le AT, Rye DC, Durrant-Whyte HF (1997) Estimation of track–soil interactions for autonomous tracked vehicles. In: Proceedings of the IEEE international conference on robotics and automation, vol 2. Albuquerque, NM-1997, pp 1388–1393
5. Wong JY (2001) Theory of ground vehicles, 3rd edn. Wiley, NewYork
6. Wang GG, Wang SH, Chen CW (1990) Design of turning control for a tracked vehicle. *IEEE Control Syst Mag* 10(3):122–125
7. Krasnenkov VI, Yegorkin VV (1971) Kinematicheskoye upravleniye krivolineynym dvizheniyem gusenichnoy mashiny. *Vestnikbronetankovoytekhniky* 5:17–22

8. Krasnenkov VI, Yegorkin VV (1972) Srovnitel'naya otsenka sistem upravleniya povоротom gusenichnoy mashiny pofazovymchastotnym kharakteristikam. *Vestnikbronetankovoytehniki* 4:10–14
9. Zabavnikov NA (1975) *Osnovy teorii transportnykh gusenichnykh mashin* [Fundamentals of the theory of transport tracked vehicles]. Moscow, Mashinostroenie Publ., 448p (in Russ.)
10. Nosov NA et al (1972) Calculation and design of tracked vehicles. «Mashinostroenie», Leningrad, 559p
11. Lozin AV et al (2014) Closed-loop control system for tracked vehicle steering, vol 3, issue no. 202. *St. Petersburg State Polytechnical University Journal*, St. Petersburg, Publishing House of Polytechnic University, pp 201–208
12. Galishev YV et al (2014) Issledovaniya i razrabotki uchenykh SPbGPU v oblasti oboronnoy tekhniki (po materialam IX-j mezhdunarodnoy vystavki vooruzheniya, voennoy tekhniki i boepripasov) [Research and development of SPBSTU scientists in defense technique (based on the IX international exhibition of arms, military equipment and ammunition)], issue no. 1. *Nauchno-tekhnicheskie vedomosti SPbGPU. Seriya Nauka i obrazovanie*, pp 26–32 (in Russ.)
13. Demidov NN et al (2019) Frictional steering mechanisms in dual-stream transmissions of tracked vehicles. *Tractory I sel'skokhozyaistvennyye mashiny* (1):60–69
14. Uvakina D et al (2018) Performance improvement of Arctic tracked vehicles. In: *Proceedings of the MATEC web of conferences, EECE-2018*, vol 245, pp 17001. <https://doi.org/10.1051/mateconf/201824517001>
15. Usov OA et al (2014) The main options for the hybrid-type electromechanical transmission scheme and the methodology for determining its parameters units for military tracked vehicles. In: *Proceedings of the actual problems of protection and security*, Saint Petersburg, Russia, vol 3, pp 111–122, 1–4 Apr 2014
16. Usov OA, Gusev MN, Loiko AV (2015) Electromechanical transmission with a hybrid power plant for a military tracked vehicle, vol 2, issue no. 219. *St. Petersburg State Polytechnical University Journal*, St. Petersburg, Publishing House of Polytechnic University, pp 167–174. <https://doi.org/10.5862/jest/18>
17. Belko V, Glivenko D, Emelyanov O, Ivanov I, Plotnikov A (2017) Current pulse polarity effect on metallized film capacitors failure. *IEEE Trans Plasma Sci.* 45(6):1020–1025. <https://doi.org/10.1109/TPS.2017.2703947>
18. Belko VO, Emelyanov OA (2016) Self-healing in segmented metallized film capacitors: experimental and theoretical investigations for engineering design. *J Appl Phys* 119(2)
19. Belko VO, Petrenya YK, Andreev AM, Kosteliyov AM, Roitgarz MB (2019) Numerical simulation of discharge activity in HV rotating machine insulation. In: *Proceedings of the 2019 IEEE conference of Russian Young Researchers in Electrical and Electronic Engineering*. Saint Petersburg and Moscow, Russia, pp 800–802. <https://doi.org/10.1109/EICOnRus.2019.8657272>
20. Ivanov VA, Yushchenko AS (1981) *Teoriya diskretnykh sistem avtomaticheskogo upravleniya*. «Nauka»
21. Rusinov RV et al (1987) With regards to the methods of the tracked vehicle cornering control modulation frequency estimation. *Operating processes of the compressors and ICE*, Inter-university articles collection, Leningrad, pp 73–78
22. http://www.irs.kit.edu/download/131213_GC_TorqueVectoring_ZF_Handout.pdf
23. Ushiroda Y, Sawase K, Takahashi N, Suzuki K, Manabe K (eds) *Development of super AYC*. *Tech Rev* 15:73–76
24. Didikov RA (2016) The method of determining the components of the balance of power mechanism of power distribution in a vehicle transmission. *Vestnik SibADI* 4(50):61–63
25. *Automatic gearboxes* (2003) Kharitonov S.A.—Moscow, LLC «AST publishing», 335p
26. Fischer R, Küçükay F, Jürgens G, Najork R, Pollak B (2015) *The automotive transmission book*. ISBN 978-3-319-05262-5, ISBN 978-3-319-05263-2 (eBook) <https://doi.org/10.1007/978-3-319-05263-2>, © Springer International Publishing Switzerland 2015, Springer Cham Heidelberg New York Dordrecht London, © 2015

27. Avramenko DN et al (2011) Modernizatsiya sistemy upravleniya dvizheniyem mtanka s BKP. In: Proceedings of the actual problems of protection and security, vol 3. Saint Petersburg, Russia, pp 213–218
28. Shelomov VB (2013) Theory of motion of a multi-purpose tracked and wheeled vehicles. Publishing House of Polytechnic University, St. Petersburg, 90p
29. Dobretsov RY (2011) Taking into account the energy parameters of steering devices in the comprehensive assessment of power losses in the chassis of tracked vehicles, vol 1, issue no 117. St. Petersburg State Polytechnical University Journal, St. Petersburg, Publishing House of Polytechnic University, pp 122–128
30. Teoriya i konstruktsiya tanka. T.8. Parametry vneshney sredy, ispolzuyemyye pri raschete tankov [Theory and design of the tank. Volume 8. Parameters of the environment used in the calculation of tanks]. Mashinostroyeniye Publ., Moscow (1987) (in Russ.)
31. Lozin AV, Dobretsov RY, Medvedev MS (2019) Hyperbolic steering for tracked vehicles. In: Proceedings of the 4th international conference on industrial engineering. Lecture notes in mechanical engineering. Springer, Cham. pp 2367–2374

The Mechatronic Device Impulse Control in Vehicle Powertrains



Roman Yu. Dobretsov and Darya V. Uvakina

Abstract Advantages of disk clutches in low-frequency pulse width modulation (PWM) mode of the hydraulic drive pressure is considered by an example of tracked vehicle steering control mechanism. It is shown that the slip control of the disk clutch using a closed-loop (follow-up controls) system can significantly improve the quality of control when using nodes of a traditional design.

Keywords Disk clutches · Slip control · Closed-loop systems · Automatic transmissions · Unmanned ground railless vehicles

1 Introduction

The general formulation researches subject are the control processes (algorithms) for the highly loaded disk clutches (DC) in transmissions of vehicles. The implementation of such algorithms is aimed at ensuring the operation of transmission units of transport and transport-traction wheeled and tracked vehicles in automatic, remote and autonomous control modes.

Currently, control objects should be considered as mechatronics objects, since a node, as a product of precise mechanics, functions in the composition under a control system, and high operational performance can only be obtained with a rational combination of mechanics and control system capabilities (in this case, the synergistic effect of the mechanical system interaction will be, and emergence will also be, that is whole system acquires properties that are unattainable for its individual components.

DC are used in automated and automatic transmissions [1, 2] of traditional and projected unmanned transport and tracked vehicles (the quality of gear shifting depends on the smoothness and timeliness of DC operation); in the steering mechanisms of tracked vehicles [3–6] (torque smooth changes and angular rate provide high operational properties of the mechanism); projected mechanisms of power distribution [7–9] and other.

R. Yu. Dobretsov (✉) · D. V. Uvakina
Peter the Great St. Petersburg Polytechnic University, St. Petersburg, Russia

In addition to providing sufficient reliability and durability, a key operational feature of the DC in a modern transmission is the ability to accurately control of the torque and angular rate of the output shaft. Without an electronic-hydraulic control system, this problem cannot be solved. In some cases (for example, the power distribution mechanism of a passenger car [7, 9]) an electromechanical drive can be used, but the hydraulic drive is better for highly loaded systems.

The task can be solved as a choice of the pressure change law in the hydraulic drive and pressure values control in real time, i.e. determining the composition of the control system, the parameters of its actuating elements and constructing algorithms for its operation. Thus, the control system should be closed-loop, taking into account the current technological development level is preferably digital, suitable for integration into the CAN interface. Feedback for the purpose of a single clutch is carried out by the output shaft rotation frequency. Feedback can be for the system as a whole—for the case of the tracked vehicle steering mechanism, the feedback is carried out according to the rotation angular rate of the machine, for the anti-lock braking system (ABS), that is based on the analysis of the wheel angular rates.

Such control problems are solved by using of amplitude and pulse width modulations of pressure in a hydraulic drive. Amplitude modulation requires more sophisticated executive equipment and is inferior to the more common pulse-width modulation of pressure (PWMP) [10, 11] in many other aspects. When using PWMP, pressure is supplied to the hydraulic system in the form of pulses (the pulse shape is close to rectangular), and the effective pressure value is formed as the average, which is free-ranging established in the hydraulic system.

The PWMP systems available on the market operate with high modulation frequencies (i.e. they provide only pressure control), require high oil purification and short hydraulic paths. It is proposed to implement PWMP in the frequency range of 5–15 Hz. Such frequencies allow to control not only the pressure in the drive, but also directly affect the compression force of the disk pack, i.e. to control the slipping process. This frequency range allows the mechanical part of the node to effectively work out the control law; the control valve has a simpler design and cheaper, is able to work with the whole spectrum of varieties of oils and is less demanding on the quality of cleaning; it becomes possible to work with long hydraulic lines, i.e. to upgrade existing units containing DC, and not completely redesign them.

The work aim is to show the capabilities of the follow-up control system for the slipping of DC in terms of the tracked vehicle steering mechanism. To achieve the goal, tasks related to modeling the operation of the tracked vehicle steering control system, the organization of bench and prototype tests were solved.

The main functions of the tracked vehicle steering control system are to ensure the best controllability of the vehicle, stability of movement, obtaining high speeds and minimizing the power demand when steering. The control system cannot realize these functions without control objects is steering mechanisms.

A detailed description of the steering mechanisms design and analysis of kinematic and force relationships in the traditional setting are given in [3]. A modern approach to the analysis of kinematics and the construction of a power budget of the steering mechanism and its control algorithms is described in [4, 5, 12–16]. The

application of these methods allows the calculation to determine the loads acting on the input and output shafts of a real transmission, and in bench conditions to set the load values close to real ones.

In a single-link tracked vehicle power steering control is most widely used due to a change in the ratio of traction forces on the lagging and running sides. The steering mechanisms used in this case are independent or onboard (side clutches, final drives, etc.)—the speed change of one track is not associated with a speed change of the other.

The kinematic control of a steering (driving wheel speeds control in the absence of slippage in the steering mechanism) requires more complex mechanisms, although it is preferable for a high-speed machine as far as drivability and stability are improved, and energy demands for a steering is reduced. The mechanisms used are usually dependent or differential - the change in airspeed is interconnected. As an example, we can mention the double differential, although now two-stream differential transmissions with hydrostatic transmission in a parallel power stream is more relevant to use.

The kinematic method of steering control on domestic tracked vehicles is rarely used. The urgent problem remains to improve the quality of steering control without significantly complicating the transmission scheme and increasing its cost. This approach leads to the search for technical solutions that can radically improve the stability and controllability of the machine movement, using the power method of steering control and commercially available transmission units.

The use of a closed-loop steering control system is an example of this approach. The traditional steering control system is open: the control position set by the driver does not correspond to the specific value of the steering radius. The driver is forced to constantly correct the vehicle trajectory. That reduces the movement speed, is accompanied by additional energy demands (as a result, increases fuel consumption), increases the driver fatigability.

The closed-loop steering system does not have these disadvantages. The variable by which the feedback is carried out is, for example, the vehicle turn angular speed. The control object can be commercially available transmission units (e.g. on-board gearboxes) or specially designed mechanisms (e.g. friction-controlled steering mechanism (FSM) for a split powertrain). The cost of upgrading the control system is relatively small.

The use of the closed-loop steering control system makes possible high-quality long-distance control of a tracked vehicle (including a tank when solving combat tasks).

When it comes to tracked vehicles with on-board gearboxes, the issues of steering control automation and the introduction of closed-loop control systems were solved earlier when the T-72 tank was modernized in Czechoslovakia, works was carried out in China and other countries. Recently, interest in the problem of a steering control automation has also been indicated in Russia (e.g. works on modernizing the T-72 at the UKBTM [17], the research started at the Bauman MVTU [18, 19], which began in the 70 s of the 20th century, is continuing).

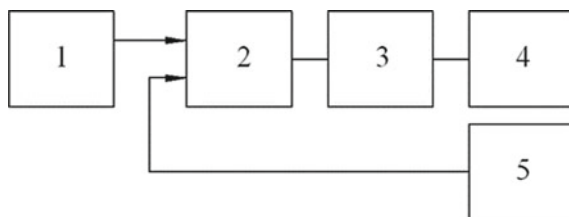


Fig. 1 An tracked steering control system arrangement with the pressure pulse width modulation: 1—a master; 2—a differential amplifier; 3—the pulse width modulator; 4—an control object (DC); 5—a feedback sensor

The DC slipping in the steering mechanism should be controlled to obtain an one-to-one association between the control member position (steering wheel or traditional levers) and the vehicle turn angular speed. A smooth and stable change in the slipping speed of disks pack depending on the position of the control should be obtained to ensure the control. Therefore, the pressure pulse width modulation principle [11] in the hydraulic cylinders of the stalled control elements is used.

It should be note two DC must be turned on simultaneously in order to obtain an operating mode in mechanisms with three degrees of freedom (for example, on-board gearboxes). However, in theoretical researches and bench tests, it can be assumed that a disk pack of only one element (having a lower safety factor for transmitted torque) will slip when turning with a radius less than the calculated (fixed) one.

The composition, structure and operation principles of the control system will be explained in the diagram (Fig. 1).

The system main elements are a master 1 connected to the machine control, a differential amplifier 2, a pressure modulator 3, an effector 4— in this case, an electromagnetic valve in the friction control line; a feedback sensor 5.

When movement is rectilinear, the steering control is in the initial position, the signals of the master 1 and the feedback sensor 5 are equal. The differential amplifier, when the input signals are equal, produces zero voltage at the output, and a signal with zero pulse ratio (infinite duty ratio) is output to pressure modulator 3, i.e. there are no voltage pulses at the modulator input. The electromagnet of the modulator 3 is de-energized, the slide-valve is in the drain position, the control element 4 is off.

For the vehicle to go round in corner, the driver moves the control member, which leads to the appearance of an error signal at the output of the differential amplifier 2. The pulse ratio of the signal at the input of modulator 3 becomes close to or equal to unity. The modulator electromagnet starts on and throws the slide-valve to the discharge position. The control cylinder is filled and turned on.

As soon as the deceleration of the steering mechanism output shaft begins, the machine drives into the curve. In this case, the error signal from the amplifier 2 will decrease, which will lead to a decrease in the pulse ratio at the input of the modulator 3. The modulator 3 enters the modulation mode and starts alternately connecting the hydraulic cylinder to the pumping or discharge line. After that, the system will

dynamically balance, and the working control will slip at a constant speed, turning with a defined radius.

The control member displacement in the opposite direction reduce the pulse ratio to zero. When the control member turns off, the car exits the turn.

The described control system was used when working on stopping brakes, a steering mechanism with on-board gearboxes, and when developing a friction steering mechanism. At different times, Ph.D., professor A.V. Boykov; Ph.D., Senior Researcher A.P. Grigoryev; Ph.D., associate professors A.D. Elizov and N.N. Demidov, Doctor of Technical Sciences, Professor V.B. Shelomov and R.V. Rusinov, engineer I.P. Dubovikov and JRF V.V. Tsvetkov and other employees of the department “Wheeled and tracked vehicles” LPI-LSTU took part in researches of the problem.

In the work, not only control system modifications and the modulator assembly design were proposed and the main parameters were selected, but an experimental bench and a system prototype for running trials were created. Currently, the bench is used mainly for educational purposes and without significant modifications, it can be used to work on a prototype of a tracked vehicle steering control system made on a present-day element base.

2 Methods and Materials

Two groups of methods were used in the research: a rated experiment (selecting the main weight and size and energy parameters of the test bench, development of control algorithms for the test object) and an engineering experiment (activation, debugging and setting of the test bench; of the control system components debugging in bench conditions, etc.). Theoretical methods (synthesis, abstraction, generalization, deduction, analogy, computer modeling) and empirical methods (description, comparison) can also be used at work various stages of the work.

The kinematic diagram of the bench created at SPbPU for studying the controlled slipping [20] is shown in Fig. 2.

The bench drive is from a three-phase asynchronous electric motor 1 with a capacity of 125 kW at 1450 rpm. A disk brake 5 is a bench controlled friction unit. A booster, into which oil is supplied from the tested pressure control system, activate the brake 5.

A flywheel 3 with a inertia variable torque is installed to simulate the inertial masses of the machine, transmission and chassis. The rotation to the flywheel 3 is transmitted from the engine 1 through a permanently closed friction clutch 2. The reduction gear 4 is installed behind the flywheel 3 and serves to obtain the required slipping speeds. Due to the slipping of the clutch 2, the rotational speed of the shaft 6 of the brake 5 can be controlled in the range from 0 to 400 rpm.

The control of the turning radius on the stand is limited to controlling the rotation frequency of the shaft 6 of the controlled brake 5.

The braking force on the lagging board, the value of that depends on the soil properties, should be created to obtain a selected turning radius in a real vehicle with

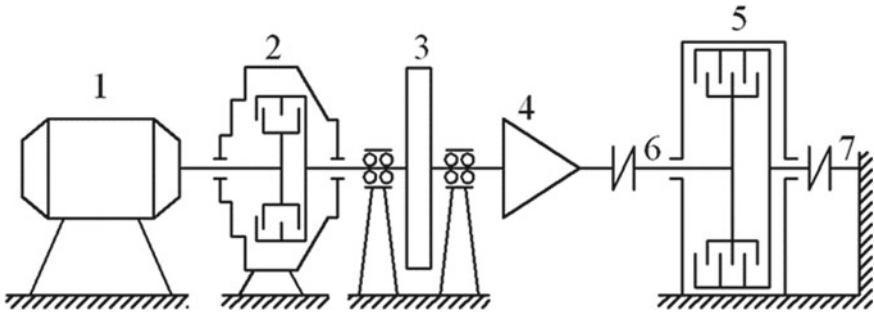


Fig. 2 The bench kinematic diagram for testing the DC and split powertrain: 1—electric motor; 2—friction clutch for bench loading; 3—flywheel; 4—reduction gear; 5—testing DC; 6—input shaft of the DC; 7—strain-measuring shaft

power control. This braking force is created by the included control element, and the torque, which should balance the friction forces in DC, is supplied to its shaft from the outside of the transmission from the side of the drive wheel. At the bench, the slipping clutch 2 creates this torque by the controller control pressure in it.

3 Results

A turning a tracked vehicle feature on most soils is the torque on a drive wheel of the lagging track is inversely proportional to the turning radius. This circumstance requires a change in the torque of the clutch 2 on the bench depending on the controlled brake shaft speed.

Magnitude of the control member, controlled brake shaft speed, pressure in the controlled brake hydraulic cylinder and torque on the brake 5 are measured on the bench.

As far as the bench contains only one controlled brake, it doesn't have a fundamental possibility to continuously study the entire range of control of turning radii from infinity to a fixed one for the case of simulating turning a vehicle with planetary three freedom degrees gearboxes.

It is for this reason, all test modes were divided into two subranges according to the turning radius: from infinity to free, i.e. a turn when the friction clutch of the rectilinear movement is controlled to be switched off; from free to fixed, that is, a turn when the clutch is in low gear.

On each of the sub-ranges along the turning radius, the test program provided for a series of experiments to study the response of the control system to various types of influences through the control member: step-by-step movement in the direction of decreasing the turning radius, on the contrary, with the shutter speed necessary to complete the transient processes; impulse action (moving the control member by

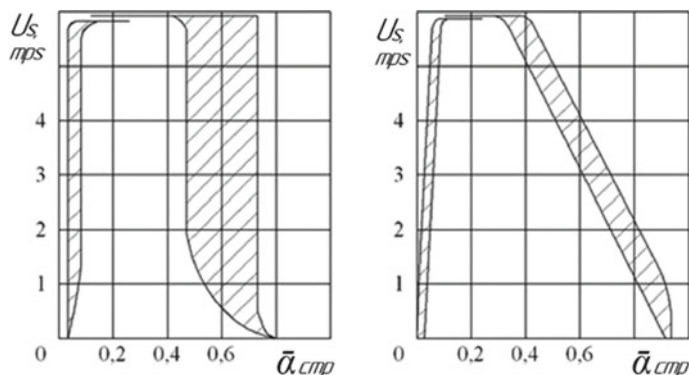


Fig. 3 Static characteristic (the dependence of the DC slipping speed U_s on the control member position $\bar{\alpha}_{cmp}$): for the serial steering control system (left) and pilot model (right)

25–50% of its full stroke with subsequent return to its original position); manual tracking of a selected trajectory with variable turning radii along the way.

At each of the test modes, the influence on the control quality of the modulation carrier frequency from 1–2 Hz (lower limit) to the maximum level that the executive electro-hydraulic element could work out (at a selected regulation depth) was checked. In practice, that upper level did not pass 15 Hz in experiments (with a regulation depth of 0.1–0.9).

As a result of testing various options for the steering control system, it was found that the most accurate pressure control in the hydraulic cylinder of the control element is made possible by the closed-loop tracking system using pulse-width modulation of the control pressure in the hydraulic system. In addition, the pressure pulsation value in the hydraulic cylinder is reduced.

The system operation stability was confirmed experimentally over the entire range of a turning radii variation and the operating modulation frequency optimal range was revealed.

The use of a discrete steering follow-up controls improves the quality of the steering control of a vehicle with an on-board gearbox in all respects. Moreover, the proposed steering control system, in comparison with the series-produced one, showed absolute stability in the entire range of turning radii from infinity to fixed; 3–5-fold less delay time for entering the turn; 3–4-fold better stability of the vehicle heading in a turn; 2–5-fold smaller amplitude of impacts on the control member when moving with large radii; almost full use of the swing lever to control the vehicle. Increasing the modulation frequency improves control (in experiments, the frequency was 8–15 Hz, depending on the type of electromagnets used). The use of faster electromagnets can increase the carrier frequency of the modulation and improve the quality of the system.

As an illustration, for comparison the static characteristics of the basic and experimental control systems (Fig. 3) are given. The static characteristic of a discrete non-feedback rotational control system is not much different from the static characteristic of a serial system.

The system has a very “nebulous” static characteristic, because the dependence of the DC slipping speed U_s on the control member position $\bar{\alpha}_{cmp}$ is very unstable with a serial steering control system.

The discrete follow-up steering control system allows to get stable speed control of control element disks slipping, therefore, its static characteristic shows that when moving the control (within the limits corresponding to the inclusion of a gear), the slipping speed U_s monotonously changes. It should be noted that due to setting up the system, the required static characteristic was obtained.

4 Discussion

The use of follow-up systems to control the DC slipping allowed to begin work in an adjacent direction is the development of the layout of the FSM. The FSM is designed to replace hydrostatic transmission in a double-flow caterpillar steering mechanism (Fig. 4). The feasibility of such a replacement was primarily due to the lack of domestic technology for the production of compact hydrostatic gears with the necessary parameters.

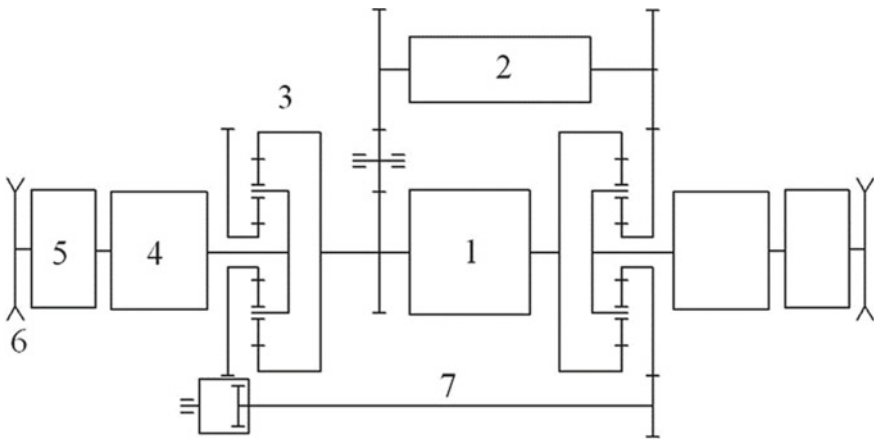


Fig. 4 The split powertrain diagram with friction-controlled steering mechanism: 1—engine; 2—FSM; 3—summing planetary gear set; 4—on-board gearbox; 5—final drive; 6—drive wheel of the side; 7—inter-board contact

In a rectilinear motion, the power from the engine 1, through the summing planetary gears 3, on-board gearboxes 4 and final drives 5, is supplied to the drive wheels of the sides 6. Parallel power flow is stopped by stopping the output shaft of the FSM 2.

When turning, part of the power comes from the engine to the FSM 2. The gear ratio implemented by the FSM determines the change in the speed of the sides and, accordingly, the radius of the turn. Power flows are summarized in mechanisms 3. Communication between the sides is ensured by transmission 7 (gear ratio is -1).

The use of a closed-loop control system in combination with the principle of pulse-width modulation in the hydraulic system of the included FSM control element allows controlling the process of slipping of the disks, which means providing a smooth change in the gear ratio of the mechanism in the entire range being implemented, i.e. steady movement when turning with any radius. It is impossible to get a turn around the center of gravity for this transmission scheme.

A single-stage FSM was manufactured and passed successful trials on a running model. The test program was curtailed due to lack of funding. For the same reasons, the two-stage FSM has reached only the stage of a conceptual design.

In terms of reducing energy consumption when a machine turning [21] and reducing the load on the engine and transmission elements [3, 21], the use of a follow-up control system and pressure pulse-width modulation in the hydraulic system provides advantages due to the reduction in slipping operation. Some gain is also achieved by accelerating the exit of the car to the path set by the driver. But the main advantages are realized precisely by improving the controllability of the machine [18, 19], and, as a result, reducing driver fatigue.

Actual in the near future is the implementation of the principles of the created control system on a modern set of components (the use of a microcontroller, more reliable electromagnetic valves with a higher response frequency, modern feedback sensors, etc.).

The development of the principle of controlling the disks slipping speed of the DC is the direct basis for working on a controlled power distribution mechanism for the vehicle's transmission [7–9]. The obtained methods of bench tests and mathematical models [10] allow us to evaluate the parameters of the control system of such a mechanism. In the domestic automotive industry, these tasks have not yet been solved.

Further prospects for the application of the PWMP principle in controlling the tracked vehicles movement seem to be associated with the development of a hyperbolic rotation mechanism based on the FSM [22], the construction of various types of hybrid transmissions [6, 23, 24], including those using electrical and electromechanical complexes developed by SPbPU scientists [25–27].

Experience with discrete control systems using the principle of pulse-width modulation can be applied to work on the car ABS. The backlog of the domestic automobile industry in this area from the world level is considerably.

5 Conclusion

In the final analysis, it can be argued that the use of a closed-loop control system for turning a tracked vehicle is efficient and appropriate, and the experimental, methodological and theoretical basis obtained when working on the system can become the basis for working on modern transmission mechanisms and car control systems.

The experience of research made by SPbPU specialists allows to conclude that it is advisable to use low-frequency PWMP with DC used in transport vehicles transmissions. It is of interest to extend the scope of application of such a control technique to transmission units of wheeled and tracked tractors and special machines based on them chassis.

Implications.

1. Control over DC slipping in the transmission nodes of transport vehicles will significantly increase the quality of vehicle traffic control. Moreover, the use of the principle of low-frequency (5–15 Hz) pressure modulation in the hydraulic drive allows to directly control the slipping of the disks.
2. The results of calculated, bench and full-scale experiments show that pulse control based on low-frequency (5–15 Hz) pulse-width modulation allows controlling the disk control element slipping and significantly increasing, for example, the quality of tracked vehicle steering control.
3. Low-frequency pulse-width modulation for hydraulic disk control elements drive can be used in traffic control systems of tracked vehicles, automated and automatic transmissions of transport and traction machines, power distribution mechanisms of wheeled vehicles, etc.

References

1. Avramenko DN et al (2011) Modernizatsiya sistemy upravleniya dvizheniyem mtanka s BKP. In: Proceedings of the actual problems of protection and security, Saint Petersburg, Russia, vol 3, pp 213–218
2. Krasnenkov VI, Yegorkin VV(1971) Kinematicheskoye upravleniye krivolineynym dvizheniyem gusenichnoy mashiny. Vestnikbronetankovoytekhniky 5:17–22
3. Krasnenkov VI, Yegorkin VV(1972) Sravnitel'naya otsenka sistem upravleniya povorotom gusenichnoy mashiny pofazovymchastotnym kharakteristikam. Vestnikbronetankovoytekhniky 4:10–14
4. Kharitonov SA (2003) Automatic gearboxes. AST Publishing, Moscow, LLC, 335p
5. Fischer R (2015) In: Fischer R, Küçükay F, Jürgens G, Najork R, Pollak B (eds) The automotive transmission book. Springer, Cham, Heidelberg, New York, Dordrecht, London. ISBN 978-3-319-05262-5, ISBN 978-3-319-05263-2 (eBook). <https://doi.org/10.1007/978-3-319-05263-2>
6. Rusinov RV et al (1987) With regards to the methods of the tracked vehicle cornering control modulation frequency estimation. In: Operating processes of the compressors and ICE, inter-university articles collection, Leningrad, pp 73–78
7. Demidov NN et al (2019) Frictional steering mechanisms in dual-stream transmissions of tracked vehicles. Tractory I sel'skokhozyaistvennyemashiny 1:60–69

8. http://www.irs.kit.edu/download/131213_GC_TorqueVectoring_ZF_Handout.pdf
9. Ushiroda Y, Sawase K, Takahashi N, Suzuki K, Manabe K (2003) Development of super AYC/ Y. Tech Rev 15:73–76
10. Didikov RA (2016) The method of determining the components of the balance of power mechanism of power distribution in a vehicle transmission. VestnikSibADI, 4(50):61–63
11. Ahmadi M, Polotski V, Hurteau R (2000) Path tracking control of tracked vehicles. In: Proceedings of the IEEE international conference on robotics and automation, San Francisco, CA, pp 2938–2943
12. Kondakov SV, Kharlapanov DV, Vansovich EI (2015) Reliability of models describing the resistance of the turn of a high-speed tracked vehicle. Russ Eng Res 10:3–7
13. Kondakov SV, Kharlapanov DV, Vansovich EI (2016) Models of the turn resistance for high— speed caterpillar vehicles. Russ Eng Res 1(36):1–5
14. Le AT, Rye DC, Durrant-Whyte HF (1997). Estimation of track–soil interactions for autonomous tracked vehicles. In: Proceedings of the IEEE international conference on robotics and automation, Albuquerque, NM, vol 2, pp 1388–1393
15. Wong JY (2001) Theory of ground vehicles, 3rd edn. Wiley, New York
16. Wang GG, Wang SH, Chen CW (1990) Design of turning control for a tracked vehicle. IEEE Control Syst Mag 10(3):122–125
17. Lozin AV etc. (2014) Closed-loop control system for tracked vehicle steering. St. Petersburg State Polytech Univ J 3(202):201–208. Publishing House of Polytechnic University, St. Petersburg
18. Nosov NA et al (1972) Calculation and design of tracked vehicles. Mashinostroenie, Leningrad, 559 p
19. Shelomov VB (2013) Theory of motion of a multi-purpose tracked and wheeled vehicles. Publishing House of Polytechnic University, St. Petersburg, 90 p
20. Usov OA et al (2014) The main options for the hybrid-type electromechanical transmission scheme and the methodology for determining the its parameters units for military tracked vehicles. In: Proceedings of the actual problems of protection and security, Saint Petersburg, Russia, 1–4 Apr 2014, vol. 3, pp 111–122
21. Usov OA, Gusev MN, Loiko AV (2015) Electromechanical transmission with a hybrid power plant for a military tracked vehicle. St. Petersburg State Polytech Univ J 2(219):167–174. Publishing House of Polytechnic University, St. Petersburg. <https://doi.org/10.5862/jest/18>
22. Uvakina D et al (2018) Performance improvement of Arctic tracked vehicles. In: Proceedings of the MATEC web of conferences, vol 245, 17001, EECE. <https://doi.org/10.1051/mateconf/201824517001>
23. Belko V Glivenko D, Emelyanov O, Ivanov I, Plotnikov A (2017) Current pulse polarity effect on metallized film capacitors failure. IEEE Trans Plasma Sci 45(6):1020–1025. <https://doi.org/10.1109/TPS.2017.2703947>
24. Belko VO, Emelyanov OA (2016) Self-healing in segmented metallized film capacitors: Experimental and theoretical investigations for engineering design. J Appl Phys 119(2)
25. Belko VO, Petrenya YK, Andreev AM, Kosteliiov AM, Roitgarz MB (2019) Numerical simulation of discharge activity in HV rotating machine insulation. In: Proceedings of the 2019 IEEE conference of russian young researchers in electrical and electronic engineering, Saint Petersburg and Moscow, Russia, pp 800–802. <https://doi.org/10.1109/EIConRus.2019.8657272>
26. Ivanov VA, Yushchenko AS (1981) Teoriya diskretnykh sistem avtomaticheskogo upravleniya. M.: «Nauka»
27. Dobretsov RY (2011) Taking into account the energy parameters of steering devices in the comprehensive assessment of power losses in the chassis of tracked vehicles. St. Petersburg State Polytechn Univ J 1(117):122–128. Publishing House of Polytechnic University, St. Petersburg

Consideration of Friction in Linkage Mechanisms



Alexander N. Evgrafov, Gennady N. Petrov and Sergey A. Evgrafov

Abstract Flat structural groups with revolute and prismatic kinematic pairs are considered. At the approach of such groups to singular positions, internal reactions in the hinges sharply increase, which can lead to the effect of self-braking, at which further movement of the links becomes impossible. Accounting for friction in kinematic pairs allows us to determine the conditions for the occurrence of such a regime. The models of plane revolute and prismatic kinematic pairs with friction are described. The algorithm for constructing structural groups with substitute ideal kinematic pairs is shown. Hitting such groups in a singular position indicates the possibility of the emergence of a mode of self-braking.

Keywords Structural group · Assur group · Mechanism · Self-braking · Replacing the ideal kinematic pair · Friction

1 Introduction

In recent years, there has been an increased interest in studying mechanisms in which frictional forces play a significant role. Le Xuan Anh in his fundamental monograph [1] considers the general theory of motion of mechanical systems with Coulomb friction. The book discusses the problems associated with deriving equations of motion, with Painleve's paradoxes, with frictional self-excited oscillations.

In paper [2], the authors consider dynamics of a solid body with a sharp edge in contact with a rough plane. Dynamics of the system is considered within the framework of three mechanical models which describe different modes of motion: the point is fixed, slides, or loses contact with the bearing.

A. N. Evgrafov (✉) · G. N. Petrov
Peter the Great Saint-Petersburg Polytechnic University, St. Petersburg, Russia
e-mail: a.evgrafov@spbstu.ru

S. A. Evgrafov
LTd "BaltStream", St. Petersburg, Russia
e-mail: es@btsm.ru

© Springer Nature Switzerland AG 2020
A. N. Evgrafov (ed.), *Advances in Mechanical Engineering*,
Lecture Notes in Mechanical Engineering,
https://doi.org/10.1007/978-3-030-39500-1_8

Klepp [3] considers solutions obtained for the same position, velocity, active forces, and friction parameters, but with different modes of contact between the sliders and their guide rails.

Paper [4] presents the analysis of friction contacts for multi-link systems with spatial prismatic joints on the basis of tiny clearances.

Acary [5] studied algorithms of numerical temporal integration for non-smooth mechanical systems, which were subject to one-way contacts, impacts, and Coulomb friction.

Paper [6] presents and discusses the finite elements method for dynamic description of multibody systems with the frictional translational connection. The contact force model is developed on the basis of the penalty method and a criterion is proposed to estimate the influence of the gap size on the nodal contact forces. The time-varying states of the node contacts are determined by applying two contact detection algorithms for sticking and sliding, respectively.

The main difficulties in solving mechanical systems with impacts and friction arise as a result of instantaneous changes in contact forces during transitions from contact to separation, as well as from sliding to sticking or backward sliding. Two types of methods were proposed to solve these problems: the trial and error algorithm [7] and the algorithm based on complementarity [8].

Researchers [9] applied the algorithm based on complementarity to work with flexible mechanical systems that include one-way contact and friction. However, such an algorithm must solve linear (or non-linear) equations of complementarity, which is rather time-consuming.

One of the most important modes of mechanisms in which friction forces are strong is a self-braking mode. In work [10], the dependencies connecting geometrical parameters with the values of the minimum coefficients of sliding friction are constructed, during the implementation of which the self-braking mechanism is ensured. In papers [11, 12], the analysis of the concept of self-braking and known analytical and geometrical criteria of this phenomenon is given. It is proposed to study the phenomenon of self-braking with the help of the parameter of a link braking equal to the inverse sign of the ratio of elementary work of internal resistance forces and driving forces. Kargin P.A. studied the efficiency of the drive of load-lifting machines with self-braking [13]. The authors of paper [14] evaluated the quality of self-tightening nuts. The main functional feature of this nut is self-braking in the absence of axial forces. This property is provided by the fact that the nut together with the bolt is a prestressed pair, in which a constant preload is created by guaranteed tension. Paper [15] presents an original method of determining reactions in kinematic pairs with allowance for friction forces. On the basis of this method, the quality criterion of the current position of the mechanism is proposed—the factor of safety of assembly, which shows the degree of remoteness for structural groups from the positions in which self-braking can occur. The authors of papers [16, 17] presented results of the research on the synthesis of gear meshes in order to achieve the self-braking effect in them. Papers [18–20] consider the processes of self-braking of linkage mechanisms on the example of an Assur group with rotational kinematic pairs (joints). The conditions under which the self-braking and braking modes arise are determined.

The aim of this paper is to examine structural groups with rotational and translational ideal and non-ideal kinematic pairs. Consideration of friction in the joints is particularly important for the approach of the mechanism’s structural groups to special positions. The task of determining reactions in the joints with considering friction forces is often not set. It is worth estimating how close to a special position it is possible to approach, without getting into a self-braking mode. Let us carry out such an analysis on the example of Assur groups consisting of two links and three kinematic pairs:

- RRR (three rotational KP),
- RRT (two rotational and a translational KP).

2 Models of the Rotational KP

Let us use the models described in [20]. For the ideal rotational KP (Fig. 1a), let us write the projections on the axis of reaction \bar{R}_2 from the first link to the second one:

$$R_{2x} = R_2 \cos \alpha,$$

$$R_{2y} = R_2 \sin \alpha,$$

where $R_2 = |\bar{R}_2|$

α is the angle between axis x and vector \bar{R}_2 .

Moment relative to rotation axis $M_2^R = 0$.

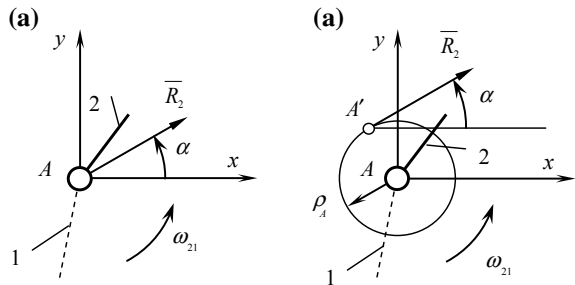
With allowance for friction forces (Fig. 1b), the value of torque can be determined from expression

$$M_2^R = -\varepsilon^V \rho_A R_2,$$

where $\varepsilon^V = \text{sign } \omega_{21} = \pm 1$ is the sign of angular velocity of the second link relative to the first one,

ρ_A is a friction circle radius.

Fig. 1 Models of the rotational KP **a** ideal RKP, **b** non-ideal RKP



The replacing ideal kinematic pair (RIKP) should have the same reactions as the initial KP with friction. In our case, the axis of the RIKP is located at point A' (Fig. 1b), through which vector \bar{R}_2 passes. A lot of such RIKPs are located inside the friction circle in the absence of the relative motion of the links ($\omega_{21} = 0$) or on the circumference of the friction circle radius ρ_A with ($\omega_{21} \neq 0$).

3 RRR Assur Group

Let us consider a dyad with three rotational kinematic pairs ABC (Fig. 2).

For a certain set of forces acting on the group and relative angular velocities of the links, it is possible to find an Assur group with RIKP $A'B'C'$ [1]. Many joints of such groups are located on circumferences with radii ρ_A, ρ_B, ρ_C or inside these radii, when the relative angular velocity of the links connected by the mentioned joint is equal to zero. If among this set there is at least one mechanism with an RIKP in a special position, when the joints are located on a straight line ($A'B'C'$, Fig. 3), the group can enter the self-braking mode, when further movement of the links becomes impossible.

Fig. 2 RRR dyads replacing IKP

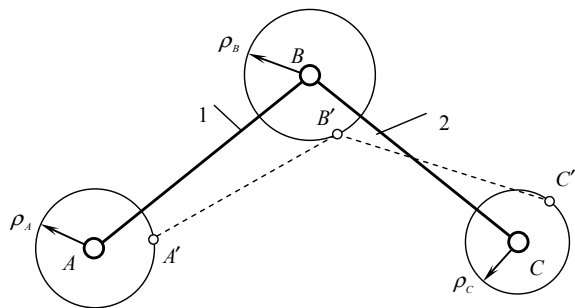
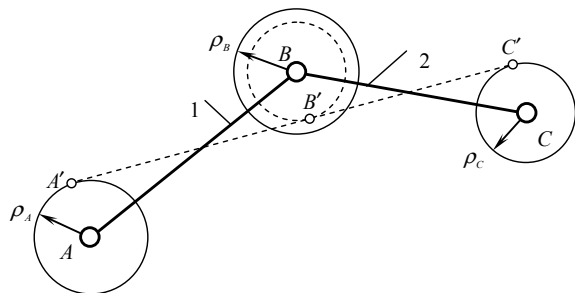


Fig. 3 Self-braking modes of the RRR dyad



4 Models of the Translational KP

Let us consider the model of the translational ideal KP (Fig. 4a). Let us orient axis x along the line of the relative motion of the links. Let us write down the projections of reaction \bar{R}_2 from the first link to the second one on the axes and torque M_2^R :

$$\begin{aligned} R_{2x} &= 0, \\ R_{2y} &= N, \\ M_2^R &= N \cdot s, \end{aligned}$$

where N is the normal reaction,

s is displacement of the normal reaction relative to the origin of the coordinates.

For a non-ideal kinematic pair, if a contact of the links occurs on one side, it is possible to introduce a force of friction which is directed against the relative motion of the links (Fig. 4b):

$$F = -\epsilon^V f |N|,$$

where f is the coefficient of sliding friction,

$\epsilon^V = \text{sign } V_{21} = \pm 1$ —is the sign of velocity of the second link relative to the first one.

Let us write down the projections of the reaction and the torque:

$$\begin{aligned} R_{2x} &= -f \epsilon^V \epsilon^N N, \\ R_{2y} &= N, \\ M_2^R &= N \cdot s - f \epsilon^V N h, \end{aligned}$$

where $\epsilon^N = \text{sign } N = \pm 1$ is the sign of the normal reaction,

h is half the height of the slider.

For this model of the translational KP, it is possible to determine the angle of friction, which is equal to the inclination angle of the RIKP (Fig. 4b):

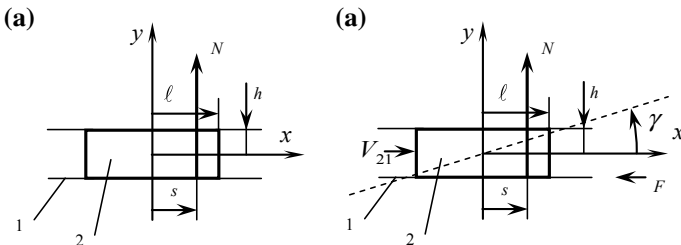


Fig. 4 Models of the translational KP **a** ideal TKP, **b** non-ideal TKP

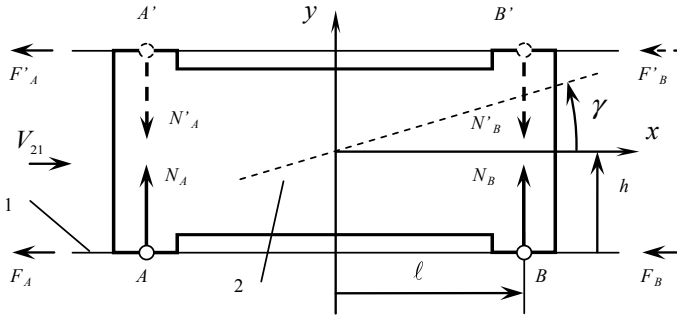


Fig. 5 Model of the translational KP with two-point contact

$$\tan \gamma = -R_{2x}/R_{2y} = f\epsilon^V \epsilon^N.$$

The above model can be used if s is within the range of

$$-1 \leq s \leq 1,$$

where l is half the length of the slider.

If this condition is not fulfilled, we receive the contact not on one, but on two surfaces of a translational pair. In this case, for example, a model with two-point contact is used [10], Fig. 5. In points A and B , there are reactions N_A , N_B and friction forces F_A , F_B . If normal reactions are negative, their application points become A' и B' , respectively. Let us write down the projections of reactions on the axes and torque:

$$\begin{aligned} R_{2x} &= -f\epsilon^V \epsilon^{N_A} N_A - f\epsilon^V \epsilon^{N_B} N_B, \\ R_{2y} &= N_A + N_B, \\ M_2^R &= l(N_B - N_A) - f\epsilon^V (N_B + N_A)h, \end{aligned}$$

where $\epsilon^{N_A} = \text{sign } N_A$, $\epsilon^{N_B} = \text{sign } N_B$.

If $\epsilon^{N_B} = \epsilon^{N_A}$, we obtain the model considered before as in this case $l(N_B - N_A) = s \cdot N$, $N_B + N_A = N$.

If $\epsilon^{N_B} = -\epsilon^{N_A} = \epsilon^N$, we obtain

$$\begin{aligned} R_{2x} &= -(f^s/l)\epsilon^V \epsilon^N N, \\ R_{2y} &= N, \\ M_2^R &= N \cdot s - f\epsilon^V N h. \end{aligned}$$

Thus, the friction angle (angle of inclination of the RIKP guide rail) increases:

$$\tan \gamma = -R_{2x}/R_{2y} = (f^s/l)\epsilon^V \epsilon^N \text{ при } |s| > l.$$

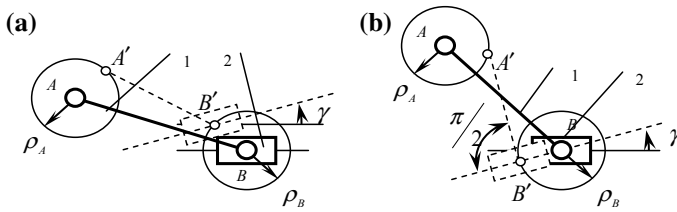


Fig. 6 RRT dyad **a** replacing IKPs, **b** self-braking mode

5 RRT Assur Group

Let us consider as an example an RRT dyad with a translational kinematic pair (Fig. 6).

If you search for a group with a RIPK at the given external forces and motion speeds of the links, joints A' and B' will be located on circumferences ρ_A and ρ_B , respectively, the guide rail of the translational pair should be inclined by friction angle γ (Fig. 6a). Similar to the RRR dyad, let us show the position in which groups exist in a special position among the set of groups with RIKPs, when the angle between segment $A'B'$ and the translational RIPK becomes equal to $\pi/2$ (Fig. 6b) and there is a possibility of self-braking.

6 Conclusion

In conclusion, we should note that if among the set of structural groups with RIKPs in a given position, there were groups in a special position, it only indicates the possibility of the self-braking mode occurring at certain external forces and relative motion speeds of the links. But even if the effect of self-braking does not occur, in this case, most often, there is a sharp increase in reactions and friction forces in the joints, which negatively affects performance of the mechanism.

References

1. Le Xuan A (2003) Dynamics of mechanical systems with Coulomb friction. Springer Science & Business Media, p 269
2. Mamaev IS, Ivanova TB (2014) The dynamics of a rigid body with a sharp edge in contact with an inclined surface in the presence of dry friction. Regul Chaotic Dyn 19(1):116–139
3. Klepp HJ (2002) Modes of contact and uniqueness of solutions for systems with friction-affected sliders. J Sound Vib 254(5):987–996. <https://doi.org/10.1006/jsvi.2001.4147>
4. Qi Z, Luo X, Huang Z (2011) Frictional contact analysis of spatial prismatic joints in multibody systems. Multibody Sys Dyn 26(4):441–468. <https://doi.org/10.1007/s11044-011-9264-9>

5. Acary V (2013) Projected event-capturing time-stepping schemes for nonsmooth mechanical systems with unilateral contact and Coulomb's friction. *Comput Meth Appl Mech Eng* 256:224–250. <https://doi.org/10.1016/j.cma.2012.12.012>
6. Zhang J, Wang Q (2016) Modeling and simulation of a frictional translational joint with a flexible slider and clearance. *Multibody Sys Dyn* 38(4):367–389. <https://doi.org/10.1007/s11044-015-9474-7>
7. Xu Z, Wang Q, Wang QY (2017) Numerical method for dynamics of multi-body systems with two-dimensional Coulomb dry friction and nonholonomic constraints. *Appl Math Mech* 38(12):1733–1752
8. Gholami F, Nasri M, Kövecses J, Teichmann M (2016) A linear complementarity formulation for contact problems with regularized friction. *Mech Mach Theory* 105:568–582. <https://doi.org/10.1016/j.mechmachtheory.2016.07.016>
9. Zhang S, Xie ZQ, Chen BS, Zhang HW (2013) Finite element analysis of 3D elastic-plastic frictional contact problem for cosserat materials. *Comput Mech* 51(6):911–925. <https://doi.org/10.1007/s00466-012-0773-z>
10. Goncharov AA (2014) Study of the influence of geometric parameters of elements upon self-locking of free running wedge mechanisms. *J Mac Manuf Reliab* 43(1):14–21
11. Timofeev GA, SamoiloVA MV, Panyukhin VV (2013) Analysis of self-locking criteria from the viewpoint of their validity. *Herald of the Bauman Moscow State Technical University. Mech Eng* 4(93):27–42
12. Timofeev GA, Panjukhin VV, Yaminsky AV (2017) Self-braking criteria analysis. *Proc High Educ Inst Mach Build* 2(683):12–18
13. Kargin PA (2013) Investigation of dynamic properties of self-braking drive for hoisting machines. *Russ Eng Res* 8:16–21
14. Artiukh VG, Nikitchenko AA, Podgornaya NV, Chigareva IN, Chernysheva NV (2017) Analysis of the working efficiency of self-leaking gauk nodes of fastening the rail jobs. *St. Petersburg State Polytech Univ J Eng Sci Technol* 23(2):223–232
15. Petrov GN (2003) Determination of the reaction forces in hinges of plane mechanisms with many degrees of freedom taking into account a friction force. *Theor Mech Mach* 1:55–62
16. Timofeyev GA, Sashchenko DV, SamoiloVA MV (2013) Rack and pinion self-locking gears. *Proc High Educ Inst Mach Build* 4:17–23
17. Timofeyev GA, Panyukhin VV, SamoiloVA MV (2013) Geometry of cylindrical self-locking gears with circular-arc tooth profiles. *Proc of High Educ Inst Mach Build* 5:21–28
18. Evgrafov AN, Karazin VI, Petrov GN (2019) Analysis of the self-braking effect of linkage mechanisms. *Lect Notes Mech Eng* 119–127
19. Evgrafov AN, Petrov GN (2017) Computer simulation of mechanisms. *Lect Notes Mech Eng* 45–56
20. Evgrafov AN, Petrov GN (2018) Self-Braking of planar linkage mechanisms. *Lect Notes Mech Eng* 83–92

Energy Flux Analysis of Axisymmetric Vibrations of Circular Cylindrical Shell on an Elastic Foundation



George V. Filippenko

Abstract Dispersion of elastic waves in an infinite circular cylindrical shell of Kirchhoff-Love type is studied. The spring-type boundary condition on the outer surface, analogous to Winkler foundation for a plate is considered. The problem of free shell vibrations is explored. The dispersion equation and the dispersion curves character in the vicinity of the veering point is analyzed. The propagating waves and their energy fluxes in the shell are investigated. The contributions to the total energy flux of various energy transfer mechanisms in the shell are compared. Their short-wave and long-wave asymptotics are analyzed.

Keywords Wave propagation · Cylindrical shell · Shell vibrations · Local and integral energy flux

1 Introduction and Statement of the Problem

Cylindrical shells in liquids have long been studied in connection with rich applications in engineering and construction. This is one of the most important elements in modeling acoustic waveguides, various pipelines, supports of offshore drilling rigs and other hydraulic structures [1–20]. Axisymmetric wave processes [6] are of particular interest due to their frequent occurrence and the convenience of analytical analysis.

Let us consider the free vibrations of an infinitely extended circular cylindrical shell of Kirchhoff-Love type [14]. The cylindrical coordinate system (r, φ, z) and local coordinate system $(\mathbf{t}, \mathbf{n}, \mathbf{k})$ are introduced. Here the axis z coincides with the cylinder axis, the vectors \mathbf{t} , \mathbf{n} are respectively the tangent and normal unit vectors to the shell and the vector \mathbf{k} is the unit vector along the axis z . The displacement vector $\mathbf{u} = (u_t, u_z, u_n)^T$ (T —is the sign of the transpose operation) describes the vibrational

G. V. Filippenko (✉)

Institute of Problems of Mechanical Engineering, V. O., Bolshoj pr., 61,
St. Petersburg 199178, Russia
e-mail: g.filippenko@spbu.ru

St. Petersburg State University, 7-9, Universitetskaya nab., St. Petersburg 199034, Russia

© Springer Nature Switzerland AG 2020

A. N. Evgrafov (ed.), *Advances in Mechanical Engineering*,
Lecture Notes in Mechanical Engineering,
https://doi.org/10.1007/978-3-030-39500-1_9

field in the shell. Only axisymmetric oscillations will be considered below, therefore φ will be omitted in the function arguments.

Similar to Winkler foundation for the plates, Winkler force acts on the boundary of the shell, normal to it (reaction of Winkler foundation)

$$f_n(z) = K_n u_n(z); \quad -\infty < z < +\infty, \quad (1)$$

where K_n is the coefficient of elasticity of Winkler foundation. The boundary condition is supplemented by the condition at infinity $z = \pm\infty$ [13]. The homogeneous waves in the shell traveling from $z = -\infty$ to $z = +\infty$ are considered.

The following notations are introduced: $c_s = \sqrt{Eh/((1-\nu^2)\rho)}$ is the velocity of deformation waves propagation of the middle surface of the cylindrical shell; E , ν and ρ_s , is Young's modulus, Poisson's ratio and volumetric density of the shell material, respectively, h is the thickness of the shell, $\rho = \rho_s h$ is the surface density, R is the radius of the cylindrical shell. The dependence of all processes on time is assumed to be harmonic with frequency ω and the time factor $\exp\{-i\omega t\}$ is omitted everywhere.

In addition, the dimensionless parameters are introduced: the dimensionless frequency $w = \omega R/c_s$ and the parameter $\alpha^2 = (1/12)(h/R)^2$ characterizing the relative thickness of the shell.

In the axisymmetric case, the balance of the forces acting on the cylinder (taking into account Winkler force as in [1]) can be written in the form ($-\infty < z < +\infty$)

$$\mathbf{L}\mathbf{u} = \begin{pmatrix} w^2 + d^2 \partial_z^2 & 0 & 0 \\ 0 & w^2 + \partial_z^2 & \nu \partial_z \\ 0 & -\nu \partial_z & w^2 - \alpha^2(1 - 2\nu \partial_z^2 + \partial_z^4) - 1 - K \end{pmatrix} \begin{pmatrix} u_t \\ u_z \\ u_n \end{pmatrix} = \mathbf{0}, \quad (2)$$

where

$$\begin{aligned} d^2 &= (1 + 4\alpha^2)\nu_-, \quad \nu_- = (1 - \nu)/2, \quad \partial_z := R \frac{\partial}{\partial z}, \\ K &= \frac{1 - \nu^2}{h/R} K_0; \quad K_0 = \frac{K_n R}{E}. \end{aligned} \quad (3)$$

Here K_0 is the dimensionless coefficient of elasticity connecting the dimensionless force f_n/E and dimensionless displacement u_n/R . Kirchhoff-Love shell model from [14] is used in this paper.

2 Getting the View for the Vibration Field

The solution of Eq. (3) is sought in the form

$$(u_t, u_z, u_n)^T = Ae^{i\lambda z}(\zeta, \xi, \gamma)^T. \quad (4)$$

Here A, ζ, ξ, γ are the arbitrary constants; λ is the wave number. Further the dimensionless coordinate $z := z/R$ and dimensionless wave number $\lambda := \lambda R$ will be used. The homogeneous algebraic system (5) is obtained after substitution (4) into (2)

$$\mathbf{L}^\lambda \mathbf{x} = \mathbf{0}, \quad (5)$$

where \mathbf{x} is the eigenvector (it will be normalized to the unit length) and matrix \mathbf{L}^λ is the Fourier image of the operator \mathbf{L} . The condition of existence of the nontrivial solution of the system is the dispersion equation $\det \mathbf{L}^\lambda = 0$. The homogeneous propagating waves are considered for a given frequency w (only the real positive roots of this equation are found). Thus three dispersion curves $w_j = w_j(\lambda)$, $j = 1, 2, 3$ arise. The curve $w_3(\lambda) = \lambda d$ corresponds the waves propagating without dispersion. Two other curves: $w_1(\lambda) \equiv w_+(\lambda)$ and $w_2(\lambda) \equiv w_-(\lambda)$ are determined by the expression

$$\begin{aligned} 2w_\pm^2 &= \lambda^2 + \beta^2 \pm \sqrt{(\lambda^2 - \beta^2)^2 + 4\lambda^2 v^2}; \\ \beta^2 &= 1 + K + \alpha^2(1 + 2v\lambda^2 + \lambda^4). \end{aligned} \quad (6)$$

Hence, starting points of these dispersion curves can be founded

$$w_+|_{\lambda=0} = 0; \quad w_0 \equiv w_-|_{\lambda=0} = \sqrt{1 + K + \alpha^2}. \quad (7)$$

After substituting the corresponding roots $w_j = w_j(\lambda)$, $j = 1, 2, 3$ in the system (5), one can find the eigenvectors \mathbf{x} and, therefore, the form of the vibration field in the system. It is important to note that general solution of the system splits into two independent solutions. One of them (corresponding root $w_3(\lambda)$) determines the purely rotational motions of the shell and it can be represented in the form $\mathbf{u} = Ae^{i\lambda z}(1, 0, 0)^T$. These waves have no dependence on K_0 . Another one contains longitudinal and bending motions. This solution has the form

$$\begin{pmatrix} u_t \\ u_z \\ u_n \end{pmatrix} = \frac{Ae^{i\lambda z}}{\sqrt{(\lambda^2 - w^2)^2 + \lambda^2 v^2}} \begin{pmatrix} 0 \\ i\lambda v \\ \lambda^2 - w^2 \end{pmatrix}. \quad (8)$$

After determining the vibration field in the system, one can find the vector of energy flux density in the shell. The only nonzero component of this vector is directed along the z axis. The integral energy flux Υ_{cyl} averaged over a period of

harmonic oscillations $T = 2\pi/\omega$ is considered (the flux through the cross section of a cylindrical shell by a plane perpendicular to the generator [7]). Further just this averaged component of the integral energy flux will be called “energy flux in the shell” for brevity. This flux can be represented in the form of sum of four components $\Upsilon_t, \Upsilon_l, \Upsilon_n, \Upsilon_m$: torsional, longitudinal, normal and the component associated with the moments, respectively

$$\begin{aligned} \Upsilon_{cyl} &= \Upsilon_t + \Upsilon_z + \Upsilon_n + \Upsilon_m; \\ \begin{Bmatrix} \Upsilon_t \\ \Upsilon_z \\ \Upsilon_n \\ \Upsilon_m \end{Bmatrix} &= \pi\omega\rho c^2 \begin{Bmatrix} d^2\lambda|u_t|^2 \\ \lambda|u_z|^2 + v\text{Im}(u_n\bar{u}_z) \\ \lambda\alpha^2|u_n|^2(v + \lambda^2) \\ \lambda\alpha^2|u_n|^2(v + \lambda^2) \end{Bmatrix}. \end{aligned} \quad (9)$$

For example, the longitudinal component Υ_z corresponds to the work of the generalized longitudinal force at the longitudinal displacement u_z , etc.

The equality $\Upsilon_n = \Upsilon_m$ follows from (9) and it is important to note that Υ_t is independent on K , due to the fact that torsional vibrations are not connected with normal vibrations u_n through which the shell interacts with the Winkler foundation.

Following expressions for the components of the energy flux normalized to its transverse component $\Upsilon_t = \pi d^2\omega\rho c^2\lambda|A|^2$ can be obtained from (8) and (9)

$$\begin{Bmatrix} S_z \\ S_n \end{Bmatrix} \equiv \frac{1}{\Upsilon_t} \begin{Bmatrix} \Upsilon_z \\ \Upsilon_n \end{Bmatrix} = \frac{1}{d^2((w^2 - \lambda^2)^2 + \lambda^2 v^2)} \begin{Bmatrix} \lambda^2 v^2 + v(w^2 - \lambda^2) \\ \alpha^2(v + \lambda^2)(w^2 - \lambda^2)^2 \end{Bmatrix}. \quad (10)$$

After substituting (6) in (10) the explicit representations of the energy fluxes (as functions of the wavenumber λ) can be obtained. Further these representations will be analyzed asymptotically on λ in order to obtain more simple formulas for them. The expressions for the dispersion branches (6) can be transformed to the form (11a) and (11b) for small λ and large λ ($\lambda \gg 1$), respectively

$$\begin{aligned} w_1(\lambda) &= \lambda \sqrt{1 - \frac{v^2}{w_0^2}} + O(\lambda^3), \\ w_2(\lambda) &= w_0 + \frac{v(2\alpha^2 w_0^2 + v)}{2w_0^3} \lambda^2 + O(\lambda^4), \end{aligned} \quad (11a)$$

$$\begin{aligned} w_1(\lambda) &= \lambda \left(1 - \frac{v^2}{2\alpha^2} \frac{1}{\lambda^4} + O\left(\frac{1}{\lambda^6}\right) \right), \\ w_2(\lambda) &= \alpha\lambda^2 \left(1 + \frac{v}{\lambda^2} + \frac{w_0^2 - \alpha^2 v^2}{2\alpha\lambda^4} + O\left(\frac{1}{\lambda^6}\right) \right). \end{aligned} \quad (11b)$$

Asymptotic expressions for $w_1(\lambda)$ and $w_2(\lambda)$ for small λ (11a) and formulas (11b) for large λ determine quasi dispersion curves. Character of the wave process

is conserved along them (exception is the transition process in the region of the veering point of dispersion curves). After substituting (11a, 11b) into the long-wave asymptotics of the normalized components of the energy fluxes (10), the asymptotic expressions (12a), (12b) (for large λ) and (13a), (13b) (for the corresponding short-wave asymptotics) for the energy flux components are obtained

$$\begin{Bmatrix} S_z^1 \\ S_n^1 \end{Bmatrix} = \frac{1}{d^2} \begin{Bmatrix} 1 - \frac{v^2}{w_0^2} - \frac{2v^2(w_0^2(1-\alpha^2v)-v^2)}{w_0^6} \lambda^2 + O(\lambda^4) \\ \frac{\alpha^2 v^3}{w_0^4} \lambda^2 + O(\lambda^4) \end{Bmatrix}, \tag{12a}$$

$$\begin{Bmatrix} S_z^2 \\ S_n^2 \end{Bmatrix} = \frac{1}{d^2} \begin{Bmatrix} \frac{v^2}{w_0^2} + \frac{2v^2(w_0^2(1-\alpha^2v)-v^2)}{w_0^6} \lambda^2 + O(\lambda^4) \\ \alpha^2(v + \lambda^2) - \frac{\alpha^2 v^3}{w_0^4} \lambda^2 + O(\lambda^4) \end{Bmatrix}, \tag{12b}$$

$$\begin{Bmatrix} S_z^1 \\ S_n^1 \end{Bmatrix} = \frac{1}{d^2} \begin{Bmatrix} 1 - \frac{v^2}{\alpha^2 \lambda^4} + O(1/\lambda^6) \\ \frac{v^2}{\alpha^2 \lambda^4} + O(1/\lambda^6) \end{Bmatrix}, \tag{13a}$$

$$\begin{Bmatrix} S_z^2 \\ S_n^2 \end{Bmatrix} = \frac{1}{d^2} \begin{Bmatrix} \frac{v^2}{\alpha^2 \lambda^4} + O(1/\lambda^6) \\ \alpha^2(\lambda^2 + v) - \frac{v^2}{\alpha^2 \lambda^4} + O(1/\lambda^6) \end{Bmatrix}. \tag{13b}$$

Here indices $j = 1, 2$ in $S_{z,n}^j$ correspond to components of the energy fluxes calculated for the waves from the first and second dispersion curves, respectively.

3 Numerical Results and Their Analysis

The dependences of the frequency w (Fig. 1a, b) and normalized energy flux components (Figs. 2, 3 and 4) on the wave number λ are considered below. The values of the shell parameters are taken as follows: $v = 0.3, h/R = 0.05$.

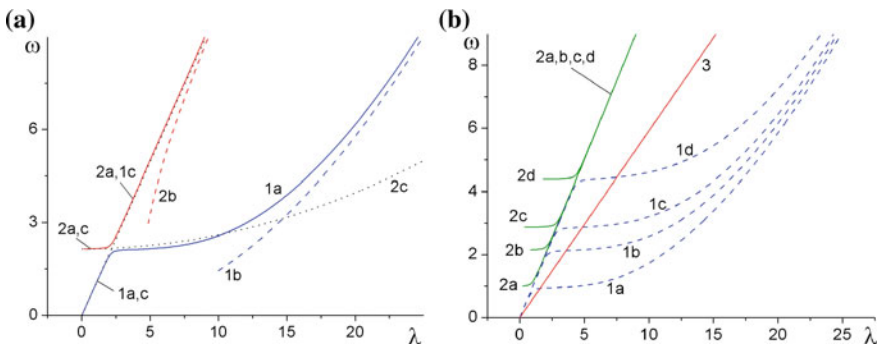


Fig. 1 **a** Dispersion curves and their asymptotics for $K_0 = 0.2$. **b** Dispersion curves for $K_0 = 0.0, 0.2, 0.4, 1.0$

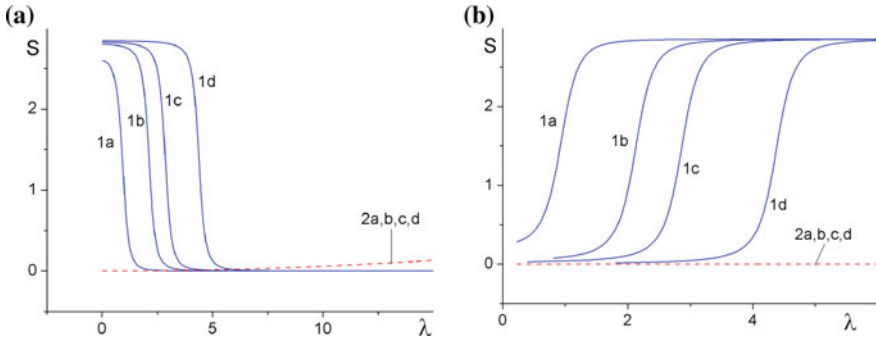


Fig. 2 **a** Components of the energy fluxes S_z^1 (1) and S_n^1 (2) for $K_0 = 0.0, 0.2, 0.4, 1.0$, **b** components of the energy fluxes S_z^2 (1) and S_n^2 (2) for $K_0 = 0.0, 0.2, 0.4, 1.0$

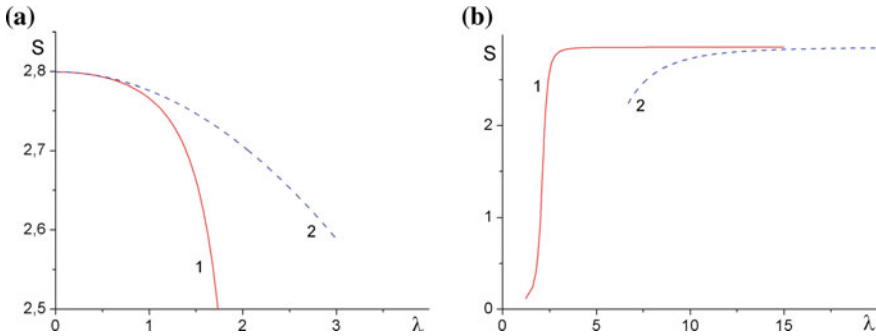


Fig. 3 **a** The component of the energy flux S_z^1 (1) and its long-wave approximation (2). **b** The component of the energy flux S_z^2 (1) and its short-wave approximation (2)

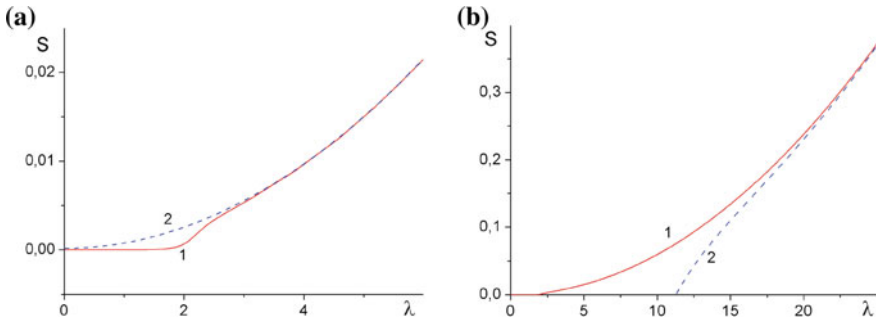


Fig. 4 **a** Component of the energy flux S_n^2 (1) and its long-wave approximation (2). **b** The component of the energy flux S_n^2 (1) and its short-wave approximation (2)

In both Figs. 1a and b the branches of the dispersion curves $w_1(\lambda)$, $w_2(\lambda)$, $w_3(\lambda)$ are marked with the digits 1, 2, 3, respectively. These branches will be called “first”, “second”, etc. Line 3 (Fig. 1b) is the dispersion curve corresponding to purely torsional vibrations. The character of the wave processes in the shell is determined by the interaction of the energy distribution channels corresponding to the components of the energy flux. This interaction is most intensive in the vicinity of the veering points (quasi-intersections of the dispersion curves 1 and 2 in the point $w = w_0$ (7) in Figs. 1a, b) [6, 7]. This effect corresponds to exchange of the oscillations character between the waves from the corresponding dispersion curves in the vicinity of this point. It is important to note that energy fluxes track this effect better than kinematic or force characteristics. It is caused by the fact that energy fluxes take into account phase shifts between these characteristics [7].

Dispersion curves (6) for values $K_0 = 0.0, 0.2, 0.4, 1.0$ (the corresponding curves are marked with letters a, b, c, d) are introduced in Fig. 1b. The influence of this parameter brings to shift of the veering point $w = w_0$ (7). Nevertheless, the short-wave asymptotics of the dispersion curves (11b) are practically independent on the value of this parameter.

The longitudinal S_z^j (curve 1) and normal S_n^j (curve 2) components of the energy fluxes for the first ($j = 1$) and second ($j = 2$) dispersion curves for the different values of parameter K_0 are shown in Fig. 2a and b. These curves are marked with letters a, b, c, d for $K_0 = 0.0, 0.2, 0.4, 1.0$ correspondingly. The normal component is practically independent of K_0 (curves 2a, b, c, d) and the influence of this parameter on the longitudinal component basically come down to shift of the corresponding curves 1a, b, c, d while their maximum weakly depends on it (12, 13).

It can be noted that the largest value of the energy flux longitudinal component S_z weakly depends on the coefficient K_0 . In this case, the normal component S_n of the energy flux is realized mainly on the waves from the dispersion curve $w_1(\lambda)$ at frequencies $w > w_0$ (and $\lambda > \lambda_0 = \lambda(w_0) > 0$ correspondingly). Moreover, component S_n is noticeably smaller than the component S_z .

The next figures illustrate energy flux components $S_{z,n}$ (curves 1) and their long and short wave asymptotics (curves 2) for the waves from the first (Fig. 3a, b) and second (Fig. 4a, b) dispersion curves, calculated for $K_0 = 0.2$. The corresponding asymptotics of these dispersion curves are shown in Fig. 1a., where the dispersion curves are marked with letter a and their long and short-wave asymptotics are indicated with letters b and c , respectively.

Let us determine the condition when the normal component S_n of the energy flux is less than its torsional component S_t (the straight line $S = 1$ would fit the component S_t in Figs. 2, 3 and 4). The representation $S_n \approx \alpha^2(v + \lambda^2)/d^2$ follows from (12b, 13b) and satisfactorily describes both the long-wave and short-wave approximations (Fig. 4a). Hence the estimation $\lambda \approx d/\alpha \leq 40$ follows that is on the boundary of Kirchhoff-Love model applicability.

The distribution of the energy fluxes corresponds, in general case, to the quasi dispersion curves character. Each of these curves retains its own type of oscillation (more accurately, its type of energy flux component dominates along appropriate quasi dispersion curves). Asymptotics (11–13) correspond to these quasi dispersion

curves. The size of the veering zone, where the transition process takes place (in the wave numbers) $\delta\lambda \approx 2$.

4 Conclusions

The analysis of energy flux analytical representations and calculations shows that shell bandwidth for the axisymmetric longitudinal component of the energy flux (normalized on its torsion component) is weakly dependent on the wave number λ (along quasi dispersion curves) except the vicinity of the veering point. In this case the longitudinal component dominates everywhere except this neighborhood, where it is comparable to the torsion component. The bending component becomes noticeable after the veering point and becomes significant only for sufficiently large λ . The influence of the parameter K_0 (dimensionless coefficient of elasticity of Winkler foundation) is appeared mainly in the shift of the veering point and, accordingly, in the moment of “switching on” the bending component of the energy flux. From another side the influence of this parameter is appeared in the longitudinal component of the energy flux in the long-wavelength region (Fig. 2a, b).

References

1. Filippenko GV (2016) The vibrations of reservoirs and cylindrical supports of hydro technical constructions partially submerged into the liquid. In: Evgrafov A (ed) Selected contributions from the conference “modern engineering: science and education”. Saint Petersburg, Russia, June 2014. Lecture Notes in Mechanical Engineering. Springer International Publishing, Switzerland, pp 115–126. <https://doi.org/10.1007/978-3-319-29579-4>. ISSN: 2195-4356
2. Yeliseyev VV, Zinovieva TV (2012) Nonlinear-elastic strain of underwater pipeline in laying process. *Vycisl meh splos sred—Comput Continuum Mech* 5(1):70–78
3. Zinovieva TV (2012) Computational mechanics of elastic shells of revolution in mechanical engineering calculations. In: Modern engineering: science and education. Proceedings of second international scientific and practical conference. Published by State Polytechnic University, SPb, pp 335–343
4. Ter-Akopyants GL (2015) Dispersion curves and modal patterns of the wave propagation in elastic cylindrical shell filled with fluid. *Estestvennye-i-tehnicheskie-nauki* 6(84):77–81. ISSN: 1684-2626
5. Ter-Akopyants GL (2015) Axisymmetrical wave processes in cylindrical shell filled with fluid. *Estestvennye-i-tehnicheskie-nauki* 7(85):10–14. ISSN: 1684-2626
6. Filippenko GV (2013) Energy aspects of axisymmetrical waves propagation in the infinite cylindrical shell fully submerged into the liquid. *Vycisl meh splos sred—Comput Continuum Mech* 6(2):187–197
7. Filippenko GV (2014) Energy aspects of waves propagation in the infinite cylindrical shell fully submerged into the liquid. *Vycisl meh splos sred—Comput Continuum Mech* 7(3):295–305
8. Sorokin SV, Nielsen JB, Olhoff N (2004) Green’s matrix and the boundary integral equations method for analysis of vibrations and energy flows in cylindrical shells with and without internal fluid loading. *J Sound Vib* 271(3–5):815–847

9. Filippenko GV (2010) Statement of the boundary-contact problems for the shells in acoustics. In: Proceedings of the international conference “days on diffraction 2010”, St. Petersburg, Russia, pp 57–626, 8–10 June 2010
10. Filippenko GV, Wilde MV (2018) Backwards waves in a fluid-filled cylindrical shell: comparison of 2D shell theories with 3D theory of elasticity. In: Proceedings of the international conference “days on diffraction 2018”, St. Petersburg, Russia, pp 112–117, 4–8 June 2018
11. Filippenko GV, Wilde MV (2018) Backwards waves in a cylindrical shell: comparison of 2D shell theories with 3D theory of elasticity. In: Proceedings of the XLVI summer school conference advanced problems in mechanics (APM 2018), St. Petersburg, Russia, pp 79–86, 25–30 June 2018
12. Cremer L, Heckl M, Petersson BAT (2005) Structure-borne sound: structural vibrations and sound radiation at audio frequencies, 3rd edn. XII, 607, p 215 illus
13. Sveshnikov AV (1951) The limit absorption principle for a wave guide. Doklady Akademiji Nauk SSSR, 80, pp 345–347 (in Russian)
14. Yeliseev VV Mechanics of elastic bodies, SPb., DPbSPU, Russia, p 336 (in Russian)
15. Filippenko GV (2018) Wave processes in the periodically loaded infinite shell. In: Evgrafov A (ed) Selected contributions from the conference “modern engineering: science and education”. Saint Petersburg, Russia, May 2018. Lecture Notes in Mechanical Engineering. Springer International Publishing, Switzerland, pp 11–20. <https://doi.org/10.1007/978-3-030-11981-2-2>. ISSN: 2195-4356
16. Filippenko GV (2018) Waves with the negative group velocity in the cylindrical shell, filled with compressible liquid. In: Evgrafov A (ed) Advances in Mechanical Engineering, Lecture Notes in Mechanical Engineering. Published by Springer International Publishing, Switzerland, pp 93–104. <https://doi.org/10.1007/978-3-319-72929-9>. ISSN: 2195-4356, ISBN: 978-3-319-72928-2
17. Zinovieva TV (2018) Calculation of equivalent stiffness of corrugated thin-walled tube. In: Evgrafov A (ed) Selected contributions from the conference “modern engineering: science and education”. Saint Petersburg, Russia, May 2018, Lecture Notes in Mechanical Engineering. Springer International Publishing, Switzerland, pp 211–220. <https://doi.org/10.1007/978-3-030-11981-2-19>. ISSN: 2195-4356
18. Zinovieva TV (2017) Calculation of shells of revolution with arbitrary meridian oscillations. In: Evgrafov A (ed) Selected contributions from the conference “modern engineering: science and education”. Saint Petersburg, Russia, June 2016. Springer International Publishing, Switzerland, pp 165–176. <https://doi.org/10.1007/978-3-319-53363-6-17>. ISSN: 2195-4356
19. Zinovieva TV (2016) Calculation of forced oscillations of shells of revolution with arbitrary meridian. In: Modern engineering: science and education. Proceedings of fifth international scientific and practical conference. Published by State Polytechnic University, SPb, pp 442–452. <http://www.mmf.spbstu.ru/mese/2016/442-452.pdf>
20. Filippenko GV (2017) Energy-flux analysis of the bending waves in an infinite cylindrical shell filled with acoustical fluid. In: Evgrafov A (ed) Selected contributions from the conference “modern engineering: science and education”. Saint Petersburg, Russia, June 2016. Lecture Notes in Mechanical Engineering. Springer International Publishing, Switzerland, pp 57–64. <https://doi.org/10.1007/978-3-319-53363-6>. ISSN: 2195-4356

Research on Possibilities of Reaching Ultra-Low Speeds on Centrifugal Workbenches, and Selection of System Components



Vladimir I. Karazin, Anna V. Karazina, Denis P. Kozlikin,
Anatolii V. Koshkin and Andrey V. Khisamov

Abstract The paper considers the issues of selecting components (electric motor, controller, control system) during the low speed rotation. The research results have shown that with the appropriate component selection it is possible to ensure fulfillment of rotation tasks at both ultra-low speeds (less than 1 rpm) and at simple low speeds (several revolutions per minute) without special equipment. Within the framework of the research the authors managed to assemble a prototype model which would ensure accurate uniform rotation in the range from 0.16 to 166 rpm.

Keywords Ultra-lowspeeds · Lowspeeds · Automation · Centrifugal workbench · SEW-EURODRIVE · Moviedrive · Kollmorgen · AKD · Industrial ethernet · EtherCAT · Etherlab · IgHEtherCATMasterlibrary · CanoverEtherCAT · PDO · SDO · Kollmorgen workbench

1 Introduction

Development of new equipment or its components, susceptible to operational conditions, always requires preliminary tests. An essential part of this process makes up mechanical testing, including linear acceleration impact tests [1, 2]. In order to facilitate the process of reproducing linear acceleration, it is common to use centrifugal workbenches. Depending on the test requirements, centrifugal workbenches can be distinguished by different velocity and accuracy.

In most tests a product has to withstand a steady load over a specific time span [3]. In such a case the accuracy of the reproduced acceleration does not meet any requirements. When it comes to important products, or a centrifugal workbench is used to test an accelerometer, the tested acceleration should be reproduced quite accurately [4–10]. In such situations strict requirements can be imposed not only on accuracy of the rotation speed, but also on the centrifugal workbench design [11, 12].

V. I. Karazin · A. V. Karazina · D. P. Kozlikin · A. V. Koshkin · A. V. Khisamov (✉)
Peter the Great Saint-Petersburg Polytechnic University, St.-Petersburg, Russia
e-mail: andrey@khis.ru

In most cases requirements for centrifugal workbenches comprise high rotation speeds (for reproduction of high linear acceleration within a confined space), high accuracy of reproducing the specified testing parameters and/or a possibility to use a product of a higher mass. Within the long history of centrifugal workbench development, all these tasks have been solved.

A less frequent task is to reproduce ultra-low rotation speeds. The uniform smooth rotation of an electric motor at the speed of under 0.5 rpm needs a specific approach to designing the whole system, a particular type of an electric motor and control system development. Having requirements for higher accuracy of the specified speed reproduction, it is extremely important to focus on all components of the system [13]. Let us consider the SEWEURODRIVE model workbench based on the MOVIDRIVEMDX61B converter (Fig. 1).

Despite its small size, the model workbench has a full-fledged frequency converter and an electric motor. The main components of the model workbench include the following:

- DFR63L4/BR/TF/EH1S/IS electric motor;
- MOVIDRIVE MDX61B frequency converter;
- hogs 74 dn 1024r encoder.

Connect the frequency converter via a standard input/output bus. This will allow us to operate the workbench in a standard way, which can show basic capacities of a frequency converter, built-in low-level control system and an electric motor [14]. Connection is provided via USB-RS485 converter (Fig. 2), which ensures connection of the workbench to PC, as the RS485 interface is realized in the converter via the RJ11 connector, rather than the standard COM port.

Having set rotation through the enclosed software (Bus Monitor, Motion Studio), or the remote control, and having set the speed of 1 rpm, it is easy to see uneven rotation, which is visible even without any measurement tools. It is caused by the fact that each component of the system provides inaccurate reproduction of low speeds. The rated rotation speed of the electric motor shows a significant difference from the specified one, the sensor has an insufficient number of marks for accurate control, the frequency converter has the lacking discreteness even in case the sensor is replaced. This example confirms that under the circumstances of low speeds, it is expedient to make the appropriate selection of all components in the system, rather than to count only on the motor power and upper limits of its operational modes.

Replace each component of the system with another which would meet our goals in the best way. At first, we will pay attention to the electric motor. Despite the design solution soft today's classical motors, which provide quite precise operational work, at low speeds only multi pole motors allow achieving uniformity of rotation. Let us test the rotary synchronous motor RT36-321-50-C-FT1-TK-RR-5000-N0-B (Fig. 3) produced by RUCHSERVOMOTOR (Republic of Belarus) (Table 1).

A scan be seen from the table, the motor in use cannot be called a low-speed one, but its rated rotation speeds are significantly lower than in the electric motor used before.

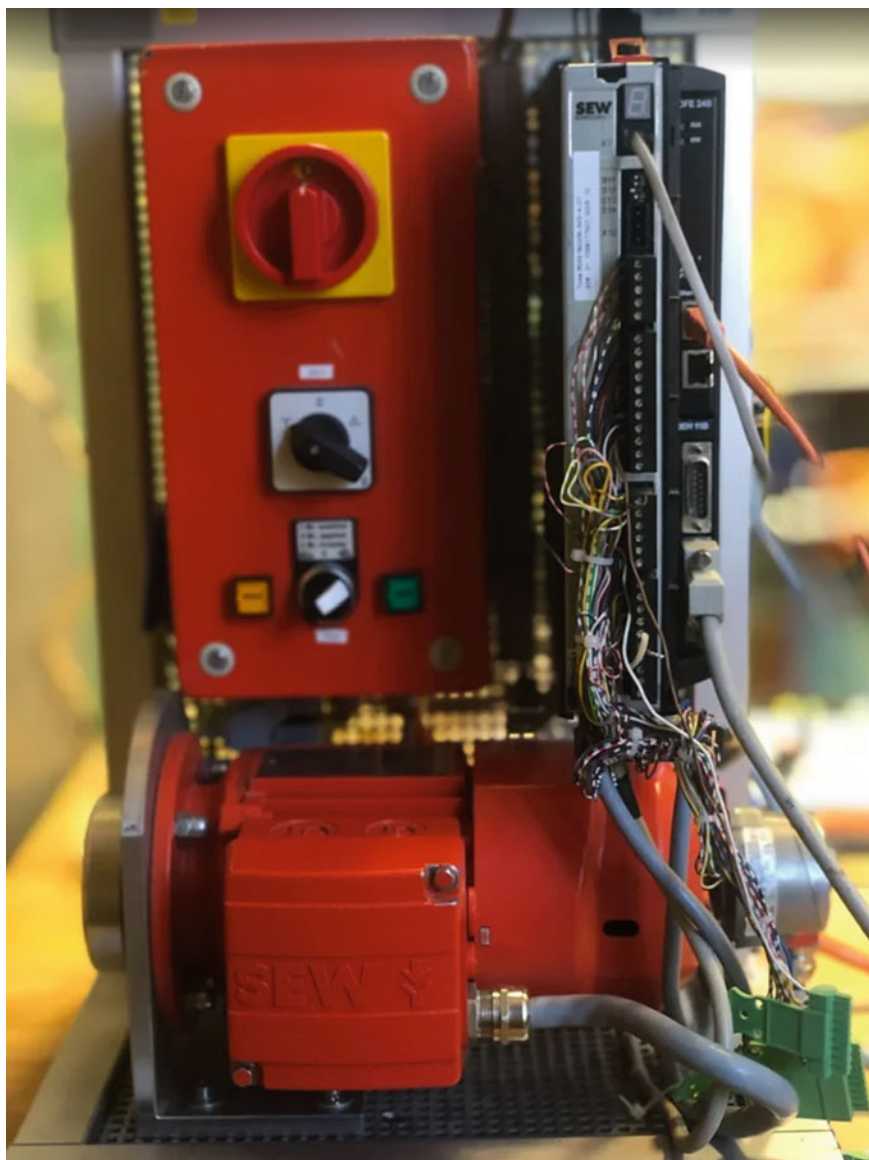


Fig. 1 SEW EURODRIVE model workbench based on the MOVIDRIVE MDX61B converter

For the accurate motion control, it is required to have a sensor with multiple tags. The electric motor is equipped with the encoder which has physical tags of 9000.

Due to its low capacity, the SEW-EURODRIVE MOVIDRIVE MDX61B converter, considered before, cannot fully process information from sensors with the tag quantity of 4096 [12]. In the research let us use the Kollmorgen AKD-P1207-NBCC



Fig. 2 SEW-EURODRIVE converter for PC connection to RS485

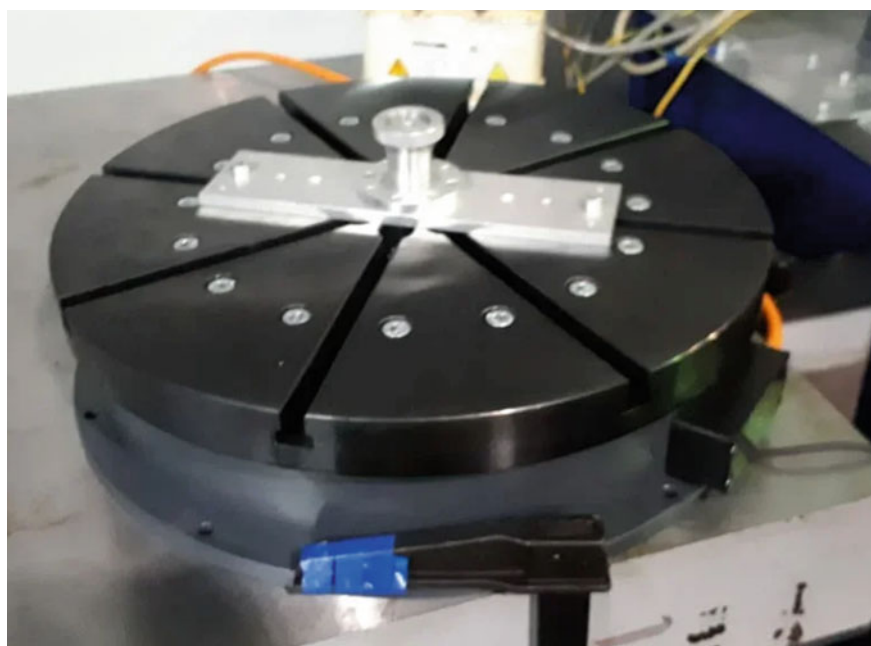


Fig. 3 Electric motor

Table 1 Certain properties of the electric motor RT36-321-50-C-FT

	Torque (Nm)	Rotation frequency (r/min)
Peak torque	429	111
Long torque	219	170
Bearing torque	5	205

servodrive. Its discreteness allows reliably specifying rotation speeds with the accuracy of 0.2 deg/s (0.03 rpm). Extra precision can be obtained via using the external control system.

Start rotation at the speed of 1 deg/s. In order to operate the motor, we will apply the authorized software for the Kollmorgen Workbench drive (Fig. 4).

The enclosed software ensures not only rotation of the motor, but it also allows doing motion studies due to rotation sensors fixed to the motor, and due to various information from the servo drive. In a majority of cases the most valuable information is a value of the actual rotation speed, and also values of the amperage from the converter. Receiving information from the servo drive, a virtual oscilloscope enables visualizing rotation in the form of graphs.

Monitoring the electric motor performance in connection with the AKD Kollmorgen drive, it is possible to note visual uniformity of rotation while testing. Let us analyze the information from the feedback sensor (Fig. 5).

A scan be seen from the graph of the current rotation speed, the resulting value of the average speed will be close to the specified one, in spite of constant sine wave variations. This is related to the tasks which are set for electric motors. The motor in use has a rather high torque, and it is aimed at large rotating masses, which smooth the reproduced rotation speed. Thus, in practice, the most important indicator is an average rotation speed.

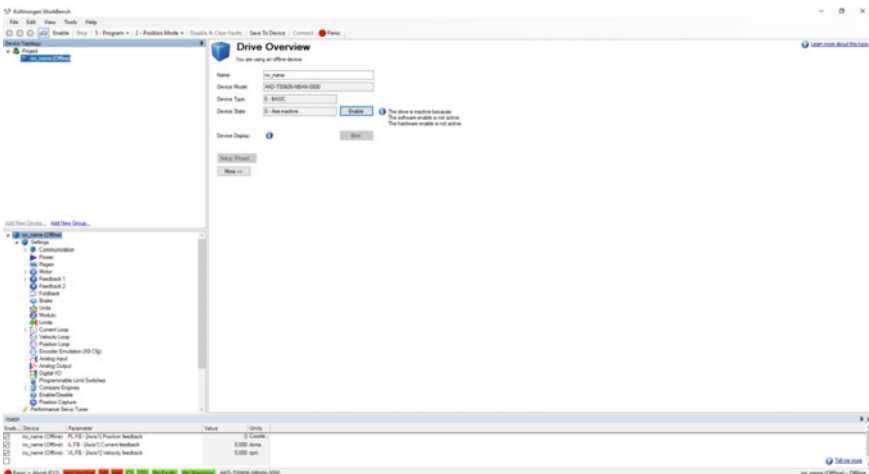


Fig. 4 Software overview for the Kollmorgen Workbench drive

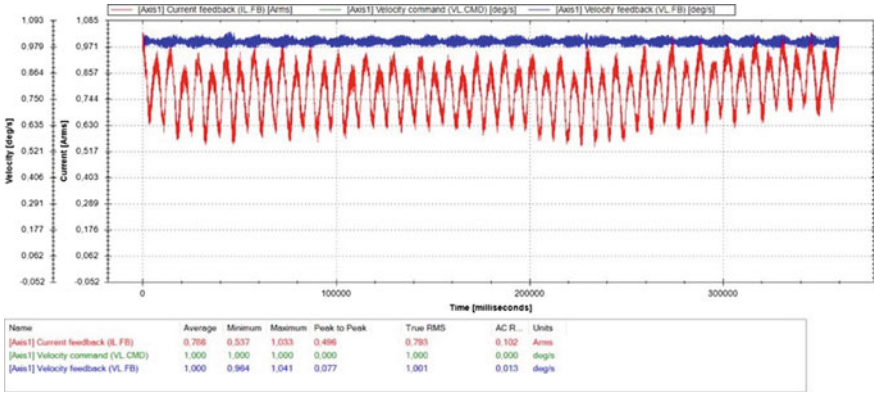


Fig. 5 Average speed value 1.000 deg/s

Let us consider accuracy of various values of the reproduced rotation speed (Table 2).

As can be seen from the table, the average value of the reproduced rotation speed is close enough to the specified one. This is ensured, among other things, by the high discreteness of the drive control system.

When developing an external control system, it should be taken into account that high discreteness of the drive requires high data exchange rates [15, 16]. For example, SEW-EURODRIVE (XT connector) has a maximum connection speed of 56 kbps. This speed may not be sufficient for the precise control. Most of today’s drives, including Kollmorgen AKD, allow for higher speed protocols. For AKD Kollmorgen, the standard protocol for external control is EtherCAT—one of the industrial implementations of the common Ethernet protocol. SEW EURODRIVE also allows controlling the MOVIDRIVE drive via this protocol if a DFE24B board is available.

Table 2 Testing results at different rotation speeds

Rotation speed (deg/s)	Average speed per revolution (deg/s)	Deviation (%)
1.000	1.001	0.1
1.002	1.002	0
5.050	5.051	0.02
10.123	10.123	0
30.203	30.205	0.0067
60.525	60.525	0
359.998	359.998	0
720.000	720.001	0.0001
1000.000	999.999	0.0001

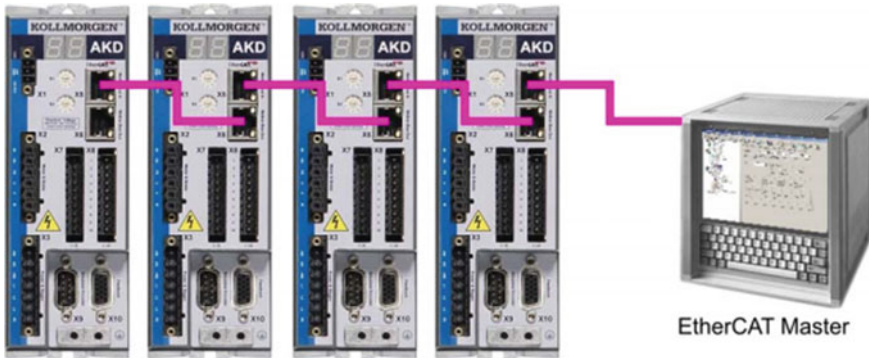


Fig. 6 EtherCAT serial connection

The signal source for the EtherCAT protocol is the Master device and the Slave device is the actuator. It is possible to connect several Slave devices in series to one Master (Fig. 6), which makes it possible to control the entire system with multiple actuators from one device (e.g. assembly workshop) [17–19].

The use of a standardized protocol, in addition to the high data exchange rate, allows using the same software for different drives. For example, both Moviedrive and Kollmorgen AKD can be controlled via the TwinCAT software.

For developing one’s own software, the special features of EtherCAT network design should be taken into account. First of all, it should be noted that a system based on EtherCAT is considered to be a real-time system. For this reason, it is recommended that separate solutions should be used as a signal source for systems requiring higher precision of task fulfilment (e.g. laser cutting), rather than a PC. In this case, for example, an expansion board is used as a master device, which is controlled via the supplied API, and there is no direct access to the Slave device from a computer with a direct connection via the Ethernet port. In the tasks where the operational error is less critical (e.g. rotation of a centrifugal workbench), a software Master can be used.

An example of the software version of a Master is the IgH EtherCAT Master software solution. This solution is free of charge and can be used with Linux operating systems. The software product distributed as a source code must be assembled into a complete solution according to the operating system kernel and the network card driver. For the Linux kernel of some versions of branch 2.6 there is a set of modules for different network cards. For other kernels it is necessary to use a generic driver. Within the framework of the tests, the work on kernels 2.6.32 and kernel 4.14 was tested. The ready solution assembly was made with x86 and ARM architecture.

After the launch of the service, another device/dev/EtherCAT [0–9] appears in the system. To work with it, the EtherCAT. So module was developed, which allows interacting with the protocol from its own software. Many examples of working with the IgH EtherCAT Master can be found on the Internet, e.g. <http://www.iram.fr/~blanchet/ethercat/akd/examples/> [20].

Apart from the IgH EtherCAT Master, there are other paid as well as free Master layers. For example: Simple Open EtherCAT Master. They are generally distinguished by the convenience of integration into the software. There are no particular differences in the EtherCAT protocol, as the protocol is strictly standardized and does not allow deviations.

In the course of the work, the system components that ensure ultra-low speeds have been selected and the sufficiently accurate (with an error of no more than 0.02% at low speeds and no more than 0.1% at ultra-low speeds) centrifugal workbench control system has been developed.

References

1. Evgrafov AN, Kolovsky MZ, Petrov GN (2015) Theory of mechanisms and machines. Publishing House of the Polytechnic University, St-Petersburg, 248 p. (rus.)
2. Popov AN, Polishchuck MN, Pulenec NE (2018) Test centrifuge arrangement analysis. Modern machine building. Science and education. 7:769–782. (rus.)
3. Evgrafov AN, Karazin VI, Khlebosolov IO (2003) Reproduction of motion parameters on rotary tables. Theory of Mechanism and machine. № 1. p. 92–96. (rus.)
4. Karazin VI, Kozlikin DP, Sukhanov AA, Tereshin VA, Khlebosolov IO (2017) Some ways of stable counterbalancing in the respect of moving masses on centrifuges. In: Evgrafov A (ed) Advances in mechanical engineering. Lecture notes in mechanical engineering. Springer, Switzerland, pp 73–85
5. Karazin VI, Kozlikin DP, Sukhanov AA, Khlebosolov IO (2016) One stable scheme of centrifugal forces dynamic balance. In: Evgrafov A (ed) Advances in mechanical engineering. Lecture notes in mechanical engineering. Springer, Switzerland, pp 75–87
6. Karazin VI, Kozlikin DP, Sukhanov AA, Tereshin VI, Khlebosolov IO (2016) Some methods of stable balancing of relative moving masses on the centrifuge. Modern machine building. Science and education. № 5. (rus.)
7. Andrienko PA, Kozlikin DP, Khisamov AV, Khlebosolov IO (2013) About the use of contactless measuring systems in centrifugal stands. Modern machine building. Science and education. № 3. (rus.)
8. Andrienko PA, Karazin VI, Kozlikin DP, Khlebosolov IO (2012) Features of playback of alternating overloads. Modern machine building. Science and education. №2. (rus.)
9. Andrienko PA, Karazin VI, Kozlikin DP, Khlebosolov IO (2019) About implementation harmonic impact of the resonance method. Lecture notes in mechanical engineering, pp 83–90
10. Andrienko PA, Karazin VI, Khlebosolov IO (2017) Bench tests of vibroacoustic effects. Lecture notes in mechanical engineering 2017, pp 11–17
11. Khisamov AV (2013) Theory of Mechanism and machine. Study of centrifuge rotor extension 1(21):C 90–97
12. Karazin VI, Kozlikin DP, Khisamov AV (2013) Features of calculating centrifuge rotor deformations. Modern machine building. Science and education. № 3. (rus.)
13. Goodman T (2007) Centrifuge rotor selection and maintenance. Am Lab 12:12–14
14. MOVIDRIVE® MDX61B (2010) DriveSync via Fieldbus. Application. SEW EURODRIVE, German
15. Evgrafov AN, Karazin VI, Khisamov AV (2018) Research of high-level control system for centrifuge engine. Int Rev Mech Eng (IREME) 12(5):400
16. Ellis G (2012) Control system design guide. Elsevier Inc. 468 p
17. Li N, Ma H, Fei Q, Li S, Chen S (2018) Motion control of 6-DOF manipulator based on EtherCAT. J Adv Comput Intell Intell Inf 22(4):415–428

18. Li N, Fei Q, Ma H, Chen S, Zhou H (2016) Driving servo slave station based on EtherCAT with Linux IGH master station. In: ISCIIA 2016—7th International symposium on computational intelligence and industrial applications
19. Cereia M, Scanzio S (2012) A user space EtherCAT master architecture for hard real-time control systems. In: IEEE international conference on Emerging Technologies and Factory Automation, ETFA
20. Example for Kollmorgen AKD with IgH EtherCAT Master library. <http://www.iram.fr/~blanchet/ethercat/akd/examples/>

Strength Capabilities of Argon-arc Welded Joints of Shape Memory Alloy Ti–55.42 wt% Ni Wires



Elisey A. Khlopkov, Dmitry V. Kurushkin, Valerii V. Burkhovetskyi, Valeri M. Khanaev, Eugeny S. Ostropiko, Sergey A. Lyubomudrov and Yuriy N. Vyunenکو

Abstract The paper presents data on the mechanical testing of argon-arc weld joints of the Ti–55.42 wt% Ni wires diameter of 2 mm. The mathematical modeling results of the temperature fields evolution of the weld zone during cooling are given. For this calculations residual stress mechanism of shape memory effect was used. The microstructure images of the weld zone were done.

Keywords Shape memory effect · Welded joints · Strength · Temperature fields · TiNi

1 Introduction

The functional properties of metals with shape memory effect have been known since the middle of the last century [1]. These unique phenomena are used in the aerospace industry and medicine [2, 3]. At the same time, there is almost no practical use of these alloys properties in machine building technological operations [4, 5]. One of the solutions was found during the development of the layered structures manufacturing process. Small-sized ScheR presses were invented, the drive of which is ring-shaped

E. A. Khlopkov (✉) · D. V. Kurushkin · S. A. Lyubomudrov
Peter the Great Saint-Petersburg Polytechnic University, Saint-Petersburg, Russia

D. V. Kurushkin
e-mail: kurushkin_dv@spbstu.ru

V. V. Burkhovetskyi
Donetsk Institute for Physics and Engineering Named After A.A. Galkin, Donetsk, Ukraine
e-mail: val-bur@ukr.net

V. M. Khanaev
OOO «OPTIMIKST LTD», Saint-Petersburg-Novosibirsk, Russia

E. S. Ostropiko
Saint-Petersburg State University, Saint-Petersburg, Russia

Y. N. Vyunenکو
OOO «OPTIMIKST LTD», Saint-Petersburg, Russia

bundle force elements (RBE, «metal muscles») made of TiNi alloy [6]. A pair of such power elements can develop forces up to 1200 N under the heating in the conditions of the development of a single shape memory effect (SME) in the device. The mass of the RBE pair is 60 g. In this mode, «metal muscles» have been showing trouble-free operation for more than 1600 cycles over 10 years.

The designing of new technological processes and martensitic devices may require the creation of conditions under which it will be necessary to implement such a phenomenon as two-way shape memory effect. This moment required the creation of rigid joints of the RBE ends, which can be realized by welding. Studies of this possibility for semi-finished products from alloys with SME are quite actively conducted [7–16]. Argon-arc [7–9], laser [10–14], friction [15] and explosion [16] welding were used. The main parameter for the joints of future power drives is the strength of the weld. In papers [7, 10], the authors obtained fairly high strength indices, which amounted to 80% of the source material limits. However, these results were for samples with a diameter/thickness of up to 1 mm. This assortment is less preferable in the fabrication of RBE, where wires with a diameter of 2 mm are more often used.

The authors of [17] succeeded in obtaining the strength of the weld of a wire with a diameter of $d = 2$ mm equal to 66% of the starting material by argon arc welding. These strength characteristics were considered sufficient for the prototyping of a ring-shaped force element, on which shape change was studied in the two-way shape memory effect mode. The possibility of generating forces during cooling through the temperature range of direct martensitic transformation was noted.

2 Experiment and Materials

The possibilities of welded joints of a wire with a 2 mm diameter from a Ti—55.42 wt. % Ni alloy made by the argon-arc welding were studied. The arc welder *Svarog TIG 315 PAC/DC* (direct current 10 A, voltage 12 V) was used. The arc welder *EWM ForceTig 552* (direct current 45 A, voltage 18.5 V) was used in the fabrication of butt welds in a He atmosphere. The samples were heat treated in the annealing mode at a temperature of 773 K for 0.5 h (cooling with the furnace). Their strength was compared with the level of tensile forces applied to continuous wire samples of the base material (BM). The dependence of the strain ε on the magnitude of the tensile forces σ was studied on universal machine *Instron 5985* at room temperature.

Microstructural studies of the weld zones were carried out using a *Jeol JSM-6490LV* scanning electron microscope. Numerical experiments to determine the evolution of the temperature field in the zone of local heating of the wire sample in the framework of the residual stress mechanism were carried out due to analyze the obtained results [18].

3 Results and Discussion

The deformation of the initial sample is carried out according to the law of elasticity up to $\sigma = 118$ MPa (Fig. 1, curve 1). The value of the deformation elastic limit ε_y takes 0.53%. After the stress reaches 163 MPa and the strain ε is 1.28%, the process of plastic flow begins. The strain ε reached 5.8% with a constant value of σ . A further increase ε from 6 to 10% raised the stress to the level of 900 MPa. The deformation process goes to the second yield point. Stress σ increased to ~ 1050 MPa and then remained practically unchanged to $\varepsilon = 20\%$. The destruction of the wire sample occurred at a strain $\varepsilon \sim 21\%$. Since the sample material was in a martensitic state, it can be assumed that the first yield area is due to the movement of twin boundaries. The second state of plastic flow is apparently the action of dislocation deformation mechanisms [19].

The deformation characteristic of a wire sample welded in an argon atmosphere (Fig. 1, curve 2) coincided with curve 1 with a change in stress σ from 0 to 445 MPa. The sample was destroyed at the boundary of the welding zones (WZ) and the heat-affected zone (HAZ).

A sample welded in a He atmosphere (curve 3) withstands a higher stress of ~ 590 MPa. However, the advantage of welding in a He atmosphere is significantly reduced after 30 thermal cycles with the transfer of the material of the welded structure from the martensitic state to austenitic and vice versa. The values of the breaking load dropped to 470 MPa as a result of repeated transformations of the crystal lattice. The limiting value of the strain ε also decreased to $\sim 6.8\%$ (curve 4). Thus, operation of welded structures made of TiNi wire with a diameter of 2 mm in the thermal cycling mode can cause a weakening of their strength characteristics.

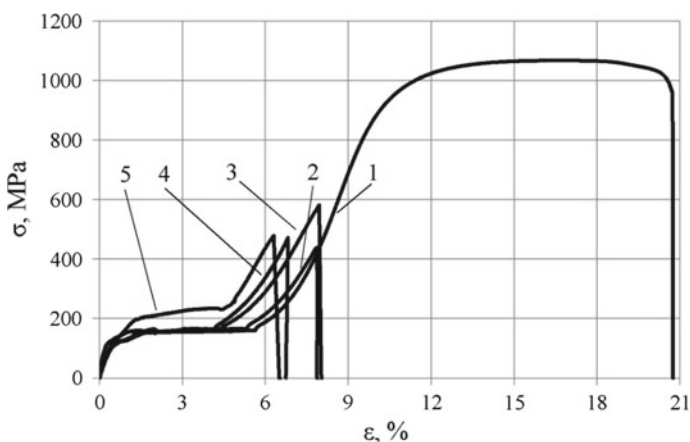


Fig. 1 Strength properties of wire samples of Ti—55.42 wt% Ni: 1—initial, 2–5—samples welded in Ar (2), He (3), He + 30 thermocycles (4), He (5); 1–4—with anneal ($T = 773$ K), 5—without anneal. The rate of motion of the movable holder is 4 mm/min for curves 1, 2, and the rate is 1 mm/min in the rest of cases

Curve 5 in Fig. 1 shows the change in σ and ε upon tensile of the sample after welding in He atmosphere without further heat treatment. In this case, the yield area is formed upon deformation close to the similar ε_y values in previous experiments. However, the stresses in this case exceeded 200 MPa, which significantly exceeded the corresponding values of σ under tension of the samples, the results of which are shown in curves 1–4. The deformation was accompanied by a slight increase in σ in the region of plastic flow. The accumulated strain ε was ~6.3% at the time of fracture. This result was the lowest among these 5 experiments. The experiments showed the preference of annealed wire samples and the need for study the thermomechanical treatments influence on the mechanical properties of welds.

Auxiliary numerical experiments to determine the evolution of the temperature field in wire samples were carried out to analyze the obtained experimental results of mechanical tests. The one-dimensional heat equation was used (1):

$$\rho \cdot c(U) \cdot \frac{\partial U}{\partial t} = k \cdot \frac{\partial^2 U}{\partial x^2} \quad (1)$$

where ρ —material density; $c(U)$ —heat capacity; U —temperature; t —time; k —thermal conduction capacity; x —coordinate. It was assumed that $c(U) = c_0 + c_1$. The value of c_1 is determined from the following relation (2):

$$Q_{tr} = \int_{A_s}^{A_f} c_1 \partial U \quad (2)$$

where Q_{tr} is the latent heat of the crystal lattice transformation; A_s and A_f are the temperatures of the beginning and end of the reverse martensitic phase transition, respectively. $c_1 = \frac{Q_{tr}}{A_f - A_s}$ is constant under a uniform distribution of Q_{tr} over the transformation interval. The physical constants in the equations were chosen close to the values of the corresponding characteristics of equiatomic TiNi. The temperatures A_s and A_f were taken equal to 333 K and 343 K, respectively.

The temperature distribution in the welding zone at the initial time in the numerical experiment was assumed to be similar to that shown in Fig. 2 (curve 1). Curves 2–6 show the distribution of heat near the weld zone in the first 25 s every 5 s. Thermal energy from the local heating zone propagates along the wire sample. The observed kink on smooth lines (curves 2–6) determines the propagation boundary of the start zone of phase transformation along the wire. In this case, the temperature begins to increase, reaches a maximum, and then decreases in each section of the wire (Fig. 3). The obtained results show that an increase of the latent heat of transformation strongly affects size and position of the austenitic and heterophase states regions (Fig. 4).

Thus, there are 5 zones of the material phase state in the design near the weld zone. Directly there are sections of the austenitic state in the locality of the welded joint. The product material may stay in a martensitic state without undergoing phase transformations at a distance from the place of heating. There are two heterophase

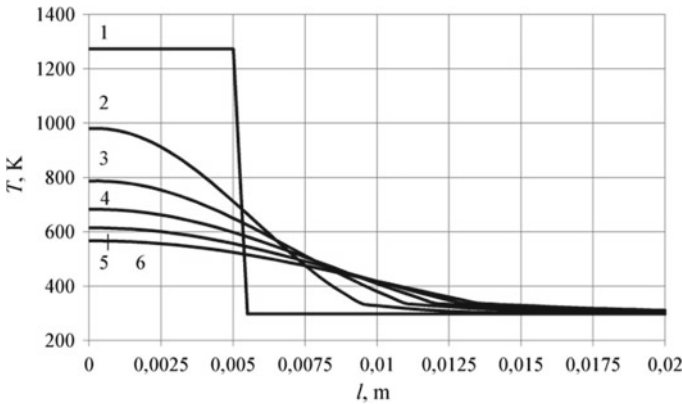


Fig. 2 Evolution of the temperature field in the welding zone at $Q_{tr} = 200000$ J/kg. Temperature field in the vicinity of the weld at a point in time t , s: 1–0, 2–5, 3–10, 4–15, 5–20, 6–25

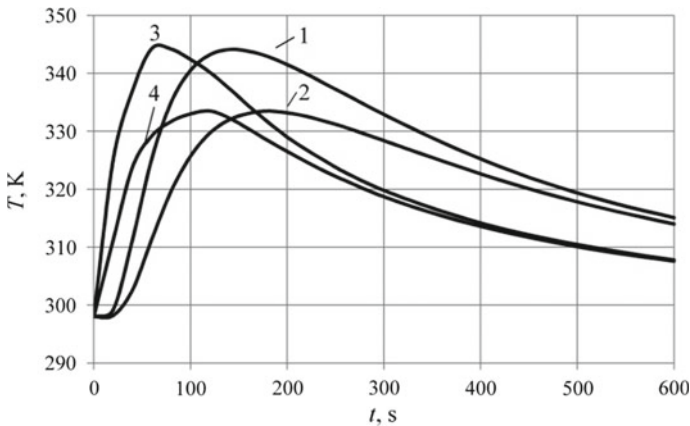


Fig. 3 Time dependence of the temperature in the wire cross section at the distance of the weld point x , mm: 1–31, 2–36, 3–15, 4–18.5; 1, 2— $Q_{tr} = 1000$ J/kg, 3, 4— $Q_{tr} = 200000$ J/kg

gradient phase zones between sections of the monophasic state (to the left and to the right of the welded joint).

The proposed division into zones differs from the traditional approach in welding technology [14]. Typically, weld zones, heat-affected zone and base material are distinguished. However, this approach does not take into account the specific properties of TiNi. Although the boundary between the heat-affected zone and the base material may coincide with the boundary of the heterophase and martensitic regions. A change in the phase structure which is reflected in the formation of complex compounds with a high Ti content is observed in the weld zone (Fig. 5d). In the heat-affected zone (initially the austenitic region, and then, possibly, the region of the heterophase state), several variants of structural formations that differ in size,

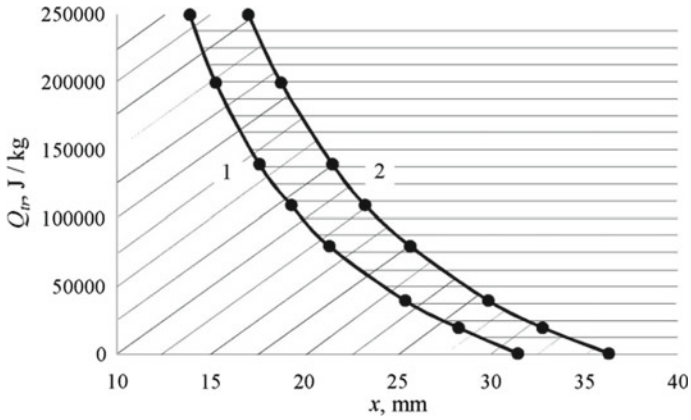


Fig. 4 Dependence of the heterophase state boundaries on Q_{tr} : 1, 2—the position of the boundaries with austenite (1) and martensite (2)

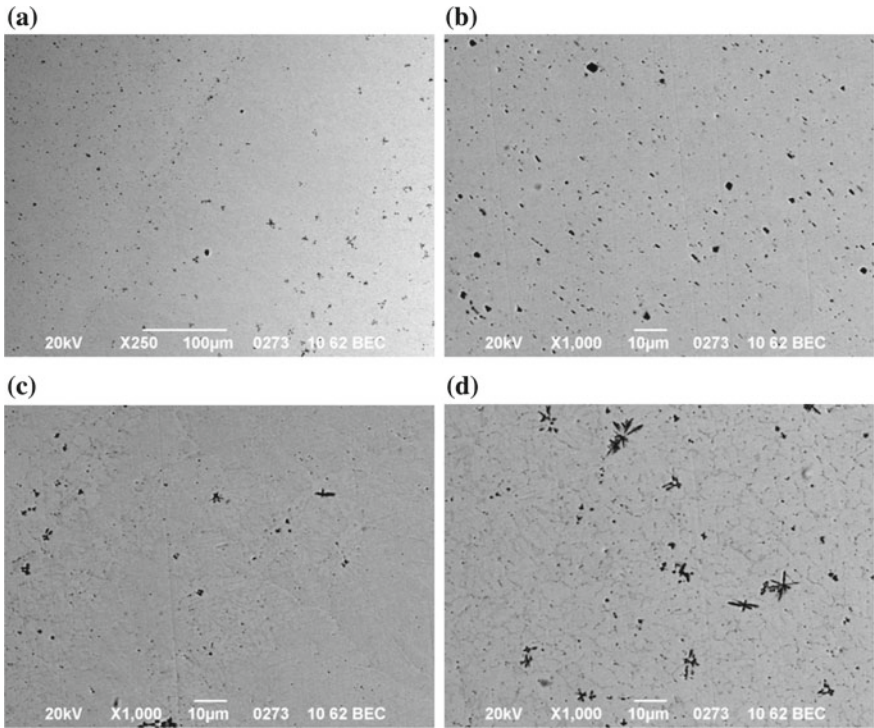


Fig. 5 Structure of TiNi: **a** welded sample, **b** BM, **c** HAZ, **d** WZ

chemical composition, and, probably, the ratio of the types of crystal lattice was observed (Fig. 5c).

Zones of the martensitic monophasic state can disappear when at the samples ends temperature can reach a value exceeding A_s . In those cases the temperatures of the direct martensitic transformation can shift to lower values throughout the volume with further cooling [20]. The transformation of the crystal lattice may be incomplete, for example, when cooling occurs to room temperature, which falls in the interval $[M_s, M_f]$ (respectively, the temperature of the beginning and end of the direct phase transition). The martensite reinforced with austenite residues and the presence of interphase boundaries in the working zone of the deformed sample introduce changes in the σ - ε dependence curve. Therefore, curve 5 in Fig. 1 differs from the stress-strain diagrams of annealed samples. The deformation characteristics can also change if the wire material in the martensitic state is completely in the grips of the tensile testing machine. However, it should be noted that the gradient structures of weld structures, apparently, can be used in the regulation of their functional capabilities in some cases.

4 Conclusion

According to the results of the work, it should be noted argon-arc welding in Ar and He atmospheres is possible in order to obtain weld joints of a TiNi wire with a 2 mm cross-section diameter. However, when the drives operate in the multiple termocycles, it is advisable to provide for the replacement of a shape memory alloy element due to the weakening of its ultimate strength capabilities.

The reported study was funded by RFBR, project number 19-38-90285.

References

1. Likhachev VA, Kuzmin SL, Kamentseva ZP (1987) The shape memory effect (Effect pamyaty formy) Leningrad State University, Leningrad, p 218 (in Russian)
2. Kravchenko YD, Likhachev VA, Razov AI et al (1996) Testing of shape memory alloys in the erection of large-scale structures in open space. *Tech Phys* 41:1167–1171
3. Gyunter VE, Kotenko VV, Polenichkin VK, Itin VI (1985) Use of alloys with shape memory in medicine. *Soviet Phys J* 28:433–437
4. Anukhin IV, Anukhin VI, Lyubomudrov SA, Murashkin SL (2015) Thermal imaging in selecting the cutting conditions for high-temperature intermetallic alloys. *Russ Eng Res* 35:544–548
5. Kolodyazhniy DY, Lyubomudrov SA, Makarova TA (2016) Quality assurance issues of hard-processing aluminum alloy parts fabrication for aircraft construction and engine-building. *J Eng Appl Sci* 11:3019–3023
6. Vyunenko YN (2010) Mathematical modeling of deformation processes and experience of technological application of the SME. *Basic Probl Mater Sci* 7:28–31 (in Russian)
7. Nishikawa M, Tanaka H, Kohda M, et.al (1982) Behaviour of welded part of Ti-Ni shape memory alloy. *Journal de Physique Colloques*. 43:C4-839-C4-844

8. Ikai A, Kimura K, Tobushi H (1996) TIG welding and shape memory effect of TiNi shape memory alloy. *J Intell Mater Syst Struct* 7:646–655
9. Kim YS, Kim JD (2000) Laser welding of Ti-Ni shape memory alloy wire and its fatigue properties. *Key Eng Mater* 183–187:1309–1314
10. Schlossmacher P, Haas T, Schussler A (1997) Laser-welding of a Ni-Rich TiNi shape memory alloy: mechanical behavior. *J Appl Phys IV Colloque.* 7(C5):C5-251–C5-256
11. Tuissi A, Besseghini S, Ranucci T et al (1999) Effect of Nd-YAG laser welding on the functional properties of the Ni-49.6at.%Ti. *Mater Sci Eng, A* 273–275:813–817
12. Falvo A, Furgiuele FM, Maletta C (2005) Laser welding of a NiTi alloy: mechanical and shape memory behaviour. *Mater Sci Eng, A* 412:235–240
13. Chan CW, Man HC (2011) Laser welding of thin foil nickel-titanium shape memory alloy. *Opt Lasers Eng* 49:121–126
14. Mehrpouya M, Gisario A, Brotzu A, Natali S (2018) Laser welding of NiTi shape memory sheets using a diode laser. *Opt Laser Technol* 108:142–149
15. Shinoda T, Tsuchiya T, Takahashi H (1992) Friction welding of shape memory alloy. *Weld Int* 6:20–25
16. Belyaev S, Rubanik V, Resnina N, et.al (2014) Functional properties of $\text{Ti}_{50}\text{Ni}_{50}\text{-Ti}_{49.3}\text{Ni}_{50.7}$ shape memory composite produced by explosion welding. *Smart Mater Struct* 23:085029
17. Vyunenکو YN, Belousov NN (2018) Two-way shape memory effect in ring-shaped designs. In: Rubanik V (ed) *Actual problems of strength*. VSTU Inc., Vitebsk, pp 482–484 (in Russian)
18. Vyunenکو YN (2003) The mechanism of shape memory effect caused by the residual stress field evolution. *Materialovedenie* 12:2–6 (in Russian)
19. Belyaev SP, Volkov AE, Ermolaev VA, et.al (1998) Shape memory materials. In: Reference book Likhachev V (ed) *(Materialy s effectom pamyati formy: Spravochnoe izdanie)* NIIKh SPbGU, St. Petersburg, p 268 (in Russian)
20. Sibirev AV, Belyaev SP, Resnina NN (2016) The influence of the maximum temperature of the thermal cycle on the martensitic transformations in the TiNi alloy. In: XXII St. Petersburg readings on strength problems: coll. materials. St. Petersburg State Polytechnic University Publishing House, St Petersburg, pp 345–347 (in Russian)

Steel Fiber Manufacturing by Turning with Intense Self-oscillations



Mikhail T. Korotkikh, Dmitriy Y. Kryazhev and Vladimir N. Kudryavtsev

Abstract This research explores the manufacturing process of steel fiber with small cross-section area. It appears that such fiber can be produced by turning machine with intense self-oscillations of the cutting tool. Conditions for occurrence and reproduction of such oscillations are shown. Control parameters of the process and dimensional ranges of reinforcing elements thus obtained are defined. On the basis of experimental studies, the properties of steel fiber concrete reinforced with fine steel fiber at high concentration are shown. Rational areas of use of such steel fiber have concrete were defined.

Keywords Steel microfiber · Turning with intense self-oscillations · Steel fiber concrete · Vibration · Steel fiber concrete structures

1 Introduction

At present, several different methods are used to produce steel fiber, among which the most common are stamping (Fig. 1a), wire cutting (Fig. 1b), milling (Fig. 1c). There are different scopes for each of these methods, which is related to their technological capabilities and cost of the obtained product [1, 2].

It should be noted that all the methods presented do not allow for the production of small cross-section fiber, which is due either to the fundamental limitations of the method, such as in stamping or milling, or to the extremely high cost of the product, such as using a small cross-section wire. At the same time blanks during stamping or wire cutting is a product of high metallurgical front, which increases the cost of fiber. Therefore, the development of a method that allows to control the dimensions of the resulting elements within wide limits by using massive blanks, for example castings, seemed to be very relevant.

As is known, when processing metals on lathes, self-oscillations of the tool may occur. The hypotheses of oscillations emergence are diverse and could be determined by many reasons [3–6]. Frequency of such oscillations is often determined by natural

M. T. Korotkikh (✉) · D. Y. Kryazhev · V. N. Kudryavtsev
Peter the Great St. Petersburg Polytechnic University, St. Petersburg, Russia

© Springer Nature Switzerland AG 2020
A. N. Evgrafov (ed.), *Advances in Mechanical Engineering*,
Lecture Notes in Mechanical Engineering,
https://doi.org/10.1007/978-3-030-39500-1_12

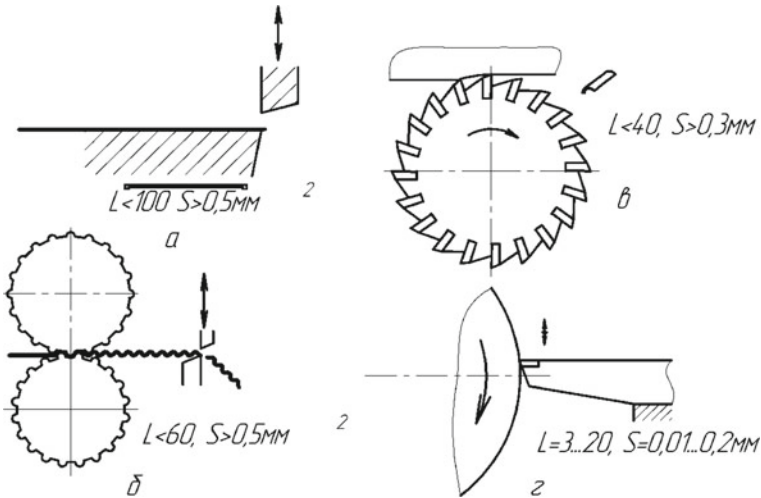


Fig. 1 Main methods of steel fiber production

oscillations in the process system, and amplitude of oscillations is determined by the least rigid link of the system. Such vibrations in cutting materials are always considered to be an adverse phenomenon, resulting in a decrease in the quality of the machined surface, a decrease of the tool-life, and sometimes in its breakage. Therefore, by metal cutting, methods of controlling these fluctuations, methods of preventing their occurrence, passive and active methods of reducing their intensity are usually considered.

A detailed study of some cases of such oscillations has shown that there may be cases where the intensity is so high that the tool loses contact with the workpiece, and the chips are separated as separate needle elements [7–11].

The reason for such intense oscillations is the strong positive feedback in the process system, which can be achieved by turning with the cutting blade, which placed above the center of the workpiece (Fig. 2). At elastic deformation of cutter holder by value f under action of cutting force blade is cut into blank at blade depression, which is accompanied by increase of effective cutting force. The tool holder may be bent at elastic deformation by an amount of fkr and may be broken or plastically deformed at greater deflection. The increase in the cutting force P_r may result in both tool failure (curve 2, Fig. 2b) or chip element cutting until a critical force occurs causing tool failure (curve 1, Fig. 2b).

When the elastic deformation force of the tool holder exceeds the shear force of the chip metal, the elastic energy of the tool holder causes it to move against the cutting speed direction and the shearing element of the chip is ejected.

By changing the stiffness of the cutter, the geometry of its cutting blade and the tool holder, and by its location relative to the center of the workpiece, it is possible to provide conditions for such vibrations to occur and maintain, at each oscillating motion, the tool blade disengages from the workpiece by removing one chip element

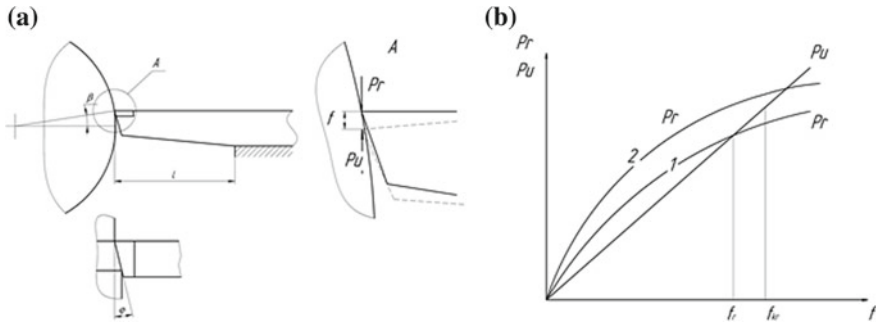


Fig. 2 Turning diagram at intensive oscillations of tool (a) and conditions of oscillations (b)

in the form of a needle of a given thickness and the length, which equal to the tool blade length. At the same time the number of obtained elements per unit time will be determined by frequency of tool holder oscillations, which can be very high (up to 2000 Hz). An important condition for such vibrations is the linear dependence of the elastic force of the tool deflection and the nonlinear dependence of the cutting force on the thickness of the cutting layer (Fig. 2b).

Experimental studies have found that such intense self-oscillations require:

- The edge of the tool must be installed above an axis of the workpiece, and at a bend of the tool introduction of an edge at an angle of β was provided (Fig. 2a)
- The thickness of the cutting layer is set to be less than a certain value determined by the vibration amplitude of the tool holder, which ensures that the tool blade is released from contact with the workpiece. Thickness of the cutting layer can be regulated due to change of the entering angle φ (Fig. 2a).
- The stiffness and strength of the tool holder is selected from the conditions ensuring its oscillations with the required amplitude f without breakage, which depends on the length of the free end of the cutter holder L , the profile of its cross section and its material.

The above-mentioned quasi-static analysis of the occurrence and maintenance of intensive self-oscillations during turning is very simplified, but it has revealed all the necessary technological factors for carrying out the process of producing steel needle elements.

It was established that the most significant factor defining conditions of emergence of intensive fluctuations is the corner β between the cutting plane and the direction of an edge movement by the bend of the tool holder. At increase of this angle it is possible to break the tool, and at its decrease formation of spiral chips.

The resulting elements have a cross-sectional shape close to a triangular (Fig. 3) and developed rough surface, which can determine their good connection with the concrete matrix. At the same time, the plane of shear strain inside the elements runs along their length, which determines their high tensile strength equal to the strength of the workpiece material, which was confirmed experimentally.

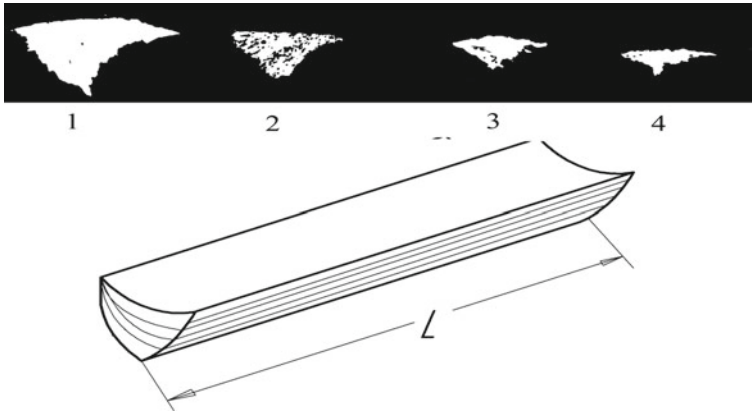


Fig. 3 The sizes of the resulting chip elements: F is the cross-sectional area ($0.01\text{--}0.2\text{ mm}^2$), L is the length of the elements ($3\text{--}20\text{ mm}$). 1— $S = 0.09\text{ mm/rev}$, 2— $S = 0.06\text{ mm/rev}$, 3— $S = 0.045\text{ mm/rev}$, 4— $S = 0.03\text{ mm/rev}$. ($V = 4\text{ m/s}$, vibration frequency 800 Hz , $\varphi = 5^\circ$)

Mathematical modeling of the process was carried out by representing the tool holder in the form of a harmonic oscillator having its own oscillation frequency depending on the parameters of the tool holder. It was found that with steel tool holders the maximum achievable oscillation frequency, and, consequently, the formation of steel elements is 1200 Hz . By using tool holders made of aluminum alloys, the frequency can be increased to 2000 Hz , which has been tested in practice.

It was found that with such intense tool vibrations, the kinematics of the process is significantly different from the usual chip formation process. The blade comes into the workpiece in the direction of the rear surface when the movement coincides with the cutting speed vector, and then moves against the cutting speed vector, ejecting material formed on the front surface.

This is confirmed by the fact that during the implementation of the process, the rear angle can be increased to 30° , without significantly reducing the strength or destruction of the cutting edge. And this even increases the stability of the cutting process, as it facilitates the initial introduction of the blade into the surface of the workpiece.

Naturally, when cutting with such intense self-oscillations, a deep relief is formed on the cutting surface and the machined surface, and after one revolution of the workpiece, the introduction of the tool blade occurs “by trace”, i.e. on previously formed relief. An analysis of the conditions for the formation of a chip element during work along the wake showed (Fig. 4c) that the phase of the oscillation process automatically adjusts to the profile of the previously formed relief, which can be seen from the regularity of the relief formed on the machined surface (Fig. 4a, b).

The conditions for the formation of elements during machining with intense tool vibrations allow them to be obtained in the size range with a cross-sectional area $F = 0.01\text{--}0.2\text{ mm}^2$, length $L = 3\text{--}20\text{ mm}$, i.e. in ranges, which other cutting methods do not provide.

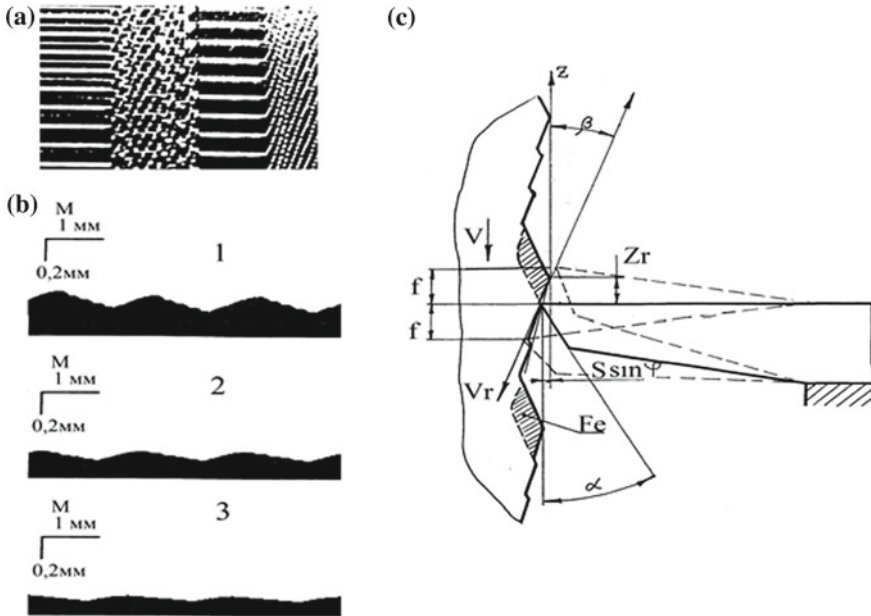


Fig. 4 The scheme of obtaining elements by turning with self-oscillations when working “by trace” a is a view of the machined surface and the cutting surface, b is the cross section of the cutting surface: 1— $S = 0.2$ mm/rev; 2— $S = 0.1$ mm/rev; 3— $S = 0.05$ mm/rev; ($V = 3.8$ m/s, $\varphi = 10^\circ$)

A very high frequency of formation of elements up to 2000 pcs/s is many times higher than the productivity of the method of producing reinforcing elements from wire. The mass productivity, of course, depends on the size of the elements and amounts to: 5.6 kg/hour for elements with $F = 0.02$ mm² $L = 5$ mm long, and 224 kg/hour for elements with $F = 0.2$ mm² $L = 20$ mm long.

In construction, the volumetric content of fiber in steel-fiber-reinforced concrete structures is used at 1–1.5%, since in large-tonnage production a greater consumption of fiber leads to a higher cost of the structure. In the case of the manufacture of steel-fiber-reinforced concrete structures of a relatively small volume (the case of machines, machine tools, tools), a high fiber content can pay off with significant economic advantages determined by the high manufacturability of shaping. In this case, the volumetric content of the fiber can be increased up to bulk density, if this leads to a significant increase in the mechanical properties of the structure. The bulk density of the fiber obtained in this way depends on its parameters (Fig. 5).

Testing of concrete samples with different concentrations of reinforcing elements (Fig. 6a) showed that the bending strength (σ) at a mass fiber concentration of $\xi_m = 21\%$ reaches 45 MPa.

The compressive strength increases significantly even with an insignificant concentration of microfiber, it significantly depends on the fiber length and approaches the strength of cast iron (Fig. 6b).

Fig. 5 Dependence of the bulk density of the fiber on its length, 1— $F = 0.026 \text{ mm}^2$, $F = 0.018 \text{ mm}^2$, 3— $F = 0.01 \text{ mm}^2$

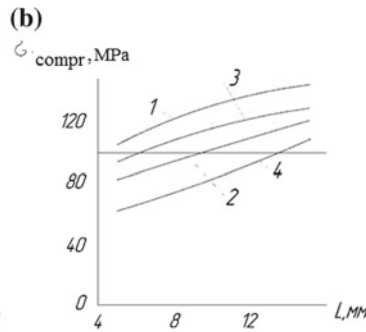
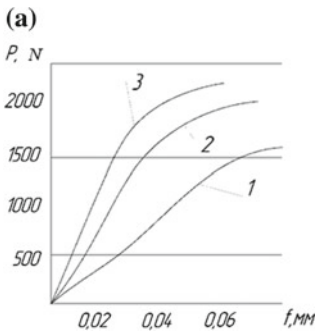
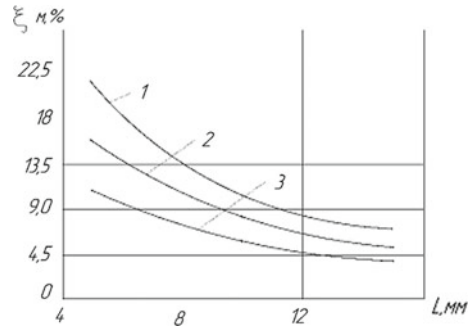


Fig. 6 a Deflection of the samples under load depending on the mass concentration of fiber: 1— $\xi_m = 7\%$, 2— $\xi_m = 14\%$, 3— $\xi_m = 21\%$; **b** Compressive strength of the samples 1— $\xi_m = 4\%$, $F = 0.01 \text{ mm}^2$, 2— $\xi_m = 2\%$, $F = 0.01 \text{ mm}^2$, 3— $\xi_m = 4\%$, $F = 0.026 \text{ mm}^2$, 4— $\xi_m = 2\%$, $F = 0.026 \text{ mm}^2$

When using steel fiber concrete as a structural material in mechanical engineering, it is essential to increase the elastic modulus of the material with a significant content of reinforcing elements. In this case, the reduced modulus of elasticity approaches the modulus of elasticity of aluminum alloys (Fig. 7a).

The most important advantage of steel fiber concrete when used in mechanical engineering is a high decrement of vibrations, which exceeds tens of times that of cast iron. This is especially important when creating enclosures of machine systems in which vibration dramatically degrades the quality of the products.

The unique properties of steel fiber reinforced concrete with a high content of steel microfiber can determine its application in the creation of machine frames, spindle units and cases of various technological equipment. This is also determined by the high adaptability of the method of producing casings that do not require metallurgical foundry or welding equipment, which is especially important for single and small-scale production.

The mechanical properties of these steel fiber concrete allow even the body of a highly loaded tool that perceives shock loads to be manufactured from it [12–15]. In

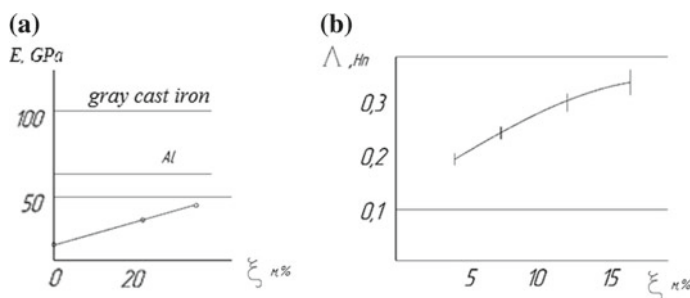


Fig. 7 **a** Change in the elastic modulus of steel fiber concrete depending on the concentration of reinforcing elements; **b** change in the decrement of vibrations with a change in the concentration of reinforcing elements

this case, the high damping properties of the material, which improve the operational properties of the tool, are especially positive [16–20].

2 Conclusions

1. There are conditions for the implementation of the turning process during intense self-oscillations of the tool, under which it is possible to obtain needle-shaped chips having a triangular cross section and material strength along the element corresponding to the strength of the workpiece material.
2. The productivity of the process of obtaining reinforcing elements with a cross-sectional area of 0.01–0.2 mm² and a length of 3–20 mm depends on the frequency of oscillations of the tool holder and can exceed 2000 elements per second.
3. The mechanical and damping characteristics of steel fiber concrete with fine fiber are largely determined by the concentration of the fiber, its length and cross-sectional area;
4. By increasing the concentration of steel fibers to a limit value limited by bulk density, a significant increase in the mechanical properties of steel fiber concrete is possible, allowing it to be used as a structural material for the manufacture of cases of technological equipment and some types of tools.

References

1. Pukhareno YV Effective fiber reinforced materials and products for construction and restoration. In: Materials of the scientific-practical conference “Restoration in the church-monument” (St. Petersburg, December 6–7, 2006). No. 2, St. Petersburg

2. Morzhukhina A, Nikitin S, Akimova E (2018) Determination of the neutralization depth of concrete under the aggressive environment influence. In: E3S Web of Conferences, 33, статья № 02010. <https://doi.org/10.1051/e3sconf/20183302010>
3. Sokolov SA (2017) The model of the elastic-plastic deformation of a structural member. In: Lecture Notes in Mechanical Engineering, pp 125–132. https://doi.org/10.1007/978-3-319-53363-6_13
4. Belyaev AN, Efremov D (2017) The suppression of slightly damped torsional oscillations in autonomous power systems. In: Proceedings of the 2017 IEEE Russia Section Young Researchers in Electrical and Electronic Engineering Conference, ElConRus 2017, статья № 7910854, pp 1483–1487. <https://doi.org/10.1109/eiconrus.2017.7910854>
5. Evgrafov AN, Karazin VI, Kozlikin DP, Khlebosolov IO (2017) Centrifuges for variable accelerations generation. *Int Rev Mech Eng* 11(5):280–285. <https://doi.org/10.15866/ireme.v11i5.11577>
6. Kumabe D (1985) *Vibration cutting/ Per. with yap./ Ed. Portnova I.I. – M. p 424*
7. Korotkikh MT, Shaterin MA, Smirnov RM (1995) The technological process of obtaining reinforcing elements of steel fiber concrete by turning with intense tool vibrations. In:// Sat “Innovative high technology for Russia.” - SPb.: SPbSPU, P 50
8. Babkin AV, Tashenova LV, Chuprov SV (2017) Management of sustainability and development of systems in the context of the synergetic paradigm. In: Proceedings of 2017 IEEE 2nd international conference on Control in Technical Systems, CTS 2017, статья № 8109556, pp 318–321. <https://doi.org/10.1109/cts.2017.8109556>
9. Ryabov VV, Kniaziuk TV, Mikhailov MS, Motovilina GD, Khlusova EI (2017) Structure and properties of new wear-resistant steels for agricultural machine building. *Inorg Mater Appl Res* 8(6):827–836. <https://doi.org/10.1134/s2075113317060120>
10. Kazakov AA, Shakhmatov A, Badrak R, Kolpishon E (2017) Metallurgical nature of the as-cast microstructure of high-nitrogen, high-manganese stainless steels. *Mater Perform Character* 6(3):271–280. <https://doi.org/10.1520/mpc20160026>
11. Bardin A, Korotkov A, Kazarnovskij V (2017) Limit of fire resistance of a steel transport structures. Simplified calculation methods. In: IOP conference series: earth and environmental science, 90(1), статья № 012207. <https://doi.org/10.1088/1755-1315/90/1/012207>
12. Korotkikh MT, Smirnov RM, Folomkin AI (2004) Face milling cutters with steel fiber reinforced concrete bodies. *Tool Technol* 21–22:67–71
13. Svatovskaya L, Kabanov A, Sychov M (2017) The improvement of foam concrete geocopro-protective properties in transport construction. In: IOP conference series: earth and environmental science, 90(1), статья № 012010. <https://doi.org/10.1088/1755-1315/90/1/012010>
14. Svatovskaya L, Kabanov A, Sychov M (2017) Lithosynthesis of the properties in the transport construction on the cement base. In: IOP conference series: earth and environmental science, 90(1), статья № 012009. <https://doi.org/10.1088/1755-1315/90/1/012009>
15. Varabanshchikov YG, Belyaeva SV, Arkhipov IE, Antonova MV, Shkolnikova AA, Lebedeva KS (2017) Influence of superplasticizers on the concrete mix properties. *Magazine Civil Eng* 74(6):140–146. <https://doi.org/10.18720/MCE.74.11>
16. Korotkikh MT, Folomkin AI (2005) Design features of face mills with steel fiber concrete housings. *Metalworking* 4(28):8–11
17. Sychova A, Sychov M, Rusanova EA (2017) Method of obtaining geonoiseprotective foam concrete for use on railway transport. *Procedia Eng* 189:681–687. <https://doi.org/10.1016/j.proeng.2017.05.108>
18. Manzhula KP, Shlepetinskii AY (2016) Stress and strain concentration in weld-joint flaws. *Russian Eng Res* 36(9):722–726. <https://doi.org/10.3103/s1068798x16090148>
19. Sokolov SA (2016) Operational risk assessment in technological systems. *Russian Eng Res* 36(1):10–15. <https://doi.org/10.3103/s1068798x16010184>
20. Manzhula KP, Naumov AV (2017) Influence of flections’ radius value to local buckling of box-shaped beams with non-linear walls. *Int Rev Mech Eng* 11(5):326–331. <https://doi.org/10.15866/ireme.v11i5.11602>

A New Way of Manufacturing Bimetal Products on the Basis of the Technology of Casting with Crystallization Under Pressure



Ruslan V. Kuznetsov and Pavel A. Kuznetsov

Abstract The paper presents the analysis of possible combinations of raw materials during manufacturing bimetallic compositions. A variety of materials makes it necessary to apply new combinations of familiar processes of materials processing and search for new ways of bimetal production meeting the needs of different branches of industry. The possibilities of obtaining bimetallic compounds on the basis of casting alloys and powder sintered materials are not sufficiently studied. By means of the analysis, carried out using a morphological matrix, a new method of manufacturing bimetallic products based on the technology of casting with crystallization under pressure was developed. An experimental press mold and an experimental stand were developed to study the main parameters of the proposed process on the samples in the form of bimetallic bushings—models of bimetallic bearings. Casting aluminum alloy AK9ch was used for the base material. The working layers were sintered powder materials made of graphite bronze and iron. The main methods of studying the obtained bimetallic samples were mechanical tests of strength of the layers interconnection and metallographic studies of their interconnection zone. The paper discusses the issues of searching for rational modes of casting with crystallization under the pressure of aluminum alloys together with the working elements made of sintered materials with special properties. The possibility of application of the obtained bimetallic products in sliding friction joints used in general mechanical engineering products is considered. Acoustic emission, radiographic testing, pressure vessels, stainless steel, cracks in the welds, sequence of application of testing methods

Keywords Composite material · Sintered material · Bimetal · Silumin · Iron powder · Bronze powder · Liquid metal stamping · Crystallization · Antifriction material · Galvanizing · Intermetallic compounds

R. V. Kuznetsov (✉) · P. A. Kuznetsov
Peter the Great Saint-Petersburg Polytechnic University, St. Petersburg, Russia
e-mail: spaun1605@rambler.ru

P. A. Kuznetsov
e-mail: pa-kuznetsov@ya.ru

© Springer Nature Switzerland AG 2020
A. N. Evgrafov (ed.), *Advances in Mechanical Engineering*,
Lecture Notes in Mechanical Engineering,
https://doi.org/10.1007/978-3-030-39500-1_13

1 Introduction

The nomenclature and volumes of bimetallic materials and products made of them are currently increasing intensively. Such innovative development is caused by both the needs of different industrial branches and emergence of new materials with unique properties and technologies of their production [1–4]. By the field of application of bimetallic materials, they are distinguished into corrosion-resistant, antifriction, electrotechnical, instrumental, wear-resistant, thermo-bimetals, bimetal for installation works, and others.

The diversity of bimetallic materials is due to the large number of possible combinations of raw materials [4–6]. The most common combinations can be considered to be “compact-compact”, “plastic-plastic”, “compact-plastic”, “composite-composite”, “composite-plastic” combinations. Application of various technological processes used in manufacture of bimetal, in turn, makes it possible to control the properties necessary to perform specific tasks [5–7]. Almost in all bimetal, one of the materials is a working layer with special properties, the second material is a “matrix”, which performs auxiliary functions, such as supporting ones, i.e. for attaching the working layer. However, such technologies of bimetal production are of considerable interest when the “matrix” serves not only for attaching the working layer, but is a product that performs certain functions [8]. Undoubtedly, from the economic point of view, the options in which the bimetal layers are connected simultaneously with the manufacture of the product itself are of a greater interest. Modern technologies that correspond to these goals are not sufficiently studied and require more thorough research. In particular, the technologies for obtaining bimetal from liquid metal and powder materials have not been sufficiently studied. Application of the powder metallurgy technology makes it possible to obtain a working layer of a bimetallic product with the highest and special physical, mechanical, and operational properties [9–12].

For the analysis of possible combinations of the process of manufacturing a bimetallic product from liquid metal and a sintered material, it is proposed to consider the morphological matrix presented in Table 1.

The proposed matrix considers only options of obtaining bimetallic products on the basis of the technology of casting with crystallization under pressure, as a process that significantly improves the quality of the cast metal. Stamping of a liquid metal is carried out together with working inserts of powder materials with the set properties. During implementation of the process, the following options are possible.

Option 1 implies making a working insert out of powder with the required properties, sintering it, installing it in a mold (matrix), pouring the liquid metal into the mold, and stamping them together to produce a high-quality bimetallic product. In order to achieve the necessary qualities, it is also possible to carry out additional machining and impregnation with lubricants.

Important features of the proposed technology are the possibility to vary the modes of operations in a wide range, as well as the possibility of intensifying the process in individual operations. Option 2 implies applying a special material (e.g. zinc) to

Table 1 Morphological matrix of comparison of technological options of production of composite layered bushings from liquid metal and sintered powders

No.	Technological operations	Production options			
		I	II	III	IV
1	Preparation of a powder material for the working layer	○	○	○	○
2	Pressing of the working insert	○	○	○	○
3	Sintering of the working insert	○	○	○	○
4	Application of an adhesive activating material to the insert		○		○
5	Installation of the working insert into the mold	○	○		
6	Pouring a liquid metal base into the mold	○	○	○	○
7	Insertion of the working insert into the liquid metal			○	○
8	Joint stamping of the liquid metal and the working insert	○	○	○	○
9	Heat treatment of the stamped Bimetallic product				○
10	Layered product calibration				○
11	Machining	○	○	○	○
12	Thermochemical treatment		○		○
13	Impregnation with lubricants	○		○	
14	Control	○	○	○	○

the sintered working insert, which activates the process of forming a strong bond between the layers during stamping. Installing the insert into the mold is done before pouring a liquid metal.

The working insert can be inserted into the already poured liquid metal, fixed in the desired position, and then the joint stamping of the liquid metal and the sintered insert can be carried out, which is reflected in options 3 and 4, different from each other by auxiliary operations of heat treatment, impregnation, etc. For example, the finishing shaping of the working surface, such as calibration, can effectively adjust the pore size (option 4).

Based on the above-stated analysis, carried out with the help of the morphological matrix, a new method of obtaining bimetallic products on the basis of the technology of casting with crystallization under pressure is offered, at which the working insert made of a sintered porous material is inserted into the liquid metal, placed into a closed heated matrix, is fixed in the desired position and the created bimetallic composition is subjected to joint stamping with holding under pressure until full crystallization of the base.

The aim of the work is to develop and study the combined process of manufacturing bimetallic products made of liquid metal and sintered powder materials on the basis of casting with crystallization under pressure.

2 Methods and Materials

As materials for the research we used: base material is cast aluminum alloy AK9ch (GOST1583-93), working layer is tin-bronze powder PA-BrO (GOST26719-85), modified with additives Sn and C, and iron powder ANS100.29.

The samples for the studies were bimetallic bushings of the following dimensions: $D = 40\text{--}55$ mm, $d = 20\text{--}25$ mm, $h = 20\text{--}40$ mm.

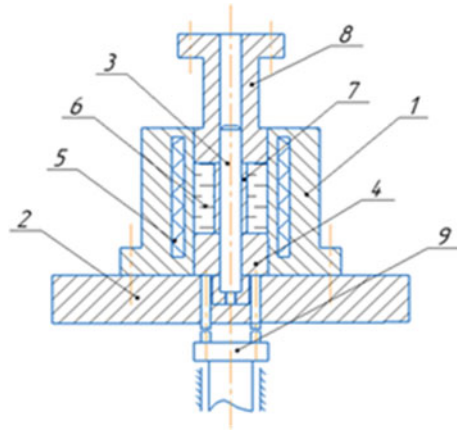
The technology of manufacturing bimetallic samples was as follows (Fig. 1): one-piece matrix 1 with coaxially installed mandrel 3 was heated to working temperature, having previously lubricated the working surfaces with non-stick coating.

The matrix was installed on the lower plate of press 2 and poured liquid metal base 6. Working insert 7 made of antifriction sintered powder material was installed on mandrel 3, introduced into the liquid metal with movable die 8, and joint stamping was carried out. Holding under pressure was carried out until full crystallization of the base material and penetration of the liquid metal into the pores of the powder material of the insert. The tooling material is 5XHM instrument die steel (GOST5950-2000). A composition based on the aqueous solution of colloidal silica was used as a non-stick coating.

An experimental batch of bimetallic blanks was produced on a special stand, stamping was carried out directly on the laboratory testing press PSU-125 with an effort of 125 ton-force (1250 kN).

From the previous works [7], it is known that the main technological parameters of the SLM (stamping of liquid metal) process are stamping pressure— P_s , temperature

Fig. 1 Principle diagram of casting with crystallization under pressure of the liquid metal and the sintered working insert 1—matrix, 2—plate, 3—mandrel, 4—support, 5—heating element, 6—liquid metal, 7—working insert, 8—movable die, 9—ejector



of tooling— T_{tool} , and time of crystallization under pressure— t_{cr} . Proceeding from this, one of the main tasks of the work was the search for optimal intervals of these parameters in relation to the pair of materials under study. The porosity of the powder blank during the study was constant—15%.

The experiment was conducted in the following technological modes: $P_s = 0$ –100 MPa, $T_{\text{tool}} = 450$ –850 °C, $t_{\text{cr}} = 10$ –60 s. Microstructure of the contact layer was studied on the samples cut out from the central part of the blank in the longitudinal section. Cutting was performed on the “POLILAB R 30 M” low-speed precision cutting machine. Manufacturing of microslices was carried out with the use of the “POLILAB S50” pressing machine and the “POLILAB P12MA” grinding and polishing metallographic complex. Visual evaluation of the contact layer was conducted with the MIM-9 metallographic microscope using a digital camera. The method used is described in detail in [13, 14].

3 Results of Mechanical Tests and Metallographic Studies

Technological testing of shear strength of layer connection was performed on $\varnothing 55 \times 20$ mm ring-shaped samples cut out of the center of the workpiece on a Losen Hausen hydraulic test rig with a nominal force of 50kN. Mechanical tests of shear strength of the bimetallic product layer connection showed the following values: for the pair “AK9ch—PA-BrO9-1” within the range of 6.8–9.1 MPa. For pair “AK9ch—ANS100.29”—in the range of 42–60 MPa.

Hardness examination of the cross-section of the central part of the workpieces was carried out using the Vickers method (GOST 2999-75) on the ITV-10-MM hardness meter. The strength of aluminum after crystallization under pressure was 62.4–77.5 NV10, for sintered iron powder—189–227 NV10.

Figure 2 shows the microstructure of the contact layer of a bimetallic sample made of aluminum AK9ch and sintered bronze powder PA-BrO9-1.

Figure 3 shows the microstructure of the sample “AK9ch + ANS100.29” obtained under the following conditions: a— $P_s = 50$ MPa, $T_{\text{tool.}} = 500^\circ\text{C}$, $t_{\text{cr.}} = 10$ s; b— $P_s = 100$ MPa, $T_{\text{tool.}} = 750^\circ\text{C}$, $t_{\text{cr.}} = 20$ s.

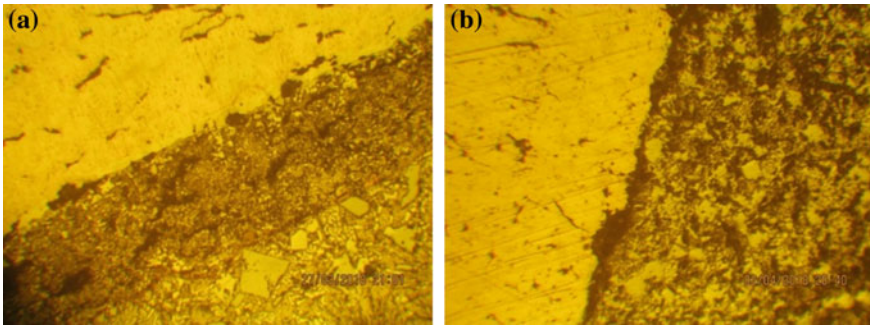


Fig. 2 Microstructure of the contact layer of the bimetallic sample “AK9ch + PA-BrO9-1”: **a** with satisfactory solubility; **b** with a strongly pronounced contact layer zone. Magnification $\times 250$

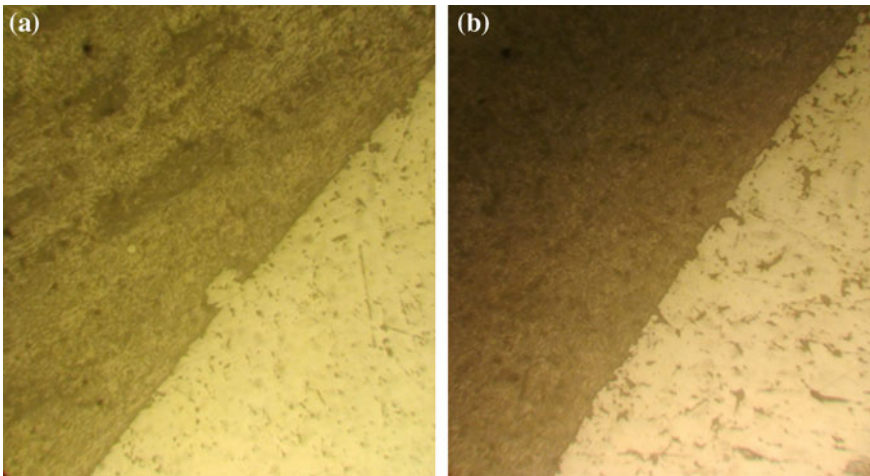


Fig. 3 Microstructure of the contact layer of bimetallic samples “AK9ch + ANS100.29”: **a** with intermetallic layer zone; **b** with satisfactory area of mutual solubility. Magnification $\times 500$

4 Discussion of Results

Shear strength of the layers in bimetallic pairs “AK9ch + ANS100.29” reaches an average of 50 MPa (Fig. 4).

The obtained result can be considered as a satisfactory result, comparable to the strength of bimetallic compounds of aluminum and steel obtained by other methods, such as welding.

Shear strength of the layers in bimetallic pairs “AK9ch + PA-BrO9-1” showed low values, which can be explained by worse weldability of materials in this pair, as well as the influence of graphite. For low-loaded bearings, this strength may be sufficient.

An increase in the hardness of aluminum is caused by pressure during its crystallization, which was observed in other works.

Studies of the contact layer microstructure have demonstrated satisfactory mutual solubility. In optimal modes of the process, penetration of aluminum into the pores of sintered iron was observed.

Optimal technological parameters of the stamping process of liquid aluminum, together with sintered iron powder, should be considered as the stamping pressure is 80–100 MPa, the temperature of the matrix is 700–800 °C and the time of holding under pressure is 15–20 s.



Fig. 4 Bimetallic samples obtained by joint stamping of liquid aluminum AK9ch and sintered powder ANS100.29

5 Conclusion

In conclusion, the most important results can be highlighted. A new method of manufacturing bimetallic products (plain bearings) on the basis of the technology of casting with crystallization under pressure has been developed [15]. The method includes pouring a liquid metal base in the cavity of a rigid matrix, placing a working insert made of a sintered powder material into the matrix after pouring the liquid metal base by immersion in a liquid metal and fixation in the desired position, the subsequent stamping with holding under pressure. The coefficient of thermal expansion of the base material is chosen by 20–30% higher than the coefficient of thermal expansion of the insert material, which contributes to the occurrence of compression stresses when materials of the base and insert cool down in the zone of their contact and provides increased adhesion. The introduction of the sintered powder insert into the liquid metal ensures destruction of the oxide film of the aluminum alloy formed during pouring of the metal, minimizes oxidation of the contact surface of the base and the insert material, and, consequently, increases adhesion and the quality of the product as a whole.

Mechanical tests of shear strength of the layers of bimetallic products “AK9ch + ANS100.29” showed strength within the range of 42–60 MPa. The achieved strength range is comparable with the strength values obtained by other methods of manufacturing bimetallic products. Therefore, the studied technology can be recommended for obtaining bimetallic products from other similar metals and alloys.

Further direction of the research on the proposed technology should be considered as modeling of thermal processes occurring at the boundary of the connected materials during their crystallization under pressure in the process of their joint stamping [16–18].

The resulting bimetallic blanks can be subjected to plastic deformation (hot bulk stamping, cold extrusion, rotational processing, etc.) to give them their final shape and dimensions. One of the effective methods of plastic processing is cold edge unrolling [19, 20].

Expansion of the product range obtained by the developed method can be the use of sintered working inserts with the gradient structure and special properties [21].

References

1. Veretennikova IA, et al (2016) Mechanical properties and a type of destruction of the « copper M1-steel 09G2S » bimetal, obtained by explosion welding//Diagnostics, Resource and Mechanics of Materials and Structures. vol 6, pp 28–38
2. Dmitrov LN, Kuznetsov EB, Kobelev AG, et al (1991) Bimetals: Monograph. In: Perm, p 415
3. Surovikin VF, Surovikin YV, Tsekhanovich MS (2007) New trends in the technology of obtaining carbon-carbon composites. In: Application of carbon-carbon composites. //Russian Chemistry Journal, vol 51(4), pp 111–119
4. Sirotenko LD, Shlykov ES, Ablyaz TR (2015) Application of bimetallic materials in mechanical engineering//Modern problems of science and education. Issue 2, pp 163–163

5. Elbaeva RI, Elbaev RA (2015) Research on the technology of manufacturing bimetallic steel bronze bearings. In: Proceeding of the Kabardino-Balkarian State University. vol 5(1), p 24
6. Zlobin BS, et al (2012) Improvement of the technology for manufacturing steel-aluminum plain bearing inserts. In: Proceedings of volgograd state technical university. Issue 14 (101)
7. Batsyshev KA (2008) Crystallization die casting of aluminum alloys. Moscow, p 143
8. Katrus OA, Radchenko AK, Grinkevich KE, Yuga AI (1997) Antifriction multilayer materials with different layer functions // Newest processes and materials in powder metallurgy: Summary of the report for the international conference, Kiev, p 349
9. Fedorchenko IM, Pugina LI (1980) Composite sintered antifriction materials. Naukova dumka, Kiev, p 404
10. Fedorchenko IM (ed) (1985) Powder metallurgy. Materials, technology, properties, application areas: Reference book, Naukova dumka, Kiev, p 625
11. Fuk D.V., Ganin S.V., Tsemenko V.N. Study of the consolidation of powder materials using the ABAQUS software package. // SPbPU Journal of Engineering Science and Technology. - 2016. - Issue 1. - p. 100–110
12. Rudskoy A.I., Rybin Y.I., Tsemenko V.N. Theory and modelling of deformation processes of porous powder materials. St. Petersburg: « Nauka », 2012. - 415 p
13. Kazakov A. A., Kur A. A., Kiselev D. V., Lazutova E. B. Development of Quantitative Methods for Estimation of Pre-eutectic Silumin Structure for Predicting their Mechanical Properties // Non-ferrous metals 2014 Issue 4. - p. 39–43
14. Kazakov A. A., Kur A. A., Kazakova E. I. Development of Quantitative Methods for Estimation of Aluminum Alloys Structure by Means of Image Analysis // Microsc. Microanal. 21 (Suppl 3), 2015
15. Kuznetsov R.V., Radkevich M.M., Kuznetsov P.A. Method of obtaining bimetallic samples by liquid metal stamping. Patent No. 2696164 clas. B22/1 18/02. Issued on July 31, 2019, Bulletin No.22
16. Rudskoy AI, Tsemenko VN, Ganin SV (2015) A Study of Compaction and Deformation of a Powder Composite Material of the 'Aluminum–Rare Earth Elements' System. Met Sci Heat Treat 56(9–10):542–547. <https://doi.org/10.1007/s11041-015-9796-3>
17. Sosenushkin E. N. et al. Modelling and adoption of the stamping technology for a crystallizing metal // Metallurgist. - 2018. - Issue 3. – p. 25–29
18. Krushenko G. G., Rezanova M. V. Producing vehicle parts of aluminum alloy by liquid metal stamping // Problems of development, production, maintenance of spacecraft equipment, and training of engineers for the aerospace industry. – 2015. – p. 186–192
19. Aksenov LB, Kunkin SN (2015) Metal flow control at processes of cold axial rotary forging. In: Evgrafov A (ed) Advances in mechanical engineering, lecture notes in mechanical Hot Orbital Forging by Tool with Variable Angle of Inclination 7 engineering. Published by Springer International Publishing, Switzerland, pp 175–181. ISSN 2195-4356
20. Aksenov LB, Kunkin SN (2014) Cold axial rotary forging of hollow shaft flanges. In: European science and technology: materials of the VII international research and practice conference, vol. II. Vela Verlag Waldkraiburg, Munich, Germany, pp 393–396
21. Kuznetsov RV, Kuznetsov PA, Karachevtsev ID (2019) Static elastic pressing of sintered working inserts with the gradient structure for bimetallic plain bearings. Contemporary mechanical engineering: Science and Education: digest of the 8th International Science-to-practice Conference / Edited by A.N. Evgrafov and A.A. Popovich. – St. Petersburg: Polytechnic University Publishing, 2019

Local Buckling of Box-Shaped Beams Due to Skew Bending



Konstantin Manzhula, Alexander Naumov and Sergei Sokolov

Abstract Local buckling efficiency of different types of beams was reviewed. For beams with non-linear walls and parameterised geometry local buckling analysis was made in ANSYS. Based on result of ANSYS calculation analytic formula was evaluated in MathCAD based on least square method. Influence of different geometrical parameters on local buckling stress value for beams with non-linear walls was analysed.

Keywords Local buckling · Beams with non-linear walls · Analysis of beam with parameterised geometry · Critical stress · FEM · ANSYS · Least square method

1 Introduction

There are different structures of beams which are in use in metal structures. The most simple of them are standard elements. This kind of beams usually included in simple structures of building and other standard constructions. More difficult structures are usually used in complicated facilities, for example box shaped beams. It has upper and lower flanges, one or two walls and different rigidity-increasing elements such as longitudinal ribs and cross members. Cross members have cut-outs to avoid interference with longitudinal ribs (Fig. 1a). This design makes production of beams more complex and expensive. Simple metal structures do not have box-shaped beams. Usually engineers prefer beams with corrugated walls for this need [1–4]. Such type of beams mostly applies in cargos and facilities. For cranes and bridges beams with corrugated walls are not popular solutions [5]. It is economically profitable to use corrugated walls in mass production manufactories, for example for freight cars (Fig. 1b). Only corrugated wall is not enough when the load to structure is intricate. In this case longitudinal ribs are required (Fig. 1c). However, welding of corrugated walls to longitudinal ribs makes production more complicated and it increases labor intensity. Due to this fact for low volume products it is better to use box-shaped beams. Walls, cross members and longitudinal beams for box-shaped

K. Manzhula · A. Naumov (✉) · S. Sokolov
Peter the Great St. Petersburg Polytechnic University, St.-Petersburg, Russia

© Springer Nature Switzerland AG 2020
A. N. Evgrafov (ed.), *Advances in Mechanical Engineering*,
Lecture Notes in Mechanical Engineering,
https://doi.org/10.1007/978-3-030-39500-1_14

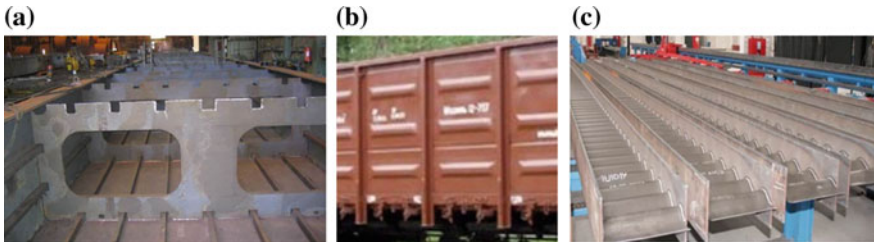


Fig. 1 Types of metal structures: **a** box-shaped beam; **b** freight cars; **c** beam with corrugated wall

beams are made from standard straight metal panels. This increases mass of beam, quantity of welding seams and as a result it increases production cost. Moreover, hard mode usage of box-shaped beams rises chance of durability deformations of welding seams [6].

Load is usually applied on the upper flange of box-shaped beams. So load can make maximum impact in each point of all beam's length. As a result, local buckling can be arisen in any area of a beam's wall. However, there are three calculating schemes for local buckling calculation (Fig. 2). In these schemes local buckling stress depends on normal stress, shear stress or combination of normal and shear stresses [7].

Calculation local buckling stress for linear wall can be done based on next formulas [8]:

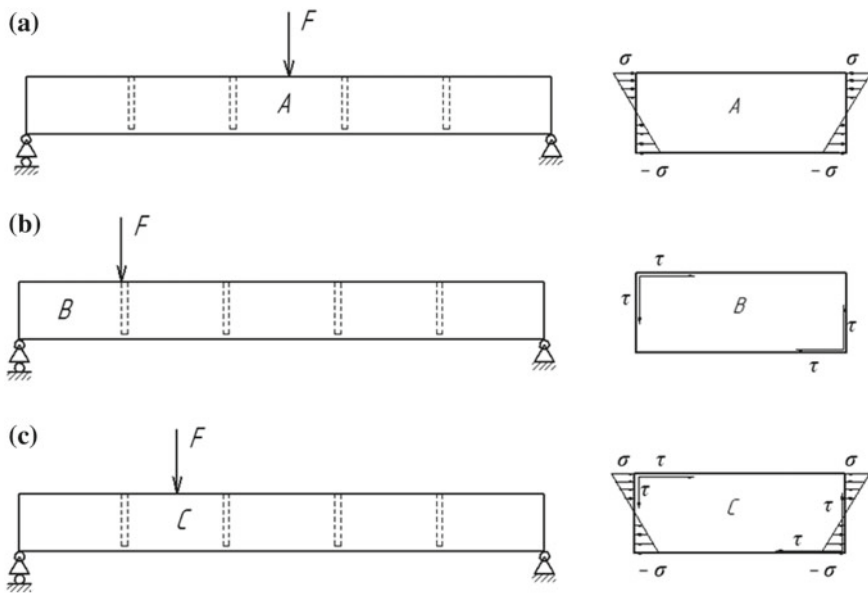


Fig. 2 Calculation schemes of local buckling stress

$$\sqrt{(\sigma/\sigma_{cr})^2 + (\tau/\tau_{cr})^2} \leq 1/n; \quad (1)$$

$$\sigma \leq \sigma_{cr}/n = [\sigma_{cr}]; \quad (2)$$

$$\tau \leq \tau_{cr}/n = [\tau_{cr}]; \quad (3)$$

σ and τ —normal and shear stresses in a beam, σ_{cr} and τ_{cr} —critical normal and shear stresses (when a beam is buckled), n —safety factor.

Formula (1) is used when a load is applied to $1/4$ of beam length (Fig. 2c). When a load is applied to the center of a beam (Fig. 2a) only normal stress makes an impact to local buckling stress. Formula (2) should be used in this case. Formula (3) is used when only shear stress affects due to load on ends of beams (Fig. 2b).

The critical stress is expressed by the formula $\sigma_{cr} = k_s K_{so} (t/d)^2$, where: k_s is the buckling factor reflecting the effect of fixing the conditions and distribution of stress across the width of the plate; K_{so} —the factor having the dimension MPa; t —plate thickness; and, d —height of the plate. The length of the plate is included in the determination of k_s .

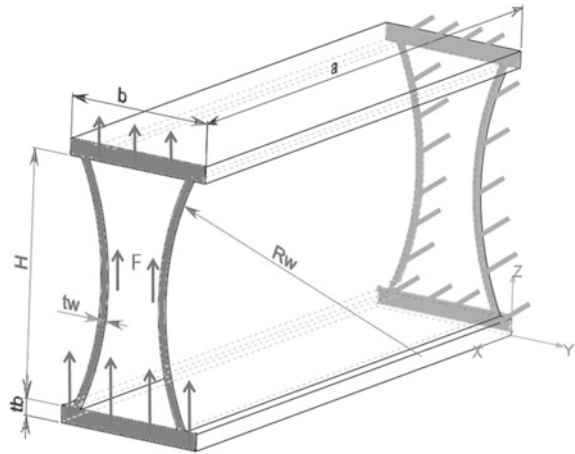
This calculating scheme was analysed in previous article [9]. In this article was reviewed influence of flection radius to local buckling. Formula for calculation local buckling stress value was found.

Second one is to apply load on the ends of beam near fixation areas (Fig. 4b). In this case local buckling depends on shear. The stability of the plate at stress is represented by the equation $\tau \leq \tau_{cr}/n = [\tau_{cr}]$, where: τ —the maximum stress in the plate; τ_{cr} —the critical stress of stability; and, n —the safety factor. The critical stress is expressed by the formula $\tau_{cr} = k_q K_{so} (t/d)^2$, where: k_q is the buckling factor reflecting the effect of fixing the conditions and distribution of shearing stress across the width of the plate; K_{so} —the factor having the dimension MPa, t —plate thickness; and, d —height of the plate. The length of the plate is included in the determination of k_q . In this case combination of normal stress and shear stress affect local buckling properties [10]. In this article will be analyzed second calculation scheme.

Flection radius application to walls of beams (Fig. 3), which are under bending load, is a solution to exclude cross members and longitudinal ribs. Production method of metal plates with radius is not new. It is always used for production of pipes. There are patents, which show beams structures with flection radius [11–13]. However, there are not any researches how radius affects local buckling stress and how to calculate it for beams with non-linear walls. Only LLOYD standard [14] describes how to calculate stress values, but only for one loading scheme.

Papers [9, 15–18] show that beams with non-linear walls have a better local buckling performance than box-shaped beams with standard walls under a pressure and a bending load.

Fig. 3 Box-shaped beam with non-linear walls



2 Methods

Previous dependencies (1)–(3) are not applicable for beams with non-linear walls, as they have not taken into account the curvature of the walls. Assessment of the beam wall local buckling was made in ANSYS Workbench. To do this, cross-section of the beam was developed. Also variable geometric parameters were selected (Table 1) [19].

After that, project in Ansys Workbench was created. Structure of calculation program includes static analysis and linear buckling analysis (Fig. 4). In this project same 3D model with geometric parameters as in the Table 1 was created. Previously discussed parameters were selected on created 3D model. It will provide opportunity to calculate all possible variant of beams geometry [20].

Second step was selection of beam material. It was performed in Ansys material manager. As a result, structural steel from Ansys engineering data was selected as material of the beam. Tensile yield strength of this steel is 250 mPa and tensile ultimate strength is 460 mPa. Last step was input type of fixation of a beam [highlighted pink on (Fig. 3)], selection of load method [F on (Fig. 3)] and definition

Table 1 Geometric parameter

Geometric parameter	Unit of measurement	Value
H	mm	1000, 1600, 2000
t_b	mm	10, 16, 20, 24
t_w	mm	6, 10, 12, 16
b	mm	400, 600, 800
R_w	mm	2000, 4000, 8000
a	mm	1000, 2000, 4000

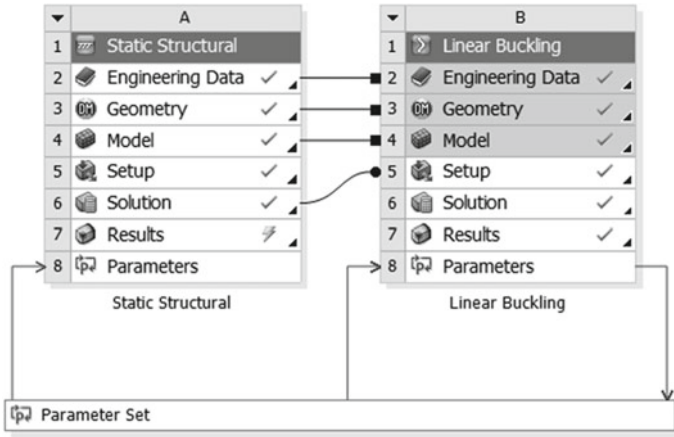


Fig. 4 Project schematic of buckling analysis in Ansys

of grid elements maximum size. Also stress and displacement values were put as preferable results of calculation. After that all geometry combinations of beams can be evaluated.

To analyse results of calculation in ANSYS, received data can be approximated with next formula

$$\tau_{cr} = A_0(X_1)^{a_1}(X_2)^{a_2}(X_3)^{a_3}(X_4)^{a_4}(X_5)^{a_5}. \tag{4}$$

To do it, value of parameters A_0 , a_i should be found. Firstly, the logarithm of formula (4) should be taken

$$\log \tau = \log \left(A_0 \prod_{i=1}^N X_i^{a_i} \right) = \log A_0 + \sum_{i=1}^N a_i \cdot \log X_i. \tag{5}$$

where X_i is geometric parameter of beams, for example $X_1 = \frac{l_b}{H}$, $X_2 = \frac{l_w}{H}$, $X_3 = \frac{R_w}{H}$, $X_4 = \frac{a}{H}$, $X_5 = \frac{b}{H}$.

Secondly, representing $\log Y = \tilde{y}$, $\log A_0 = a_0$, $\log X_i = \tilde{x}_i$ formula (5) can be rewritten as:

$$\tilde{y} = a_0 + a_1\tilde{x}_1 + a_2\tilde{x}_2 + \dots + a_N\tilde{x}_N = a_0 + \sum_{i=1}^N a_i\tilde{x}_i. \tag{6}$$

Now, Eq. (6) can be solved with least square method. This method based on next fact, that difference between values of critical stresses y_m , which were found in Ansys workbench, and values of critical stresses, which can be found by solving Eq. (6), should be approached to 0

$$\Delta = \frac{1}{n} \sum_{m=1}^n (y_m - \tilde{y}_m)^2 = \frac{1}{n} \sum_{m=1}^n \left(y_m - \left(a_0 + \sum_{i=1}^N a_i \tilde{x}_{im} \right) \right)^2 \rightarrow \min \quad (7)$$

where n is quantity of beams variant calculated in Ansys workbench. Solution of formula (7) is partial derivative, which should be alike 0

$$\frac{\partial F}{\partial a_{0,i}} = 0.$$

Applying this solution all parameters a_i can be found from set of equations:

$$\left\{ \begin{array}{l} \frac{\partial F}{\partial a_0} = \sum_{m=1}^n \left(y_m - \left(a_0 + \sum_{i=1}^N a_i \tilde{x}_{im} \right) \right) = 0 \\ \frac{\partial F}{\partial a_1} = \sum_{m=1}^n \left(\left(y_m - \left(a_0 + \sum_{i=1}^N a_i \tilde{x}_{im} \right) \right) \cdot \tilde{x}_{1m} \right) = 0 \\ \dots \\ \frac{\partial F}{\partial a_i} = \sum_{m=1}^n \left(\left(y_m - \left(a_0 + \sum_{i=1}^N a_i \tilde{x}_{im} \right) \right) \cdot \tilde{x}_{im} \right) = 0 \\ \dots \\ \frac{\partial F}{\partial a_N} = \sum_{m=1}^n \left(\left(y_m - \left(a_0 + \sum_{i=1}^N a_i \tilde{x}_{im} \right) \right) \cdot \tilde{x}_{Nm} \right) = 0 \end{array} \right. \quad (8)$$

Set of equations can be represented as

$$\left\{ \begin{array}{l} \sum_{m=1}^n y_m = a_0 \sum_{m=1}^n 1 + a_1 \sum_{m=1}^n \tilde{x}_{1m} + a_2 \sum_{m=1}^n \tilde{x}_{2m} + \dots + a_N \sum_{m=1}^n \tilde{x}_{Nm} \\ \sum_{m=1}^n y_m \tilde{x}_{1m} = a_0 \sum_{m=1}^n \tilde{x}_{1m} + a_1 \sum_{m=1}^n \tilde{x}_{1m} \tilde{x}_{1m} + a_2 \sum_{m=1}^n \tilde{x}_{2m} \tilde{x}_{1m} + \dots + a_N \sum_{m=1}^n \tilde{x}_{Nm} \tilde{x}_{1m} \\ \dots \\ \sum_{m=1}^n y_m \tilde{x}_{im} = a_0 \sum_{m=1}^n \tilde{x}_{im} + a_1 \sum_{m=1}^n \tilde{x}_{1m} \tilde{x}_{im} + a_2 \sum_{m=1}^n \tilde{x}_{2m} \tilde{x}_{im} + \dots + a_N \sum_{m=1}^n \tilde{x}_{Nm} \tilde{x}_{im} \\ \dots \\ \sum_{m=1}^n y_m \tilde{x}_{Nm} = a_0 \sum_{m=1}^n \tilde{x}_{Nm} + a_1 \sum_{m=1}^n \tilde{x}_{1m} \tilde{x}_{Nm} + a_2 \sum_{m=1}^n \tilde{x}_{2m} \tilde{x}_{Nm} + \dots + a_N \sum_{m=1}^n \tilde{x}_{Nm} \tilde{x}_{Nm} \end{array} \right. \quad (9)$$

and rewritten in matrix form $\tilde{Y} = A \cdot \tilde{X}$, where

$$\tilde{Y} = \begin{pmatrix} \sum_{m=1}^n y_m \\ \sum_{m=1}^n y_m \tilde{x}_{1m} \\ \sum_{m=1}^n y_m \tilde{x}_{2m} \\ \dots \\ \sum_{m=1}^n y_m \tilde{x}_{Nm} \end{pmatrix} \quad A = \begin{pmatrix} a_0 \\ a_1 \\ a_2 \\ \dots \\ a_N \end{pmatrix},$$

$$\tilde{X} = \begin{pmatrix} \sum_{m=1}^n 1 & \sum_{m=1}^n \tilde{x}_{1m} & \sum_{m=1}^n \tilde{x}_{2m} & \dots & \sum_{m=1}^n \tilde{x}_{Nm} \\ \sum_{m=1}^n \tilde{x}_{1m} & \sum_{m=1}^n \tilde{x}_{1m}\tilde{x}_{1m} & \sum_{m=1}^n \tilde{x}_{1m}\tilde{x}_{2m} & \dots & \sum_{m=1}^n \tilde{x}_{1m}\tilde{x}_{Nm} \\ \sum_{m=1}^n \tilde{x}_{2m} & \sum_{m=1}^n \tilde{x}_{2m}\tilde{x}_{1m} & \sum_{m=1}^n \tilde{x}_{2m}\tilde{x}_{2m} & \dots & \sum_{m=1}^n \tilde{x}_{2m}\tilde{x}_{Nm} \\ \dots & \dots & \dots & \dots & \dots \\ \sum_{m=1}^n \tilde{x}_{Nm} & \sum_{m=1}^n \tilde{x}_{Nm}\tilde{x}_{1m} & \sum_{m=1}^n \tilde{x}_{Nm}\tilde{x}_{2m} & \dots & \sum_{m=1}^n \tilde{x}_{Nm}\tilde{x}_{Nm} \end{pmatrix}.$$

From matrix equation $\tilde{Y} = A \cdot \tilde{X}$ parameters a_i can be found as

$$A = \tilde{X}^{-1} \cdot \tilde{Y} \tag{10}$$

3 Results and Discussion

In ANSYS 240 beams with different geometrical parameters were calculated. Diagrams of local buckling have same shape: two big beads on both walls (Fig. 5). Same shape have beams with linear walls. However beams with non-linear walls have higher value of critical buckling stress.

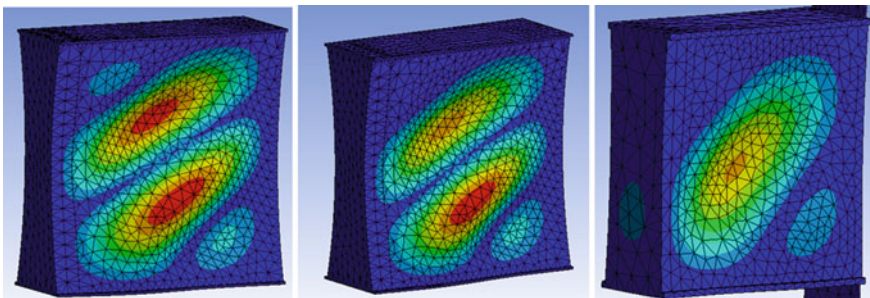


Fig. 5 Movements diagrams with loss of local stability for different beam geometry

Table 2 Values of parameters a_i

a_0	6.035
a_1	-0.926
a_2	2.32
a_3	-0.385
a_4	-0.41
a_5	0.483

Evaluations based on least square method from previous article section can be used to find analytic formula of local buckling stress. To do it, calculations were done in MathCad software. Solutions of parameters a_i from formula (7) are showed in Table 2.

Finally, all parameters a_i can be applied to formula (4) and it can be represented as

$$\tau_{cr} = \frac{1.086 \times 10^6 \cdot \left(\frac{b}{H}\right)^{0.483} \cdot \left(\frac{t_w}{H}\right)^{2.32}}{\left(\frac{R_w}{H}\right)^{0.385} \cdot \left(\frac{a}{H}\right)^{0.41} \cdot \left(\frac{t_b}{H}\right)^{0.926}}. \quad (11)$$

Also in formula (7) can be added constant $K_{s0} = 0.759$ MPa for structural steels [8]

$$\tau_{cr} = \frac{1.43 \times 10^6 \cdot K_{s0} \cdot \left(\frac{b}{H}\right)^{0.483} \cdot \left(\frac{t_w}{H}\right)^{2.332}}{\left(\frac{R_w}{H}\right)^{0.385} \cdot \left(\frac{a}{H}\right)^{0.41} \cdot \left(\frac{t_b}{H}\right)^{0.926}}. \quad (12)$$

The assessed value of formula (11) error can be found as

$$\delta = \frac{\tau_{ansys} - \tau_{cr}}{\tau_{ansys}} \cdot 100\%. \quad (13)$$

Average value of formula (11) error is 8.1%. Distribution of formula (12) results to Ansys stress calculation is on a Fig. 6.

Graphic was created to understand which how radius makes impact to the value of buckling critical stress (Fig. 7).

4 Conclusions

In this study box-shaped beams with non-linear walls were analyzed. This type of beams is not frequently used in metals structures, but there are patents described layout and geometric of beams. Advantage of such kind beams is bigger value of local buckling stress. This property is important for main beams of traveling cranes, so it can improve robustness of current structures. This is the reason why it is actual

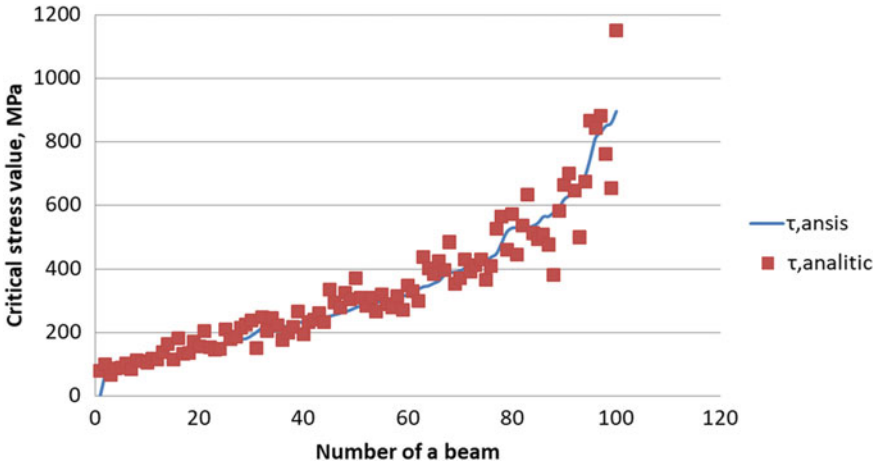


Fig. 6 Graphic of ansys and analytic formula (12) buckling stress

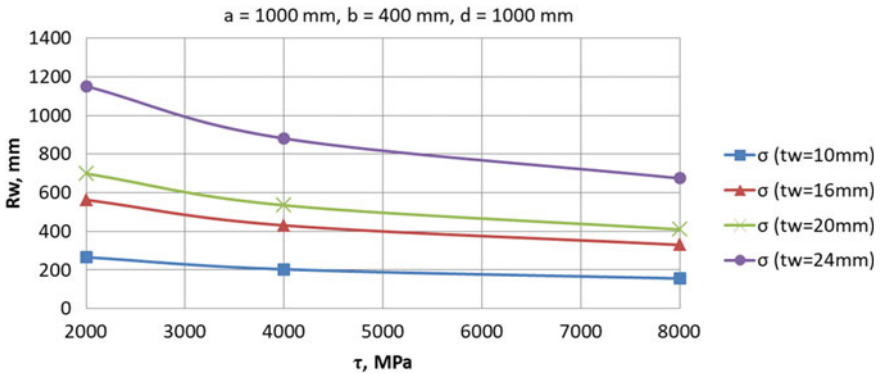


Fig. 7 Impact of a radius to a stress value for different thickness of a wall

to study beams with non-linear beams. Only finite element method can be used for calculation stress value of beams with non-linear walls. Mechanic properties variations of these beams due to flection radius increase are not studied.

Also it was defined that local buckling critical force of beams with non-linear walls is bigger than critical force of standard box-shaped beams. Value of critical force is increasing with gain of flections' radius. The most important result of the study is development of analytic formula for local buckling stress. It can be used on earlier stages of metal structures engineering to get estimated values of stress and geometric parameters.

References

1. Pasternak H, Kubieniec G (2010) Plate girders with corrugated webs. *J Civil Eng Manag* 16(2)
2. Fainstein A (2007) Steel beams with minimal weight, vol 95. Publishing House of Polytechnic University
3. Balzannikov M, Holopov I, Soloviev A, Lukin A (2013) Steel beams with corrugated walls in hydraulic facilities, vol 11. *Vestnik MGSU*
4. Azhermachev S, Semenov P (2005) Beams with corrugated walls in decked structures. *Building and technogenetic safety*, vol 10
5. Kulkova NN (2004) Stress-strain behavior aspects of crans beams. VNIIPtmash
6. Manzhula KP, Petinov SV (2001) Strength and durability of metal structures, vol 76. SPBGU, Saint Petersburg
7. EN 1993-1-5 (2006) (English): Eurocode 3—Design of steel structures—Part 1–5: plated structural elements
8. Sokolov S (2011) Construction mechanics and metal structures of machines. SPB Politechnika publishing house, vol 450
9. Manzhula KP, Naumov AV (2017) Influence of flections' radius value to local buckling of box-shaped beams with non-linear walls. *Int Rev Mech Eng (IREME)* 11(5)
10. Tovstik PE (2005) Local buckling of plates and shapes. RAN
11. Patent. 1989834 USA. Method for reinforcement beams. G. Watson published. 5 Feb 1935
12. Patent EP 0293789 A1 Germany. Als Kastenträger ausgebildeter Kranträger. Richar Aust published 10 Oct 2001
13. Patent 2478557, Russia. Travalng beam. Alexander Belyi, published 1 June 2011
14. LLOYD Rules for classification and construction IV industrial services. Germanischer Lloyd SE
15. Manzhula KP, Naumov AV (2017) Local buckling of beams with non-linear walls under pressure with bending. *Modern mechanic engineering: science and education*. In: 6th international scientific-practical conference, Publishing House of Polytechnic University
16. Manzhula KP, Naumov AV (2016) Analysis of non-linear plates in metal structures. *Interstoyemch-2016*, collection of reports of the XX international scientific and technical conference, vol 244, MGSU, Moscow
17. Manzhula KP, Naumov AV (2016) Influence of non-linear walls to local buckling. In: *Modern machine building: science and education: materials of the 5th international scientific and practical conference*, vol 841, Publishing House of Polytechnic University
18. Manzhula KP, Naumov AV (2016) Local buckling analysis of beams with non-linear walls. *Science Week SPbPU*. Materials of the scientific conference with international participation, vol 70. Best reports
19. Sidnyaev NI, Vilisova NT (2011) Theory of experiment planning. MGTU, Moscow
20. Basov KA (2005) Guide for ANSYS. DMK-PROSS, Moscow

Thinnest Finishing Treatment with a Focused Jet of Electrolytic Plasma



Alexander I. Popov, Mikhail M. Radkevich and Vasily G. Teplukhin

Abstract The article presents the results of experimental data on the formation of thin layers of the surface of stainless steels by jet focused electrolyte-plasma treatment. An experimental electrolyte-plasma installation is shown, which makes it possible to remove the thinnest layers from the surface of samples using an electrolyte-plasma discharge. In the work, hollow and type-setting current leads were used. The surface roughness parameters during the processing of samples from 08X18H9T, AISI 304, and HVG stainless steels are studied. Samples with a low level of surface roughness were obtained. A decrease in the mass of samples after electrolyte-plasma treatment is shown. The minimum removal of metal from the surface of the samples was recorded. The theoretical regularities of the formation of the surface layer geometry are considered. The results of the work can be applied to metallurgical, machine-building or turbine production.

Keywords Hollow cathode · Type-setting current lead · Electrolyte-plasma discharge · Material removal depth

1 Introduction

The formation of the surface layers of the product is an important final point of manufacture. The quality of the surface layers largely determines the performance and durability of the product. In the manufacture of accurate and critical products, very stringent requirements are often met for the accuracy of the size to be performed, the state of the surface layer, and the roughness parameter of the treated surface [1–5]. Obtaining these products in engineering is a technologically challenging task. To solve this problem, both traditional and advanced technologies are used. Traditional technologies include felt polishing, honing, shaving and superfinishing. Modern technologies include technologies of electric discharge machining, waterjet processing, magnetically abrasive processing, ultrasonic processing and electrolyte-plasma processing. Electrolytic-plasma treatment occupies a special place. This technology

A. I. Popov (✉) · M. M. Radkevich · V. G. Teplukhin
Peter the Great Saint-Petersburg Polytechnic University, St. Petersburg, Russia

© Springer Nature Switzerland AG 2020
A. N. Evgrafov (ed.), *Advances in Mechanical Engineering*,
Lecture Notes in Mechanical Engineering,
https://doi.org/10.1007/978-3-030-39500-1_15

includes wide technological capabilities including surface treatment by polishing, dimensional processing by removing surface layers, applying functional coatings. Among the features of this method, several methods for producing electrolyte plasma can be indicated. This is treatment in an electrolytic bath [6–10] using metal or electrolytic electrodes [11–13], processing by the intersection of two or more electrolytic jets [14, 15], and treatment with an electrolytic jet of a metal anode (cathode). Each method, considered separately, has its advantages and disadvantages. Processing in an electrolytic bath is characterized by high polishing speeds, high product temperatures, high radiated output power, significant evaporation from the electrolytic bath, and uneven removal at sharp edges and corners of the product [16–18]. Processing with an electrolytic jet (jets) is characterized by equal processing speed, low power allocated to the discharge, high precision processing over the entire surface, the ability to process products of any area, dimensional processing, and a small amount of electrolyte evaporation [19, 20].

This makes it possible to consider jet electrolyte-plasma processing as a method suitable for the accurate processing of various curved surfaces, including for critical medical devices, cutting tools, gear profiles, steam and gas turbine blades, turbine wheels for various purposes, 3D metal printing [1–5, 21–24]. Therefore, for blasting, studies are carried out on temperature, the forms of existence of a plasma discharge, methods for supplying an electrolytic jet, surface roughness and depth of removal, research on the processing of various materials. There is practically no data on the effect of jet electrolyte-plasma treatment on thin surface layers of the processed material. Based on this, the goal of our work is to study the features of the thinnest finish electrolyte-plasma treatment. The objectives of the work are to assess the range of voltages and currents to obtain polished layers of high quality, the influence of technological modes on the roughness parameters of the surface layer, the assessment of the state of the surface after processing, and the consideration of the theoretical aspects of thin layer removal.

Equipment and Materials

In the course of the experiments we used the installation assembled in accordance with [25], based on a power source assembled according to the Larionov scheme [7]. The installation includes an electrolyte supply system and a power supply. The negative pole of the power supply is connected to a hollow or stacked current supply, and the positive to the sample being processed (Fig. 1).

The voltage supplied to the sample was set equal to 20–500 V. Processing of the samples was carried out with a fixed current supply. To analyze the surface of the samples, an LV-41 metallographic microscope (Lomo, Russia) was used. The depth of removal of the processed material was measured by a digital electronic indicator «Micron» with a division value of 1 μm . The weight of the samples was measured on a laboratory balance BM213M balance with a division value of 0.001 mg. The studies used hollow [26] and stacked [27] current leads. Solutions of ammonium sulfate (Na_2SO_4)—5 g and ammonium citrate ($(\text{NH}_4)_3\text{C}_6\text{H}_5\text{O}_7$)—5 g in tap water, ammonium sulfate ($(\text{NH}_4)_2\text{SO}_4$) and sodium sulfate (Na_2SO_4)—30 g in tap water were used as electrolytes.

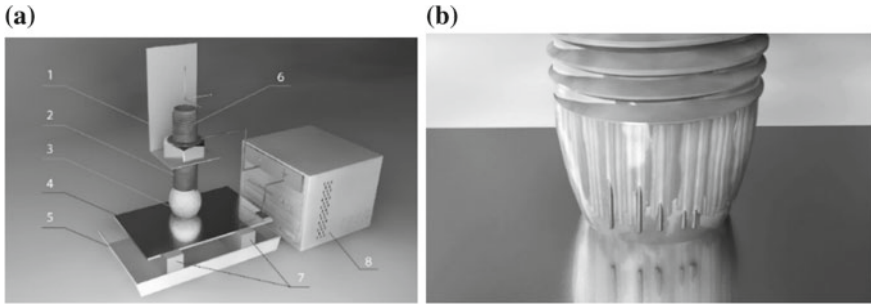


Fig. 1 Schematic diagrams of electrolytic-plasma surface treatment: **a** 1—current lead holder, 2—hollow current lead, 3—electrolytic cathode, 4—sample, 5—electrolyte intake bath, 6—electrolyte supply pipe, 7—insulated supports, 8—Power Supply; **b** type-setting current lead

The electrolyte was supplied by a jet through a tube with a diameter of 3 mm with a flow rate of 2.4–9.0 l/h. The measurement of the flow rate of the electrolyte was carried out by passing an electrolyte of 100 g mass with fixation of the transit time along the stopwatch. The experiment was carried out at atmospheric pressure. Used 25 marked samples with a size of 45 × 50 mm, 100 × 200 mm from stainless steel 08X18H9T, AISI 304, HVG.

2 Experiment Results

2.1 Assessment of Volt–Ampere Characteristics

Volt–ampere characteristic is one of the important technological indicators of the process. We have fixed the parameters of the change in the electric discharge current depending on the applied voltage. The research results are presented in Fig. 2. It is shown that a limited voltage range corresponds to the polishing region to obtain thin surface layers of high quality. This range fits into voltages from 180 to 360 V. An important parameter of the process is the electrolyte feed rate. With an increase in the electrolyte feed rate of more than 6 l/h. the intensity of the processing mode changes. This leads to a decrease in the surface roughness parameter.

2.2 Determination of Surface Roughness Parameters

During the experiments, the roughness of the samples was obtained in the range of operating voltages from 20 to 500 V. It was shown that in the voltage range from 220 to 380 V, a sharp decrease in the roughness parameter to Ra 0.034 μm is observed (Fig. 3).

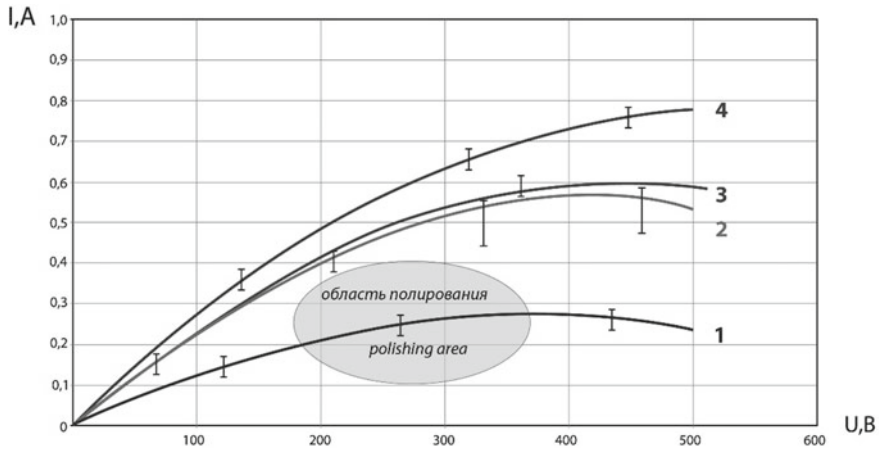


Fig. 2 Volt–ampere process characteristic: 1—electrolyte flow rate 2 l/h; 2—flow rate of electrolyte 4 l/h; 3—electrolyte flow rate 6 l/h; 4—electrolyte flow rate of 8 l/h

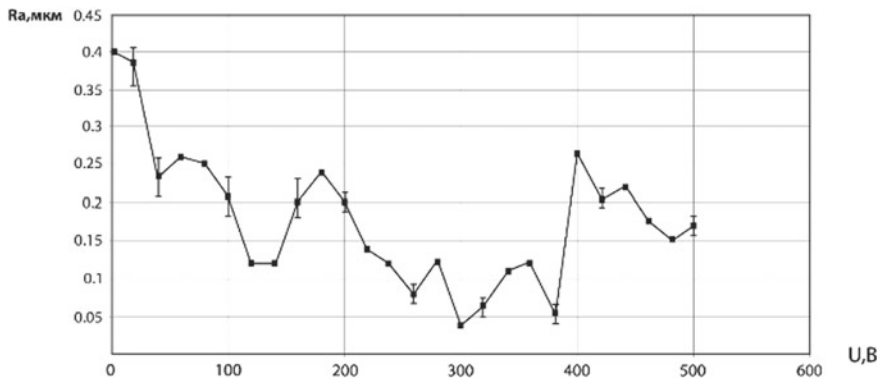


Fig. 3 The dependence of the roughness parameter on voltage during electrolytic-plasma treatment of AISI 304 steel using a type-setting current supply

It is shown that for different stresses a surface is formed with a different level of roughness and a microrelief. It was noted that in the electrolysis mode 20–80 V. The steel surface has a smoothed microrelief with a matte surface without gloss. In the process of stepwise increase in voltage, a transition is observed from the matte surface to the appearance in the middle part of the treatment of a polished zone with a characteristic specular gloss (Fig. 4).

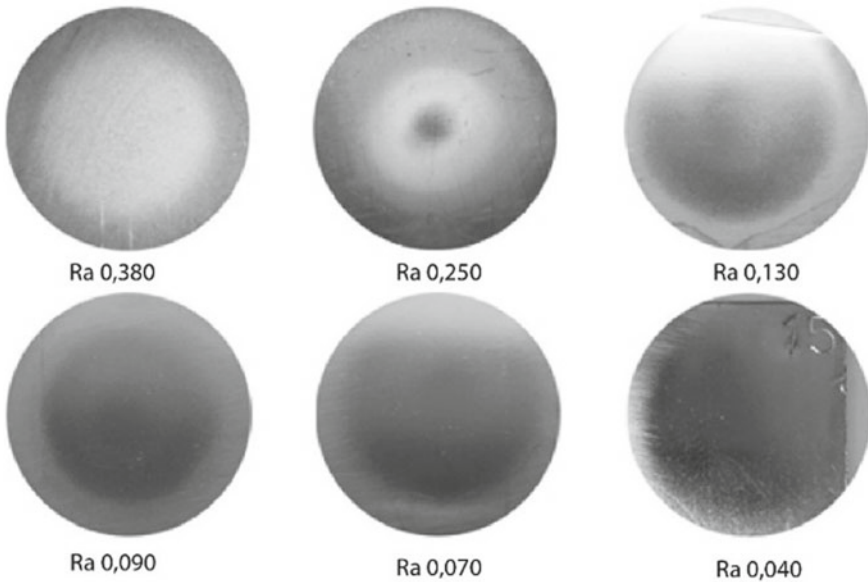


Fig. 4 Appearance of the surface of samples made of AISI 304 steel during electrolyte-plasma processing using a type-setting current supply

2.3 Reflectivity

In the process of plasma jet processing, the surface acquires high reflectivity. An example of surface treatment quality is shown in Fig. 5.

2.4 Determination of Material Weight Loss

With a change in the state of the surface of the sample, a change in its mass also occurs. An example of a change in mass loss for samples from HVG steel is shown in Fig. 6.

The range from 160 to 300 V is characterized by an increased removal of metal in the electric discharge zone. This leads to a change in surface shape. With a fixed current lead and a sample, a spherical hole is usually formed in the processing zone. Its depth depends on the flow rate of the electrolyte, the time of formation of the electric discharge, the composition of the electrolyte, the current and the distance between the current leads.

Fig. 5 An example of the reflectivity of the surface of AISI 304 steel after finishing electrolytic-plasma treatment

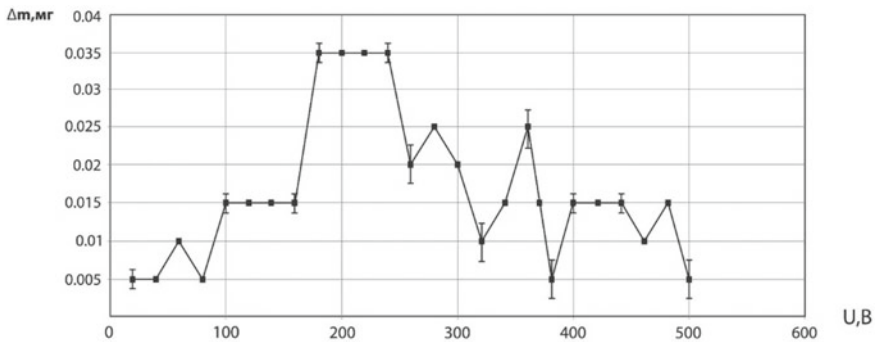
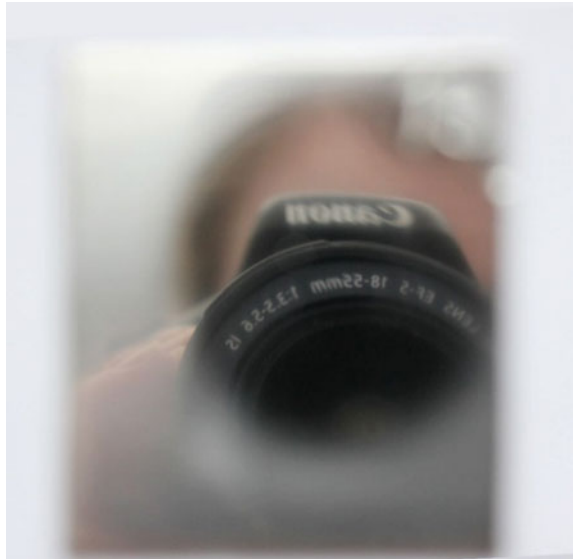


Fig. 6 Dependence of sample mass loss on voltage during electrolytic-plasma treatment of HVG steel using hollow current supply

2.5 Shaped Polished Surface with Minimal Removal Depth

Thin surface treatment with a minimum removal depth implies a low surface roughness parameter Ra. For accurate processing, it is necessary to obtain a low surface roughness parameter Ra while removing the surface layer corresponding to the maximum height Rmax of the microprofile.

When this condition is met, a superthin surface treatment is provided Experiments show that with the combined processing of steel 20X13 using stacked and hollow current leads, it is possible to achieve a minimum thickness of removal from the metal surface (Table 1).

Table 1 Depth of material removal from the surface of the samples using hollow current lead

Modes					Surface parameters	
Voltage U, V	Current I, A	Electrolyte feed rate, l/h	Feed S, mm/min	The number of passes n, pcs	Length of the processed surface, mm	Depth of removal, mm
225	1,02	9,0	34,1	1	50	0,112
230	0,71	9,0	17,1	1	50	0,130
230	0,65	6,1	17,1	1	50	0,058

The parameters of the depth of material removal using hollow and type-setting current leads, and an electrolyte containing a solution of ammonium sulfate and sodium sulfate in tap water, are fixed in Table 2.

The experimental results show that the minimum depth of removal from the metal surface was 0.016 mm, which corresponds to the minimum surface roughness parameter Ra 0.083 μm . The results of measuring the depth of processing with a fixed hollow current supply during the treatment of AISI 304 steel show that a change in the depth of the surface layer is possibly less than 16 μm . Measurements of the depth of removal of the surface layer are presented in Table 3.

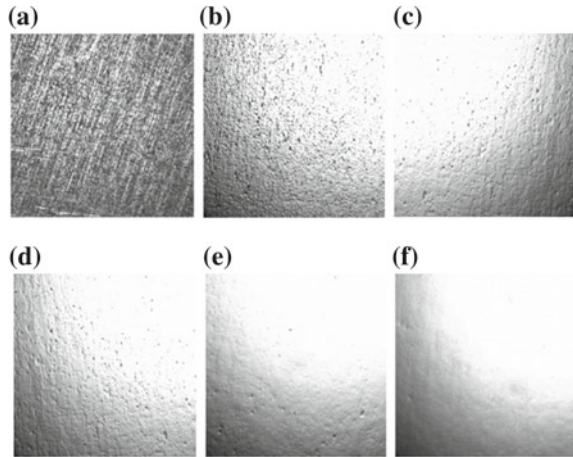
Table 2 Depth of material removal from the surface of the samples with sequential use of type-setting and hollow current leads

Modes				Surface parameters		
Voltage U, V	Current I, A	Electrolyte feed rate, l/h	Number of passes type-setting/hollow current lead n, pcs	Processing area cm^2	Roughness parameter Ra surface, μm	Depth of removal, mm
250–260	1,2–1,5	4–6	2/1 (3)	36	0,062	0,020
260	1,1	5	3/2 (5)	4	0,036	0,045
260	1,1	5	1	48	0,083	0,016

Table 3 Depth of material removal from the surface of the samples using fixed hollow current lead

Modes				Surface parameters	
Voltage U, V	Current I, A	Electrolyte feed rate, l/h	t, s	Processing area, cm^2	Depth of removal, mm
240	0,4	4	600	0,78	0,005
300	0,3	2	133	0,28	0,001
240	2,5	5	15	3,14	0,006

Fig. 7 Changes in the surface state of samples during the processing of AISI 304 steel using sequentially stacked and hollow current leads: **a** is the initial surface, **b** is the formation of microdefects on the surface, **c–e** is the process of leveling the surface, **f** is the polished surface



2.6 Polished Surface Forming Mechanism

During the action of an electrolyte-plasma discharge on the surface of the sample, a complex mechanism for removing the surface layer was recorded. It depends on the initial roughness parameter and on the quality of preparation of the surface layer. Figure 7 shows the change in the state of the surface of the samples during the processing of AISI 304 steel during processing.

3 Results Discussion

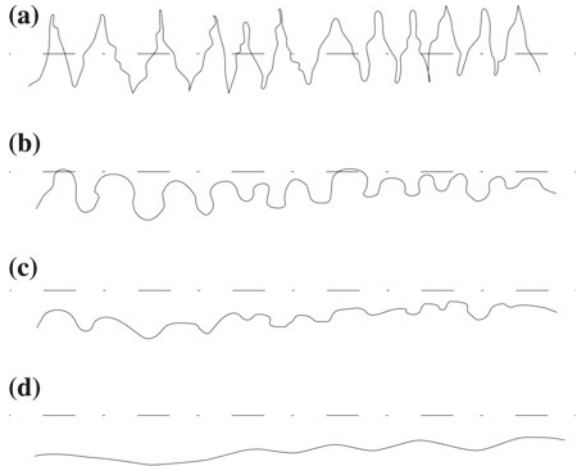
Analysis of changes in the surface layer of samples during jet focused electrolyte-plasma treatment shows the complex nature of changes in the surface microprofile.

The initial level of surface roughness (Fig. 8a) is characterized by a developed surface microprofile having unevenly distributed microroughness apexes. These peaks are usually formed in the technological process of preliminary grinding of the surface. This is due to the plowing of the original surface with abrasive grains. After numerous acts of exposure to the surface with abrasive grain, an uneven profile forms with deep depressions between the peaks.

When voltage is applied to the current leads, the electrolytic jet changes its geometric shape and is formed in accordance with the lines of the electromagnetic field strength [20].

With an appropriate distance, voltage, and electrolyte concentration, the formation of a shallow bubble phase of the entire discharge region occurs. In the local zone above the surface of the sample, a vapor-gas shell is formed, which is a thin layer equal to 50–100 μm according to different authors [11, 14, 16]. The electrolyte-plasma

Fig. 8 Scheme of surface layer formation during electrolyte-plasma treatment: **a** initial surface, **b** surface during the initial treatment period, **c** surface during the processing process, **d** surface during the final treatment period



layer exceeds the parameter of the initial surface roughness Ra 0.4–0.8 microns more than 50–100 times. The electric field strength in this region reaches $10^4 - 10^6$ V/m.

This leads to the occurrence of low power discharges at the tops of microroughnesses. Numerous discharges arising at the vertices of the microroughness lead to their smooth rounding and increase in radius for each individual vertex (Fig. 8b, c).

The removal depth $R\Sigma$ of the surface to remove the occurrence of these microcraters can be calculated by the formula.

$$R\Sigma = Ra + KRa$$

where,

Ra —roughness parameter of the initial surface;

$K = 1-40$ —defective layer coefficient.

The value of K can take values in the range from 1 to 40.

It depends on the initial roughness parameter Ra , the presence of contaminants on the surface of the samples, the technological mode of processing, the electrolyte used, the thickness of the oxide film on the surface of the sample and the type of current supply, the distance between current leads.

A decrease in K leads to a decrease in the depth of the defective layer and the achievement of superthin treatment is facilitated by the preparation of the surface before treatment by purification from fatty and other contaminants, a decrease in the current of the electrolyte-plasma discharge, and selection of the electrolyte, which helps to reduce the thickness of the oxide film.

The increase in the distance between the current leads and the formation of an electrolyte-plasma discharge in the form of a straight cone using stacked current leads helps to remove thin layers from 5 to 1 μm from the surface, which allows you to remove from the surface a value corresponding to R_{max} .

4 Conclusions

1. Selection of modes for thinnest processing makes it possible to exclude formation of primary defects occurring in zones of valleys between tops of micro relief.
2. The technology of processing the thinnest layers allows to remove the volume of material equal to the initial value R_{max} . Thus, it is possible to remove the thinnest layer corresponding to the height of the surface micro relief.
3. This type of processing allows to treat products with small tolerances for size from 1 to 20 μm . This makes it possible to process a wide range of products. These include: cardio-surgical stents, gears, blades of gas and steam turbines, mono wheels.

Acknowledgements The authors express their gratitude to graphic designer Diana A. Popova.

References

1. Babichev D, Storchak M (2018) Quality characteristics of gearing. *Mech Mach Sci* 51:73–90. https://doi.org/10.1007/978-3-319-60399-5_4
2. Babichev D (2018) Development of geometric descriptors for gears and gear tools. *Mech Mach Sci* 51:231–254. https://doi.org/10.1007/978-3-31960399-5_11
3. Eliseev VV, Moskalets AA (2018) Vibrations of turbine blades as elastic shells. Lecture notes in mechanical engineering, Part F5, pp 53–60. https://doi.org/10.1007/978-3-319-72929-9_7
4. Zinovieva TV, Moskalets AA (2018) Modal analysis of turbine blade as one- and three-dimensional body. Lecture notes in mechanical engineering, PartF5, pp 195–204. https://doi.org/10.1007/978-3-319-72929-9_20
5. Drozdov A, Galerkin Y (2017) The numerical study of the rake angle of impeller blade in centrifugal compressor. In: IOP conference series: materials science and engineering, vol 232, issue no 1, статья № 012036. <https://doi.org/10.1088/1757-899X/232/1/012036>
6. Kulikov IS, Vashenko SV, Kamenev AY (2010) Elektrolitno-plazmennaya obrabotka materialov [Electrolytic plasma processing of materials]. Belarusian science, Minsk, p 232. ISBN 978-985-08-1215-5 (in Russian)
7. Ushomirskaya LA, Veselovskiy AP (2010) Intensifikatsiya tekhnologicheskikh protsessov izgotovleniya detaley mashin pri ispolzovanii razlichnykh vidov energii [Intensification of technological processes of manufacturing machine parts using different types of energy]. *Metalloobrabotka [Metalworking]* 2(56):C.46 (in Russian)
8. Novikov VI, Popov AI, Tyukhtayev MI, Zeydan MN (2011) Vozmozhnosti elektrolitno-plazmennogo polirovaniya pri obrabotke detaley s razlichnym nachalnym urovnem sherokhovatosti poverkhnosti [Possibilities of electrolyte-plasma polishing in the processing of parts with different initial levels of surface roughness]. *Metalloobrabotka [Metalworking]* 1(61):C.13 (in Russian)
9. Nestler K, Böttger-Hiller F, Adamitzki W, Glowa G, Zeidler H, Schubert A (2016) Plasma electrolytic polishing—an overview of applied technologies and current challenges to extend the polishable material range, *Procedia CIRP* 42(Isem Xviii):503–507. ISSN: 22128271, DOI:10.1016/j.procir.2016.02.240
10. Aliakseyeu YG, Korolyov AY, Parshuto AE, Niss VS (2017) Electrolyte-plasma treatment under non-stationary mode in a high-gradient electric field. *Sci Tech* 16:391–399. <https://doi.org/10.21122/2227-1031-2017-16-5-391-399>

11. Fortov VE (2008) Encyclopedia of low-temperature plasma. High Temp 46:1–2. <https://doi.org/10.1134/S0018151X0801001X>
12. Gaisin AF, Son EE (2005) Vapor-air discharges between electrolytic cathode and metal anode at atmospheric pressure. High Temp 43:1. <https://doi.org/10.1007/s10740-005-0040-5>
13. Witzke M, Rumbach P, Go DB, Sankaran RM (202) Evidence for the electrolysis of water by atmospheric-pressure plasmas formed at the surface of aqueous solutions. J Phys D Appl Phys 45:5. <https://doi.org/10.1088/0022-3727/45/44/44200>
14. Barinov YA, Shkolnik SM (2016) Razryad s zhidkim nemetallicheskim katodom (vodoprovodnaya voda) v potoke vozdukhha atmosfernogo davleniya [Discharge with a liquid non-metallic cathode (tap water) in an atmospheric pressure air stream]. J Tech Phys 86(11):156 (in Russian)
15. Galimzyanov II, Gaisin AF, Fakhrutdinova IT, Shakirova EF, Akhatov MF, Kayumov RR Characteristics of the development of electric discharge between jet anode and liquid cathode. High Temp 56(2):296–298. <https://doi.org/10.1134/s0018151x18020086>
16. Slovetskii DI, Terentyev SD, Plekhanov VG (1986) Mekhanizm plazmenno-elektrolitnogo nagreva metallov [The mechanism of plasma-electrolyte heating of metals]. High Temp 24(2):353 (in Russian)
17. Dyakov IG, Shadrin SY, Belkin PN (2004) Osobennosti anodnogo nagreva pri dvizhenii elektrolita v rezhime svobodnoy konveksii [Features of anode heating during electrolyte movement in free convection mode]. Electron Met Process 4:9 (in Russian)
18. Danilov I, Hackert-Oschätzchen M, Zinecker M, Meichsner G, Edelmann J, Schubert A (2019) Process understanding of plasma electrolytic polishing through multiphysics simulation and inline metrology. Micromachines 10:214. <https://doi.org/10.3390/mi10030214>
19. Popov AI, Tyukhtyaev MI, Radkevich MM, Novikov VI (2016) Analiz teplovykh yavlenij pri strujnoj fokusirovannoj elektrolitno-plazmennoj obrabotke [The analysis of thermal phenomena occurring under jet focused electrolytic plasma processing]. The journal “Nauchno-tehnicheskie vedomosti SPbGPU” (St. Petersburg State Polytechnical University Journal) 4(254):141 (in Russian)
20. Popov AI, Novikov VI, Radkevich MM (2019) Characteristics of the development of electric discharge between the jet electrolyte cathode and the metal anode at atmospheric pressure. High Temp 57(4):483–495
21. Popov AI, Radkevich MM, Medko VS, Shilling NG, Rudavin AA Magnetronnaya raspylitel'naya golovka [Magnetron spraying head]. Patent for an invention Russian Federation № 2656318. IPC: C25F7/00. 04.04.2017
22. Novoselov MV, Shilling NG, Rudavin AA, Radkevich MM, Popov AI (2018) Otsenka vozmozhnosti polirovaniya nerzhaveyushchikh staley struynoy elektrolitno-plazmennoj obrabotkoy [Assessment of the possibility of polishing stainless steels by jet electrolytic—plasma treatment]. Bull PNIPU 1:95 (in Russian)
23. Popov AI, Radkevich MM, Novoselov MV (2019) Osobennosti elektrolitno-plazmennogo polirovaniya stentov [Features of electrolyte-plasma polishing of stents]. Tekhnologiya metallov [Metal technology] 5:18 (in Russian)
24. Abyaz TR, Muratov KR, Radkevich MM, Ushomirskaya LA, Zarubin DA (2018) Electrolytic plasma surface polishing of complex components produced by selective laser melting. Russ Eng Res 38:491–492. <https://doi.org/10.3103/S1068798X18060035>
25. Popov AI, Radkevich MM, Kudryavtsev VN, Zakharov SV, Kuzmichev IS Ustanovka dlya elektrolitno-plazmennoj obrabotki turbinnih lopatok [Plant for electrolyte-plasma treatment of turbine blades]. Patent for an invention Russian Federation № 2623555. IPC: C25F7/00. 27.06.2017 (in Russian)
26. Gaisin AF Ustrojstvo dlya polucheniya elektricheskogo razryada [Electric charge generation method]. Patent of Russian Federation № 2457571. IPC: H01J13/02. 27.07.12 (in Russian)
27. Popov AI, Radkevich MM, Medko VS, Novoselov MV Ustrojstvo dlya elektrolitno-plazmennoj obrabotki metallicheskih izdelij [Device for electrolyte-plasma treatment of metal products]. Patent of Russian Federation № 2681239. IPC: C25F7/00. 13.06.2018 (in Russian)

On the Calculation of Blades Highly-Effective Impellers of Centrifugal Compressors



Vladimir A. Pukhliy, Sergey T. Miroshnichenko, Olga G. Lepekha,
Alexander A. Zhuravlev and Alexandra K. Pomeranskaya

Abstract An example of weld-joints testing of a new pressure vessel made of stainless steel is considered. The main methods of testing were the method of radiography and the method of acoustic emission. Dangerous defects in the refinery column were detected before running began as a result of the joint application of these methods. This example demonstrates the effectiveness of using such the properties of acoustic emission method, as the integral nature of testing, high sensitivity and the ability to record developing (the most hazardous) defects in the application to the diagnosis of the industrial pressure vessels state. Also the results of metallographic examination of the specimen of column shell with detected defects are presented. The question of the sequence of application of different methods of nondestructive testing for optimization of the procedure for inspection of large-sized equipment is discussed.

Keywords Acoustic emission · Radiographic testing · Pressure vessels · Stainless steel · Cracks in the welds · Sequence of application of testing methods

1 Introduction

Earlier, Seleznev et al. [1, 2] at the Department of Compressor Engineering of St. Petersburg Polytechnic Institute conducted aerodynamic tests of centrifugal compressor wheel models, using the blade shape formed by conjugating two curves (arcs) with different curvature radii (R_1 and R_2) (Fig. 1). Figure 1 shows the impeller of a centrifugal compressor with S-shaped blades.

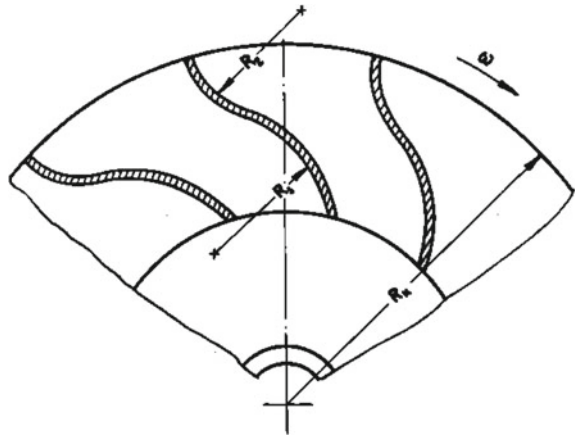
Designed wheels with S-shaped blades are not inferior in their aerodynamic qualities, and in some cases surpass similar production samples of wheels. Thus, the developed mill fan with S-shaped blades [3] has significantly better aerodynamic parameters compared to similar production samples. This fact can be explained by the following: the initial section of the rotor blades, which is bent back, contributes to

V. A. Pukhliy (✉) · S. T. Miroshnichenko · O. G. Lepekha · A. A. Zhuravlev
Sevastopol State University, Sevastopol, Russia

A. K. Pomeranskaya
Enterprise Aerotex, Moscow, Russia

© Springer Nature Switzerland AG 2020
A. N. Evgrafov (ed.), *Advances in Mechanical Engineering*,
Lecture Notes in Mechanical Engineering,
https://doi.org/10.1007/978-3-030-39500-1_16

Fig. 1 Centrifugal impeller with S-blades

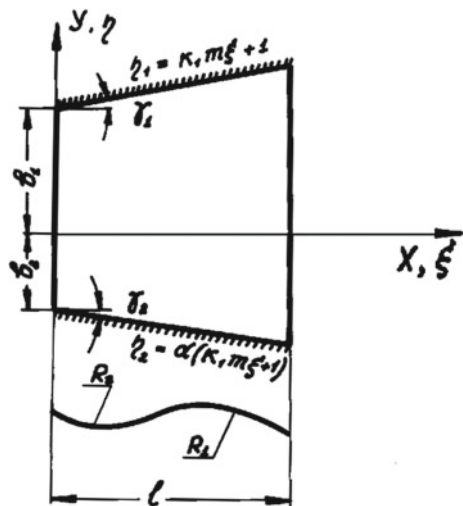


a continuous potential flow around the blade cascade, at the final section the velocity diagram changes, which in turn contributes to an increase in pressure. As a result, the impellers of such centrifugal compressors have advanced aerodynamic parameters.

2 Statement of the Problem and Its Solution

Let us consider the stress-strain state of S-shaped rotor blades of centrifugal compressors. Figure 2 shows the geometry and coordinate system of a trapezoid S-shaped

Fig. 2 Centrifugal impeller with S-blades



blade. The calculation of the blade can be made by dividing it into two interconnected cylindrical panels [4].

The problem reduces to the calculation of these panels for the load, conditioned by the centrifugal inertia forces of the panels' masses, taking into account the conditions of their mutual conjugation [5].

The stress state of the panel is described by linear equations of Vlasov–Donnell shallow shell theory [6, 7], which are written in the dimensionless coordinate system $\xi = x/l$ and $\eta = y/b_1$ as follows:

$$\left. \begin{aligned} \frac{\partial^2 \bar{u}}{\partial \xi^2} + \frac{1-\nu}{2} m^2 \frac{d^2 \bar{u}}{d\eta^2} + \frac{1+\nu}{2} m \frac{d^2 \bar{v}}{d\xi d\eta} + \frac{l}{R} \frac{\partial \bar{w}}{\partial \xi} &= -\frac{(1-\nu^2)l^2 p}{Eh^2}; \\ \frac{1+\nu}{2} m \frac{\partial^2 \bar{u}}{\partial \xi d\eta} + m^2 \frac{\partial^2 \bar{v}}{\partial \eta^2} + \frac{1-\nu}{2} \frac{\partial^2 \bar{v}}{\partial \xi^2} + \frac{\nu ml}{R} \frac{\partial \bar{w}}{\partial \eta} &= 0; \\ 12 \frac{l^3}{Rh^2} \frac{\partial \bar{u}}{\partial \xi} + 12 \frac{\nu ml^3}{Rh^2} \frac{\partial \bar{v}}{\partial \eta} + \nabla_m^4 \bar{w} + 12 \frac{l^4}{R^2 h^2} \bar{w} &= 12 \frac{(1-\nu^2)ql^4}{Eh^4}. \end{aligned} \right\} \quad (1)$$

Here $\bar{u} = u/h$; $\bar{v} = v/h$; $\bar{w} = w/h$ are dimensionless displacement functions; $m = l/b_1$ is geometric parameter of the blade; q and p are the normal and tangential components of the centrifugal load:

$$\begin{aligned} q &= (\gamma/g)\omega^2 h R_2 \cos \beta_2; \\ p &= (\gamma/g)\omega^2 h (R_2 \sin \beta_2 - \xi l), \end{aligned} \quad (2)$$

where β_2 is the angle of the stream exit.

The boundary conditions at the edges $\eta_1 = (k_1 m \xi + 1)$ and $\eta_2 = \alpha(k_1 m \xi + 1)$, adjacent to the disks, correspond to rigid fixing conditions:

$$\bar{w} = \frac{\partial \bar{w}}{\partial n} = \bar{u} = \bar{v} = 0 \quad (3)$$

Here $k_1 = tg\gamma_1$; $\alpha = -b_2/b_1$ are geometric parameters of the blade.

It should be noted that the boundary conditions (3) are somewhat idealized. In real life, due to the difference in radial movements of the main and covering discs, the edge of the blade adjacent to the covering disc is shifted at some value $\Delta(\xi, \eta)$. However, for the considered class of centrifugal compressors with medium-width blades, the formulation of the boundary conditions (3.35) is quite acceptable, the operational margin in this case is about 10% [8].

The boundary conditions for the leading ($\xi = 1$) and exit ($\xi = 0$) edges of the blade correspond to the conditions of the free edge (Fig. 2). In this case we have:

$$N_{11} = N_{12} = M_{11} = Q_1^0 = 0,$$

or in the displacement functions:

$$\left. \begin{aligned} \frac{\partial \bar{u}}{\partial \xi} + \nu m \frac{\partial \bar{v}}{\partial \eta} - \frac{\nu}{R} \bar{w} &= 0; \\ m \frac{\partial \bar{u}}{\partial \eta} + \frac{\partial \bar{v}}{\partial \xi} &= 0; \\ \frac{\partial^2 \bar{w}}{\partial \xi^2} + \nu m^2 \frac{\partial^2 \bar{w}}{\partial \eta^2} &= 0; \\ \frac{\partial^3 \bar{w}}{\partial \xi^3} + (2 - \nu) m^2 \frac{\partial^3 \bar{w}}{\partial \xi \partial \eta^2} &= 0. \end{aligned} \right\} \quad (4)$$

3 Conjugation (Matching) Conditions

We now proceed to the conditions for connecting cylindrical panels I and II [5, 9]. On the joint straight edge $\xi = \xi_0$ for panels I and II, the following equations should be valid (Figs. 3 and 4).

Fig. 3 On the development of conjugation (matching) conditions (power factors in the panels)

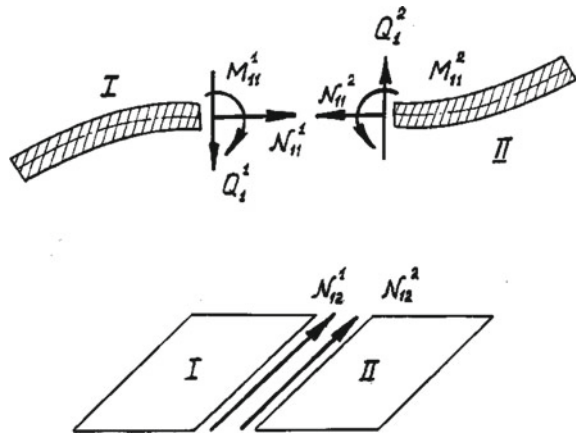
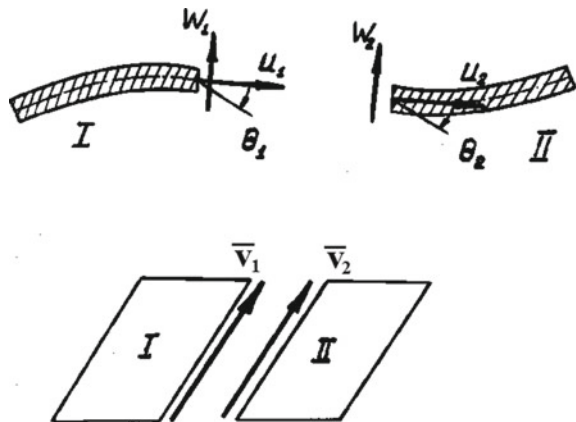


Fig. 4 On the development of conjugation (matching) conditions (displacement in the panels)



$$\left. \begin{aligned} N_{11}^1 &= N_{11}^2; \\ N_{12}^1 &= N_{12}^2; \\ Q_1^1 &= Q_1^2; \\ M_{11}^1 &= M_{11}^2. \end{aligned} \right\} \tag{5}$$

$$\left. \begin{aligned} \bar{u}^1 &= \bar{u}^2; \\ \bar{v}^1 &= \bar{v}^2; \\ \bar{w}^1 &= \bar{w}^2; \\ \frac{\partial(\bar{w}^1)}{\partial\xi} &= \frac{\partial(\bar{w}^2)}{\partial\xi}. \end{aligned} \right\} \tag{6}$$

Applying (5) and (6) into the elastic shell conjugation conditions instead of the forces and moments of their expression through displacements, and also assuming $R = -R_2$ for panel I and $R = R_1$ for panel II, we obtain the following group of conjugation conditions:

$$\left. \begin{aligned} \frac{\partial\bar{u}_1}{\partial\xi} + \nu m \frac{\partial\bar{v}_1}{\partial\eta} - \frac{\nu l}{R_2} \bar{w}_1 &= \frac{\partial\bar{u}_2}{\partial\xi} + \nu m \frac{\partial\bar{v}_2}{\partial\eta} + \frac{\nu l}{R_1} \bar{w}_2; \\ m \frac{\partial\bar{u}_1}{\partial\eta} + \frac{\partial\bar{v}_1}{\partial\xi} &= m \frac{\partial\bar{u}_2}{\partial\eta} + \frac{\partial\bar{v}_2}{\partial\xi}; \\ \frac{\partial^2\bar{w}_1}{\partial\xi^2} + \nu m^2 \frac{\partial^2\bar{w}_1}{\partial\eta^2} &= \frac{\partial^2\bar{w}_2}{\partial\xi^2} + \nu m^2 \frac{\partial^2\bar{w}_2}{\partial\eta^2}; \\ \frac{\partial^3\bar{w}_1}{\partial\xi^3} + (2 - \nu)m^2 \frac{\partial^3\bar{w}_1}{\partial\xi\partial\eta^2} &= \frac{\partial^3\bar{w}_2}{\partial\xi^3} + (2 - \nu)m^2 \frac{\partial^3\bar{w}_2}{\partial\xi\partial\eta^2}; \\ \bar{u}_1 = \bar{u}_2; \bar{v}_1 = \bar{v}_2; \bar{w}_1 &= \bar{w}_2; \frac{\partial\bar{w}_1}{\partial\xi} = \frac{\partial\bar{w}_2}{\partial\xi}. \end{aligned} \right\} \tag{7}$$

4 Solution of a Two-Dimensional Boundary Value Problem

For the solution of the boundary value problem for the system of elliptic Eq. (1), we apply the analytical approach based on a combination of the method of integral relations, developed by Dorodnitsyn [10, 11] and the modified method of successive approximations, developed by professor Pukhliy and published in the academic press [12, 13].

Subsequently, the method was extended to the solution of initial and initial-boundary value problems of mathematical physics [14, 15]. The problems of the method convergence were considered in [12, 15]. It should be noted that earlier this approach was used in the authors' work [16] for purposes of calculating the of working blades of diagonal turbomachines.

In accordance with the method of integral relations, the initial system of Eq. (1) will be presented in a divergent form:

$$\frac{\partial\bar{X}}{\partial\xi} + \frac{\partial\bar{Y}}{\partial\eta} + \bar{L} = 0, \tag{8}$$

where

$$\begin{aligned} \bar{X} &= \{X_i\} = \{\bar{u}, \bar{v}, \bar{w}, z_1, z_2, z_3, z_4, z_5\}; \\ \bar{Y} &= B_0\bar{X} + B_1 \frac{\partial \bar{X}}{\partial \eta} + B_2 \frac{\partial^2 \bar{X}}{\partial \eta^2} + B_3 \frac{\partial^3 \bar{X}}{\partial \eta^3}; \\ \bar{L} &= B\bar{X} + \bar{b}. \end{aligned}$$

Using functions z_1, z_2, \dots, z_5 , derivatives are denoted:

$$z_1 = \bar{u}_{,1}; \quad z_2 = \bar{v}_{,1}; \quad z_3 = \bar{w}_{,1}; \quad z_4 = \bar{w}_{,11}; \quad z_5 = \bar{w}_{,111}. \tag{9}$$

Upon that, the elements of the matrices $B_r = \{b_{mn}^S\}$ and $B = \{b_{mn}\}$, ($S = 0, 1, 2, 3$; $m, n = 1, 2, \dots, 8$) take the following values:

$$\begin{aligned} b_{28}^0 &= 12 \frac{ml^3}{Rh^2}; \quad b_{35}^0 = \frac{2ml}{(1-\nu)R}; \quad b_{15}^0 = \frac{1+\nu}{1-\nu}m; \\ b_{54}^0 &= \frac{1+\nu}{2}m; \quad b_{14}^1 = \frac{1-\nu}{2}m; \quad b_{25}^1 = \frac{2m^2}{1-\nu}; \\ b_{78}^1 &= 2m^2; \quad b_{38}^3 = m^4; \quad b_{38} = \frac{12l^4}{h^2R^2}; \\ b_{48} &= 12 \frac{\nu l^2}{Rh^2}; \quad b_{64} = \frac{\nu l}{R}; \quad b_{41} = b_{52} = b_{63} = b_{76} = b_{87} = -1. \end{aligned} \tag{10}$$

The remaining elements equal to zero. The components of the vector \bar{b} will be the following:

$$b_8 = -1; \quad b_1 = b_2 = b_3 = b_4 = b_5 = b_6 = b_7 = 0. \tag{11}$$

In accordance with the method of integral relations, the solution to system (8) is found as follows:

$$X_i(\xi, \eta) = \begin{cases} \sum_{j=1}^n X_{ij}(\xi) P_j(\xi, \eta) & (i = 3, 6, 7, 8); \\ \sum_{j=1}^n X_{ij}(\xi) P_{j,2}(\xi, \eta) & (i = 1, 2); \\ \sum_{j=1}^n X_{ij}(\xi) P_{j,22}(\xi, \eta) & (i = 4, 5). \end{cases} \tag{12}$$

where the Jacobi orthogonal polynomials [17, 18] were chosen as the system of approximating functions $P_j(\xi, \eta)$, constructed for the oblique edges of the blade.

$$\begin{aligned} P_j(\xi, \eta) &= P_1(\xi, \eta) \sum_{j=1}^n \left[\eta - \frac{(1 + \alpha)r}{2} \right]^{j-1}, \\ P_1(\xi, \eta) &= \eta^4 - 2(1 + \alpha)r\eta^3 + (1 + 4\alpha + \alpha^2)r^2\eta^2 - 2\alpha(1 + \alpha)r^3\eta + \alpha^2r^4, \\ r &= 1 + km\xi. \end{aligned} \tag{13}$$

Let us turn our attention to the properties of polynomials $P_j(\xi, \eta)$. Polynomials $P_j(\xi, \eta)$ on the interval $[r, \alpha r]$ fulfil the orthogonality conditions:

$$(P_i, P_k) = \int_r^{\alpha r} P_i P_k d\eta = 0 \text{ when } i \neq k. \tag{14}$$

They form a system of linearly independent functions and fulfil the boundary conditions (3). The constructed polynomials have another important property: their first and second derivatives are also orthogonal. To demonstrate it, let us consider the value

$$\cos(P_i, P_j) = \frac{(P_i, P_j)}{\|P_i\| \|P_j\|},$$

in this case, the polynomials P_i and P_j are considered as generalized vectors in a Hilbert space L_2 [18].

For specific values for polynomials (13) we obtain:

$$\cos(P_1, P_2) = 0; \quad \cos(P_{1,2}, P_{2,2}) = 0; \quad \cos(P_{1,22}, P_{2,22}) = 0,$$

which corresponds to angles of 90°.

5 Application of the Modified Method of Successive Approximations to the Integration of Systems of Ordinary Differential Equations

Applying the procedure of the method of integral relations to the initial system of partial differential Eq. (8), we obtain a system of ordinary differential equations of order $8n$ with variable coefficients, which can be presented in the normal Cauchy form:

$$\frac{dX_m}{d\xi} = \sum_{v=1}^{m*} A_{m,v} X_v + f_m \quad (m = 1, 2, \dots, m*) \tag{15}$$

Here $A_{m,v}$ is a variable coefficient;

Following that, a modified method of successive approximations, developed by Professor V. A. Pukhliy and published by him in the academic press [12–15], is applied to solve the system of Eq. (15). The method has been widely used to solve a number of practical problems, for example, for studying the SSS of working blades of diagonal turbomachines [16], as well as for studying the SSS of wing-shaped blades of centrifugal pumps [19].

Here, to accelerate the convergence of the solution, the method of telescopic shift of the Lanczos power series is used [20]. The idea of the method is that the Maclaurin series at our disposal is telescopically shifted to a much shorter series,

without losing accuracy. For this purpose, the possibility of representing any power series in terms of shifted Chebyshev polynomials on the interval [0, 1] is used.

In accordance with the method and in order to accelerate the convergence of the obtained solution, variable coefficients $A_{m,v}$ and free terms f_m are represented through the shifted Chebyshev polynomials $T_k^*(\xi)$:

$$A_{v,m} = \sum_{r=0}^q a_{v,m,r} d_r^{-1} \sum_{k=0}^r a_k T_k^*(\xi), \quad f_m = \sum_{r=0}^q f_{m,r} (d_r \cdot r!)^{-1} \sum_{k=0}^r a_k T_k^*(\xi). \quad (16)$$

Here q —is the degree of the interpolation polynomial; a_k —coefficients of expansion ξ^2 in a series of Chebyshev polynomials. In the expression (16) $d_r = 1$ for $r = 0$ and $d_r = 2^{2r-1}$ for the other r .

The general solution of the system of Eq. (15) can be written as:

$$X_m = \sum_{\mu=1}^s C_{\mu} \left[d_0^{-1} a_0 T_0^*(\xi) \delta + \sum_{n=1}^{\infty} X_{m,\mu,n} \right] + \sum_{j=0}^q t_{m,j,0} [d_{j+1} (j+1)!]^{-1} \sum_{k=0}^{j+1} a_k T_k^*(\xi) + \sum_{n=2}^{\infty} X_{m,n}, \quad (17)$$

where $t_{m,j,0} = f_{m,r}$ when $j = r$; μ —is the number of the fundamental function; C_{μ} —constants of integration.

In solution (17), $\delta = 1$ if $m = \mu$ and $\delta = 0$ for the other μ . The first approximation $X_{m,\mu,1}$ is obtained by substituting the zeroth-order approximation:

$$d_0^{-1} a_0 T_0^*(\xi) \delta \text{ to the right side of the homogeneous system } \frac{dX_m}{d\xi} = \sum_{v=1}^s B_{v,m} X_v.$$

Subsequent approximations are carried out according to recurrence formulas:

$$X_{m,\mu,n} = \sum_{j=1}^{\beta} t_{m,\mu,n,j} [d_{n+j-1} (n+j-1)!]^{-1} \sum_{k=0}^{n+j-1} a_k T_k^*(\xi);$$

$$X_{m,n} = \sum_{j=1}^{\beta} t_{m,n,j} [d_{n+j-1} (n+j-1)!]^{-1} \sum_{k=0}^{n+j-1} a_k T_k^*(\xi), \quad (18)$$

where $\beta = n(q+3) - 2$.

The systems of fundamental functions (18) are uniformly converging series. Therewith, coefficients $t_{m,\mu,n,j}$ and $t_{m,n,j}$ are determined through the coefficients of the previous approximation using recurrence formulas:

$$t_{m,\mu,n,j} = \sum_{v=1}^s \sum_{r=0}^q b_{v,m,r} t_{v,\mu,n-1,j-r} (n+j-1)^{-1} \prod_{\gamma=0}^r (n+j-1-\gamma),$$

$$t_{m,\mu,n,j} = \sum_{v=1}^s \sum_{r=0}^q b_{v,m,r} t_{v,\mu,n-1,j-r} (n+j-1)^{-1} \prod_{\gamma=0}^r (n+j-1-\gamma),$$

The constants C_μ , included in the general solution (17) are found from the conditions of the panels connection (7).

Further on, the system of Eq. (1) is solved for each panel of an S-shaped blade, under the boundary conditions (3) and (4) when the panels are interconnected (7).

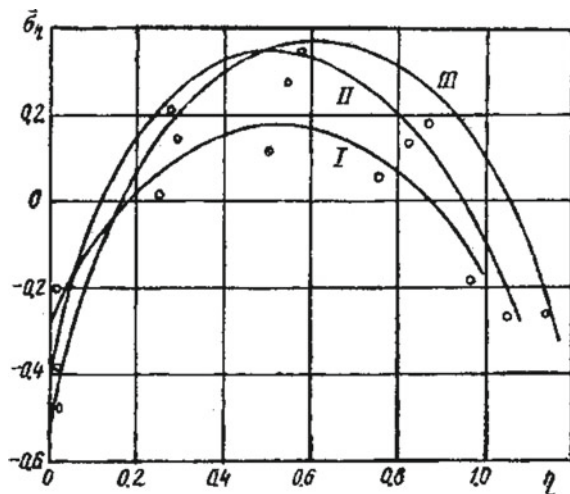
The dimensionless stress functions for each panel of the blade are determined by the following expressions:

$$\begin{aligned} \bar{\sigma}_\xi &= \frac{l}{h} \left[\frac{\partial \bar{u}}{\partial \xi} + v \left(m \frac{\partial \bar{v}}{\partial \eta} + \frac{l}{R} \bar{w} \right) \right] - \frac{1}{2} \left(\frac{\partial^2 \bar{w}}{\partial \xi^2} + v m^2 \frac{\partial^2 \bar{w}}{\partial \eta^2} \right); \\ \bar{\sigma}_\eta &= \frac{l}{h} \left[m \frac{\partial \bar{v}}{\partial \eta} + \frac{l}{R} \bar{w} + v \frac{\partial \bar{u}}{\partial \xi} \right] - \frac{1}{2} \left(m^2 \frac{\partial^2 \bar{w}}{\partial \eta^2} + v \frac{\partial^2 \bar{w}}{\partial \xi^2} \right); \\ \bar{\sigma}_{\xi\eta} &= \frac{1}{2} \frac{l}{h} \left(m \frac{\partial \bar{u}}{\partial \eta} + \frac{\partial \bar{v}}{\partial \xi} \right) + \frac{(1+v)m}{2} \frac{\partial^2 \bar{w}}{\partial \xi \partial \eta}. \end{aligned}$$

Calculation example. In accordance with the above algorithm, a software program for numerical implementation of the suggested analytical solution, was developed.

The initial data for the calculation: for the wheel: $R_k = 40$ cm, the number of blades $z = 8$, $n = 25 \text{ s}^{-1}$ (1500 rpm); for the blade $l = 30$ sm, $m = 1$, $\alpha = 0$, $\gamma^{-1} = 10^\circ$, with $R_1 = R_2 = 44$ sm, $h = 0.3$ sm, the material used for the blade—is Steel-20. Figure 5 shows the distribution diagrams of dimensionless stresses $\bar{\sigma}_\eta$ in the key sections of the blade (solid lines).

Fig. 5 Distribution diagrams of the dimensionless stresses $\bar{\sigma}_\eta$ in the key sections of the S-shaped blade: I—the exit edge of the blade; II—the middle part of the blade; III—the leading edge of the blade; o—the results of strain measurement of the blade



The results of strain measurement (circles) are also presented here; therewith, the divergence between the calculation results and the strain measurement data does not exceed 15%.

6 Conclusions

1. Professor K.R.Seleznev at the Department of Compressor Engineering of the Leningrad Polytechnic Institute, according to the results of aerodynamic tests of impellers of centrifugal compressors, received significantly better aerodynamic parameters for impellers with S-shaped blades.
2. An analytical approach to calculating the stress-strain state of S-shaped blades based on the theory of conjugated cylindrical shells is presented.
3. The original boundary-value problem described by systems of partial differential equations, by the method of integral relations Dorodnitsyn is reduced to systems of ordinary differential equations, in the general case with variable coefficients.
4. To solve the resulting system of differential equations, the modified method of successive approximations developed by Professor V.A. Pukhliy and presented by him in the academic press is subsequently applied.

Acknowledgements The authors thank Alexander Evgrafov, professor at the St. Petersburg Polytechnic University, for valuable comments on the article.

References

1. Seleznev KP et al (1969) On the shape of blade channels of stationary compressors. *Power Eng* 5:23–27
2. Galerkin YuB, Seleznev KP et al (1973) Experience in designing centrifugal compressor wheels for a given speed distribution. *Chem Petrol Eng* 4:8–12
3. Pukhliy VO (2002) The mill fan. Patent of Ukraine No. 43966A, Ukrpatent, Kyiv, Bull.№. 1
4. Novozhilov VV (1962) Theory of thin shells. 2nd edn. Rev. and add. Shipbuilding, p 431
5. Pukhliy VA (1989) On the calculation of conjugated shells of variable stiffness. *Appl Mech* 25(11):31–37
6. Vlasov VZ (1949) General theory of shells and its applications in technology. In: Gostekhizdat ML, p 784
7. Donnel LH (1933) Stability of thin walled tubes under torsion, NACA Report No. 479, p 24
8. Pukhliy VA (1975) Some issues of aerodynamics, durability and thermoelasticity of impellers of radial turbomachines. In: Osaka M (ed) Materials of the 3rd Soviet-Japanese symposium: Air conditioning, Central research institute of industrial publications publishing house, 1976, p 31–39
9. Pukhliy VA, Shalashilin VI (1989) On a problem for conjugate shells of revolution of variable stiffness. In: Proceedings of the USSR Academy of Sciences. *Solid Mechanics*, vol 4, p 146–152
10. Dorodnitsyn AA (1958) On a method of numerical solution of some nonlinear problems of aerohydrodynamics. In: The book: Proceedings of the 3rd All-Union Mathematical Congress, Publishing House of the Academy of Sciences of the USSR, vol III, pp 447–543

11. Dorodnitsyn AA (1960) On a method for solving the equations of a laminar boundary layer. *J Tech Phys* 3:111–118
12. Pukhliy VA (1978) A method for the analytical solution of two-dimensional boundary value problems for systems of elliptic equations. *J Comput Math Math Phys* 18(5):1275–1282
13. Pukhliy VA (1979) On an approach to solving boundary value problems of mathematical physics. *Differ Equ* 15(11):2039–2043
14. Pukhliy VA (2017) The solution of initial-boundary value problems of mathematical physics by the modified method of successive approximations. *Rev Appl Indus Math* 24(1):37–48
15. Pukhliy VA (2016) On the acceleration of convergence in the modified method of successive approximations. *Rev of Appl Indus Math* 23(4):381–383
16. Pukhliy VA, Zhuravlev AA (2016) Statics of working blades of diagonal turbomachines. In: *Proceedings of the 5th ISTC “modern engineering: science and education”*, Publishing House S.-P. Polytechnic University, St. Petersburg, p 521–529
17. Luke YL (1975) *Mathematical functions and their approximation*, Academic Press Inc., New York, p 608
18. Courant R, Hilbert D (1953) *Methods of mathematical physics*. In: Gostekhizdat M (ed) vol 1
19. Pukhliy VA, Miroshnichenko ST, Zhuravlev AA, Pomeranskaya AK (2019) Durability of wing-shaped rotor blades of centrifugal pumps. In: *Theory of Mechanisms and Machines (TMM)*, vol 17(1), pp 14–27
20. Lantsosh K (1961) Practical methods of applied analysis. In: *Fizmatgiz M (ed)*, p 524

Determination of Dynamic Errors in Machines with Elastic Links



Yuri A. Semenov and Nadezhda S. Semenova

Abstract One of the important objectives in the design of machines is the reduction of dynamic errors caused by elastic vibrations of actuating mechanisms in a steady state and transient conditions. This objective is especially relevant in the production of high-performance machines, such as industrial robots, positioning stages, and others. The open kinematic structure of actuating mechanisms results in a significantly lower stiffness of the structure and greater dynamic loads, which in turn leads to intensive vibrations of operating elements in transient conditions. Furthermore, dynamic errors caused by free vibrations several times exceed static positioning errors of actuating mechanisms. Therefore, conventional methods of reducing dynamic errors with the use of flywheels, counterbalance mechanisms, shock absorber, dynamic dampers and other passive means do not always prove to be efficient. Instead feedback control systems have broader functional capabilities.

Keywords Chain system with the fixed end · Dynamic errors · Frequency equation · Fundamental mode

1 Introduction

In modern machines, gears remain the primary way of transmitting power. This is due to their small size, well-developed manufacturing technology, the ability to accurately provide the required gear ratio. However, it is known that gears are a source of internal vibration activity of the machine unit. The measure of this vibroactivity is the perturbing moments caused by the rigidity of the gearing, the kinematic error of the gear, and leading to dynamic errors. Under dynamic error understand deviations of laws of movement of links from their program values. The vibrations caused by them can lead to both the opening of the mating profiles of the teeth, and to the shifting of the lateral gaps between the teeth of the wheels. Dynamic loads arising in the drive, can thus be several times higher than the load from the moment of the

Y. A. Semenov (✉) · N. S. Semenova (✉)
Peter the Great Saint-Petersburg Polytechnic University, St. Petersburg, Russia

© Springer Nature Switzerland AG 2020
A. N. Evgrafov (ed.), *Advances in Mechanical Engineering*,
Lecture Notes in Mechanical Engineering,
https://doi.org/10.1007/978-3-030-39500-1_17

resistance forces applied to the working body of the machine and determined from the strength calculation of the transmission.

2 The Building of a Machine Aggregate Simulation Model

Earlier machine aggregate simulations incorporated a model of a mechanism with rigid links [1]. However, in practice, structural elements of links and kinematic joints transform under the action of static and dynamic loads emerging in a steady state and in motion. As a result, laws of motion for a machine's operating elements differ from laws of motions imposed exclusively by engines. Therefore, one of the primary objectives of machine dynamics is identification of static and dynamic errors caused by the transformation of links and kinematic joints.

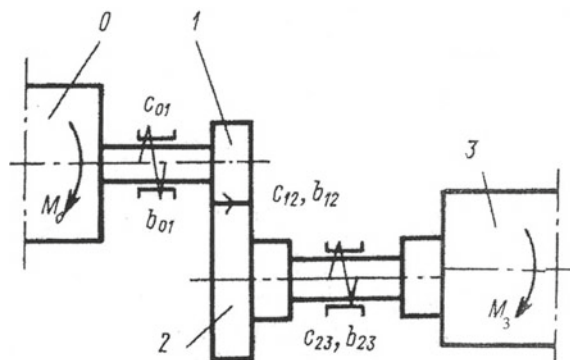
First, amplitudes of dynamic errors of a machine aggregate resulting from the flexibility of its bearings should be estimated [2–7]. Figure 1 shows a dynamic model of a machine aggregate. Gears 1 and 2 of a single-stage gear reducer and the actuating element 3 are set into rotation by the engine rotor 0. The figure depicts elements that are considered elastic; c_{01} , c_{12} , c_{23} are their stiffness; b_{01} , b_{12} , b_{23} are the damping coefficients; J_0 , J_1 , J_2 , J_3 are the moments of inertia of the masses relative to their axes of rotation; M_0 and M_c are the driving torque and the drag torque respectively. The bending flexibility of shafts and the flexibility of the bearings shall be neglected.

The system under consideration has four degrees of freedom. Absolute rotation angles of the engine rotor q_0 , gears $q_1 - q_2$ and the actuating element q_3 can be chosen as generalized coordinates. It should be more convenient to align these coordinates to the axis of the engine rotor, thus introducing new generalized coordinates:

$$\varphi_0 = q_0; \varphi_1 = q_1; \varphi_2 = i_{12}q_2; \varphi_3 = i_{12}q_3, \quad (1)$$

where i_{12} is a transmission ratio of the gearing. Deformations of shafts and gears connected to driving wheels can be defined as:

Fig. 1 A dynamic model of a machine aggregate



$$\theta_{01} = \varphi_1 - \varphi_0; \theta_{12} = r_{b2}q_2 - r_{b1}q_1 = r_{b1}(\varphi_2 - \varphi_1); \theta_{23} = i_{12}^{-1}(\varphi_3 - \varphi_2), \quad (2)$$

where r_{b1}, r_{b2} are radii of the base circles.

Next, kinetic and potential energies and the dissipative functions should be determined to generate Lagrangian equations of the second order.

The kinetic energy of the system is defined as:

$$T = \frac{1}{2} \sum_{s=0}^3 J_s \dot{q}_s^2 = \frac{1}{2} \sum_{s=0}^3 J_s \left(\frac{\dot{\varphi}_s}{i_{0,s}} \right)^2 = \frac{1}{2} \sum_{s=0}^3 J_{s*} \dot{\varphi}_s^2 \quad (3)$$

where

$$J_{0*} = J_0; J_{1*} = J_1; J_{2*} = i_{12}^{-2} J_2; J_{3*} = i_{12}^{-2} J_3 \quad (4)$$

are the moments of inertia of links of the transmission device added to the rotation axis of the engine rotor.

The potential energy of the system is defined as:

$$\Pi = \frac{1}{2} \sum_{s=1}^3 c_{s-1,s} \theta_{s-1,s}^2 = \frac{1}{2} \sum_{s=1}^3 c_{s*} (\varphi_s - \varphi_{s-1})^2 \quad (5)$$

where

$$c_{1*} = c_{01}; c_{2*} = r_{b1}^2 c_{12}; c_{3*} = i_{12}^{-2} c_{23}. \quad (6)$$

The dissipative functions of system are defined as:

$$\Phi = \frac{1}{2} \sum_{s=1}^3 b_{s-1,s} \dot{\theta}_{s-1,s}^2 = \frac{1}{2} \sum_{s=1}^3 b_{s*} (\dot{\varphi}_s - \dot{\varphi}_{s-1})^2, \quad (7)$$

where

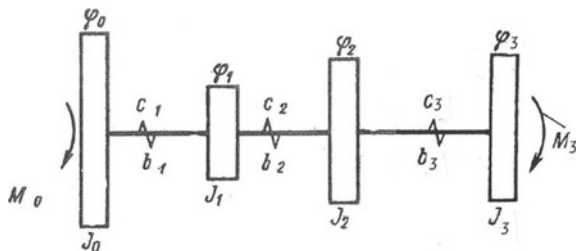
$$b_{1*} = b_{01}; b_{2*} = r_{b1}^2 b_{12}; b_{3*} = i_{12}^{-2} b_{23}. \quad (8)$$

External forces in a mechanical system are the driving torque M_0 , applied to the engine rotor, and the drag torque M_c , applied to the actuating element. The elementary work of external forces in the virtual deformation of the system should be expressed as:

$$\delta W = M_0 \delta q_0 + M_c \delta q_3. \quad (9)$$

The generalized drag force for the generalized coordinate φ_3 can be derived as: $M_3 = i_{12}^{-1} M_c$.

Fig. 2 The reduced model of a free chain system



By applying the following Lagrange equations:

$$\frac{d}{dt} \left(\frac{\partial T}{\partial \dot{\varphi}_s} \right) - \frac{\partial T}{\partial \varphi_s} = - \frac{\partial \Pi}{\partial \varphi_s} - \frac{\partial \Phi}{\partial \varphi_s} + M_s, \tag{10}$$

it is apparent that ($s = 0, 1, 2, \dots, 3$):

$$J_s \ddot{\varphi}_s + b_s (\dot{\varphi}_s - \dot{\varphi}_{s-1}) - b_{s+1} (\dot{\varphi}_{s+1} - \dot{\varphi}_s) + c_s (\varphi_s - \varphi_{s-1}) - c_{s+1} (\varphi_{s+1} - \varphi_s) = M_s. \tag{11}$$

An asterisk is omitted in the system parameters for clarity and $c_0 = b_0 = c_4 = b_4 = 0$, are applied.

The derived differential Eq. (11) describe motions in a transmission device as belonging to a system of perfectly rigid bodies interconnected in series by instantaneous elastic and dissipative elements. As each rigid body has one degree of freedom, such a one-dimensional model can be considered as a chain system. Figure 2 shows a four-mass oscillating system compatible with the differential Eq. (11).

It is possible to produce a set of equations for obtaining $\varphi_0 - \varphi_3$ and the driving torque when combining these equations with an engine performance equation M_0 .

The equations of motion in a mechanical system can also be written in another way if the law of motion for the engine rotor is known. In this case, an equation can be easily derived from the equations of motion (11), where $s = 0$:

$$J_0 \ddot{\varphi}_0 - b_1 (\dot{\varphi}_1 - \dot{\varphi}_0) - c_1 (\varphi_1 - \varphi_0) = M_0$$

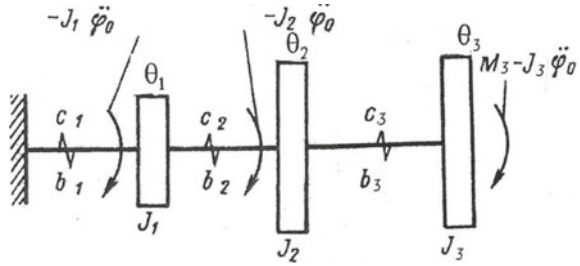
Next, deformation coordinates should be considered that define the shifting of masses relative to the engine rotor:

$$\theta_s = \varphi_s - \varphi_0(t). \tag{12}$$

Finally, the equations of the system motion can be written as:

$$\left. \begin{aligned} J_s \ddot{\theta}_s + b_s (\theta_s - \dot{\theta}_{s-1}) - b_{s+1} (\dot{\theta}_{s+1} - \dot{\theta}_s) + c_s (\theta_s - \theta_{s-1}) \\ - c_{s+1} (\theta_{s+1} - \theta_s) = M_s - J_s \ddot{\varphi}_0(t), \quad s = 1, 2, 3, \\ J_0 \ddot{\varphi}_0 - b_1 \dot{\theta}_1 - c_1 \theta_1 = M_0. \end{aligned} \right\} \tag{13}$$

Fig. 3 The reduced model of a chain system with the fixed end



where $\theta_0 = \dot{\theta}_0 = 0$, $c_4 = b_4 = 0$, $M_1 = M_2 = 0$. are taken into account.

Figure 3 demonstrates a chain oscillating system. Its equations of forced oscillations caused by the applied active inertia forces and the forces of moving space $-J_s \ddot{\varphi}_0(t)$ coincide with Eq. (13). The system depicted in Fig. 2 will be further called a free system, while the system in Fig. 3 will be called a system with the fixed left end [8–25].

3 Determination of Dynamic Errors in Transient Conditions

First, the equations of motion (13) should be presented in a matrix:

$$\begin{aligned} J\ddot{\theta} + B\dot{\theta} + C\theta &= M - J\ddot{\varphi}_0 \cdot 1, \\ J_0\ddot{\varphi}_0 - b_1\dot{\theta}_1 - c_1\theta_1 &= M_0, \end{aligned} \tag{14}$$

where $\theta = (\theta_1, \theta_2, \theta_3)^T$ is a three-dimensional column matrix, the generalized force matrix is $M = (0, 0, M_3)^T$, $1 = (1, \dots, 1)^T$ is a single column, and three-dimensional symmetric matrices of dissipative and elastic system parameters are:

$$\begin{aligned} J &= \begin{pmatrix} J_1 & 0 & 0 \\ 0 & J_2 & 0 \\ 0 & 0 & J_3 \end{pmatrix}; \quad B = \begin{pmatrix} b_1 + b_2 & -b_2 & 0 \\ -b_2 & b_2 + b_3 & -b_3 \\ 0 & -b_3 & b_3 \end{pmatrix}; \\ C &= \begin{pmatrix} c_1 + c_2 & -c_2 & 0 \\ -c_2 & c_2 + c_3 & -c_3 \\ 0 & -c_3 & c_3 \end{pmatrix}. \end{aligned}$$

Next, based on the generalized coordinates of a mechanical system, principal coordinates can be calculated with the help of a linear conversion:

$$\theta = \sum_{m=1}^3 h_m z_m. \quad (15)$$

As columns h_m , which are fundamental modes, are linearly independent, Eq. (15) establishes one-to-one correspondence between generalized coordinates θ_m and principal coordinates z_m .

By introducing (15) into the first matrix system Eq. (14), the following equation can be generated:

$$J \sum_{m=1}^3 h_m \ddot{z}_m + B \sum_{m=1}^3 h_m \dot{z}_m + C \sum_{m=1}^3 h_m z_m = M - J \ddot{\varphi}_0 \cdot 1.$$

Next, the equation should be consecutively multiplied by fundamental modes h_s :

$$\sum_{m=1}^3 (J h_m)^T h_s \ddot{z}_m + \sum_{m=1}^3 (B h_m)^T h_s \dot{z}_m + \sum_{m=1}^3 (C h_m)^T h_s z_m = M^T h_s - (J \cdot 1) h_s \ddot{\varphi}_0. \quad (16)$$

Taking into consideration the mode orthogonality:

$$(J h_m)^T h_s = 0; \quad (C h_m)^T h_s = 0 \quad \text{if } s \neq m,$$

Eq. (16) can be written as follows:

$$\alpha_m \ddot{z}_m + \sum_{m=1}^3 \beta_{ms} \dot{z}_s + \gamma_m z_m = Z_m - g_m \ddot{\varphi}_0 \quad (m = 1, 2, 3), \quad (17)$$

where

$$Z_m = M^T h_m, \quad g_m = (J \cdot 1)^T h_m = \sum_{r=1}^3 J_r h_{mr}, \quad \beta_{ms} = (B h_m)^T h_s.$$

The coefficient $\alpha_m = (J h_m)^T h_m$ is called a modal moment of inertia (from the English word *mode*), and a scalar $\gamma_m = (C h_m)^T h_m$ is called modal stiffness, or stiffness adduced to the mode m .

A complete separation of variables in Eq. (17) may occur if the damping coefficients are zero or proportional to the respective stiffness ($b_m = \lambda c_m$), or masses. In this case, Eq. (17) can be defined as follows:

$$\alpha_m \ddot{z}_m + \beta_m \dot{z}_m + \gamma_m z_m = Z_m - g_m \ddot{\varphi}_0 \quad (m = 1, 2, 3). \quad (18)$$

Next, Eq. (18) should be presented in an operator form ($d()/dt \rightarrow p()$):

$$(\alpha_m p^2 + \beta_m p + \gamma_m)z_m = Z_m - g_m \ddot{\varphi}_0 \quad (m = 1, 2, 3). \quad (19)$$

Thus,

$$z_m = (\alpha_m p^2 + \beta_m p + \gamma_m)^{-1} Z_m - (\alpha_m p^2 + \beta_m p + \gamma_m)^{-1} g_m \ddot{\varphi}_0. \quad (20)$$

Now, based on the principal coordinates, initial coordinates can be computed. For $s = 1, 2, 3$, they are the following:

$$\begin{aligned} \theta_s &= \sum_{m=1}^3 h_{ms} z_m = \sum_{m=1}^3 h_{ms} (\alpha_m p^2 + \beta_m p + \gamma_m)^{-1} Z_m \\ &- \sum_{m=1}^3 h_{ms} (\alpha_m p^2 + \beta_m p + \gamma_m)^{-1} g_m \ddot{\varphi}_0 = \sum_{r=1}^3 e_{sr}(p) M_r - \sigma_s(p) \ddot{\varphi}_0, \end{aligned} \quad (21)$$

where the operator of dynamic compliance linking the external moment with a deformation error is:

$$e_{sr}(p) = \sum_{m=1}^3 \frac{h_{ms} h_{mr}}{\alpha_m p^2 + \beta_m p + \gamma_m}, \quad (22)$$

and the transfer function linking the kinematic force with a deformation error is:

$$\sigma_s(p) = \sum_{m=1}^3 \frac{h_{ms} g_m}{\alpha_m p^2 + \beta_m p + \gamma_m}. \quad (23)$$

Assuming the engine rotor rotates steadily ($\dot{\varphi}_0 = \text{const}$), the drag torque $M_3 = -M_{30} + M_{31} \sin \nu t$ is applied to the latest mass of a chain system and the positional damping coefficient is $b_s = \psi c_s / 2\pi \nu$ ($\psi = 0.2 - 0.6$ —is the absorption coefficient), a deformation error in a fixed end system in accordance with (21–22) $\ddot{\varphi}_0 = \text{const}$ may be defined as follows ($s = 1, 2, 3$):

$$\begin{aligned} \theta_s &= \Delta_s + \tilde{\theta}_s = -M_{30} |e_{s3}(j0)| + M_{31} |e_{s3}(j\nu)| \sin[\nu t + \arg e_{s3}(j\nu)] \\ &= -M_{30} \sum_{m=1}^3 \frac{h_{ms} h_{m3}}{\gamma_m} + M_{31} \sum_{m=1}^3 \frac{h_{ms} h_{m3}}{\gamma_m \sqrt{\left[1 - \left(\frac{\nu}{k_m}\right)^2\right]^2 + \left(\frac{\psi}{2\pi}\right)^2}} \sin(\nu t + \xi_m). \end{aligned} \quad (24)$$

The equation includes $\text{tg} \xi_m = \frac{\psi/2\pi}{(\nu/k_m)^2 - 1}$, $\gamma_m = k_m^2 \alpha_m$.

Next, deviations in the laws of motion $\varphi_s(t)$ from the program ones should be determined through identification of dynamic errors in the machine aggregate

depicted in Fig. 1 under the following system parameters (see Fig. 3): $c_1 = 8 \times 10^5 \text{ N} \cdot \text{m}$; $c_2 = 1.44 \times 10^6 \text{ N} \cdot \text{m}$; $c_3 = 1.2 \times 10^6 \text{ N} \cdot \text{m}$; $J_0 = 0.6 \text{ kg} \cdot \text{m}^2$; $J_1 = 2.9 \times 10^{-3} \text{ kg} \cdot \text{m}^2$; $J_2 = 1.5 \times 10^{-2} \text{ kg} \cdot \text{m}^2$; $J_3 = 2.7 \text{ kg} \cdot \text{m}^2$; $M_{30} = 10 \text{ N} \cdot \text{m}$; $M_{31} = 50 \text{ N} \cdot \text{m}$.

The frequency equation can be generated:

$$\begin{vmatrix} c_1 + c_2 - J_1 k^2 & -c_2 & 0 \\ -c_2 & c_2 + c_3 - J_2 k^2 & -c_3 \\ 0 & -c_3 & c_3 - J_3 k^2 \end{vmatrix} \\ = 0.00011745k^6 - 111443k^4 + 1.041333 \times 10^{13}k^2 \\ - 1.3834 \times 10^{18} = 0,$$

that can be used to calculate fundamental frequencies: $k_1 = 364 \text{ s}^{-1}$; $k_2 = 10243 \text{ s}^{-1}$; $k_3 = 29048 \text{ s}^{-1}$ and fundamental modes:

$$h_1 = (1, 1, 1)^T; \quad h_2 = (1.5553, 1.3442, -0.1437)^T; \\ h_3 = (2.219, -0.0057, 0.00007)^T.$$

Modal stiffness:

$$\gamma_1 = (Ch_1)^T h_1 = 8 \times 10^5 \text{ N} \cdot \text{m}; \quad \gamma_2 = (Ch_2)^T h_2 = 4.656289 \times 10^6 \text{ N} \cdot \text{m}; \\ \gamma_3 = (Ch_3)^T h_3 = 1.106678 \times 10^6 \text{ N} \cdot \text{m}.$$

Static errors in principal coordinates $z_{m0} = -M_{30}h_{m3}/\gamma_m$, in particular $z_{10} = -0.27 \times 10^{-4}$, $z_{20} = 0.12 \times 10^{-7}$, $z_{30} = -0.68 \times 10^{-10}$, and dynamic errors in principal coordinates ($m = 1, 2, 3$):

$$\tilde{z}_1 = \frac{M_{31}h_{13}}{\gamma_1 \sqrt{\left[1 - \left(\frac{\nu}{k_1}\right)^2\right]^2 + \left(\frac{\psi}{2\pi}\right)^2}} \sin(\nu t + \xi_1) = 0.137 \times 10^{-2} \sin(350t - 0.681), \\ \tilde{z}_2 = \frac{M_{31}h_{23}}{\gamma_2 \sqrt{\left[1 - \left(\frac{\nu}{k_2}\right)^2\right]^2 + \left(\frac{\psi}{2\pi}\right)^2}} \sin(\nu t + \xi_2) = 0.613 \times 10^{-7} \sin(350t - 0.063), \\ \tilde{z}_3 = \frac{M_{31}h_{33}}{\gamma_3 \sqrt{\left[1 - \left(\frac{\nu}{k_3}\right)^2\right]^2 + \left(\frac{\psi}{2\pi}\right)^2}} \sin(\nu t + \xi_3) = 0.342 \times 10^{-10} \sin(350t - 0.063).$$

Thus, the static and dynamic errors are:

$$\begin{aligned} \theta_{10} &= h_{11}z_{10} + h_{21}z_{20} + h_{31}z_{30}, & \tilde{\theta}_1 &= h_{11}\tilde{z}_1 + h_{21}\tilde{z}_2 + h_{31}\tilde{z}_3, \\ \theta_{20} &= h_{12}z_{10} + h_{22}z_{20} + h_{32}z_{30}, & \tilde{\theta}_2 &= h_{12}\tilde{z}_1 + h_{22}\tilde{z}_2 + h_{32}\tilde{z}_3, \\ \theta_{30} &= h_{13}z_{10} + h_{23}z_{20} + h_{33}z_{30}. & \tilde{\theta}_3 &= h_{13}\tilde{z}_1 + h_{23}\tilde{z}_2 + h_{33}\tilde{z}_3. \end{aligned}$$

4 Determination of Dynamic Errors in Transient Conditions

Determination of deformation errors in transient processes is of great significance for the dynamic analysis of machines with program management (various machines, robot manipulators, multi-moving platforms and others), transient processes of which take a considerable amount of the operation time.

External moments in transient processes are assumed to be zero for clarity. It should not be complicated to consider these moments in the calculation as the equations of motion are presented in a linear set.

Eq. (21) at $M_r = 0$ ($r = 1, 2, 3$) can generate the following ($s = 1, 2, 3$):

$$\theta_s = -\sigma_s(p)\ddot{\varphi}_0 = -\sum_{m=1}^n \frac{g_m h_{ms}}{\alpha_m p^2 + \beta_m p + \gamma_m} \ddot{\varphi}_0 = -\sum_{m=1}^n \frac{\rho_s^{(m)}}{\tau_m^2 p^2 + 2\zeta_m \tau_m p + 1} \ddot{\varphi}_0, \tag{25}$$

where

$$g_m = (J \cdot 1)^T h_m = \sum_{r=1}^3 J_r h_{mr}; \quad \rho_s^{(m)} = g_m h_{ms} / \gamma_m.$$

The Duhamel integral should be applied to determine dynamic errors:

$$\theta_s(t) = -\sum_{m=1}^n \frac{\rho_s^{(m)} k_m}{\sqrt{1 - \xi_m^2}} \int_0^t e^{-\xi_m k_m(t-\xi)} \sin\left[\sqrt{1 - \xi_m^2} k_m(t - \xi)\right] \varepsilon(\xi) d\xi \quad (s = 1, 2, 3). \tag{26}$$

It is evident that $\theta_s(t)$ represents free vibrations emerging in a system as a result of disturbances caused by accelerated motion. These vibrations, which continue after the positioning, are considered highly undesirable as they lead to oscillations in a machine's operating elements hindering proper operating processes.

In Eq. (26) the first summand is of the most significance. This is due to two reasons. First, the coefficients $\rho_s^{(m)}$ decline rapidly with a higher m . Second, the duration of a transient process usually exceeds by several times the longest free vibrations period of the system, that is T_1 . The most significant summand in Eq. (26) is the first one

($m = 1$), that corresponds to damped vibrations in the first mode:

$$\theta_s(t) \approx -\frac{\rho_s^{(1)} k_1}{\sqrt{1 - \xi_1^2}} \int_0^t e^{-\xi_1 k_1 (t - \xi)} \sin[\sqrt{1 - \xi_1^2} k_1 (t - \xi)] \varepsilon(\xi) d\xi \quad (s = 1, 2, \dots, 3). \quad (27)$$

A dynamic error of a gear $\theta_2(t)$ in a constant run-up and braking in a three-mass system with the fixed end (see Fig. 3) can be determined with the Duhamel integral:

$$\varepsilon(t) = \varepsilon_0 \eta(t) - 2\varepsilon_0 \eta(t - t_p) + \varepsilon_0 \eta(t - t_T),$$

where $\varepsilon_0 = 10 \text{ s}^{-2}$ is the acceleration amplitude, $\eta(t)$ is the unit-step function, $t_p = 3 \text{ s}$ is the run-up time, $t_T = 2t_p$ is the braking time. In the system under consideration

$$\begin{aligned} g_1 &= J_1 h_{11} + J_2 h_{12} + J_3 h_{13} = 6.017 \text{ kg m}^2; \\ g_2 &= J_1 h_{21} + J_2 h_{22} + J_3 h_{23} = 0.0076 \text{ kg m}^2; \\ g_3 &= J_1 h_{31} + J_2 h_{32} + J_3 h_{33} = 0.948 \times 10^{-6} \text{ kg m}^2; \\ \rho_2^{(1)} &= \frac{g_1 h_{12}}{\gamma_1} = 0.169 \times 10^{-4} \text{ s}^2; \\ \rho_2^{(2)} &= \frac{g_1 h_{22}}{\gamma_2} = 0.229 \times 10^{-8} \text{ s}^2; \\ \rho_3^{(2)} &= \frac{g_3 h_{32}}{\gamma_3} = -0.126 \times 10^{-10} \text{ s}^2, n_1 = 1. \end{aligned}$$

Thus, the dynamic error in the transient process is:

$$\theta_2(t) \approx -\rho_1^{(2)} k_1 I_1(t),$$

where

$$I_1(t) = \begin{cases} \varepsilon_0 k_1^{-1} (e^{-n_1 t} \cos k_1 t - 1) & 0 \leq t \leq t_p, \\ \varepsilon_0 k_1^{-1} [1 + e^{-n_1 t} \cos k_1 t - 2e^{-n_1(t-t_p)} \cos k_1(t-t_p)] & t_p \leq t \leq t_T, \\ \varepsilon_0 k_1^{-1} [e^{-n_1 t} \cos k_1 t - 2e^{-n_1(t-t_p)} \cos k_1(t-t_p) + e^{-n_1(t-t_T)} \cos k_1(t-t_T)] & t \geq t_T. \end{cases}$$

Equation (27) demonstrates that amplitudes of dynamic errors with a predetermined terminal angular velocity (in the case of run-up and braking) or with a predetermined rotation angle (in the case of positioning) are inversely proportional to the time of the transient process and the square of the first fundamental frequency. Therefore, the reduction of errors in transient processes can be achieved through decreased

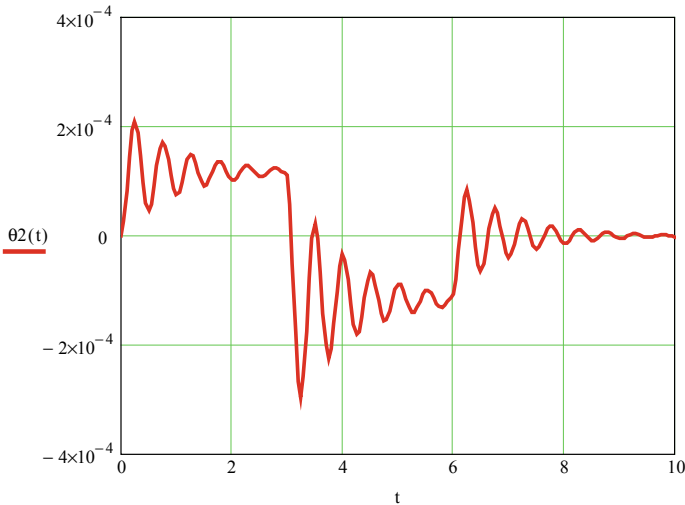


Fig. 4 The graph of the dynamic error that occurs in the machine during the run-up

masses or a greater stiffness of a transmission device and a longer transient process. Figure 4 shows the dependency graph $\theta_2(t)$.

In practice, implementation of these recommendations is limited. A greater stiffness of a transmission device is usually accompanied by greater reciprocating masses, thus failing to significantly increase the first fundamental frequency. A longer transient process results in a decreased machine performance, which is undesirable. In conclusion, it can be stated that the reduction of dynamic errors in contemporary machines is a complicated technical task.

References

1. Semenov YA, Semenova NS (2015) Theory of mechanisms and machines in examples and problems. Part I. Publishing house Polytechnic, University, SPb 284 p (rus)
2. Wulfson II (2013) Dynamics of cyclic machines. Polytechnic, SPb, 425 p (rus)
3. Wulfson II (2015) Dynamics of cyclic machines. Series: foundations of engineering mechanics. Springer, 390 p
4. Weitz VL (1969) Dynamics of machine units. Mechanical Engineering, 370 p (rus)
5. Wolfson II, Kolovsky MZ, Semenov Yu A, Slouch AV, others, Smirnov GA (1996) Machine mechanics. Higher School, 511 p (rus)
6. Semenov YA (2008) Mechanics. The theory of mechanical vibrations. Publishing house Polytechnic University, SPb, 412 p (rus)
7. Kolovsky MZ, Evgrafov AN, Semenov YA, Slouch AV (2000) Advanced theory of mechanisms and machines. Springer, Berlin, 394 p
8. Wicker JJ, Pennock GR, Shigley JE (2010) Theory of machines and mechanisms. Oxford University Press, 832 p
9. Dresig H, Holzweißig F (2010) Dynamics of machinery. Springer, Berlin, 554 r

10. Semenov YA (2010) Dynamics of machines. Part 1. Publishing house Polytechnic University, SPb, 318 p (rus)
11. Semenov YA (2012) Dynamics of machines. Part 2. Publishing House Polytechnic University, SPb, 252 p (rus)
12. Evgrafov AN, Kolovsky MZ, Petrov GN (2015) Theory of mechanisms and machines: a textbook. Publishing house Polytechnic University, SPb, 248 p (rus)
13. Beitelshmidt M, Dresig H (2015) *Machinedynamik. Aufgaben und Beispiele*. Springer, Berlin, 407 S
14. Harris CM, Crede CE (2010) *Shock and vibration handbook*, 6th edn. McGraw-Hill Book Company, New York
15. Kolovsky MZ (1989) *The Dynamics of machines*. Mechanical Engineering, 263 p (rus)
16. Dresig H (2005) *Schwingungen mechanischer Antriebssysteme*. 2. Aufl. Springer, Berlin
17. Semenov Yu A, Semenova NS, Egorova OV (2018) Dynamic mesh forces in accounting of the time variable mesh stiffness of a gear train. *IREME* 12(9):736–741
18. Andrienko PA, Karazin VI, Kozlikin DP, Khlebosolov IO (2019) About implementation harmonic impact of the resonance method. *Lecture notes in mechanical engineering*, pp 83–90
19. Andrienko PA, Karazin VI, Khlebosolov IO (2017) Bench tests of vibroacoustic effects. *Lecture notes in mechanical engineering*, pp 11–17
20. Evgrafov AN, Karazin VI, Khisamov AV (2018) Research of high-level control system for centrifuge engine. *Int Rev Mech Eng* 12(5):400–404
21. Evgrafov AN, Karazin VI, Petrov GN (2019) Analysis of the self-braking effect of linkage mechanisms. *Lecture notes in mechanical engineering*, pp 119–127
22. Evgrafov AN, Petrov GN (2018) Self-braking of planar linkage mechanisms. *Lecture notes in mechanical engineering*, Part F5, pp 83–92
23. Evgrafov AN, Petrov GN (2016) Drive selection of multidirectional mechanism with excess inputs. *Lecture notes in mechanical engineering*, pp 31–37. https://doi.org/10.1007/978-3-319-29579-4_4
24. Evgrafov AN, Karazin VI, Kozlikin DP, Khlebosolov IO (2017) Centrifuges for variable accelerations generation. *Int Rev Mech Eng* 11(5):280–285. <https://doi.org/10.15866/ireme.v11i5.11577>
25. Evgrafov AN, Burdakov SF, Tereshin VA (2018) Ways of controlling pendulum conveyor. *Int Rev Mech Eng* 12(9):742–747

Localization of Plastic Deformation in Austenitic Steel at Low-Temperature Cycling Loading



Margarita A. Skotnikova, Angelina A. Strelnikova, Galina V. Ivanova, Alexander A. Popov and Ilnur S. Syundyukov

Abstract Using electron microscopy, the instability (localization) of plastic deformation in austenitic steel CHS-52 (Chelyabinsk steel) at low temperature cyclic loading of welded vessels intended for transportation and storage of cryogenic liquids to increase their service life was studied. It is shown that with a decrease in the deformation temperature from 293 (room) to 20 K, steel CHS-52 is intensively strengthened, and its plasticity characteristics are intensively reduced, while remaining at a sufficiently high level. The lower the deformation temperature and the smaller the value of the cyclic loading, the greater the number of cycles the localization of plastic deformation occurs and the destruction of the sample is achieved.

Keywords Austenitic steel · Low temperatures · Electron microscopy · Fatigue · Service life

1 Introduction

It is known that the durability and reliability of machines and mechanisms are largely determined by the resistance of their material to premature localization of plastic deformation and to the emergence of cracks capable of propagation in these places.

The transition from uniform plastic deformation to localized, in the vast majority of cases, parts of machines undergo a decrease in the test temperature, with an increase in the loading rate, under the influence of cyclic loads (fatigue, friction pairs, vibrations, high-speed blade treatment), especially from materials with low energy of package defect (for example, from highly alloyed austenitic steels or titanium alloys) [1–10].

The characteristic feature of low-temperature deformation of alloys is the occurrence of a strongly excited resiliently stressed field in them and formation of non-equilibrium solid solutions supersaturated by alloying elements and point defects. In these conditions, energy dissipation is in the occurrence of additional effects of

M. A. Skotnikova (✉) · A. A. Strelnikova · G. V. Ivanova · A. A. Popov · I. S. Syundyukov
Peter the Great St. Petersburg Polytechnic University, St. Petersburg, Russia



Fig. 1 Welded vessel for transportation and storage of cryogenic liquids

mass transfer (high-growth drift skips), in the appearance of metastable structures and phases [11, 12].

Therefore, low temperature tests and electron microscopic studies were carried out to develop and investigate welded vessels for the transport and storage of cryogenic liquids (see Fig. 1).

The purpose of this work was to study the instability (localization) of plastic deformation in austenitic steel CHS-52 during low-temperature cyclizing loading of welded vessels intended for transportation and storage of cryogenic liquids to increase their service life.

2 Methodology and Materials

Cryogenic steel should provide the necessary strength in combination with high viscosity and plasticity, low sensitivity to stress concentration and low tendency to brittle fracture. Given the technology of manufacturing products operating at low temperatures, such steels should have good weld ability and high corrosion resistance. Therefore, chromium nickel austenitic steel CHS-52 was selected as the test material, see Table 1.

Table 1 Austenitic steel chemical composition CHS-52

Steel grade	Mass fraction, %							
	C	Si	S	P	Cr	Mn	Ni	N
CHS-52	<0.07	<0.6	<0.025	<0.035	12.0–14.8	19.0–22.0	3.8–5.3	0.08–0.18

The study examined the effect of low-cycle fatigue on austenitic steel structure after room temperature tests in air (293 K), liquid nitrogen (77 K) and liquid helium (4.2 K).

Material in an initial state represented a sheet semi-finished product 12 mm thick after an austenization lasting 0.5 h at a temperature of 1050 °C and coolings in water. Cylindrical five-fold samples (without incision) with 4 mm working diameter were cut across the rolling direction. Cyclic tests at zero tension with a frequency of 15–20 cycle/min were carried out on a $\mathcal{V}M7-10TM$ machine at loading speeds of 0.58–57.9 mm/min.

Structural studies were carried out with a microvisor of a metallographic invariant μ Vizo-MET-221 and a transmission electron microscope $\mathcal{E}M-200$ using microdiffractive analysis.

3 Results of Work

As showed standard mechanical tests on active stretching, Fig. 2, with fall of temperature of deformation from 293 (room) to 20 K, ChS-52 steel was intensively strengthened (strength of σ_B and a limit of fluidity of $\sigma_{0.2}$), and its characteristics of plasticity (relative narrowing of ψ and lengthening of δ increased) decreased, in too time remaining at rather high level.

However, in the transition from 20 to 4.2 K, a decrease temporary burst resistance of 120 MPa and a sharp increase in the relative steel narrowing of 30–50% were

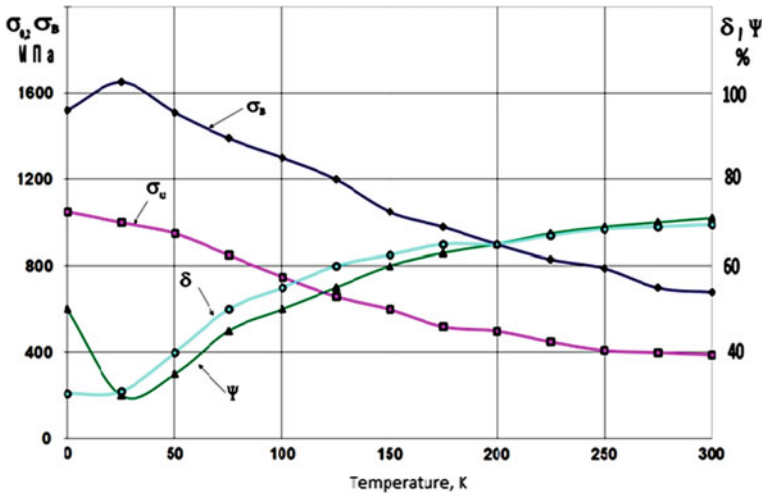


Fig. 2 Results of standard mechanical tensile tests steel CHS-52 at temperatures between 4.2 and 293 K

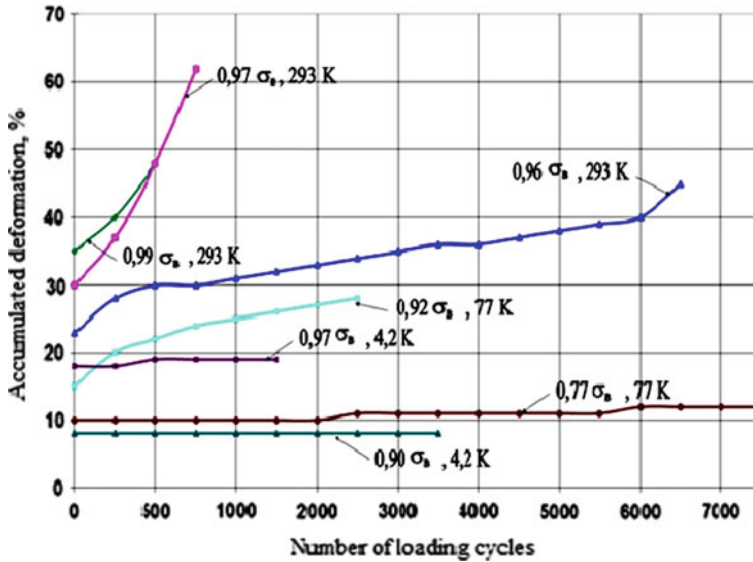


Fig. 3 Curves of cyclic creep at various temperatures and sizes of the enclosed circulating tension: $0.96\text{--}0.99 \sigma_B$, 293 K; $0.77\text{--}0.92 \sigma_B$, 77 K; $0.90\text{--}0.97 \sigma_B$, 4.2 K steel CHS-52

observed. At the same time values of yield strength and relative elongation changed little.

Low-cycle fatigue of the steel CHS-52 structure was studied on the basis of 104 loading cycles. Apparently from Fig. 3, the curve of cyclic creep received at a temperature 293 K under the influence of the enclosed circulating tension $0.96 \sigma_B$ consisted of three sites: the unsteady, established and accelerated creep. With increase in the enclosed tension from 0.97 to $0.99 \sigma_B$, the course of curves of the saved-up plastic deformation became more accelerated.

The curves of cyclic creep received at a temperature 77 K with increase in the enclosed circulating tension 0.77 and $0.92 \sigma_B$ consisted of sites of the established and unsteady creep, respectively, Fig. 3.

The curves of cyclic creep received at a temperature 4.2 K with increase in the enclosed circulating tension from 0.90 to $0.97 \sigma_B$ consisted of sites of the established creep and differed in only a level in the saved-up plastic deformation, Fig. 3.

The structure of the steel CHS-52 in its original state, Fig. 4, contained austenite grains with chaotic dislocations, with an average density of 106 cm^{-2} . Dislocations were often split, indicating low packing defect energy (P.D.E.) of steel, Fig. 4a. Second phase releases were not observed in austenite, Fig. 4b.

Cyclic loading at a temperature of 293 K showed, Fig. 4 that at $\sigma = 0.96 \sigma_B$ increase in number of cycles from 1000 Fig. 4c to 2200 led Fig. 4d to emergence of the 2nd system of sliding in which places of crossing, conditions for localization of deformation, strengthening of rotary (rotational) fashion of deformation, Fig. 4d and origin of micro cracks are created.

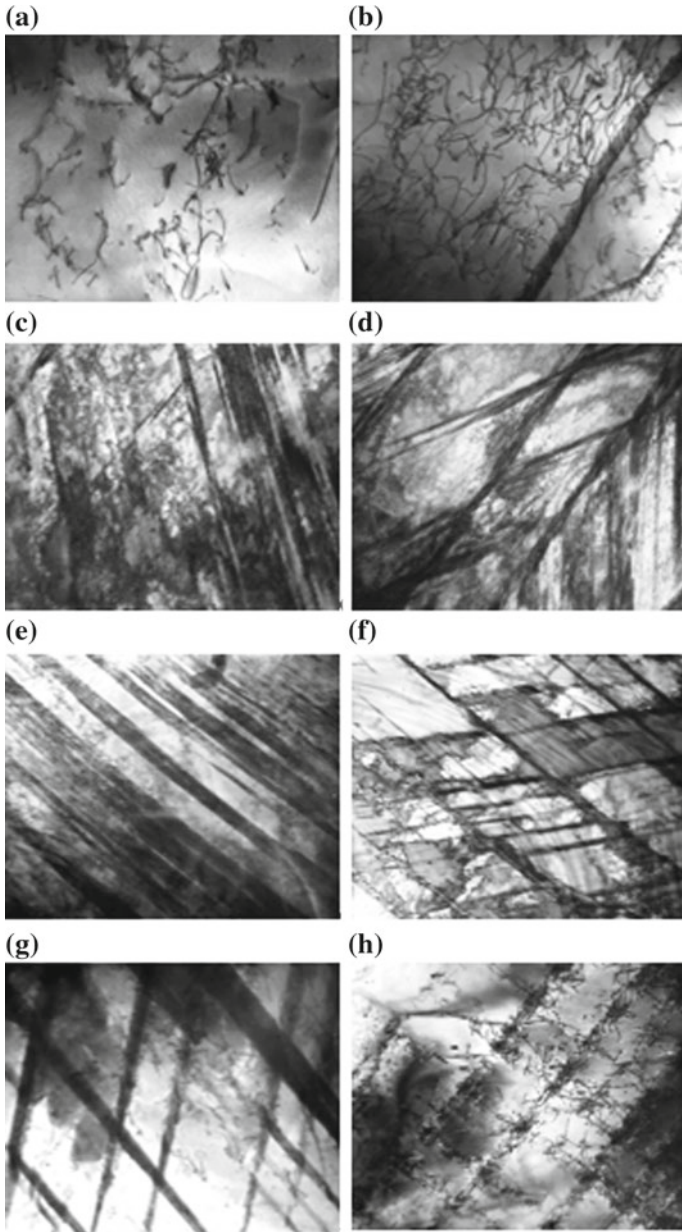


Fig. 4 Electron-microscopic images of steel structure CHS-52 in initial state (a, b) and after cyclic tests: at 293 K, 1000 cycles (c), 2200 cycles (d); At 77 K, 100 cycles (e); 6600 cycles (f); At 4.2 K, 207 cycles (g); 3530 cycles (h). X20000 (a, d, f, g), x30000 (b, c, e, h)

Cyclic loading at a temperature of 77 K showed, Fig. 4 that at $\sigma = 0.77 \sigma_B$ already at 100 cycles of test sliding strips with sharper outlines were formed, Fig. 4e compared to structure obtained at 293 K, Fig. 4c. This can be explained by the fact that at room temperature the sliding strips were formed at a time and uniformly in terms of sample volume, Fig. 4c. At nitrogen temperature sliding strips were not formed at a time. Therefore, strips with increased dislocation density where deformation localization occurred earlier compared to bands with lower dislocation density had sharper outlines, Fig. 4e.

At a temperature of 77 K, the increase in the number of cycles from 100, Fig. 4e to 6600 Fig. 4f resulted in the emergence of a second sliding system, at the points of intersection of which conditions are created for localization of deformation and equalization of dislocation density in areas free from them. The increase in dislocation density was accompanied by the formation of separate textures, tangled up to the formation of rectangular cellular structures, the cell boundaries being extended along crystallographic directions corresponding to sliding along prismatic planes, Fig. 4f. Dislocations were so redistributed in grain volume that their plexuses formed blurred walls (boundaries) between parallel rows of flat clusters in their (two) intersecting sliding systems, Fig. 4f.

Cyclic loading at a temperature of 4.2 To, Fig. 4, showed that at $\sigma = 0.90 \sigma_B$, increase in number of cycles from 207, Fig. 4g to 3530, Fig. 4h led to disintegration of flat dislocation congestions and formation of rectangular cellular structures. The multi-stage disintegration of austenite was not observed at these temperatures, and therefore the energy released was spent on heating. Possible local warms along the sliding lines can be judged from the traces of dislocation polygonization in individual areas.

4 Conclusion

Thus, as the results obtained with the use of transmission electron microscopy showed, there are no qualitative changes in the deformation and destruction of steel CHS-52 with reduction of low-temperature cyclizing loading in the working range from 293 to 20 K in the material of welded vessels intended for transportation and storage of cryogenic liquids. The intensity of plastic deformation accumulation processes varies only quantifiably.

It is known that the durability and reliability of machines and mechanisms are largely determined by the resistance of their material to premature localization of plastic deformation and to the emergence of cracks capable of propagation in these places.

The lower the deformation temperature and the lower the cyclic loading value, the localization of plastic deformation occurs after a larger number of cycles and the destruction of the sample is achieved.

At the same time, the ability to resist cyclic creep does not change, and destruction also, as at room temperature, occurs as a result of formation and development

to a critical value of fatigue crack. Only the kinetics (intensity) of plastic deformation accumulation change (slows down). The failure is due to the reinforcement at low localisation temperatures of the plastic deformation in the individual areas of intersection of the sliding strips and, as a result, to the reinforcement of the rotary modes.

As the temperature decreases during the cyclic creep of the steel, its ability to accumulate residual deformation decreases dramatically. This is because the bulk of the accumulated deformation is realized in the first loading cycle. The increase in the number of loading cycles leads to the disintegration of flat clusters and the formation of rectangular cellular structures (a grid of dislocation cells).

Increase of regularity and frequency of distribution of dislocation clusters lines, reduction of deformation localization step indicates decrease of overvoltage intensity inside grain body and probable redistribution of stresses at their boundaries.

At the stage of steady-state creep processes of plastic deformation accumulation, as well as processes of dynamic structural and concentration relaxation are in equilibrium.

References

1. Shlepetinskiy AY, Manzhula KP (2018) Size of a zone dangerous by damage at the root of cruciform weld joint. In: Modern engineering: science and education, Sankt-Petersburg, pp 669–677
2. Troshchenko VT (ed) (1985) Tsiklicheskie deformatsii i ustalost' metallov (Cyclic Deformation and Fatigue of Metals), vol 2, Naukova Dumka, Kiev
3. Skotnikova MA, Ivanova GV, Popov AA, Paitova OV (2017) Localization of plastic deformation HCP—crystals during indentation and scratching/“modern engineering: science and education”, Saint-Petersburg, pp 402–412
4. Skotnikova MA, Krylov NA (2016) About nature of dissipative processes at cutting treatment of titanium vanes. In: Modern engineering: science and education, Sankt-Petersburg, pp 530–539
5. Skotnikova MA, Ivanova GV, Popov AA, Paitova OV (2018) Localization of plastic deformation HCP—crystals during indentation and scratching. In: Advances in mechanical engineering. selected contributions from the conference “modern engineering: science and education”, Saint Petersburg, Russia, Springer, Berlin, Heidelberg, pp 143–150
6. Skotnikova MA, Krylov NA, Ivanov EK, Tsvetkova GV (2016) Structural and phase transformation in material of steam turbines blades after high-speed mechanical effect. In: Advances in mechanical engineering. selected contributions from the conference “modern engineering: science and education”, Saint Petersburg, Russia, Springer, Berlin, Heidelberg, pp 159–168
7. Skotnikova MA, Krylov NA (2017) About the nature of dissipative processes in cutting treatments of titanium vanes. In: Advances in mechanical engineering. Selected contributions from the conference “modern engineering: science and education”, Saint Petersburg, Russia, Springer, Berlin, Heidelberg, pp 115–124
8. Skotnikova MA, Tsvetkova GV, Lanina AA, Krylov NA, Ivanova GV (2015) Structural and phase transformation in material of blades of steam turbines from titanium alloy after technological treatment. In: Advances in mechanical engineering. Selected contributions from the conference “modern engineering: science and education, Saint Petersburg, Russia, Springer, Berlin, Heidelberg, pp 93–101
9. Finkel VM (1970) The Physics of fracture. In: Metallurgy, p 322
10. Mikljaev PG, Neshpor GS, Kudryashov VG (1979) Kinetics of fracture. In: Metallurgy, p 279

11. Panin VE, Grinyaev YV, Danilov VI, et al. (1990) Structural levels of plastic deformation and fracture. Nauka, Novosibirsk, p 255
12. Likhachev, VA, Panin, VE, Zashchuk, EE et al (1989) Cooperative processes and localization of deformation. Sciences. Dumka, Kiev, p 320

Research of Vibrations of the Drive of Cycle Machines Under Powering Closure of Mechanisms



Iosif I. Vulfson

Abstract A number of dynamic models have been proposed for studying the vibrations of the drive of cyclic machines, taking into account the gaps and characteristics of electric motors. Compared with the known works, new factors are investigated that affect the vibrational activity of the drive. It is established that the power force closure used to eliminate breaks in the kinematic chain is also a source of excitation of oscillations. Under certain conditions, these fluctuations can lead to a decrease in the efficiency of the power circuit and to an increase in the vibrational activity of the system, which requires appropriate correction of the methods for the dynamic synthesis of machines of this class. The obtained dynamic effect is confirmed by the results of computer simulation.

Keywords Cycle machines · Dynamic models · Vibrations · Gaps · Force closure · Computer modelling

1 Introduction

In many modern machines of textile, printing, light and a number of other industries, technological operations are performed by the so-called cyclic mechanisms (leverage mechanism, cam, Maltese, etc.), that perform a given programmed movement [1–6]. Typically, this class of machines operates at high operating speeds, at which programmed motion is substantially distorted by excited vibrations.

In order to facilitate the subsequent presentation, we will first briefly dwell on some general issues related to the problem under consideration. Rational dynamic synthesis of oscillatory systems in this case plays a special role because of gaps that can lead to large distortions of a given programmed movement of the working bodies, as well as to increased noise, dynamic loads and vibration activity of the drive. The gap, as a rule, is a concomitant factor of any kinematic pair that carries out the movable connection of the links of the mechanism. Often, it is the size of the

I. I. Vulfson (✉)

Saint Petersburg State University of Industrial Technologies and Design, Bolshaya Morskaya str.18, 191186 Saint Petersburg, Russia

gaps that ultimately limits the performance and operational characteristics, which makes it significantly toughen the accuracy requirements for their manufacture and assembly. Then the kinematic pairs can be considered non-restraining bonds, which usually include the moving connections of links with one-way contact. Although the kinematic pair as a whole implements two-way communication, with gaps this function is only partially fulfilled. When shifting in the gap, local breaks in the kinematic chain occur, which are typical for systems with unilateral constraints [1, 2].

According to the effect on the oscillatory system, two typical cases of the manifestation of the gap can be distinguished, each of which corresponds to a corresponding region of variation of parameters and external disturbances. In the first case, the gap manifests itself as a nonlinear element that significantly affects the frequency spectrum of free vibrations.

In the second case, the influence of the gap mainly manifests itself as an impulse perturbation over a limited time interval of the kinematic cycle in the absence of any noticeable distortion of the frequency spectrum of the original linear system. At the same time, however, the possibility of multiple collisions, leading to vibroshock modes, in which the dynamic effect of the gaps approaches the first case, remains. As the analysis performed using the results of [7] shows, at practically feasible parameter values, the transition from one phase to another with the so-called quasi-plastic impact. In this case, a rapidly damping high-frequency bounce occurs. In essence, the effect observed in this case is close to an absolutely inelastic shock.

2 Dynamic Models

Let us turn to the dynamic models shown in Fig. 1, which reflect the characteristics of the oscillatory drive system (“input”) and the working body (“output”).

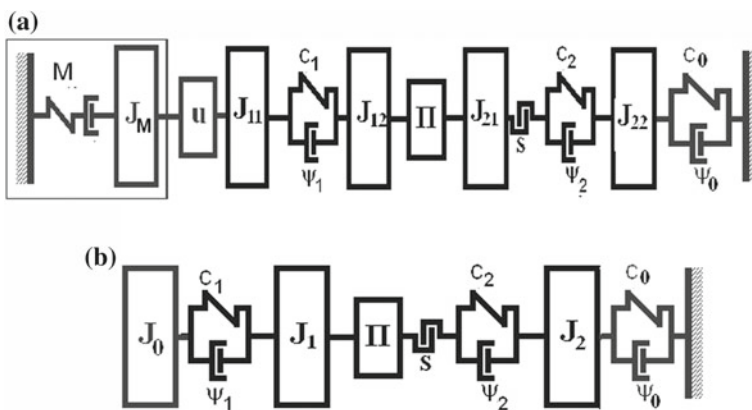


Fig. 1 Dynamic models

The following conventions are accepted here: J moments of inertia; c —stiffness factors; ψ —scattering coefficients; Π —a position function realizing the relationship between the input and output links; s —clearance; u —gear ratio of the gearbox. Dynamic model 1 (Fig. 1a) also includes the characteristics of an electric motor (subsystem M), which can be represented as a series connection of conventional “elastic” and “dissipative” elements [4, 9]. Equivalent compliance of the engine, as a rule, significantly exceeds the compliance of the drive. In some cases, this makes it possible to use the simplified dynamic model 2 (Fig. 1b), in which the motor effect can be properly allowed by taking into account the reduced inertia moment of the rotor [3, 4, 8, 9]. Both models take into account the force characteristic of the oscillatory system.

As shown in [1–7], if we restrict ourselves to taking into account the characteristics at the “output”, then passing through the gap without a power circuit, the level of additional vibrations excited when the kinematic contact is restored is determined by a criterion that is equal to the ratio of the extremum of the additional acceleration after sampling the gap to the extremum of ideal acceleration [1, 2]:

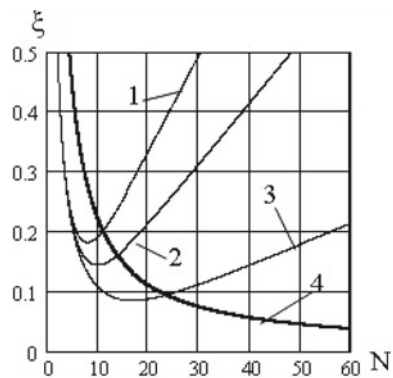
$$\xi = \Pi_*''' \sqrt{(4.5)^{2/3} \beta_1^4 N^2 + N^{-2}}, \tag{1}$$

where, $\beta_1 = \sqrt[3]{s/|\Pi_*'''|}$, $N = k_2/\omega_*$, s is the gap value, $k_2 = \sqrt{c_2/J_2}$ is the natural frequency in the absence of a gap ($c_0 \ll c_2$), ω_* —is the ideal angular velocity of the input link, $\Pi_*''' = d^3\Pi/d^3\varphi^3$ (the asterisk corresponds to the moment of contact breaking).

Figure 2 shows a family of curves for $\xi(N, \beta_1)$, $\beta_1 = 10^{-3}$ (curve 1), $\beta_1 = 5 \times 10^{-4}$ (curve 2), $\beta_1 = 10^{-4}$ (curve 3).

Based on the formula (1) can be determined system parameters that satisfy the requirement $\xi \leq \xi_*$, where ξ_* is the permissible value of the level of accelerations caused by the gap (usually $\xi_* < 0.1 - 0.2$). When cross the gap, it is very important to eliminate repeated collisions. As shown in [1, 2, 8], in order to exclude the possibility

Fig. 2 Determination of additional accelerations at a single intersection of the gap zone



of vibro-shock modes in a first approximation, the condition must be satisfied. In Fig. 2, this condition corresponds to the region located below curve 4.

3 Dynamic Analysis

In the development of previous studies in this article, the main attention will be paid to the role of the drive (“input”) in the excitation of oscillations of the working body and the resulting dynamic errors. Below is a system of differential equations for models 1 (Fig. 1a). To give a more general view of the analysis results, let us move on to a new variable, for which we take “dimensionless time” $\varphi = \omega_* t$, where ω_* is the angular velocity of the “ideal” engine.

$$\begin{aligned} & \nu \tau \omega_*^2 J_0^* \Delta \bar{\omega}' + \nu J_0^* \omega_* \Delta \bar{\omega}' + \omega_*^{-1} \Delta \bar{\omega} - \nu \bar{k}_1^2 \omega_*^2 q_1 = 0; \\ & q_1'' + \left\{ \mu \Pi \bar{k}_2^2 \left[2\delta_2 \bar{k}_2^{-1} (q_1' \Pi_*' - q_2') + q_1 \Pi_*' - q_2 - 0.5s \operatorname{sgn}(\Pi_*' q_1 - q_2) \right] \right\} \\ & \quad \times \Phi(|\Pi_*' q_1 - q_2| - 0.5s) + \bar{k}_1^2 (2\delta_1 \bar{k}_1^{-1} q_1' + q_1) = 0; \\ & q_2'' + \bar{k}_2^2 [2\delta_2 \bar{k}_2^{-1} (-q_1' \Pi_*' + q_2') - q_1 \Pi_*' + q_2 - 0.5s \operatorname{sgn}(-\Pi_*' q_1 + q_2)] \\ & \quad \times \Phi(|\Pi_*' q_1 - q_2| - 0.5s) + \Pi_*'' (1 + \Delta \bar{\omega})^2 + \Pi_*' \Delta \bar{\omega}' + \bar{k}_0^2 (\Delta_0 + \Pi_*) = M_2/J_{22}, \end{aligned} \quad (2)$$

where $\Delta \omega$ is the dynamic error of the angular velocity at the “input” (see below); q_1, q_2 - coordinates in disk sections; $(\prime) = d/d\varphi$; ν, τ —the coefficient of slope of the static characteristic and the electromagnetic time constant of the electric motor, reduced to the cross section [1, 2, 9]; J_{11} (see Fig. 1a); $\bar{k}_i = k_i/\omega_*$; $k_1 = \sqrt{c_1/J_1}$, $k_2 = \sqrt{c_2/J_2}$, $k_0 = \sqrt{c_0/J_2}$; $\mu = u^2 J_M/J_{11}$; $J_0^* = J_1 u^{-2}$; $\delta_i = \psi_i/(4\pi)$; Δ_0 —preload of the closing device; M_2 —moment of external forces; u is ratio of the reduction gear; $\Phi(\varphi, s, q_1, q_2)$ —unit function, equal $\Phi = 0$, $\Phi = 1$, respectively, with a negative and a positive argument. Here and below, the dimensionless parameters marked with a dash correspond to their initial value, referred to ω_* .

The characteristic of an asynchronous electric motor and a DC motor can be represented as a rheological model of Maxwell, in which the rotor is connected to the stator by means of an “elastic element” with a stiffness coefficient $c_* = (\nu \Omega_{m0} \tau)^{-1}$ and a series-connected damper with a moment of resistance $b_m \Omega_{m0}$. Here $b_m = \nu_m^{-1}$; Ω_{m0} is the angular velocity of the ideal engine idle [1–4, 8, 9]. In relation to the drives of cycle machines, the analysis of the influence of the electric motor is considered in detail in the monograph [1].

In articles [8, 9] it was shown that the conditional equivalent stiffness coefficient of the electric motor is significantly lower than the reduced stiffness coefficient of the mechanical drive subsystem. In practice, this means that often sufficient accuracy

in the operating speed range gives an assumption in which the influence of the motor on the drive dynamics is limited by taking into account the moment of inertia of the rotor. Dynamic model 2 corresponds to this assumption. The system of differential equations corresponding to this model coincides with (2), if we accept, i.e., neglect the variability of rotation of the motor rotor. For engineering estimates, one can also use the method of successive approximations, taking as a solution to the first equation of system (2), in which one can restrict oneself to the static characteristic of the engine ($\Delta\omega \equiv 0$). Reactive moments associated with the coordinates, in this case, can be replaced by the moment of resistance, based on the results of kinetostatic analysis. However, it should be noted that some errors of not only quantitative, but also qualitative level are possible due to changes in the frequency and modal characteristics (see below).

4 Dynamic Synthesis

In engineering calculations, to identify the most important factors, preference is usually given to relatively simple dynamic models, which at the same time make it possible, if necessary, to determine the appropriateness of their further complication. First, we consider some features of the influence of force closure at the kinetostatic level using on the dynamic model shown Fig. 1b. In so doing we select the stiffness coefficient in such a way as to exclude the breaking of the kinematic chain ($c_1 = \infty$; $c_2 = \infty$). If we restrict ourselves to the case of kinematic excitation, then the condition must be met

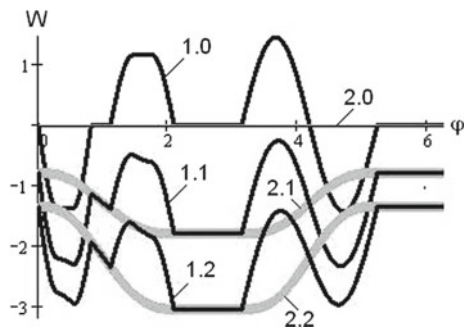
$$W_* = \bar{p}_*^2 [h_0 + \Pi(\varphi)] > |-\Pi''(\varphi) + W_2(\varphi)|, \tag{3}$$

where $\bar{p}_* = p_0/k_2$; $p_0 = \sqrt{c_0/J_2}$; $W_2(\varphi) = M_2(\varphi)/J_2$; h_0 is the preload.

Figure 3 shows examples of the dynamic component functions of W .

The function W_2 (curves 2.0; 2.1; 2.2) displays the position of static equilibrium, which in the last two cases changes when the closing system deforms. Function W_*

Fig. 3 Typical function graphs $W_*(\varphi)$; $W_2(\varphi)$: 1.0; 2.0—
 $\bar{p}_* = 0$; 1.1; 2.1 — $\bar{p}_* = 1$; 1.2; 2.2 — $\bar{p}_* = 1.3$



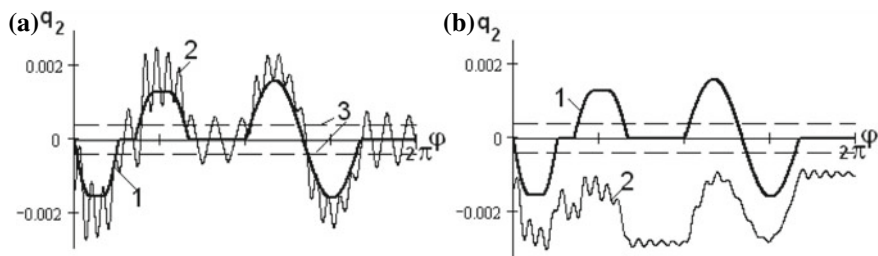


Fig. 4 Graphs q_2 : 1—deformations from the moment of inertial forces of the working body; 2—dynamic errors when accounting vibrations; 3—the boundaries of the gap

(curves 1.0; 1.1; 1.2) correspond to the reactive moment at the input of the output link. Obviously, in a first approximation, to eliminate the discontinuity in the continuity of motion, the graphs of this function should not intersect the abscissa axis. Curve 1.0 is a mirror image of the graph of a given function of the accelerations of the working body. When taking into account the elasticity of the drive elements, the simplest model is described by the second equation of system (2) when, only the elastic-dissipative properties of the working body are taken into account.

Figure 4 illustrates the dynamic effect of the preload of the power circuit at. In the absence of a force closure (Fig. 4a), significant oscillations are excited when hifting in the gap, and when it is connected (Fig. 4b), only accompanying vibrations arise, caused by kinematic excitation [1–3].

At first glance, the model used provides an exhaustive result for solving the problem. However, the reliable operation of the closure system can be disturbed for various reasons, among which the drive oscillations, excited by, among other factors, the closing force, play a significant role. If dynamic loads are predominant, the condition $F = \xi |P^i|_{\max}$ must be met, where P^i is the inertia force, F is the closing force, $\xi > 1$ is the safety factor. During oscillations, both the closing force and the inertia forces determined on the basis of the kinetostatic model can vary significantly. This can lead to a violation of the power circuit, which cannot be eliminated by an increase in the closing force. This effect is associated with the non-stationary kinematic connection, due to which, with a nonlinear position function, even the constant component of the closing force is transformed into a variable moment $M_0 = \Pi' F_0$, acting on the drive. In this case, additionally forced oscillations of the input link are excited, which cause an increment of inertial loads on the output link. Let $F = F_0 + c_0 \Pi$, where c_0 , F_0 is the stiffness coefficient and the force from the preliminary deformation of the closing spring. Between F_0 and $|P^i|_{\max}$ there is a functional connection $|P^i|_{\max} = \Psi(F_0)$. The function $\Psi(F_0)$ at the kinetostatic level in a first approximation can be determined on the basis of (3):

$$\Psi = \min W_* > \max |-\Pi''(\varphi) + W_2(\varphi)|. \quad (4)$$

However, excite oscillations are not taken into account (see below). We give a certain increment F_0 in force equal to ΔF_0 . Then, restricting ourselves to the linear approximation, we have

$$|P^i|_{\max} + \Delta P^i \approx \Psi(F_0) + \frac{\partial \Psi}{\partial F_0}(F_0)\Delta F. \tag{5}$$

We introduce the concept of an ideal increment of the safety factor $\Delta \xi_0 = \Delta F / |P^i|_{\max}$ for an absolutely rigid drive, i.e., for $\Delta P^i = 0$. Using (5), it can be shown that, $\Delta \xi = \zeta \Delta \xi_0$, where $\zeta = (1 - h) / (1 + h \delta \xi_0)$; $h = \frac{\partial \Psi}{\partial F_0}(F_0)$; $\delta \xi_0 = \Delta \xi_0 / \xi_0$. If $h > 1$, the parameter $\zeta < 0$. Then it can be expected that an increase in the closing force will lead to an increase in the intensity of breaks in the kinematic coupling and a further deterioration of the mechanism. This means that an attempt to eliminate breaks in the kinematic contact by increasing the closing force will be unsuccessful, and the closure system will completely lose its sensitivity to installation and operating adjustments, i.e., in fact, it will be uncontrollable.

The formula (5) does not take into account the excited oscillations. To eliminate the effect of uncontrollability by force closure, remaining within the framework of dynamic model 2, it can be shown that in a first approximation [1, 2]:

$$h \approx (3 - 4) \frac{\sigma |P_*^i \Pi''|_{\max}}{c_1(\sigma - 1)}. \tag{6}$$

Here c_1 is the reduced torsional stiffness of the drive; $\sigma = p_1 / p_2$, where p_1, p_2 are the partial frequencies of the leading and driven subsystems of the mechanism; P_*^i —the ideal inertia force (or moment of inertial forces) in the zone of possible breaking of the kinematic chain. From (6) it follows that with some margin the condition $\sigma > 1$ must be satisfied.

Next, we will analyze the results of computer modeling of the system of Eq. (2). At the same time, the data obtained in the calculations of a number of knitting machines were used as basic initial parameters [1]: $J_0 = 0.1$; $J_1 = 0.16 \text{ kg m}^2$; $J_2 = 0.2 \text{ kg m}^2$; $v = 0.05 \text{ Nm}$; $\tau = 0.002 \text{ s}$.(the rest of the data is given in the course of the presentation).

In Fig. 5 shows graphs of normalized values of deviations of the angular velocity of the engine from the average value. In this case, only the partial frequency of the drive subsystem was varied, and the partial frequency of the working body remained unchanged.

Figure 6 presents graphs that complement the previously given graphs taking into account the excited oscillations. Here, curves 1 and 2 coincide with curves 1.2 and 2.1 in Fig. 3, and curve 3 corresponds to the function

$$W_* + q_2'' = -[\Pi'' + p_*^2(h + q_2'')].$$

The analysis of the results of computer simulation showed the effectiveness of the force closure, which was manifested in a significant reduction in the level of

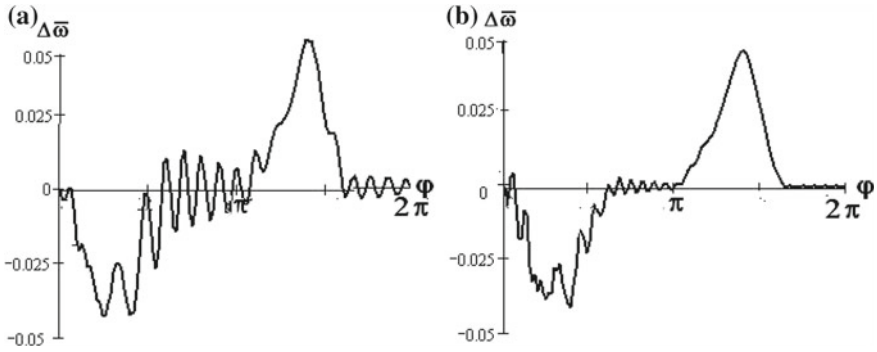


Fig. 5 Graphs of the characteristics of the drive with the angular speed of the electric motor: **a** $p_* = 1.3; \bar{k}_1 = 20; \bar{k}_2 = 30$; **b** $p_* = 1.3; \bar{k}_1 = 40; \bar{k}_2 = 30$

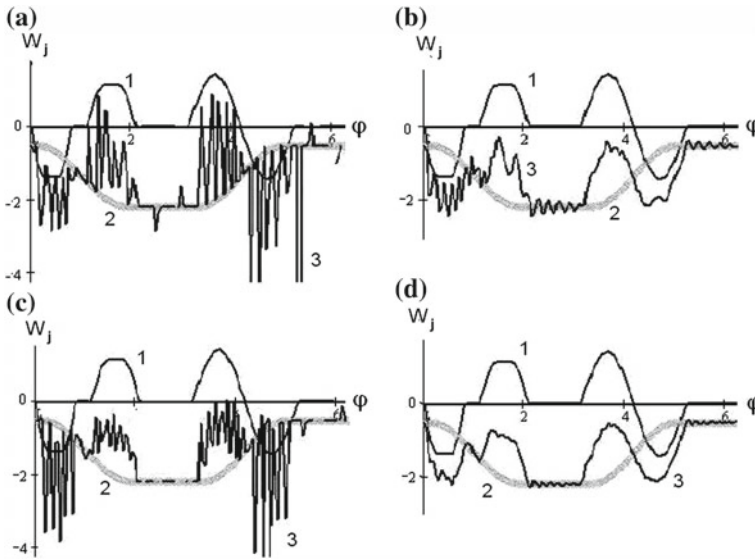


Fig. 6 Graphs $W_j(\phi)$: **a** $p_* = 0; \bar{k}_1 = 20; \bar{k}_2 = 30$; **b** $\bar{p}_* = 1.3; \bar{k}_1 = 20; \bar{k}_2 = 30$; **c** $p_* = 0; \bar{k}_1 = 40; \bar{k}_2 = 30$; **d** $\bar{p}_* = 1.3; \bar{k}_1 = 40; \bar{k}_2 = 30$

vibrations and the elimination of vibrational modes when shifting in the gaps. We also note that the growth of the vibrational activity of the system was confirmed when the conditions for the uncontrollability of the fault system are violated (see formula (6)). The optimal values of the parameters correspond to the graph in Fig. 6g. The comparison of this graph with the graph in Fig. 6b (curves 3) indicates that when using a power short circuit, it does not guarantee the possibility of vibro-shock modes in the gap.

In conclusion, we note that the high-frequency oscillations detected during the force closure of cyclic mechanisms can also lead to a violation of the conditions of dynamic stability in the zones of parametric resonances [1–4]. This problem requires a separate consideration.

References

1. Vulfson II (2015) Dynamics of cyclic machines. Springer, Heidelberg
2. Vulfson II (1989) Vibroactivity of branched and ring structured mechanical drives. Hemisphere Publishing Corporation, New York
3. Kolovsky MZ (1989) The dynamics of machines. Mechanical Engineering, Leningrad (in Russian)
4. Veits VL, Kolovsky MZ, Kochura AE (1984) Dynamics of controlled machine aggregates. Nauka, Moscow (in Russian)
5. Dresig H (2001) Schwingungen mechanischer Antriebssysteme. Springer, Berlin
6. Dresig H, Vulfson I (1990) Maßnahmen und Beispiele zur Lösung dynamischer Probleme bei Verarbeitungs-Maschinen. Konstruktion, vol 42
7. Nagaev RF (1985) Mechanical processes with repeated damping vibration. Nauka, Moscow (in Russian)
8. Vulfson II (2017) To the problem of reducing the vibratory activity of drive of machines while taking into account the dynamic characteristics of the electric motor. Probl Mach Build Mach Reliab 4:173–182
9. Vulfson I (2018) Some Peculiarities of electric drive impact on the dynamics of cyclic machines. In: Evgrafov A (ed) Advances in mechanical engineering. Selected contributions from the conference “Modern Engineering: Science and Education”. Saint Petersburg, Russia, 2017:2–14

Electrolyte-Plasma Polishing Ionization Model



Sergey V. Zakharov and Mikhail T. Korotkikh

Abstract The analysis of the current state of research in the field of electrolyte-plasma processing. The models of electrolyte-plasma polishing (EPP) are compared and analyzed. An ionization model of the EPP process is proposed, which matches the observed phenomena with physicochemical phenomena in the treatment zone. The proposed model is experimentally confirmed by EPP of various metals and alloys. The proposed model of the EPP process allows one to reasonably choose the process parameters and the composition of electrolytes both during polishing of metals and during the implementation of their oxidation processes.

Keywords Electrolyte-plasma polishing · Electrolyte-plasma processing · Finishing · Roughness reduction · Vapored gas layer · Ionization model

1 Introduction

A promising method of electrolyte-plasma polishing originates in the nineteenth century from the works of Sluginov [1–4] and is associated with the development of experimental studies on the processes of luminescence and heating that occur near the electrode surface. In technology, it was proposed to use these phenomena in 1956 [5], but this technology found practical application only in 1979 [6]. Despite the expanding application of this technological method, it is still in the stage of intensive study [7–10].

The constantly growing interest in high-voltage electrolyte-plasma processes is associated with the following reasons:

1. Improving decorative properties.

The use of electrolyte-plasma polishing in the cycle of manufacturing products allows you to achieve a consistently high quality surface of products of almost any geometry. This is due to the introduction of technology in the production cycle of luxury segment products, as increases marginality of products. A number of North-West

S. V. Zakharov (✉) · M. T. Korotkikh
Peter the Great St. Petersburg Polytechnic University, St. Petersburg, Russia

of Russia companies, such as ACEA-SPB, Baltex, Olympus, Sunerazh, Center for Actual Technologies and others, process their products with this method, primarily in order to obtain decorative product properties. Most often, EPGs are used for such products as: chippers and dampers, railings and fences, towel rails and plumbing, underframes and furniture frames, lighting and decoration elements for buildings, CCTV and intercom systems, jewelry and souvenirs.

2. Decrease in technological roughness.

If it is necessary to process the surface to a certain technological roughness and the impossibility of obtaining the required quality for one reason or another by standard methods like:

- The outer surfaces of the spheres of ball valves of large and extra-large sizes;
- Especially narrow landing necks of the pressed shafts;
- Closing pores, smoothing the edges and surfaces on the housings of auxiliary equipment nuclear reactors, etc.

The use of EPP allows solving this problem without special technological difficulties.

3. Lack of a unified theory.

To date, there is no generally accepted consistent model of both electrolyte-plasma treatment in general and EPP in particular, which causes the appearance of conflicting articles, monographs and patents in this field that do not allow making sound and practical recommendations for the implementation of these processes.

The articles and monographs on this subject mainly describe empirical results and interpret them in various ways, construct process control models, and propose regime parameters with solution compositions without disclosing the physical principle of substance transformation and the process phenomenology. Thus, the number of publications on the topic is progressively increasing, and a qualitative transition from empiricism to theory does not occur. A direct consequence of this is the invariability of the regime-compositional processing parameters at industrial enterprises. In the absence of a single theoretical basis, practitioners often refuse to work with materials other than stainless steels, since the composition and mode of this treatment have been known for more than 30 years [11].

The aim of the presented work was to form a theoretically substantiated model of a high-voltage electrolyte-plasma process.

2 Theoretical Part

In formal terms, EPP coincides with anodic electrochemical processes, and the distinguishing features are the composition of the solution and the high voltage (200–400 V) applied between the workpieces (anode) and an auxiliary electrode (cathode).

As a rule, the composition of the aqueous solution includes salts in a low concentration (1–10%). Operating temperature range 40–100 °C. When trying to process products in classical solutions for electrochemical processing under EPP modes, the surface of the samples is destroyed, undergoes severe erosion or is covered with an amorphous non-functional layer.

To understand the processes occurring near the anode during EPP and differences from electrochemical polishing, it is necessary to consider the current-voltage characteristic (CVC) of the EPP (Fig. 1) in the metal-electrolyte system. With increasing voltage, the current value and the metal-electrolyte interface have different parameters, several sections can be noted. After applying voltage, the anode gradually passes through each section to the rated voltage. At relatively low voltages ($U_1 - U_2$), the kinetics of electrode processes obeys the Faraday law [12]. The CVC of the cell changes in accordance with Ohm's law- an increase in voltage leads to a proportional increase in the current.

At this stage, electrolysis occurs, accompanied by the release of oxygen at the anode. The increase in current is limited by the partial screening effect of gaseous products on the electrode surface. In areas free of oxygen bubbles, where the electrode remains in contact with the electrolyte, the current density continues to increase, causing local boiling of the electrolyte surrounding the electrode (Fig. 2) and the formation of a vapor-gas layer (VGL). An increase in current leads to an increase in heat release, in accordance with the Joule-Lenz law.

As a result, in the voltage range U_3 , an increase in voltage leads to the appearance of spark discharges in the VGL (Fig. 3). When approaching the voltage U_4 , the electrode is surrounded by a continuous VGL with low electrical conductivity. Almost all the voltage applied to the cell now drops on this thin near-electrode layer. The electric field reaches a value of $10^6 - 10^8$ V/m, which is sufficient to start the process of ionization of the VGL.

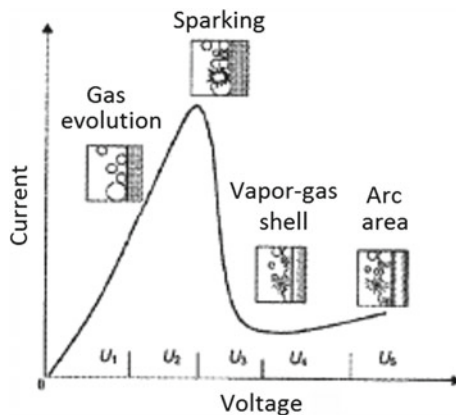


Fig. 1 Current-voltage characteristic of EPP

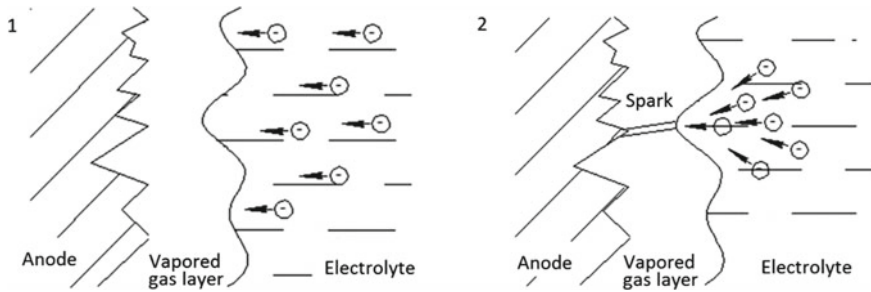


Fig. 2 Forming spark discharges in VGL

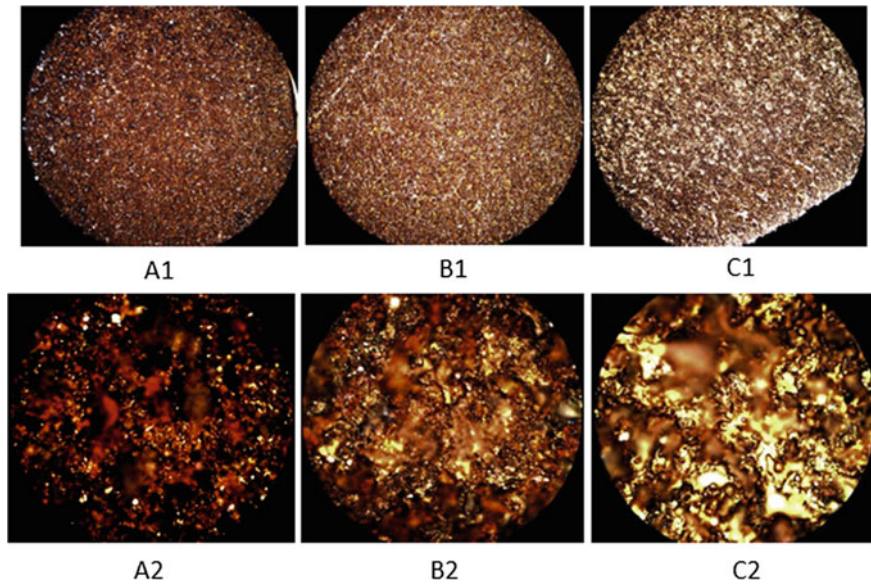


Fig. 3 Comparison of surfaces after electric discharge machining in finishing conditions

Subsequent processes after ionization of VGL are an area of current research. Professor Mirzoev [13] formulated the questions that need to be answered by the theoretical model of the EPP process:

- What is the nature of the current passing through the gas layer;
- What is the metal removal mechanism;
- What is the surface leveling mechanism;
- Whether the metal surface is in contact with the ionized gas layer (plasma) or is the oxide (oxide-salt) film separated from it;
- Whether at least short-term local touches of the electrolyte with the surface of the metal or oxide film take place.

In addition, a consistent model should coordinate the loss of mass of the anode with the Faraday law, as well as take into account and explain the actually recorded and repeatedly confirmed phenomena that occur during EPI:

- The presence and generation of valence unbound ions in VGL [14–20]. The same is confirmed [21–24] by analysis of emission spectra;
- The presence of a gas electric (glow) discharge in the VGL [25, 26], which is the process of electric current flowing through a gas due to the formation of free charge carriers by the avalanche-like generation of charged particles during shock ionization of a gas by electrons accelerated by an electric field;
- The presence of high-frequency current oscillations [5, 27] caused by the action of an electric field on a charge arising from a violation of the plasma quasineutrality. This field seeks to restore disturbed balance. Returning to the equilibrium position, the charge passes by inertia this position, which again leads to the appearance of a strong returning field, typical mechanical (sinusoidal) oscillations occur. Fluctuations occurring in electrolyte plasma are high-frequency (~3 MHz) and, as we have shown, do not depend on the area of the treated surface.

Currently, for the EPP process, there are a sufficient number of process models that can be divided into the following groups:

Spark model [5, 28, 29].

The earliest model first proposed by Muras in 1956. The basis of this model is the assumption that electrolyte bridges (Fig. 2), acting on the surface of the anode, subject it to erosion polishing. The material evaporates at the point of spark breakdown.

This assumption is not confirmed, since the researchers, including us, could not find traces of evaporation or condensation of the metal in the electrolyte solution, melting on the surface of the workpiece. Observation of the treated surface in an optical microscope (Figs. 3, 4) disproves this thesis.

Figure 3 [30] shows samples of steel grade 65G after finishing electroerosive processing. Increase the top row $\times 10$, the bottom row $\times 100$. Micro roughness of the surface from left to right: Ra 1.8 μm , Ra 1.86 μm , Ra 3.48 μm . In all three cases, there are traces of melting on the surface. Figure 4 shows a sample of steel 15KhNFSH after EPP. Magnification $\times 250$. Roughness Ra 0.4. On the surface of the sample, no traces of fusion and holes from spark discharges are observed.

Ionization-spark model [31].

The basis of this model is the assumption that spark discharges affecting the surface ionize the material in the zone of spark breakdown (Fig. 5), which subsequently enters into physicochemical interaction with the components of the electrolyte solution.

Compared to the original model, the absence of condensed vaporized material is explained, but there are still no traces of spark breakdown.

Plasma-cavitation model [32].

Updating a less common model, published in 2014. The basis of this model is the assumption that, as a result of melting of the upper layer of the anode, it is carried out by high-temperature plasma, which forms inside the bubble at significant voltages. When expanding, the gas bubble creates a high shock wave, creating an effect similar



Fig. 4 The surface after electrolyte-plasma polishing of steel 15KhNFSH, magnification $\times 250$

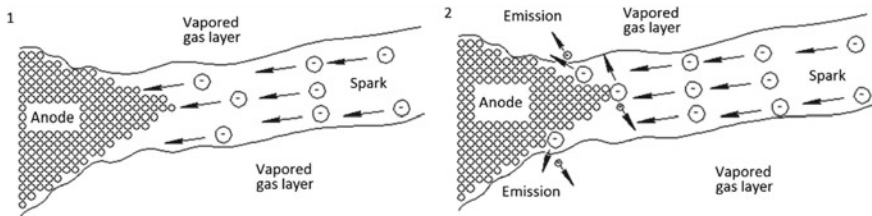


Fig. 5 Emission of atoms from the surface of the anode

to the phenomenon of cavitation. Ions and anions fall into the resulting void, which form a new oxide layer, destroyed by a new shock wave (Fig. 6).

This model is not widely used because it is very controversial, built on assumptions and not confirmed by calculations of the energy balance during the implementation of the process.

Thermionic emission model [33–35].

First proposed by Duraji V.N. in 1988. The basis of this model is the observation that the current passing through the system causes heating of the anode surface, as a result of which the anode emits ions from its surface (Fig. 7), which, in turn, provide the electric conductivity of the VGL and support non-stationary glow discharge.

However, both other researchers [29] and we have found that during processing by the EPP, the workpiece is not subjected to any significant heating, above 120 °C.

An adsorption-complex model [36].

Based on practical observations of polishing corrosion-resistant steels and titanium alloys on known solutions, this model, proposed in 2013, most closely describes the processes that occur during EPI. The basis of this model is the assumption that

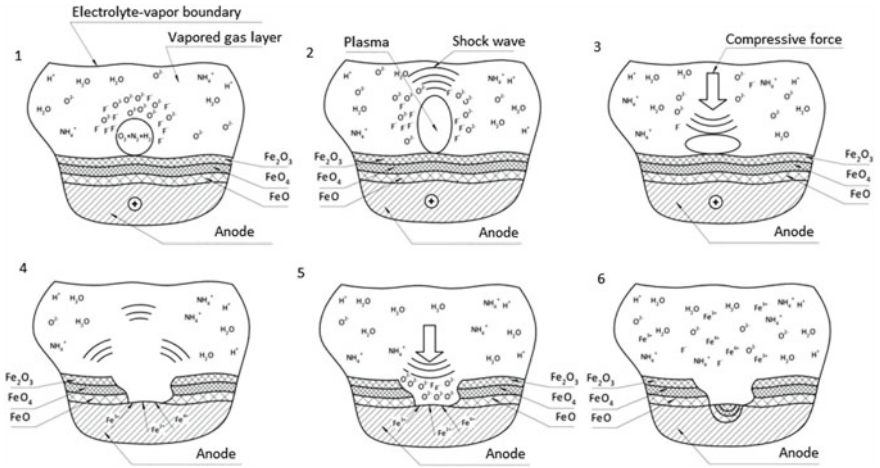


Fig. 6 Plasma-cavitation model

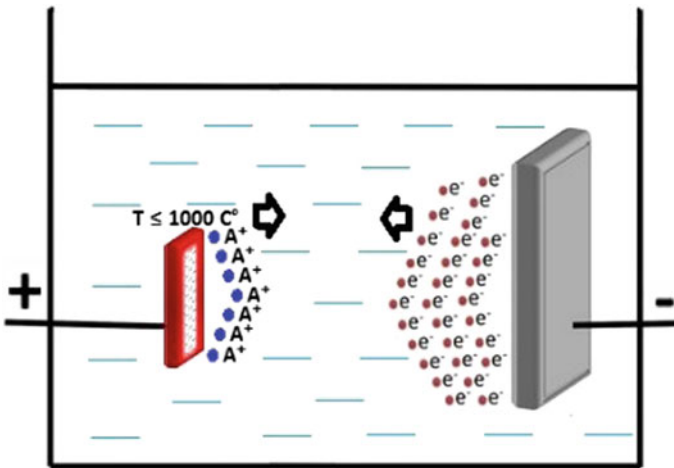
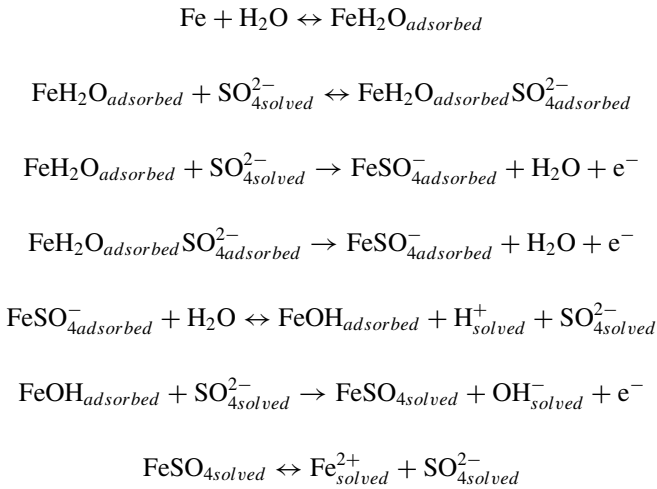


Fig. 7 Thermionic emission

the anodic dissolution of metals occurs by the complexation mechanism through a series of sequential or sequentially parallel intermediate stages. At the first stage, complexes with the participation of water molecules are formed on the surface of metals. In the subsequent stages, anions of the electrolyte solution and (or) water molecules take part. At the final stage of dissolution, water-soluble compounds are formed on the surface of the anode, which upon transition into the solution dissociate into simple ions.

Anodic dissolution of metals under EPI conditions occurs in the field of mixed electrochemical and diffusion kinetics. Diffusion limitations arise as a result of hindered ion mass transfer through surface salt, oxide, and hydroxide adsorption-phase films. When dissolving the components of corrosion-resistant and structural carbon steels, a significant role is played by chemical processes.

To illustrate this model, we consider an example of a reaction proposed by the authors:



This model explains the appearance of oxide films of various properties on the anode surface; during the processing, the ionic nature of the electrolyte solution and its effect are taken into account.

However, in the proposed mechanism of anodic dissolution, the role of electric current in the process of formation of the adsorption layer is not described, the influence of electrolyte plasma on the processes occurring on the surface of the workpiece is not shown.

Proposed Ionization Model of the EPI Process

The main mechanism of ionization is ion-electron emission. The source of the ions are the components of the solution. Depending on the number, activity and mass of molecules in solution, the plasma treatment process can begin at various temperature and technological conditions [9]. At the moment of contact of the electrolyte bridge with the surface of the anode, anions moving in an electric field to the surface of the anode with an energy exceeding a certain threshold (~10 eV) colliding with the surface of the anode interact with it, causing electron emission [25]. Energy is transferred to the target electrons during the Auger neutralization of the bombarding ion. This process is observed if the ion has an unoccupied energy level lower than the Fermi level in the bombarded metal. In this case, one of the electrons from the conduction band can go to this level, thereby neutralizing the ion. When neutralized,

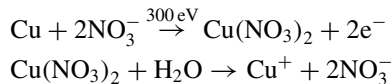
energy is released that is transferred to another electron of the metal, which already gets the opportunity to leave the metal atom. Potential ion-electron emission is possible only if the inequality $I_p > 2\Phi$ is satisfied, where I_p is the ionization energy of atoms, and Φ is the electron work function from the metal.

Emission efficiency is characterized by the so-called pull-out coefficient γ , which is equal to the average number of knocked out electrons per ion. For potential knock-out, γ increases with increasing ionization energy I_p and for singly charged ions it can reach several tens of percent. For multiply charged ions, the coefficient γ can exceed unity due to the multistep process of ion neutralization. The coefficient γ for potential ion-electron emission weakly depends on the energy of the bombarding ions, up to energies of the order of 1 keV. At higher energies, the emission efficiency begins to decrease and tends to zero in the limit of high energies.

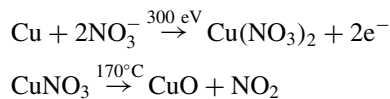
As a result of the movement of charged particles through the VGL, collisions with the atoms of the gaseous vapor layer occur. In this case, an avalanche-like increase in the number of charged particles occurs, since new ions and electrons are formed in the ionization process, which also begin to participate in collisions with atoms, causing their ionization.

These processes lead to the formation of a thin, unsteady layer of gas plasma in the VGL around the anode, in which, in the ionized form, there are ions of all components of the electrolyte solution. The temperature of a low-temperature plasma in the case of formation in an aqueous medium can be in the range of 373–10,000 °C. The lower temperature limit is caused by such a parameter of the aquatic environment as the boiling crisis. Thus, the formation of gas plasma around the treated anode is a consequence of the processes occurring between the liquid cathode and the metal anode, causing the removal of atoms from the surface of the anode.

During the interaction of the anion with a metal atom, an intermediate substance is formed, which, depending on its physical properties and the intensity of formation, in turn, depends on the number of ions in the solution. At low formation intensities, soluble salts have time to dissolve from the surface at the moment of subsequent contact of the electrolyte bridge with the surface. Consider the example of copper:



At high formation intensities, soluble salts do not have time to dissolve upon subsequent contact of the electrolyte bridge with the surface, interacting with the plasma layer surrounding it. It undergoes plasma-chemical interactions, heating and transition to a less energy-consuming state.



After such a transition, around the anode to be treated the VGL and plasma layer will remain stable, and depending on the properties of the oxide, anodic dissolution may continue or stop. What determines the conditions for the formation of oxide layers by the microarc oxidation process, which is also used in technological processes.

To increase the dissolution rate of salts formed on the surface, various complexing agents are used (citric acid, oxalic acid, Trillion B, glycerin, ethanol, urotropine, etc.).

Experimental confirmation of the proposed model of electrolyte-plasma treatment.

To confirm the ionization model of the process, it was considered necessary:

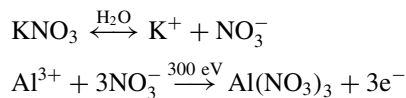
- determine the total energy of the process;
- determine the energy spent on heating the electrolyte solution, equipment, heat loss during the process;
- determine the energy spent on the removal of the anode material;
- evaluate the data obtained by comparing with the physical parameters of the material.

3 Practical Part

To conduct an experiment to determine the amount of energy, a laboratory setup was created that allows you to measure the amount of heat released in the electrolyte, determine the shape and energy of the high-frequency current pulses in the plasma discharge, and the mass loss of the processed product, the electrolyte composition before and after processing.

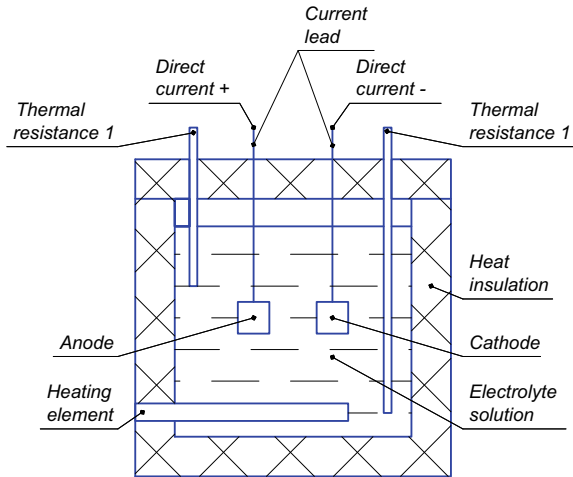
The conditions of the experiment. A sample with a precisely measured mass (anode) was installed in a bath with an electrolyte heated to 70 °C. An electrode made of 08Kh18N10T steel was used as a cathode. The bath with electrolyte is multilayer insulated. During the EPI process, the electrolyte temperature continuously increased to 95 °C (Fig. 8), which allowed us to record the current-voltage characteristics of the process at various temperatures and high-frequency current components with an oscilloscope. When the electrolyte solution reached a temperature of 95 °C, the process stopped and the mass of the removed material was determined.

Processing of experimental data. Based on the proposed model, knowing the composition of the electrolyte, we compose the reaction equation. The processing of samples from aluminum alloy was carried out in potassium salts of nitric or hydrochloric acid. Consider the example of potassium nitrate and aluminum:



When dissolved in water, KNO_3 dissociates into K^+ and NO_3^- ions, which, in turn, participate in the directed motion of charged particles, accelerating in an electric field.

Fig. 8 Working area



The calorimetry of the EPP process was carried out on a narrower sample of metals. Almost pure metals and alloys were processed. Their parameters are summarized in Tables 1, 2.

Processing mode: 300 V, initial temperature 70 °C (in the case of AMg5 with 80 °C), final 95 °C. The composition of the aqueous electrolyte solution: KNO₃—5%, C₆H₈O₇—3% [7–9, 21].

The energy required for ionization of a distant mass is determined by the formula:

$$E_i = M \cdot E$$

where, E_i is the calculated ionization energy of the removed metal, M is the molar mass of the removed metal, E is the energy of sequential ionization of the electron.

The calculated ionization energy for the treated metals is presented in Table 3.

Table 1 Energy sequential ionization of the processed materials

Metal	Molar mass, μ (g/mol)	Energy of sequential ionization of 1 electron, E (J/mol)	Energy of sequential ionization of 2 electron, E (J/mol)	Energy of sequential ionization of 3 electron, E (J/mol)	Energy of sequential ionization of 4 electron, E (J/mol)
Magnesium	24,305	737,778	1,450,682	7,732,758	–
Aluminium	26,981	577,600	1,660,734	2,744,090	11,578,000
Ferrum	55,845	762,479	1,561,160	2,957,423	5,499,550
Niccolum	58,693	737,141	1,752,976	3,393,448	5,596,033
Cuprum	63,546	745,574	1,958,122	3,551,295	5,682,868
Zincum	65,409	906,182	1,732,879	3,829,620	5,943,373

Table 2 The proportions of the components in the composition of the processed substance

Metal alloy	Remote mass (g)	Remote mole mass (mol)	Mole mass M and proportions of components							Impurities (%)
			Mg	Al	Fe	Ni	Cu	Zn		
AMg5	0.08	0.002951722	0.000164 (5.3%)	0.002787 (93.5%)						1.2
U12	0.545	0.009563972			0.009563 (98%)					1
NPA1	0.105	0.00177108				0.001771 (99%)				1
M1	0.445	0.006932773					0.0693277 (99%)			1
L63	0.395	0.006090074					0.003916 (63%)	0.002174 (36%)		1
Zn0	1.145	0.005751502						0.005751 (99%)		1

Table 3 Estimated ionization energy

Metal alloy	Ionization energy of a remote metal, J	Calculated ionization energy, J					
		Mg ²⁺	Al ³⁺	Fe ²⁺	Ni ⁴⁺	Cu ²⁺	Zn ²⁺
AMg5	7876	253	7623				
U12	14,726			14,930			
NPA1	9981				9981		
M1	13,575					13,575	
L63	11,435					7668	3767
Zn0	15,843						15,843

The results of processing the experimental data are summarized in Tables 4, 5.

The error of the total calculated and practical total energy does not exceed 2%, while the calculated ionization energy of the removed metal is significantly higher than the practical one. This is due to the fact that aluminum and copper can form substances with a valence of Al⁺ and Cu⁺ [37], which in turn requires less energy. Obviously, it is necessary to apply a correction factor that corrects the calculated results, but this has not been found in the literature.

The significance of this deviation can be estimated by comparing the energy cost components of the ionization removal mechanism with other known material removal mechanisms.

The comparison was carried out with mathematically simulated process models, which is the spark model of material evaporation. When comparing energy costs (Table 5), it is obvious that the mechanism of material evaporation in the discharge

Table 4 Calorimetric results of the EPI process

Metal alloy	Energy, J					
	AMg5	U12	NPA1	M1	L63	Zn0
Practical total energy	219,767	310,885	285,494	300,177	272,188	264,595
Practical heating energy	214,260	296,158	273,062	288,241	257,834	247,331
Practical remote energy	5507	14,726	9850	11,936	11,875	14,893
Calculated remote energy	7876	14,930	9981	13,573	11,435	15,843
Deviation of the practical from the calculated energy of metal removal	-2369	-204	-130	-1636	440	-949
Comparison of the calculated and practical total energy (%)	101.1	100.07	100.05	100.55	99.84	100.4
Comparison of the calculated and practical removal energy (%)	143	101.39	101.32	133.71	96.29	106.4

Table 5 Comparison of energy calculations for various mechanisms

Metal alloy	Energy	Model	
		Ionization	Spark
AMg5	Total	101.1	98
	Removal	143.0	18.4
U12	Total	100.1	96.6
	Removal	101.4	27.5
NPA1	Total	100.05	96.8
	Removal	101.32	7.7
M1	Total	100.5	96.9
	Removal	113.7	22
L63	Total	99.8	96.4
	Removal	96.3	17
Zn0	Total	100.4	97.2
	Removal	106.4	49.8

requires significantly less energy. The closest values to the practically expended energy according to the comparison results of the ionization mechanism.

In order to confirm the transition of the treated metal ions to the electrolyte solution, the solutions after treatment with a known amount of solute were titrated. The result confirms the transition of anode ions to solution with an accuracy of at least 98% regardless of the material of the treated anode (AMg5, U12, M1, 08KP, 20Kh13), which is a direct confirmation of the proposed model and a direct refutation of the results of other authors [16].

4 Practical Value

The formation of an electrolyte solution for the metal being treated is reduced to assessing the solubility of the salt formed as a result of processing. If you need to handle a wide range of materials, the rational use of nitrates, as they have a wide range of soluble metal salts and therefore provide the largest range of polished metals. In the case of polishing a particular metal, it is worth giving preference to cheaper salts, forming soluble compounds with this metal. The boundary of the production of an electrolyte solution when it is saturated with ions of the processed material still needs to be clarified, as well as the influence of the quantitative value of the solubility of salt.

When using ammonium salts to form an electrolyte solution, in the process of intensive work, active evolution of ammonia, changes in the pH of the solution, as well as the formation of colonies of microorganisms on the electrolyte mirror during downtime are observed. These factors negatively affect the workflow. To avoid this, metal-based salts should be preferred.

5 Conclusions

1. An ionization model of the EPP process is proposed, which matches the observed phenomena with physicochemical phenomena in the treatment zone.
2. The proposed model is experimentally confirmed by EPP of various metals and alloys.
3. The proposed model of the EPP process allows one to reasonably choose the process parameters and electrolyte composition both during polishing of metals and during the implementation of their oxidation processes.

References

1. Sluginov P (1882) Discharge of galvanic current through a thin layer of electrolyte. *Zh Fiz Total X*:241–243
2. Sluginov P (1882) About the light phenomena observed in liquids during their electrolysis. *Zh F H General X11*:193–203
3. Sluginov P (1882) *Reportorium der Exp. phys XVI*(11):333–339
4. Sluginov P (1883) About electrolytic glow. *Zh Fiz Total XV*:232–292
5. Muras VS (1956) Some elements of the process of electrolytic heating. In: *Proceedings of the physicochemical Institute. Academy of Sciences of the BSSR, Minsk*, vol 3, pp 53–58
6. Duraji VN, Bryantsev IV, Tokarov AK (1979) The study of erosion of the anode under the influence of electrolytic plasma. *Electron Process Mater* 5:15–19
7. Zakharov SV, Korotkikh MT (2016) Improving the technology of electrolyte-plasma polishing of aluminum alloy D16. *SPbPU Science Week, St. Petersburg*, pp 162–165
8. Zakharov SV, Korotkikh MT (2017) Electrolytic-plasma polishing of complex products from aluminum alloy D16. *Bulletin of the East Kazakhstan Concern “Almaz-Antey”* vol 3, pp 84–87. ISSN 2542-0542
9. Zakharov SV, Korotkikh MT, Volkov AA, Martsinkevich IA (2018) The influence of the components of the electrolyte solution on the lower boundary of the beginning of the process of electrolyte-plasma polishing. In: *Electrophysical processing methods in modern industry: materials of the II international scientific and practical conference of young scientists, graduate students and students (December 18–20, 2018)*. Publisher PNIIPU, pp 122–128
10. Popov AI, Radkevich MM, Novikov VI (2019) Features of the formation of an electric discharge between a jet electrolytic cathode and a metal anode at atmospheric pressure. *Thermophys High Temp* 57(4):1–12. <https://doi.org/10.1134/S0018151X19030118>
11. Patent GDR (DD) No. 238074 (A1), IPC C25F 3/16 publ. 08/06/1986
12. Parfyonov EV, Nevyantsva RR, Gorbatkov SA, Erokhin AL (2014) *Electrolyte-plasma processing: modeling, diagnostics, control: monograph*. Mashinostroenie, Moscow, 380p. ISBN 978-5-94275-732-8
13. Mirzoev RA (2013) *Anode processes of electrochemical and chemical processing of metals: textbook. manual*. In: Mirzoev RA, Davydov AD (eds) *Publishing house of the Polytechnic University, SPb*, 82p
14. Bakovets VV, Polyakov OV, Dolgovesova IP (1991) *Plasma-electrolytic anodic processing of metals*. Science. Siberian Dep., Novosibirsk, 168p
15. Sternberg Z (1970) Gas discharges. In: *International conference, London, Institute of Electrical Engineers, London*, pp 68–71
16. Hicling A (1971) Electrochemical processes in glow discharge at the gas solution interface. In: *Modern aspects of electrochemistry*, Butterworth, London, vol 6, pp 329–373

17. Polyakov OV (2001) Semi-empirical evaluation of cross sections and the efficiency of the formation of geminal pairs in water by slow protons. Electron J “Investigated Russia” [Electron Resour]. 143:1632–1641. Access mode: <http://zhurnal.ape.relarn.ru/articls/2001/143/pdf>. Date of access 05 May 2010
18. Goodman J, Hicling A, Schofield B (1973) The yield of hydrated electrons in glow-discharge electrolysis. *J Electroanal Chem* 48(2):319–323
19. Polyakov OV, Badalyan AM, Bakhturova LF (2003) The outputs of the radical products of the decomposition of water during discharges with electrolyte electrodes. *Chem High Energies* 37(5):367–372
20. Polyakov OV, Badalyan AM, Bakhturova LF (2005) The role of electrolyte concentration during water decomposition and electron generation under the conditions of anode microdischarges. *Chem High Energies* 39(2):140–142
21. Lazarenko BR et al (1971) Switching current at the metal—electrolyte interface. Chisinau: AN MSSR, 74p
22. Gaysin AF (2007) Multi-channel jet discharge between solid and electrolytic electrodes in the process of modifying materials at atmospheric pressure: abstract dis. Doct Tech Sciences: 01.02.05. Kazan state. tech. un-t them. A.N. Tupolev Kazan, 35p
23. Slovetsky DI, Slovetsky SD (2003) Terentyev parameters of an electric discharge in electrolytes and physicochemical processes in an electrolyte plasma. *Chem High Energies* 37(5):355–361
24. Maximov AI, Titov VA, Khlyustova AV (2004) Radiation from a glow discharge with an electrolyte cathode and the processes of transfer of neutral and charged particles from a solution to a plasma. *Chem High Energies* 38(3):227–230
25. Reter G (1968) Electronic avalanches and breakdown in gases: trans. from English under the editorship of V.S. Komelkova. Mir, Moscow, 390p
26. Reiser YuP (1980) Fundamentals of gas discharge processes. Nauka, Moscow, 416p
27. Lieberman MA, Lichtenberg AJ (2005) Discharges and materials processing. Principles of plasma. Wiley, ISBN 0-471-72001-1
28. Kulikov IS, Vashchenko SV, Kamenev AY (2010) Electrolyte-plasma processing of materials. Belarusian Science, Mn, 231p
29. Novikov VI (2010) Improving the efficiency of manufacturing complex parts from alloy steels by electrolyte-plasma polishing. SPbSPU
30. Panov DO, Abyaz TR, Abrosimova AA (2014) Electron-microscopic analysis of the surface of 65 g steel after electrical discharge machining. In: Modern problems of science and education, vol 2. <http://www.science-education.ru/en/article/view?id=12610>. Date of access 21 Dec 2019
31. Cornelsen M, Deutsch C, Seitz H (2018) Electrolytic plasma polishing of pipe inner surfaces. *MDPI Metals* 8:12
32. Plotnikov NV, Smyslov AM, Timindarov DR (2013) To the question of the model of electrolyte-plasma polishing of the surface. *Bulletin of UGATU*, T.17 4(57):90–95. Ufa: USATU
33. Duraji VN, Parsadanyan AS (1988) Heating of metals in electrolyte plasma. Under the general. In: Parsadanyan (ed) Shtiintsa, Chisinau, 216p
34. Shiryaeva SO, Grigoryev AI, Morozov VV (2003) About some features of the appearance of ions near the charged surface of an intensively evaporating electrolyte. *J Tech Phys* 73(7):21–27
35. Grigoryev AI (2004) On the transfer of energy and the formation of an electric current in the vicinity of an electrode lowered into an electrolyte, strongly heated by a flowing current. *J Tech Phys* 74(5):38–43
36. Ivanova NP, Sinkevich YuV, Sheleg VK, Yankovsky IN (2013) The mechanism of anodic dissolution of corrosion-resistant and structural carbon steels in the conditions of electric pulse polishing. *Sci Technol* 1:24–30
37. Plasma Electrolytic Polishing (2016) An overview of applied technologies and current challenges to extend the polishable material Range. In: 18th CRIP conference on electro physical and chemical machining (ISEM XVIII). *Procedia CIRP*, vol 42, pp 503–507

Research and Development of a Spring Drive with Recovery Energy in the Presence of a Variable Inertial Load



Victor L. Zhavner, Wen Zhao, Chuanchao Yan and Long Wu

Abstract A spring drive with energy recovery, working with an external variable inertial load that occurs in devices for unwinding and pulling packaging material in packaging equipment, is considered. In order to reduce energy costs, the device does not have a brake installed on the supporting device for a roll with packaging material, due to this, areas with freely sagging packaging material appear. Operating modes are considered when the packaging material is not stretched and in this case the energy consumption is minimal. In the case of tension of the packaging material, an external inertial load appears due to the acceleration of the roll with the packaging material to the required maximum speed of the spring drive carriage. The dependence for determining the turn-off coordinate of the pneumatic drive depending on the current value of the mass of the roll is determined.

Keywords Spring drive · Energy recovery · Pneumatic cylinder · External inertial load · Spring battery · Dissipative losses

1 Introduction

Reducing energy consumption by process equipment remains a priority. There is an extensive range of tasks in which the working bodies make reciprocating movements with high energy costs due to the acceleration and braking of the working masses (machine elements). Moreover, with an increase in productivity, for example, by 2 times, energy consumption increases by 4 times, and the required engine power by 8 times [1]. Energy costs can be reduced by using mechatronic spring motors with energy recovery.

The history of the development of mechatronic spring drives began with a mechanical arm developed by Electrolux (Sweden) for loading stamping equipment [2]. In practice, it was a robotic system combining a feed conveyor, a mechanical arm with a mechatronic spring drive, stamping equipment, an information-measuring system, and a control device. The spring drive, built on the basis of a spiral spring, provided

V. L. Zhavner · W. Zhao (✉) · C. Yan · L. Wu
Peter the Great St. Petersburg Polytechnic University, St. Petersburg, Russia

© Springer Nature Switzerland AG 2020
A. N. Evgrafov (ed.), *Advances in Mechanical Engineering*,
Lecture Notes in Mechanical Engineering,
https://doi.org/10.1007/978-3-030-39500-1_21

acceleration and braking and a controlled technological dwell. The spring-loaded spiral drive completely coincided with the drive explaining the operation of the reciprocating compressor, in accordance with the German patent [3] obtained by L. Szilard and A. Einstein in 1932.

The initial stage of development of spring drives with energy recovery was characterized by the study of spring drives using spiral springs [4] pp. 218–224, and an electric drive to compensate for dissipative losses. There, the ultimate performance characteristics were determined. At the same time, mechatronic spring drives using standard helical coil springs [5, 6] were proposed, which made it possible to increase the mass of transported products. At low speed, hydraulic drives can be used to compensate for dissipative losses, while simultaneously securing the output link in extreme positions. It was shown in [7] that the use of pneumatic cylinders to compensate for dissipative losses provides the highest speed, while the appearance on the market of pneumatic cylinders with brakes ensures that the drive output link is fixed in extreme positions. Since the mechatronic spring drive is a self-oscillating system, in which to maintain the required period of oscillations, it is possible to construct a control system in accordance with the Erie theorem [8, 9].

In [10], the use of mechatronic regenerative drives in robotic systems was examined in detail, and in [11, 12] for the automation of loading and auxiliary operations.

In [13], a mechatronic spring drive was considered, in which a pneumatic cylinder with a compression spring located in the rod cavity was used. In this case, the main power element of the drive is a non-linear spring battery. It is shown in the work that in the particular case, if the preliminary spring force is equal to the product of the spring stiffness by a number equal to the minimum distance between the axis of the hinged joint of the pneumatic cylinder body and the guides, the spring accumulator acquires the properties of a linear oscillator. We also note the work [14] in which nonlinear spring accumulators with an output rotary link are considered and, when used in mechatronic springs, the drives provide a sinusoidal law of variation of speed and acceleration [15]. With regard to the smoothness of motion, this law does not seem to be much better: both speed and acceleration theoretically change continuously, and they begin and end their change with zero values. In [16], nonlinear spring accumulators with an output link performing reciprocating movements at various values of spring pretension in the neutral position were studied. In [17], mechatronic spring actuators based on pneumatic cylinders with return springs were investigated. In all the works discussed above, drives with no technological load with constant mass were considered and their use reduces energy costs for the selected type of work operations by 5 times.

The aim of this work is to study a mechatronic spring drive with energy recovery in the presence of a variable inertial load that occurs, in particular, in devices for unwinding and pulling packaging material in packaging equipment.

2 Research Methods and Results

A typical example of the possible use of mechatronic spring drives with energy recovery in devices for unwinding and pulling packaging material operating in discrete mode is studied. Figure 1 shows a diagram of the device under study, consisting of a pneumatic drive, a roll with packaging material, guides and tension rollers, and a device for folding the packaging tape. Note the following features of the device:

1. A variable moment of inertia of the roll, since during the operation both the diameter of the roll and its mass decrease.
2. The device does not have a brake, which in typical devices provides constant tension of the packaging material, so the following configurations of packaging material are possible. The first configuration with a constant tension of the packaging material, the second configuration, when the length of the sagging material provides the device with a stationary roll. The third configuration, when the start of work occurs when the roll is stationary, the packaging material is pulled and then its rotation begins.
3. There are restrictions on the collision speed of the drive carriage with the stop block. This is due to the fact that during the packing of loose materials, many loose materials behave like a liquid and can rise up at the edge of the bag at high collision speeds.

When the axis of the tension roller is at point O_1 , the packaging material is tensioned and the roll is stationary. When the drive is turned on, we have an inertial load mode, depending on the current value of the moment of inertia of the roll.

If the axis of the tension roller is between points O_1 and O_2 , it is necessary to accelerate the roll with the packaging material to an angular speed when the linear speed of the packaging material that escapes from it becomes equal to the linear

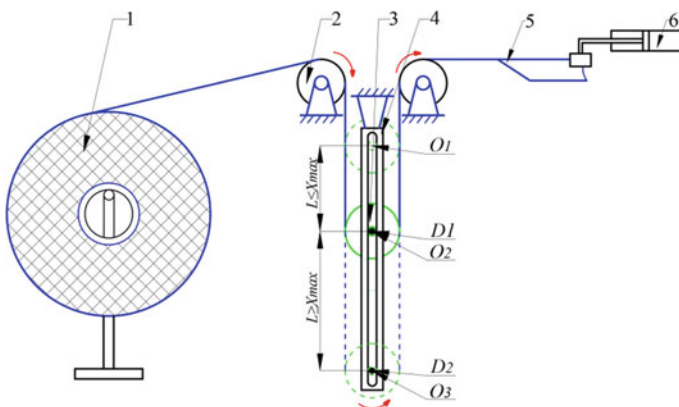


Fig. 1 Diagram of a device for unwinding and pulling packaging material. 1—roll, 2—guide roller, 3—tension roller, 4—guide, 5—packaging material, 6—pneumatic cylinder

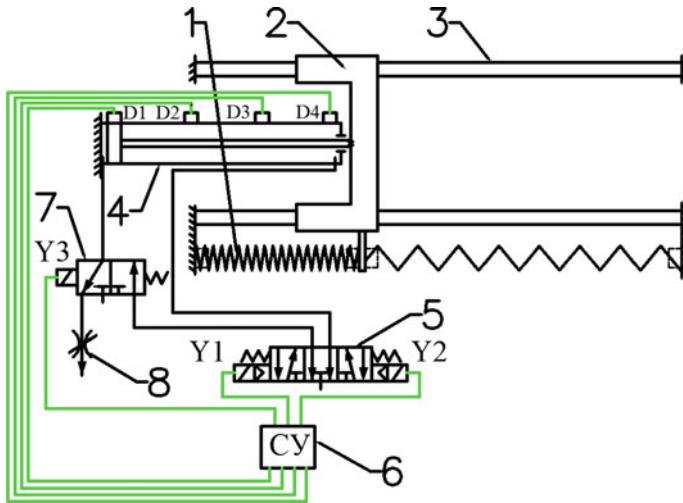


Fig. 2 Diagram of a mechatronic spring drive with energy recovery and using a pneumatic cylinder to compensate for dissipative losses

speed of the drive carriage. In this case, we are dealing with an inertial load, but it does not occur immediately.

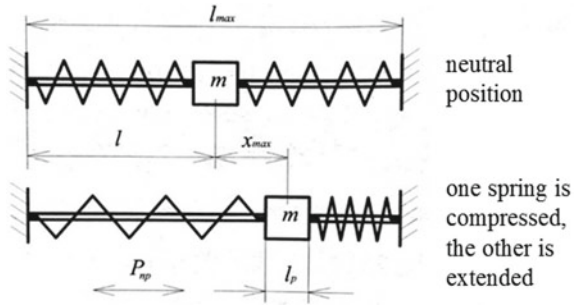
If the axis of the tension roller is located between points O_2 and O_3 , then there is no variable inertial load, since the roll is stationary during the process of pulling the packaging material, and the axis of the tension roller rises vertically by an amount equal to half the stroke of the device for pulling. Work without inertial load occurs until the axis of the tension roller is above the point O_2 .

From the point of view of reducing energy costs for pulling the packaging material, it is advisable to have a sufficiently large length of sagging packaging material, since in this case there are no energy costs for accelerating the roll.

Figure 2 shows a mechatronic spring drive with energy recovery for pulling packaging material using a pneumatic cylinder to compensate for dissipative losses.

The considered spring drive consists of a linear spring battery with two tension springs installed on both sides of the carriage 2, moving along the guides 3. To compensate for dissipative losses, a pneumatic cylinder 4 is used, the working cavities of which are connected to the distributor 5, the electromagnetic drives of which Y1 and Y2 are connected to the control system 6. In addition, on the case of the pneumatic cylinder 4, position sensors D1, D2, D3 and D4 are installed, the outputs of which are connected to the control system 6. The drive is also equipped with an additional distributor 7, the electromagnetic drive Y3 of which is also connected to the control system 6. The input of the pneumatic distributor 7 is connected to one of the outputs of the pneumatic distributor 5, and the second input of the distributor 7 is connected to the atmosphere through an adjustable throttle 8. The distributor 7 is designed for pre-charging the spring battery.

Fig. 3 Diagram of a spring battery with two tension springs



Mechatronic spring recovery drives with energy recovery are self-oscillating systems with external energy pumping to compensate for dissipative losses. All the main characteristics of such drives are determined by the used spring batteries.

Without taking into account dissipative losses, the considered spring drive is a conservative linear oscillator with an oscillation frequency independent of the amplitude, therefore, in this case, all the dependencies used for linear oscillators are applicable. To compensate for dissipative losses, a double-acting pneumatic cylinder 1 with a pneumatic distributor 2 is used, in which the cavities of the pneumatic cylinder are connected to the atmosphere in the neutral position. This drive configuration allows to programmatically organize, in accordance with Erie’s theorem [10], any possible option for the pneumatic cylinder to compensate for dissipative losses and to ensure maximum carriage speed in the middle position, which provides kinetic energy in the middle position for potential energy accumulation in the device and coming to an extreme position. Figure 3 shows a diagram of a spring battery with two tension springs.

In the spring battery in question, the working elongation of each spring is:

$$h_{max} = 2x_{max} \tag{1}$$

The maximum potential energy of each spring is equal to:

$$U_{max} = 0.5c \cdot h_{max}^2 = 2cx_{max}^2 \tag{2}$$

In the neutral position of the system, the potential energy of the spring battery is minimal and equal to the effective potential energy:

$$U_3 = cx_{max}^2 \tag{3}$$

The total spring stiffness is $2c$ and the oscillation half-period t is equal to:

$$t = \pi \sqrt{\frac{m}{2c}} \tag{4}$$

Spring force during working deformation:

$$F_2 = 2cx_{\max} \quad (5)$$

The maximum speed is equal to:

$$\dot{x}_{\max} = \frac{\pi}{t} \cdot x_{\max} \quad (6)$$

where t is the set travel time between the extreme positions.

The maximum acceleration is equal to:

$$\ddot{x}_{\max} = \frac{2cx_{\max}}{m} \quad (7)$$

The work to overcome dissipative forces is equal to:

$$A_d = \varphi U_{\max} \quad (8)$$

where φ is the loss coefficient in the spring battery

From the equation of mechanical energy of the system without taking into account dissipative losses, having the form:

$$U_{\max} = U_T + T_T, \quad (9)$$

after transformations, Eq. (9) will sequentially take the form:

$$cx_{\max}^2 = cx_T^2 + \frac{1}{2}m\dot{x}_T^2 \quad (10)$$

and

$$\frac{x_T^2}{x_{\max}^2} + \frac{\dot{x}_T^2}{x_{\max}^2 \cdot \frac{2c}{m}} = 1 \quad (11)$$

which corresponds to the ellipse equation:

$$\frac{x_T^2}{a^2} + \frac{\dot{x}_T^2}{b^2} = 1$$

where:

$$a^2 = x_{\max}^2 \quad (12)$$

$$b^2 = \frac{\pi^2}{t^2} \cdot x_{\max}^2 \quad (13)$$

Figure 4 shows the graphs of speed and acceleration when the system parameters in the stroke and idle modes are the same and there is no external inertial load.

After the middle carriage passes through its middle position, its speed decreases and if before that the packaging material was pulled and the roll with packaging material rotated, the roll will continue to rotate in the free-run mode, and the speed of the carriage will also decrease due to inertia forces, in accordance with Eq. (10).

Figure 5 shows the cyclograms of the operation of the spring drive and the inclusion of the pneumatic cylinder in various modes.

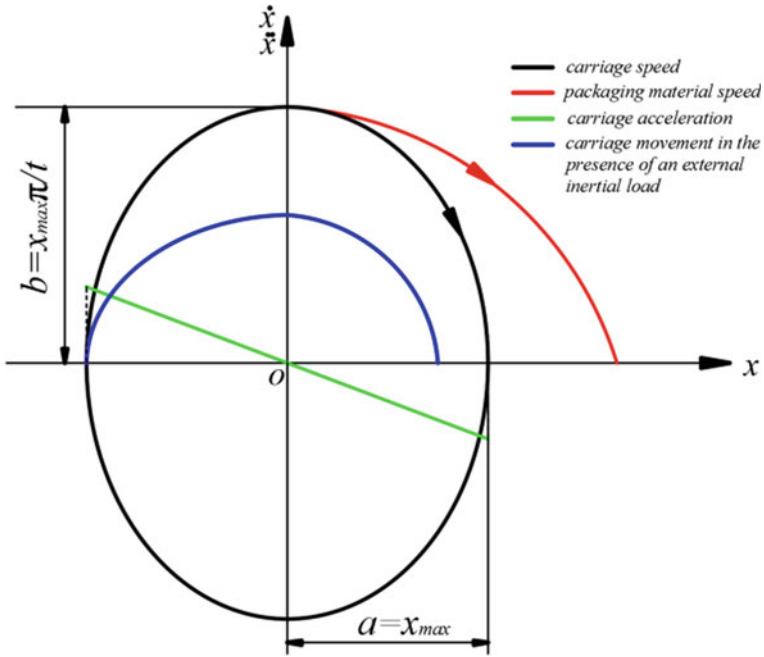


Fig. 4 Graphs of speed and acceleration of the output link of the spring drive

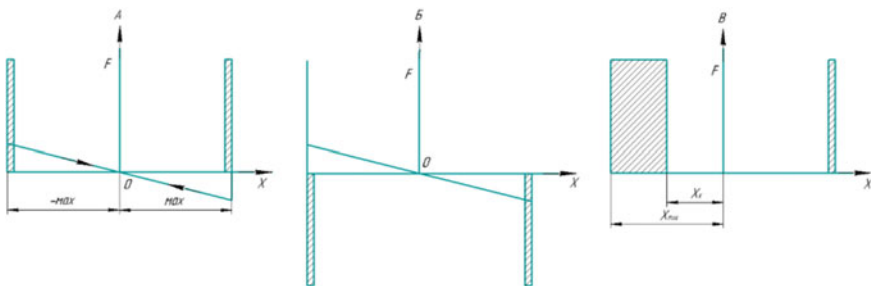


Fig. 5 With three cyclograms

Figure 5a shows the cyclogram for turning on the pneumatic cylinder at the beginning and end of displacement to compensate for dissipative losses, which provides the upper part of the curve in Fig. 4.

Figure 5b shows the cyclogram for turning on the pneumatic cylinder in idle mode.

If there is an external inertial load during the working stroke, in order to ensure maximum speed when the carriage passes through the middle position, the duration of the pneumatic cylinder activation increases and depends on the current value of the moment of inertia of the roll. Figure 5d shows the cyclogram for turning on the pneumatic cylinder, where the coordinate x_k corresponds to the coordinate of the carriage at which the pneumatic cylinder is turned off.

If for a working stroke in the presence of an external inertial load, use the cyclogram in Fig. 5a. then the blue curve shows the curve of the change in the speed of the carriage from its coordinate. It is seen that the kinetic energy of the carriage will be less than required and it will not reach the extreme position. In connection with these increases the duration of the inclusion of the pneumatic cylinder. Let us determine the coordinate for turning off the pneumatic cylinder.

The equation of mechanical energy for this regime has the form:

$$U_3 + F_{\Pi} \cdot (x_{\max} - x_k) = 0.5 \cdot m_{np} \cdot \dot{x}_{\max}^2 \quad (14)$$

From Eq. (14) can find the value of the turn-off coordinate of the pneumatic cylinder:

$$x_k = x_{\max} - \frac{0.5 \cdot m_{np} \cdot \dot{x}^2 - U_3}{F_{\Pi}} = x_{\max} - \frac{0.5 \cdot m_{np} \cdot \dot{x}^2 - c x_{\max}^2}{F_{\Pi}} \quad (15)$$

The choice of parameters for a pneumatic cylinder is determined from two conditions:

1. The force on the rod of the pneumatic cylinder F_{Π} must be equal to or greater than the maximum spring force. In this case, locking in the extreme positions automatically occurs and there is no need to install controlled clamps, which simplifies the design and increases the reliability of the drive.
2. The speed of the rod at the time of turning on or off the pneumatic cylinder must be higher than the speed of the spring battery. As a rule, the maximum rod speed of a pneumatic cylinder is in the range of 0.5–1 m/s. Otherwise, the pneumatic cylinder will begin to perform the function of the brake

Determine the length of the packaging material being rewound after the middle carriage has passed with a rotating roll, since get two dynamic systems: a freely rotating roll with a wrapping packaging material and a carriage in which the kinetic energy of the elements performing a rectilinear motion passes into the potential energy of a spring drive.

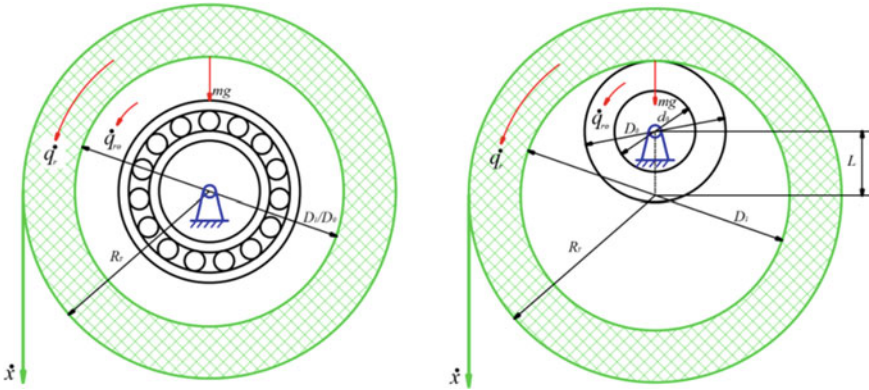


Fig. 6 Two options for installing the roll on the supporting device

The kinetic energy of a rotating roll is determined from the expression:

$$T = \frac{1}{2} \cdot J_T^* \cdot \frac{\dot{q}_{\max}^2}{2} = \frac{1}{2} \cdot \frac{1}{2} \cdot m_T \cdot R_T^2 \cdot \frac{\dot{x}_{\max}^2}{R_T^2} = \frac{1}{4} \cdot m_T \cdot \dot{x}_{\max}^2 \quad (16)$$

Figure 6 shows two options for installing the roll on the supporting device: one is a typical version, when the axis of the roll coincides with the axis of rotation of the supporting device, in the second version, the roll is freely mounted on the supporting device and a friction gear is formed, while the supporting device has an angular velocity greater than the angular velocity roll.

The moment of friction in the support is determined from the expression:

$$M_{\text{on}} = 0.5 \cdot m_T \cdot g \cdot f \cdot d \quad (17)$$

The work of the friction forces during the free run of the roll to a complete stop is

$$A = 0.5 \cdot m_T \cdot g \cdot f_{\text{np}} \cdot d \cdot q \quad (18)$$

From the joint solution of Eqs. (17) and (18) we obtain an expression for determining the angle of rotation of the roll q to its full stop

$$q = \frac{\dot{x}_{\max}^2}{2gd f_{\text{np}}} \quad (19)$$

which allows to determine the length of the material being wound:

$$L = q \cdot R_T = \frac{\dot{x}_{\max}^2}{2gd f_{\text{np}}} \cdot R_T \quad (20)$$

When the roll is freely mounted on a rotating support (see Fig. 6). In the case, the angle of rotation of the support device is

$$q = \frac{\dot{x}_{\max}^2}{2gd_{\text{np}}} \cdot \frac{D}{d} \quad (21)$$

In this case, the length of the wrapped packaging material with a free run-out will decrease by D/d , since the work to overcome the friction forces is increased.

From Eq. (20) it follows that the length of the material being wound is determined by the design parameters, the maximum speed of the carriage and the current value of the roll radius. With the maximum radius of the roll, the largest length of wrapped packaging material takes place

Define the relationship between the geometric and inertial characteristics of the roll.

Consider the roll as a solid disk, then the moment of inertia of the roll of packaging material is determined from the expression:

$$J = 0.5 \cdot m_{\text{T}} R_{\text{T}}^2 \quad (22)$$

where R_{T} is the current value of the radius of the roll

m_{T} is the current value of the mass of the roll

The maximum angular velocity of rotation of the roll \dot{q} is equal to:

$$\dot{q} = \frac{\dot{x}_{\max}}{R} \quad (23)$$

where \dot{x}_{\max} is the maximum tape speed

The design characteristics of the drive are reduced mass. The work is interested in the relationship between the reduced mass of the coil and its current mass.

The estimated mass m_{p} includes the reduced mass of the coil to the spring drive carriage m_{np} and the mass $m_{\text{дч}}$ of all moving translational elements of the drive, for example, the mass of the carriage, rod and piston of the pneumatic cylinder, the mass of the gripper.

$$m_{\text{p}} = m_{\text{np}} + m_{\text{дч}} \quad (24)$$

the relationship between the reduced mass of the roll and the actual value of

$$m_{\text{np}} = 0.5m \quad (25)$$

As can be seen from Eqs. (24) and (25), both the calculated and reduced masses are variable and depend on the current value of the mass of the roll with packaging material.

3 Results Discussion

The developed mechatronic spring drive for unwinding and pulling packaging material using a pneumatic cylinder to compensate for dissipative losses can also be used when working with external inertial loads, reducing energy costs and providing favorable dynamic modes of operation.

It is shown that in the mode when the packaging material is stretched, the linear speed of the packaging material is equal to the speed of the spring drive carriage. When passing the middle position of the carriage, the maximum kinetic energy of the system is achieved and two dynamic systems arise: the free run-out of the roll and the corresponding unwinding of the packaging material until the roll stops completely and the carriage moves to the stop.

The length of the rewind tape during free run-out does not depend on the mass of the roll, but depends only on the current value of the outer diameter of the roll and the peripheral speed of the packaging material at the time the free-run starts.

The next study, taking into account the results obtained, will be associated with the use of timer control in the construction of control systems

The developed mechatronic spring drive reduces energy costs due to energy recovery and the choice of operating modes taking into account the current value of the mass of the coil and the automatic determination of the configuration of the packaging material and the value of the current value of the mass of the coil.

The results of the work were used in the development of a mechatronic pneumatic drive system for a filling and packaging machine for bulk products. The results of the work can be used by developers of energy-saving technological equipment.

4 Conclusion

The problem of using a spring drive with energy recovery in the presence of an external variable inertial load is solved. Further development of the work will be the study of the possibility of using timer control of the moment the pneumatic cylinder is turned off, which will further reduce energy consumption, simplify the design and increase the reliability of the system.

Further research will determine the ultimate performance for this type of drive.

References

1. Zhavner VL, Matsko ON, Zhavner MV (2014) Recuperative drives for cyclic movements. Saarbrücken, Palmarium Academic Publishing, Deutschland, p 90
2. Kellhoff G (1897) La formule d'Airy-Mem Acad Bel 5(11)
3. Patentschrift No. 562040 Dr. Leo Szilard und Dr. Albert Einstein (1933) Elektromagnetische Vorrichtung zur Erzeugung einer oszillierenden Bewegungen. Prioritätsdatum 1. Juni 1928

4. Korendyasev AI, Salamander BL, Tyves LI (2006) Theoretical foundations of robotics. In 2 book. Science, Moscow, 376p
5. Zhavner VL, Feokstistova NA, Yezhov GG (1987) Russian patent No. 1283083. Link moving drive. 1/15/87. Blue, No. 2. 5s
6. Babitsky VI, Kotlyachkov AA, Chechurov VA, Shipilov AV (1990) Russian patent No. 1544550. Resonant drive. 02/23/90. Bleu. No. 7 5s
7. Zhavner VL, Matsko ON (2016) Spring drives for reciprocal motion. J Mach Manuf Reliab 45(1):1–5 (Allerton Press, Inc., Moscow)
8. Landau LD, Lifshits EM (1988) Theoretical physics. M.: In 10 vol. T. 1: Mechanics. Moscow, Science, Ch. ed. Phys.-Math. lit., 1988. 216s
9. Bautin NN (1986) Dynamic clock theory. Nauka, Moscow, 192s
10. Levin AI (1978) Mathematical modeling in research and design of machines. M., “Engineering”, 184s
11. Nazemtsev AS (2004) Hydraulic and pneumatic systems. Part 1. Pneumatic drives and automation: A training manual. FORUM, Moscow, 240s, ill
12. Sysoev SN, Glushkov AA (2010) Cycle drives of the oscillatory type: monograph. Feder. Education Agency, Vladimir. state un-t. Publishing house Vladimir. state University, Vladimir, from 184
13. Nadezhdin IV (2008) Highly dynamic mechanisms of auxiliary operations of automated assembly plants. Mechanical Engineering, Moscow, 270s
14. Kolchin NI (1972) Mechanics of machines. T. 1. Engineering, 456p
15. Pelupessi DS, Zhavner MV (2016) Spring batteries for step drives. Modern Engineering. Science and education, Moscow, vol 5, 499–509s
16. Wen Z, Leonidovich ZV (2019) The use of pneumatic cylinders with a return spring to compensate for balance losses in mechanical regenerative drives for reciprocating movements. In: 6th international BAPT conference “Power Transmissions 2019” 2019 VARNA, vol 1, pp 107–112
17. Zhao V, Zhavner VL, Smirnov AB, Yan Ch (2019) The use of pneumatic cylinders with return springs in mechatronic and regenerative drives, Scientific and technical statements of St. Petersburg Polytechnic University. Natural and engineering sciences, vol 25, no 1, pp 111–123

Research of Spring Accumulators with Output Rotary Link Used in Technological Equipment to Reduce Energy Consumption



Milana V. Zhavner, Sen Li and Chuanchao Yan

Abstract Mechatronic spring drives with energy recovery for step movements based on pneumatic cylinders with return springs are investigated. Mechatronic spring drives are used in conveyor lines and rotary tables of filling and packaging equipment of the food and pharmaceutical industries. Mathematical models of the spring accumulator with pre-tensioning of the spring are built. A mechatronic spring drive has been developed for rotary tables of a filling and packaging machine, using two pneumatic cylinders. One of the pneumatic cylinders with a return spring. The second pneumatic cylinder provides the output of the rotary link from the position of unstable equilibrium in which the system is located during technological dwell. Dependences are given for determining dissipative losses in the elements of a spring accumulator, the total values of which determine the energy consumption of the engine to compensate for dissipative losses. The energy costs in the considered drives are several times less than the energy costs in other types of drives. The scheme of a mechatronic spring drive for rotary tables of filling and packaging equipment using two pneumatic cylinders with return springs has been developed.

Keywords Spring drive · Dissipative losses · Energy recovery · Pneumatic cylinders with return springs

1 Introduction

In cyclic drives in the extreme positions of which a controlled dwell is provided [1, 2], energy consumption is reduced by using mechatronic spring drives with energy recovery [3–5], while energy consumption can be reduced several times [6–8]. Traditionally, a mechatronic spring drive with energy recovery contains a linear or non-linear spring battery, a control system, controlled clamps and an engine to compensate for dissipative losses [9–11]. When moving products with sufficiently large masses

M. V. Zhavner (✉) · S. Li · C. Yan (✉)
Peter the Great St. Petersburg Polytechnic University, St. Petersburg, Russia

S. Li
e-mail: 15952261994@163.com

© Springer Nature Switzerland AG 2020
A. N. Evgrafov (ed.), *Advances in Mechanical Engineering*,
Lecture Notes in Mechanical Engineering,
https://doi.org/10.1007/978-3-030-39500-1_22

(more than 1000 kg) and at low speed, it is advisable to use a hydraulic drive to compensate for dissipative losses. The use of electric motors to compensate for dissipative losses is limited by low speed, since the compensation of dissipative losses occurs throughout the movement and, at high speed, engine power increases, and gears with a large gear ratio are required [12]. At high speed, it is preferable to use pneumatic cylinders, which, in addition to compensating for dissipative losses, provide fixation of the output link in the extreme positions [13–15].

2 Statement of the Problem and Research Methods

This paper discusses mechatronic drives with energy recovery for step movements. Such drives are built on the basis of non-linear spring batteries with an output rotary link [3–5]. Pneumatic cylinders are used to compensate for dissipative losses. Also, in drives with one-sided load, pneumatic cylinders with return springs are used [12]. In this paper, it is proposed to use pneumatic cylinders with return springs in step-by-step drives that perform three functions: a spring accumulator, an engine for compensating dissipative losses, and a fixing device.

3 Research Methodology

The object of research is mechatronic spring drives with energy recovery for step movements using pneumatic cylinders with return springs. Traditionally, such pneumatic cylinders are used in drives with one-sided load, where the return springs provide, after completing the operation, the movement of the working body to its original position. Since these pneumatic cylinders contain the basic elements necessary and sufficient for the implementation of mechatronic spring drives with energy recovery, the task is to analyze the characteristics of pneumatic cylinders and the synthesis of mechatronic spring drives with energy recovery to obtain step movements, for example, for turntables of packaging and packaging equipment, which will ultimately simplify their design, increase reliability, reduce costs for both design and energy consumption during operation.

The mechatronic spring drive for step movements is a self-oscillating system consisting of a non-linear spring battery, an engine for compensating dissipative losses, an information-measuring system and a control system [15–17]. To compensate for dissipative losses, it is preferable to use pneumatic engines with the highest speed.

In Fig. 1 shows a step mechatronic drive with energy recovery, constructed using pneumatic cylinders with return springs located in the rod cavity. The mechatronic stepper drive is implemented according to the scheme of a non-linear spring battery with a single spring.

The rotary Table 1 is connected by a transmission with a flexible connection 2 with a rotary link 3, which is pivotally connected to two pneumatic cylinders.

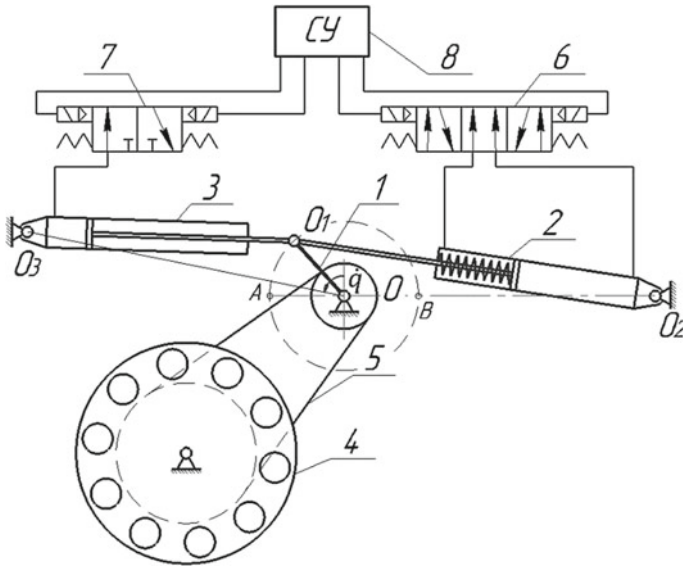


Fig. 1 Diagram of a stepper drive with energy recovery and the use of pneumatic drives. 1—rotary link, 2—pneumatic cylinder with return springs, 3—pneumatic cylinder, 4—rotary table, 5—toothed belt drive, 6—pneumatic distributor 5/3, 7—pneumatic distributor 3/2, 8—control system

Table 1 The value of the coefficient K_{tq} depending on the parameters \bar{s}_1 and a'

	2	4	6	8	10	12	14	16
0	21.74	20.00	19.38	19.07	18.88	18.75	18.66	18.59
1	17.61	16.17	15.67	15.41	15.25	15.15	15.07	15.01
2	15.20	13.95	13.51	13.29	13.15	13.06	12.99	12.95
3	13.57	12.45	12.06	11.86	11.74	11.65	11.59	11.55
4	12.37	11.35	10.99	10.81	10.70	10.62	10.57	10.53
5	11.44	10.50	10.17	10.00	9.89	9.82	9.77	9.74
6	10.70	9.81	9.50	9.34	9.25	9.18	9.14	9.10
7	10.08	9.25	8.95	8.80	8.71	8.65	8.61	8.67
8	9.56	8.77	8.49	8.35	8.26	8.20	8.16	8.13
9	9.11	8.36	8.09	7.96	7.87	7.82	7.78	7.75
10	8.72	8.00	7.75	7.62	7.53	7.48	7.45	7.42

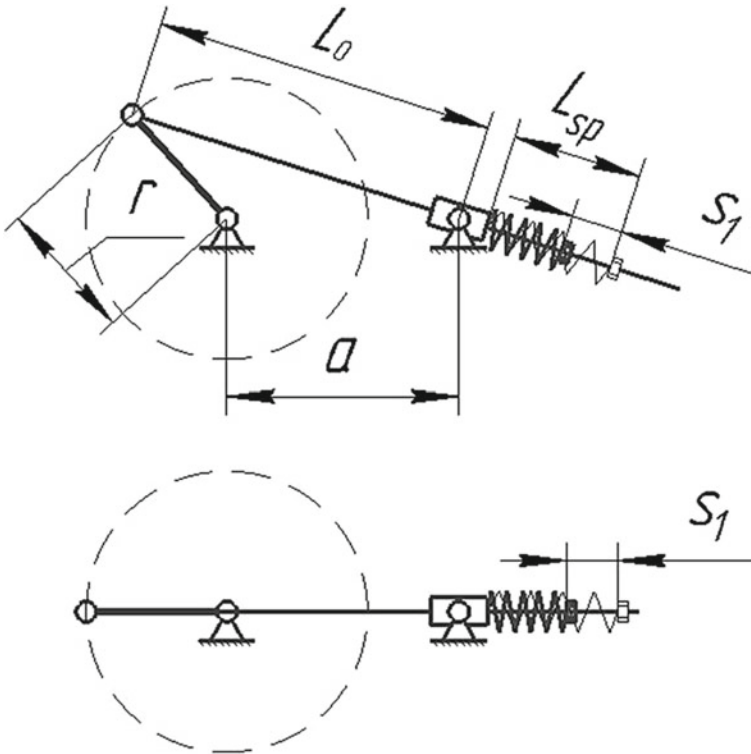


Fig. 2 Nonlinear spring accumulator with output rotary link based on compression spring

A diagram of a non-linear spring battery with an output rotary link for step movements is shown in Fig. 2.

Figure 2 shows a diagram of a spring battery on the basis of which mechatronic spring drives with energy recovery for step movements are built [3–5]. A feature of the spring battery shown in Fig. 2, is the presence of pre-compression of the spring S_1 , which provides a minimum spring force F_H (show Table 1.)

The geometrical characteristics of the spring battery is:

a —the distance between the axes of the ball joints of the output rotary link and the rocker rock mechanism.

R —is the radius of the output rotary link.

L_0 —is the size between the axis of the swivel of the output link, with the link that performs translational motion, in a stable equilibrium position.

The energy characteristics of a spring battery are: potential energy $V(q)$ and moment characteristic $M(q)$.

We determine the characteristics of spring batteries using pneumatic cylinders with return springs.

$$s_1 = F_H/c \tag{1}$$

Then the minimum potential energy of the spring is

$$V_{\min} = 0.5F_H^2/c \tag{2}$$

The maximum potential energy of the spring is

$$V_{\max} = 0.5c(h + s_1)^2 = \frac{1}{2}c(2r + s_1)^2 \tag{3}$$

Current value of potential energy

$$V_T = \frac{1}{2}c\Delta L_{sp}^2 \tag{4}$$

ΔL_{sp} —current spring extension

$$\Delta L_{sp} = \sqrt{r^2 + a^2 + 2ar \cos q} - (L_0 - s_1) \tag{5}$$

In view of Eq. (5), expression (4) takes the form

$$V_T = \frac{1}{2}cr^2\left(\sqrt{1 + a'^2 + 2a' \cos q} - (\bar{L} - \bar{s}_1)\right)^2 \tag{6}$$

Where s_1 —is the value of spring precompression.

$a' = \frac{a}{r}$, $\bar{L} = \frac{L_0}{r}$, $\bar{s}_1 = \frac{s_1}{r}$ —dimensionless coefficients defining geometric relations.

When using standard pneumatic cylinders with return springs, the force characteristics of the spring are set: F_H, F_K , and the stroke of the rod h , which makes it possible to determine the spring stiffness c and the value of the spring precompression s_1 .

In the general case, a work operation that is associated with step movements is determined by three parameters:

q —the maximum angle of rotation,

t —the rotation time at the maximum angle,

J —the reduced moment of inertia of the rotation mechanism, reduced to the axis of rotation of the output link of the spring battery.

In [3], the problem was solved for determining the time of rotation of the spring accumulator by an angle equal to 2π , when $s_1 = 0$.

The basic rotation time for a given reduced moment of inertia J is determined by the stiffness of the spring c and the design parameters of the spring battery: dimensions a and r .

$$t = \sqrt{\frac{J}{2}} \cdot \int_0^{2\pi} \frac{dq}{\sqrt{V_{\max} - V_T}} \tag{7}$$

Equation (7) can be written as

$$t = \int_0^{2\pi} \frac{dq}{\dot{q}(q)} = \frac{1}{r} \sqrt{\frac{J}{c}} \cdot K_{tq} \quad (8)$$

where

$$K_{tq} = \int_0^{2\pi} \frac{dq}{\sqrt{(2 + \bar{s}_1)^2 - \left(\sqrt{1 + a'^2 + 2a' \cos q} - (\bar{L} - \bar{s}_1)\right)^2}} \quad (9)$$

Table 1 presents the value of the coefficient depending on the parameters \bar{s}_1 and a' .

As can be seen from Table 1, with an increase in the value of the parameters \bar{s}_1 , a' and the coefficient K_{tq} decreases, which means that the speed increases.

The maximum value of the reduced moment of inertia J for known values of K_{tq} and a given value of t , after the conversion of Eq. (8), we obtain from the following expression

$$J = \frac{t^2 \cdot r^2 \cdot c}{K_{tq}^2} \quad (10)$$

Table 2 presents the characteristics of pneumatic cylinders with return springs of the Italian company Pnevmax [12], in which the coefficient values are added K_{tq} .

The use of modern control systems allows you to compensate for the energy costs of dissipative losses in any part of the movement and thereby synthesize a variety of laws of motion, in the case of linear spring batteries. In the case of constructive solutions with non-linear spring batteries, the supply of a compensation pulse in the middle position of the output link is impossible [15].

To determine the speed of the output link, we write the equation of total mechanical energy without taking into account dissipative losses:

$$V_{\max} - V_T = T \quad (11)$$

Maximum kinetic energy

$$T = \frac{J \cdot \dot{q}^2}{2} \quad (12)$$

where J —reduced moment of inertia of the links of the drive of the rotary table to the output link; \dot{q} —output link angular velocity.

The current angular velocity is determined from the joint solution of Eqs. (11) and (12) and is equal to:

Table 2 Characteristics of pneumatic cylinders with return springs of the Italian company Pnevmax

Series	piston diameter (mm)	F_H (N)	F_K (N)	c (N/m)	K_{Iq}
Microcylinders series ISO 6431-1260 (travel 0–40 mm)	ø 12	9.9	26.5	415	14.84
	ø 16	10.8	22.6	295	13.56
	ø 20	10.8	22.6	295	13.58
	ø 25	7.9	49.1	1030	17.22
	ø 32	19.7	53.0	832.5	14.76
	ø 40	39.3	106.0	1667.5	14.71
Microcylinders series ISO 6431-128 «MIR» (travel 0–50 mm)	ø 12	4.0	8.7	94	13.83
	ø 16	7.5	21.0	270	15.12
	ø 20	11.0	22.0	220	13.32
	ø 25	16.5	30.7	284	12.79
	ø 32	23.0	52.5	590	11.16
	Cylinders Series ISO 15552-1319-20-21 (travel 0–50 mm)	ø 32	17.2	41.7	490
ø 40		24.6	83.4	1176	15.57
ø 50		51.0	114.8	1276	13.74
ø 63		51.0	114.8	1276	13.71
ø 80		98.1	194.2	1922	12.89
ø 100		98.1	194.2	1922	12.87

Where F_H —Initial force, with extended stem; F_K —Maximum force with spring retracted; c —spring stiffness

$$\dot{q} = \sqrt{\frac{2(V_{\max} - V_T)}{J}} \quad (13)$$

After substituting the values of the maximum and current potential energies, the above formula will take the form:

$$\dot{q} = r \sqrt{\frac{c \left[(2 + \bar{s})^2 - \left(\sqrt{1 + a'^2 + 2a' \cos q} - (\bar{L} - \bar{s}) \right)^2 \right]}{J}}, \quad (14)$$

or

$$\dot{q} = r \sqrt{\frac{c}{J}} \cdot \dot{q}', \quad (15)$$

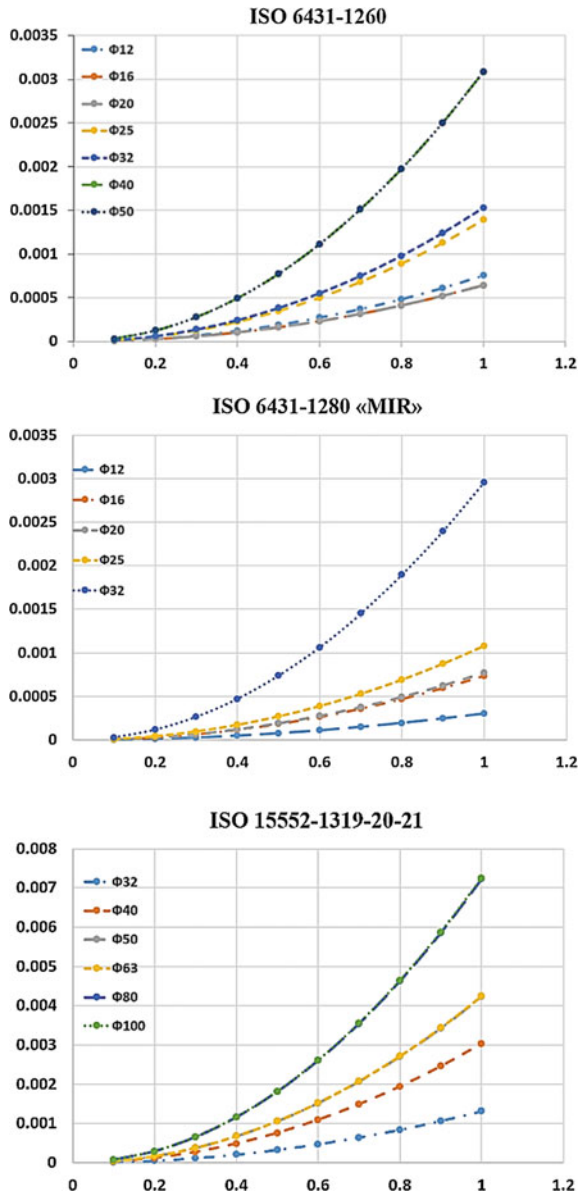
where

$$\dot{q}' = (2 + \bar{s})^2 - \left(\sqrt{1 + a'^2 + 2a' \cos q} - (\bar{L} - \bar{s}) \right)^2 \quad (16)$$

– an equation that determines the value of the angular velocity in a dimensionless form.

In Fig. 3 presents graphs of the change in the reduced moment of inertia of the rotary table J from a given travel time t for pneumatic cylinders, the parameters and characteristics of which are given in Table 1.

Fig. 3 Graphs of the change of the given moment J from the given time of movement t



Dissipative losses in a spring battery are determined by internal friction losses in the spring and losses in kinematic pairs.

The total losses to overcome the friction forces are determined by the equation:

$$A_{dis} = A_1 + A_2 \quad (17)$$

where A_{dis} —is the total work of the drive to overcome all dissipative forces;

A_1 —drive operation to overcome internal friction in the spring;

A_2 —operation of the drive to overcome friction in the articulated joints of the spring battery.

The operation of the drive to overcome internal friction in the spring is determined by the following equation

$$A_1 = 2\psi cr^2 = \psi V_{max} \quad (18)$$

For springs, the dispersion coefficient can be taken equal to $\psi = 0.01-0.015$ [4].

The work of the friction forces in the articulated joints of the spring battery is determined by the formula [3]

$$A_2 = 4rcf(d + d_2) \quad (19)$$

where f —articulation friction coefficient,

d —diameter of the axles of the hinge joints of the spring battery,

d_2 —diameter of the axis of the output link of the drive.

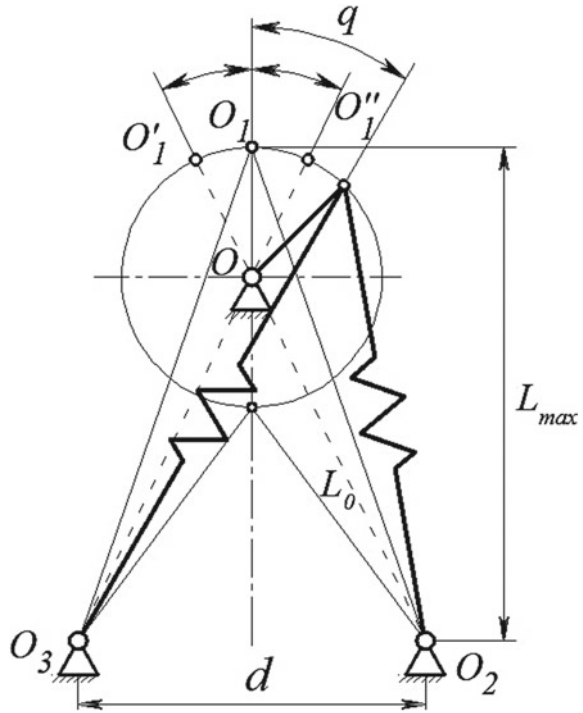
To ensure rotation, you can use a spring battery with two springs, shown in Fig. 4.

To ensure rotation at any angle, you can use a spring battery with two pneumatic cylinders with return springs, shown in Fig. 5.

4 Results Discussion

Mathematical dependencies are obtained, which make it possible to determine the characteristics of a mechatronic spring drive by the parameters of pneumatic cylinders. It is established that the pre-tensioning of the spring increases the speed. For each standard cylinder, the limit values of the moments of inertia of the rotary tables are set, which are reduced to the output link of the spring drive, depending on the rotation time, up to 1 s. It is shown that the energy consumption of a mechatronic spring drive with energy recovery is determined by the friction losses in the elements of the spring battery. In connection with these, energy consumption is several times reduced. Calculation formulas for determining dissipative losses are given.

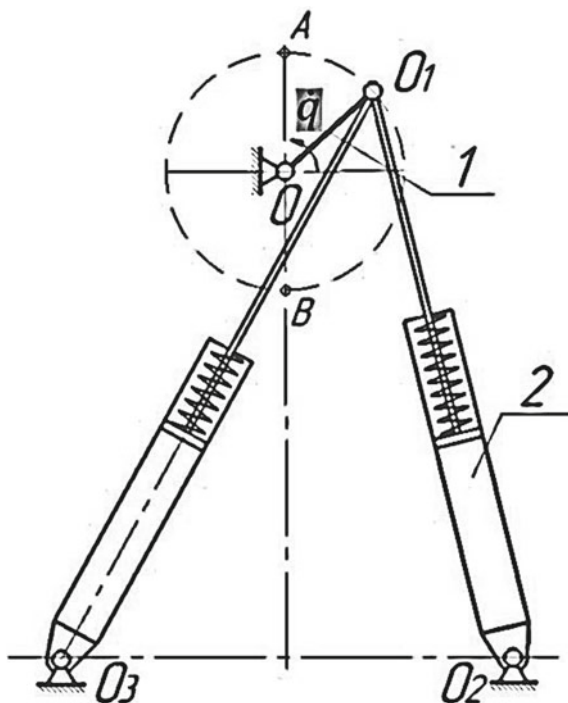
Fig. 4 Diagram of a spring battery with two tension springs



5 Conclusions

A comparative analysis of spring accumulators with an output rotary link with spring pre-tensioning with spring accumulators without preliminary tension is carried out. It is shown that an increase in pre-tension leads to an increase in speed with a slight increase in size. It is established that with an increase in the initial length of the pneumatic cylinder with a return spring, it leads to an increase in speed. The maximum values of the moments of inertia of the rotary tables are determined when using each standard size of a standard pneumatic cylinder with a return spring, which can be moved by such mechatronic drives at a given rotation time. The results of the work were used to develop a mechatronic pneumatic drive system for a filling and packaging machine for bulk food products. The results of the work can be used in the development of energy-saving technological equipment.

Fig. 5 Spring accumulator diagram with two pneumatic cylinders with return springs



References

1. Volkov AN, Andreyev ID, Matsko ON (2017) Science Week SPbPU: M-Iy Scientific Conference with International Participation. School of Metallurgical Engineering and Transportation. Part 2-SPb: Polytechnic Press, pp 30–32
2. Brilina OG, Yazikov YS (2016) To the comparative analysis of pneumatic, hydraulic and electric drives. Energy and resource saving, vol 4, issue no 1. South Ural State University
3. Pelupessi DS, Zhavner MV (2016) Spring accumulators with an output rotary link for stepping movements, vol 10, issue no 679. In: Proceedings of higher educational institutions. Engineering, pp 9–17
4. Pelupessi DS, Zhavner MV (2016) Spring accumulators with an output rotary link. News of the Samara Scientific Center of the Russian Academy of Sciences. Tom 18. vol 1, issue no 2, pp 256–259
5. Pelupessi DS, Zhavner MV (2016) Spring battery for stepper drives. In: Modern engineering. Science and education: Proceedings of the Fifth International Conference on Scientific Practice (June 30 to July 1, 2016). Publishing Vocational and Technical College, pp 499–509
6. Zhavner VL, Matsko ON (2016) Spring drives for reciprocal motion. J Machinery Manuf Reliab 45(1):1–5
7. Zhavner VL, Matsko ON, Zhavner MV (2018) Comparative analysis of mechatronic drives for reciprocal motion. Int Rev Mech Eng (IREME) 12(9):784–789
8. Nadezhdin IV, Mochanov AA (2015) Dynamics of mechatronic recuperative drives of loading devices of automated assembly systems. Bulletin of the Rybinsk State Aviation Technological Academy. P. A. Solovyov 1(32):19–24
9. Zhavner VL, Matsko ON (2016) Spring drives with balancing for horizontal reciprocating movements. Bull Sci Technol Dev 5(105):12–17

10. Zhavner VL, Matsko ON (2016) Spring drives with energy recovery for reciprocating movements. *Modern mechanical engineering. Sci Educ* 5:645–653
11. Nikitina KV (2016) Robot of parallel structure with spring battery. In: *Science Week SPbPU Proceedings of a scientific conference with international participation*, pp 8–11
12. The company “Pnevmaks”: the company’s website. Access mode: <https://www.pneumax.ru/>
13. Salamandra BL (2017) Analysis of ways to stabilize the position of the label on automatic packaging machines. *Probl Mech Eng Mach Reliab* 2:106–112
14. Nadezhdin IV, Mochanov AA (2015) Dynamics of mechatronic recuperative drives of loading devices of automated assembly systems. *Bulletin of the Rybinsk State Aviation Technological Academy. P.A. Solovyov* 1(32):19–24
15. Zhavner VL, Matsko ON (2016) Pruzhinnyye privody s uravnoveshivaniyem dlya gorizontalnykh vozvratno-postupatelykh peremeshcheniy. *Vestnik nauchno-tekhnicheskogo razvitiya* 5:12–17
16. Nadezhdin IV, Molchanov AA (2018) Energy efficient drives of mechatronic loading devices of automated assembly systems. *Fundam Appl Probl Eng Technol* 1:86–95
17. Nadezhdin IV (2015) *Actuators of cyclic automatic machines and mechatronic systems*. LAP LAMBERT Academic Publishing, Deutschland, 280p

Author Index

A

Aksenov, L. B., 1
Andrienko, Pavel A., 11
Asheichik, Anatoly A., 17

B

Babichev, Dmitry T., 27
Burkhovetskiy, Valerii V., 103

C

Chekanin, Alexander V., 41
Chekanin, Vladislav A., 41

D

Demidov, Nicolai N., 49
Dobretsov, Roman Yu., 49, 63

E

Evgrafov, Alexander N., 75
Evgrafov, Sergey A., 75

F

Filippenko, George V., 83

I

Ivanova, Galina V., 175

K

Kaninskii, Andrei O., 49

Karazina, Anna V., 93
Karazin, Vladimir I., 11, 93
Khanaev, Valeri M., 103
Khisamov, Andrey V., 93
Khlebosolov, Igor O., 11
Khlopkov, Elisey A., 103
Korotkikh, M. T., 111, 193
Koshkin, Anatolii V., 93
Kozlikin, Denis P., 11, 93
Kryazhev, Dmitriy Y., 111
Kudryavtsev, Vladimir N., 111
Kunkin, S. N., 1
Kurushkin, Dmitry V., 103
Kuznetsov, A. Pavel, 119
Kuznetsov, V. Ruslan, 119

L

Lebedev, Sergey Yu, 27
Lepekha, Olga G., 151
Li, Sen, 221
Lyubomudrov, Sergey A., 103

M

Manzhula, Konstantin, 129
Miroshnichenko, Sergey T., 151

N

Naumov, Alexander, 129

O

Ostropiko, Eugeny S., 103

P

Petrov, Gennady N., 75
Pomeranskaya, Alexandra K., 151
Popov, Alexander A., 175
Popov, Alexander I., 139
Potapov, N. M., 1
Pukhliy, Vladimir A., 151

R

Radkevich, Mikhail M., 139

S

Semenova, Nadezhda S., 163
Semenov, Yuri A., 163
Skotnikova, Margarita A., 175
Sokolov, Sergei, 129
Strelnikova, Angelina A., 175
Syundyukov, Ilnur S., 175

T

Teplukhin, Vasily G., 139

U

Uvakina, Darya V., 63

V

Vulfson, Iosif I., 183
Vyunenکو, Yuriy N., 103

W

Wu, Long, 209

Y

Yan, Chuanchao, 209, 221

Z

Zakharov, S. V., 193
Zhao, Wen, 209
Zhavner, Milana V., 221
Zhavner, Victor L., 209
Zhuravlev, Alexander A., 151
Zorin, Daniil K., 17